

Low-cost pH sensors based on discrete PCB ion-sensitive field effect transistors

Rhys David Ashton

-

Doctor of Philosophy

-

University of York

-

Physics, Engineering and Technology

-

September 2023

Abstract

Diagnostic technologies will play a critical role in addressing current and future healthcare challenges, with the greatest impact through implementing these technologies at the point of care (PoC). For truly widespread deployment, these PoC technologies should be low-cost and amenable for mass manufacture, even in resource-limited settings, without compromising analytical performance.

Discrete, extended gate pH-sensitive field-effect transistors (dEGFETs) fabricated on widely used printed circuit boards (PCBs) are a low-cost, simple to manufacture analytical technology. Electrodeposited iridium oxide (IrOx) films have emerged as a promising pH-sensitive transducer due to their facile deposition. While IrOx is predicted to have a beyond-Nernstian pH sensitivity, the performance measured experimentally is typically lower and variable.

This thesis demonstrates a dEGFET pH sensor based on PCB extended gate electrodes and electrodeposited IrOx, which repeatedly displays beyond-Nernstian pH response. Using complementary surface-analysis techniques, it is shown the high pH sensitivity and repeatability is determined both by the chemical composition and critically the uniformity of the IrOx film. Electrochemical polishing of the extended gate electrode prior to electrodeposition enhances IrOx uniformity, leading to a median pH sensitivity of 70.7 ± 5 mV/pH (n=56) compared to 31.3 ± 14 mV/pH (n=31) for non-polished electrodes.

The applicability of these devices is demonstrated through the quantification of the β -lactam antibiotic ampicillin, via the pH change that occurs due to hydrolysis catalysed by β -lactamase enzymes. This lays the foundations for a susceptibility assay towards the public health challenge of antimicrobial resistance (AMR). Additionally, this thesis explores the integration of electronically controlled microfluidic valves onto the PCB substrates, towards the development of lab-on-chip systems and PoC diagnostics.

The highly sensitive and repeatable dEGFET sensors presented here show great promise as a low-cost diagnostic technology. Moreover, the use of PCB substrates is suitable for manufacture in resource-limited settings, enabling widespread diagnostic testing.

Contents

List of Figures	vi
List of Tables	x
Acknowledgements	xi
Declaration	xii
1 Introduction	1
1.1 Motivations for Widespread Deployment of Diagnostic Testing	1
1.1.1 Antimicrobial Resistance (AMR)	1
1.1.2 Faecally Contaminated Water	2
1.2 Thesis Goal & Overview	3
2 Sensor Theory & Literature Review	6
2.1 Biosensors	6
2.1.1 Bio-recognition	6
2.1.2 Signal Transduction	8
2.2 pH	10
2.2.1 Measuring pH	11
2.3 ISFET Theory	13
2.3.1 MOSFET	13
2.3.1.1 MOSFET Varieties	14
2.3.2 ISFET	17
2.3.3 Site Binding Model	17
2.3.4 Electrochemical Double Layer (ECDL)	18
2.3.4.1 ECDL Capacitance	19
2.3.4.2 ECDL Potential	21
2.3.5 Nernst Equation	22
2.3.6 Reference Electrodes	23
2.3.6.1 Ag/AgCl/Saturated KCl	24

2.4	pH targeted Ion-sensitive Electrode Literature	25
2.4.1	ISFET	25
2.4.2	EGFET & dEGFET	26
2.4.3	dEGFET pH Sensors Based on PCB Substrates	27
2.4.4	Iridium Oxide pH Sensing Layers	28
3	Methods & Experimental Techniques	33
3.1	Chemicals	33
3.2	PCB Design	33
3.3	Discrete EGFET Readout and Bias Circuit	34
3.4	Electrochemical Techniques	35
3.4.1	Electrochemical Cells	36
3.4.2	Chronoamperometry	37
3.4.3	Cyclic Voltammetry	37
3.4.3.1	Electrodeposition of Iridium Oxide	38
3.4.4	Electrochemical Polishing	40
3.5	Physical Characterisation Techniques	43
3.5.1	Atomic Force Microscopy (AFM)	43
3.5.2	Scanning Electron Microscopy (SEM)	44
3.6	Chemical Characterisation Techniques	47
3.6.1	Energy-dispersive X-ray Spectroscopy (EDX)	47
3.6.2	X-ray Photoelectron Spectroscopy (XPS)	48
4	PCB ISFET Characterisation	51
4.1	Electrode Preparation	51
4.2	Characterisation	52
4.2.1	pH Sensitivity of IrOx Coated PCB Electrodes: unpolished vs. polished	52
4.2.2	Electrochemical Analysis of IrOx Deposition	54
4.2.3	Physical Characterisation via SEM & AFM	57
4.2.4	Energy-dispersive X-ray Spectroscopy (EDX)	58
4.2.5	X-ray Photoelectron Spectroscopy (XPS)	61
4.2.6	Discussion	66
4.2.7	pH Sensitivity within Polished Sensors	69
4.3	Conclusion	69
5	Biological Assay & Detection	71
5.1	Introduction & Literature	71

5.2	Assay Theory	73
5.3	Determining Suitable Assay Buffer	73
5.3.1	pH Buffer Theory	75
5.3.2	Buffer Calculations	75
5.4	Assay Method	78
5.5	Kinetic Assay	78
5.5.1	Kinetic Raw Data Response	79
5.5.2	Kinetic Secondary Trends	81
5.5.3	Kinetic Analysis	85
5.5.4	Kinetic Conclusions	88
5.6	Endpoint Methodology	88
5.6.1	Endpoint Calibration Curve without pH Calibration	90
5.6.2	Endpoint Calibration Curve	91
5.6.3	Endpoint Conclusion	91
6	Electrowetting Valves	93
6.1	Introduction & Literature	93
6.2	Methods	95
6.2.1	Surface Wettability Modification	95
6.2.2	UV Ozone	97
6.2.3	Plasma Treatment	97
6.2.4	Washburn Equation Theory	98
6.2.4.1	Flow Velocity Dependence on Channel Meniscus Distance	99
6.3	Capillary Flow	100
6.3.1	FR4 Contact Angle	100
6.3.2	PDMS Flow Channels	101
6.3.3	PDMS Contact Angle vs. UV-ozone Duration	101
6.3.4	PDMS 3D Master Mould Characterisation	103
6.3.4.1	Master Height	103
6.3.4.2	Mould Width	105
6.3.4.3	Mould Surface Roughness	106
6.3.5	Washburn Simulations of Capillary Flow Channels	106
6.3.6	Device Assembly & Clamping	107
6.3.7	FR4 Capillary Flow	109
6.3.8	Flow Rate Empirical Analysis	110
6.3.9	Blank Cu Impeding Flow	111
6.4	Investigating PFDT Deposition	114

6.4.1	Polished Electrode CV & CA Repeatability	115
6.4.2	PFDT Deposition Methods CV & CA	116
6.4.3	Sonication After PFDT Deposition	118
6.4.4	FR4 Contact Angle	119
6.4.5	Stopping Capillary Flow Using PFDT electrodes	121
6.5	PFDT Electrochemical Cleaving	121
6.5.1	PFDT Thiol Desorption at -1.3 V	122
6.5.2	Disruption of PFDT Layers Using Positive Potentials	123
6.5.3	PFDT Disruption in Flow Channels	123
6.5.4	Conclusion	124
7	Conclusions & Future Work	125
7.1	Summary	125
7.2	Electrowetting Valves Future Work	126
7.3	β -lactamase Assay Future Work	127
7.4	DNA Amplification Assay	127
7.4.1	DNA	128
7.4.2	pH Change by Nucleotide Incorporation	128
7.4.3	Loop Mediated DNA Amplification (LAMP)	128
7.5	LAMP Towards <i>E. coli</i>	132
7.5.1	Methods	132
7.5.2	Target	135
7.5.3	Optical Assay Development	137
7.6	LAMP on PCB dEGFET	139
7.6.1	Dri-Ref Electrode & Fluidics	140
7.6.2	Kinetic Assay	140
7.6.2.1	Material Inhibition	144
7.6.3	Conclusions	144
	Abbreviations	146
	Bibliography	150

List of Figures

2.1	General schematic of a biosensor	7
2.2	pH scale showing H^+ and OH^- concentrations	10
2.3	Chemical structure of Phenol Red pH indicator dye	12
2.4	Double junction glass pH meter schematic	13
2.5	Schematic of MOSFET structure	14
2.6	MOSFET modes of operation	15
2.7	BSS159 MOSFET drain-source current	16
2.8	Schematic of ISFET structure	17
2.9	Site binding model	18
2.10	Representation of the ECDL and site binding model	20
2.11	Ag/AgCl/potassium chloride (KCl) reference electrode	24
2.12	Diagrams of EGFET and dEGFET structures	27
3.1	System diagram including readout circuitry	34
3.2	Readout circuitry output vs. applied potential at transistor gate	35
3.3	Typical three-electrode electrochemical cell	36
3.4	Chronoamperometry and cyclic voltammetry input waveforms	37
3.5	Typical cyclic voltammogram for single reversible redox couple	38
3.6	Iridium oxalate deposition solution	40
3.7	Custom 3D printed IrOx electrodeposition jig	41
3.8	Schematic representation of electrochemical polishing	42
3.9	Generalized schematic of an AFM	45
3.10	Schematic of SEM and EDX setup	46
3.11	SEM interaction volume	46
3.12	Production of characteristic X-rays within EDX	49
3.13	Schematic Diagram of XPS system	50
4.1	CV during IrOx electrodeposition	52
4.2	Unpolished vs. polished dEGFET pH sensitivity	53
4.3	CV comparing unpolished vs. polished sensors during IrOx electrodeposition	55

4.4	CV in alternative electrolytes to isolate redox peaks	56
4.5	SEM images of blank and IrOx coated Cu electrodes	59
4.6	AFM images and analysis of blank Cu electrodes	60
4.7	ImageJ analysis of IrOx coated electrode SEM images	60
4.8	EDX compositional analysis of blank and IrOx coated electrodes	61
4.9	EDX elemental maps of blank electrodes	62
4.10	EDX elemental maps of IrOx coated electrodes	63
4.11	XPS broad scan spectra	64
4.12	XPS spectra and elemental analysis of blank Cu electrodes	65
4.13	XPS spectra and elemental analysis of IrOx Cu electrodes	67
4.14	Additional XPS spectra and elemental analysis of IrOx Cu electrodes	68
4.15	Impact of IrOx oxidation state on performance of polished electrodes	70
5.1	Penicillin β -lactam antibiotic structures	74
5.2	Dissociated H^+ ions of ampicillin for varying pH	74
5.3	KPI buffer capacity vs. pH	76
5.4	KPI buffer capacity vs. buffer concentration	77
5.5	pH delta of KPI buffer after addition of ampicillin concentrations	78
5.6	Kinetic β -lactam assay and controls as measured by PCB dEGFET	80
5.7	Kinetic β -lactam assay as measured by gold electrode dEGFET	82
5.8	Pre-hydrolysed ampicillin performed on dEGFET sensor	83
5.9	Kinetic β -lactam assay as measured by PCB dEGFET	84
5.10	Extracted pH change 5 minutes after injection of β -lactamase	84
5.11	Smoothed and linearly adjusted dEGFET output	85
5.12	Rate of pH change after smoothing and linear correction	86
5.13	Calibration curve for kinetic β -lactam assay	87
5.14	Control experiments for kinetic β -lactam assay	87
5.15	Endpoint β -lactam assay dEGFET voltage output	89
5.16	Unstable endpoint β -lactam assay dEGFET voltage output	90
5.17	dEGFET concentration curve	91
5.18	Calibrated dEGFET concentration curve	92
6.1	Schematic of PCB electrode and PDMS flow channel layout	95
6.2	Interfacial energies of water droplet on a flat surface	96
6.3	Images from CA goniometer	96
6.4	Schematic of UV-ozone surface cleaning	98
6.5	Simulated flow velocity based on fluid distance	99
6.6	CA of FR4 substrate after various sensor treatment steps	100

6.7	3D printed PDMS mould	102
6.8	CA of PDMS after UV-ozone exposure	102
6.9	Profilometer data of 3D printed PDMS mould channels	104
6.10	Analysis of 3D printed PDMS mould channel height	104
6.11	Analysis of 3D printed PDMS mould channel width	106
6.12	Python simulation using the Washburn equation showing the flow velocity in a 250 μm high flow channel	108
6.13	Python simulation using the Washburn equation showing the flow velocity in a 100 μm high flow channel	108
6.14	Final clamp design used for all testing of flow channels	109
6.15	Capillary flow in PDMS channels on FR4 substrate	110
6.16	Measured flow velocity as a function of meniscus channel distance	111
6.17	Blank Cu electrodes stopping flow in PDMS channels on FR4 substrate	112
6.18	CA of unpolished and polished Cu electrodes	113
6.19	Polished blank Cu electrodes allowing flow in PDMS channels on FR4 substrate	113
6.20	White precipitate forming around the working electrodes at high potentials . .	115
6.21	CV of 4 separate Cu electrodes after polishing	116
6.22	CV before and after deposition of the PFDT layer via stamping, dropcasting and submersion	117
6.23	Ratio of Cu reduction peak after PFDT deposition vs. before deposition	118
6.24	CA of Ox-plasma treated electrodes after PFDT deposition	119
6.25	Impact of PFDT deposition method on the FR4 CA	120
6.26	FR4 CA after treatment steps during sensor fabrication	121
6.27	PFDT coated Cu electrodes halting capillary flow in PDMS channels on FR4 substrate	122
6.28	CVs measured after application of a -1.3 V potential	123
6.29	CVs measured after application of a +2 V potential	124
7.1	Molecular structure of DNA	129
7.2	Mechanism of H^+ ion production at the point of nucleotide incorporation . . .	130
7.3	LAMP amplification process to reach stem-loop structures	131
7.4	LAMP amplification process beyond stem-loop structures	133
7.5	Gel electrophoresis showing extracted DNA sample	136
7.6	LAMP optical assay using Phenol Red pH indicator	137
7.7	Threshold region of LAMP optical assay	138
7.8	LAMP optical assay calibration curve	139
7.9	OCP stability of Dri-Ref reference electrode	141

7.10 Fluidic manifold for use with low volume LAMP assay	141
7.11 Kinetic LAMP assay dEGFET output voltage	142
7.12 Kinetic LAMP assay control measurements from dEGFET	143
7.13 Tarnished PCB electrodes after running LAMP assay	143
7.14 Colourmetric LAMP assay initial investigation into material inhibition	144

List of Tables

2.1	Possible Iridium Oxide complexes	29
2.2	Comparison of state-of-the-art PCB based pH sensors	31
2.3	Comparison of state-of-the-art pH sensors that employ IrOx as a pH sensitive layer	32
3.1	IUPAC notation of electron energy levels	48
4.1	XPS elemental atomic % and notable species analysis	62
6.1	3D printed PDMS mould channel height analysis	105
6.2	3D printed PDMS mould channel width analysis	105
6.3	Values used within the Washburn equation to simulate flow velocity	107
7.1	Reagents used in LAMP assay	134
7.2	LAMP primers targeting <i>E. coli</i>	134

Acknowledgements

Undertaking a PhD has been a life changing experience full of highs and lows. I am grateful to all of those people who have been part of the journey, it would not have been possible without you.

Prof. Steve Johnson, meeting you on a tour for prospective undergraduate students and then being allocated to your supervision group has directed my education in ways I could not have imagined, and undoubtedly changed my life. To this point you have taught me almost everything I know, no one could have equipped me better for the rest of my career. Steve, you managed to do all that with an ever-present sense of humour and humility, for that I am incredibly grateful.

Thank you to Dr. Simon Bale and Prof. Andy Tyrrell in your role as thesis advisor's, your outside perspective was invaluable. Thanks extends to the numerous support and technical staff at the university for always being willing to assist.

To those in the BIT and Photonics research groups, to each member past and present, thank you for the enriching environment you all helped create. If I had to single out one thing you have all taught me, it would be the importance of passionately discussing science and challenging understanding.

A heartfelt thanks to those I spent the most time with, Lisa (our morning chats), Casper & Matt (wise advisers), Callum (a joint love of ISFETs), Kalum (our shared PhD journey) and Fran (the omni-positive desk buddy). Your knowledge and friendships have been equally important, I truly do not know if this would have been possible without your support everyday. Alex Pembery, thank you for your hard work as a summer undergraduate student. To geese with 4 legs everywhere and particularly tall ducks, for making the days a little lighter.

I feel incredibly privileged to have been able to dedicate 4 years of my life to this arguably self-indulgent pursuit. To my family who have worked hard to provide me that opportunity, Mom, Dad, Nan & Grandad, I will forever be in your debt and hope that I have made you proud. Sully, thank you for always being happy to see me, no matter how little I visited. I will always appreciate the Eames family, Mark, Caroline and Alicia, especially for your support during the uncertainty of the initial covid lockdown.

To those I didn't get to spend enough time with, especially Herman, Will & Nico, thank you for your support from afar. UYLC and a honorary membership to the Biology football team served as an essential identity outside of the lab.

Kaity, some *three* years that turned out to be? I know this body of work has involved just as much sacrifice from you as it has from me, I hope you appreciate how important your support has been. I am glad we have so many more years to enjoy.

Declaration

I, Rhys Ashton, declare that this thesis is a presentation of original work and I am the sole author. This work has not previously been presented for a degree or other qualification at this University or elsewhere. All sources are acknowledged as references. Below is an exhaustive list of exceptions to this statement:

- Work presented in chapter 4 is published as a lead authorship journal article. Rhys Ashton, Callum D. Silver, Toby W. Bird, Ben Coulson, Andrew Pratt, Steven Johnson. “*Enhancing the repeatability and sensitivity of low-cost PCB, pH-sensitive field-effect transistors*”, *Elsevier: Biosensors and Bioelectronics*, Volume 227, 1 May 2023, 115150. ISSN 0956-5663. <https://doi.org/10.1016/j.bios.2023.115150>.
- X-ray photoelectron spectroscopy measurements presented in this *Elsevier* publication and in chapter 4 were undertaken by Dr. Ben Coulson and Dr. Toby Bird. Peak fitting was performed by Dr. Toby Bird.
- Measurements on glass substrate, Au/Cr electrode dEGFET sensors, presented in chapter 5, were performed by Dr. Callum Silver.
- DNA purification and gel electrophoresis utilised in chapter 7 were performed by Hannah Walker.
- The PCB clamp presented in chapter 6 was designed and tested in collaboration with an undergraduate student, Alex Pembury, under my supervision.

Chapter 1

Introduction

This chapter provides the rationale for this research and articulates its specific objectives, after which the thesis outline is presented.

1.1 Motivations for Widespread Deployment of Diagnostic Testing

There exist many current and future healthcare issues globally where diagnostic testing is a key component of the solution. This was clearly illustrated by the covid-19 pandemic where a broad array of tests were essential to inform the response [1].

“Gold standard” methods such as polymerase chain reaction (PCR) provided highly sensitive, accurate and reliable results to inform policymakers and clinicians, but require skilled operators and are costly. Lateral flow devices (LFDs) were used widely to offer rapid results to end users and highlighted the power of diagnostic tests that can be deployed at point of care (PoC).

Beyond global pandemics, there remains an urgent need to develop diagnostic tests that are suitable for deployment at PoC. This requires the development of new technologies that must be simple to use, while still providing analytical performance metrics that are suitable for clinical utility. Critically, for routine use towards common healthcare problems, sensor fabrication must be low-cost, high yield and ideally utilise existing infrastructure.

1.1.1 Antimicrobial Resistance (AMR)

There is continued and growing concern about the impact of antimicrobial resistance (AMR), sometimes referred to as drug resistant infections (DRI). These terms refer to the ability of

microbes, including viruses, fungi, parasites and bacteria, to continue to grow in the presence of antimicrobial compounds such as antibiotics.

It is already estimated that AMR causes 700,000 deaths per year and has been predicted to grow to 10 million per year by 2050, alongside the associated healthcare repercussions costing \$100 trillion globally [2]. Although this exact value is disputed [3], there is consensus that its impact will worsen and could lead to the development of AMR in many common bacterial infections, posing a risk to patients undergoing otherwise low-risk procedures.

Bacteria that survive exposure to an antibiotic intended as a treatment can evolve to become resistant to that drug. This process, known as drug resistance, has occurred naturally since the first antibiotics were discovered. Historically, the periodic introduction of new antibiotics was effective in combating drug resistance, however the reserve of new antibiotics has been depleted faster than new drugs can be developed, due to the complexity of drug discovery and lack of return on investment [4]; even with the impending need for additional antibiotics.

Many health organizations demand that healthcare staff reduce antibiotic distribution in all settings, where antibiotics should only be prescribed when the infection is known to be susceptible to that specific treatment [2, 5]. Currently, healthcare staff do not have the technology to test for antibiotic susceptibility at the point of prescription, as the established methods using bacterial growth take approximately 24 hours to return a result. Often the best balance of time, cost and patient satisfaction is to prescribe antibiotics without knowledge of the susceptibility to the drug, which may be updated following testing at a later time.

An informed approach is required at the PoC, based on rapid testing of patient samples to assist healthcare staff. Information on the susceptibility of an infection to available antibiotics will result in better patient outcomes and potentially slow the evolution of DRIs so we can maintain essential access to potent antibiotics. For healthcare challenges such as the fight against AMR, any PoC diagnostic test must be simple and cheap to manufacture to enable widespread deployment.

1.1.2 Faecally Contaminated Water

The importance of low-cost sensor technologies is exemplified by deployment of healthcare technologies in low- and middle-income countries (LMICs). A notable example is the contamination of drinking water with pathogenic bacteria, which leads to unnecessary illness and death across developing nations; 2.39 billion cases of diarrhoeal disease were estimated in 2015 alone, resulting in 1.8 million deaths [6], many of which are associated with the consumption of contaminated drinking water.

In economically developed nations, treated water is often distributed through piped infras-

structure resulting in few outbreaks or deaths from contamination [7]. In LMICs, without this infrastructure, contamination can enter a water source through many pathways [8], including run-off from animal waste. It is widely agreed, testing is the only reliable method of identifying if a water source is contaminated and forms an essential part of a multi-faceted solution, in tandem with appropriate water treatment and education [9].

Water testing in developed countries is performed by bacterial culture. While well established, this is a slow and skilled process which is rarely suitable for deployment in LMICs. New approaches to monitor water quality are urgently required. For widespread usage in LMICs, these analytical technologies would ideally be suitable for manufacture using existing infrastructure and capabilities within the country.

Current practices for diagnostic testing across these and many other global issues are imperfect. The quantity of tests performed is often inadequate and a delayed time to result may limit their impact. PoC diagnostic testing is ideal, with automation to ensure simplicity and a rapid response that can better inform decisions. To fully realise their potential, PoC tests should not sacrifice sensitivity or specificity compared to lab based methods, and most importantly they must be suitable for widespread deployment by reducing the cost and complexity of fabrication.

1.2 Thesis Goal & Overview

Motivated by the need for PoC diagnostic technology that can be fabricated using low-cost and simple processes, this thesis focuses on the development of a pH sensor based on discrete field effect transistors (FETs) and printed circuit board (PCB) substrates that can be applied as a biosensor towards a broad range of global issues. This platform technology is demonstrated towards an assay that can detect the enzymatic turnover of the antibiotic ampicillin; the mechanism of action of β -lactam resistant bacterial infections. This thesis also presents an initial exploration of electronically actuated microfluidic valves integrated onto the PCB substrate towards PoC automation and a complete lab-on-chip (LoC) device. Finally, early stage testing of the PCB pH sensor for detection and quantification of deoxyribonucleic acid (DNA) amplification is presented.

Chapter 2: Literature Background and Theory

This chapter begins by briefly discussing the wide variety of biosensors that have been employed within the literature, before focusing on ion-sensitive field effect transistors (ISFETs) as pH sensors. Underlying theory required to understand operation of electrochemical pH sensors is presented, before moving onto topics specific to ISFET and derivative devices. The

broad array of substrates and pH sensing materials used across literature including current and emerging technologies are also presented.

Chapter 3: Methods and Experimental Techniques

This chapter details the fabrication procedures of the pH-sensitive, extended gate ion-sensitive field effect transistors (EGFET) based on discrete FETs, alongside operating principles of the key experimental and characterisation techniques used within the experimental chapters.

Chapter 4: PCB dEGFET Characterisation

This chapter explores development of the discrete extended gate ion-sensitive field effect transistor (dEGFET) in which the extended gate electrode is fabricated on PCB and modified by electrodeposition of iridium oxide (IrO_x). It showcases a facile approach for electrode treatment prior to electrodeposition, which drastically increases median pH sensitivity and significantly enhances reproducibility. A combination of complimentary surface analysis techniques are used to understand the electrochemical, physical and chemical properties, which show the high pH sensitivity and repeatability of the dEGFETs are dependent on both the chemical composition and, critically, the uniformity of the IrO_x film.

Chapter 5: Biological Assay & Detection

Work in this chapter applies the IrO_x, PCB-based dEGFET to detection and quantification of enzymatic activity via turnover of β -lactamase antibiotics towards the global issue of AMR. In this assay, enzymatic turn-over of ampicillin leads to a bulk pH change based on the selection of a suitable buffering capacity, as discussed at the beginning of the chapter alongside the underlying principles and relevant literature. Results demonstrate the ability of the dEGFET to detect this pH change using both kinetic and endpoint measurements.

Chapter 6: Electrowetting Valves

In this chapter, the motivation for the development of automated sample delivery onto the sensor surface using on PCB microfluidics and electronically controlled electrowetting valves is presented, including current literature on lab-on-PCB devices suited for PoC. The theory that enables device operation and manipulation of system characteristics is presented, before capillary flow is realised on the PCB substrate through polydimethylsiloxane (PDMS) flow channels. Electrochemical techniques are used to characterise the deposition and removal of a hydrophobic film applied to the valve electrodes.

Chapter 7: LAMP Future Work & Conclusions

The chapter initially summarises the work presented across this thesis before a brief discussion of future work related to the β -lactamase assay and electrowetting valves. Initial research is also presented towards the detection and quantification of isothermal DNA amplification using the low-cost PCB dEGFET sensors, alongside discussion of future work that could fully realise such an assay on discrete PCB based sensors.

Chapter 2

Sensor Theory & Literature Review

This chapter begins by briefly discussing biosensor modalities that have been employed within the literature, before focusing on ion-sensitive field effect transistors (ISFETs) as pH sensors. Underlying theory required to understand the operation of electrochemical pH sensors is presented, before moving onto topics specific to ISFET and derivative devices. The broad array of emerging substrates and pH sensing materials reported across literature are also presented.

2.1 Biosensors

Biological sensors (biosensors) can be considered as having two key aspects, a component for recognition of a biological or chemical target and a physico-chemical transducer to detect the interaction between the recognition element and the target [10]. Figure 2.1 shows a variety of modalities across both aspects, which are often followed by signal conditioning and processing.

2.1.1 Bio-recognition

The recognition stage utilises an interaction with the target in the form of a physical, biological or chemical alteration. The biochemical target (biomarker) dictates suitable recognition elements, where the interaction is selective and specific to that molecule, protein, cell or nucleic acid [12].

Perhaps the most common of these bio-recognition elements are antibodies, which are proteins that bind to their antigen, often another protein or virus. Assays utilising this mechanism are named immunoassays [13] where the antibody-antigen binding can be detected directly, for example through the associated change in mass or electrical charge, or indirectly through the inclusion of additional label such as an enzyme [14] or fluorophore, leading to a change in redox activity, colour or fluorescence.

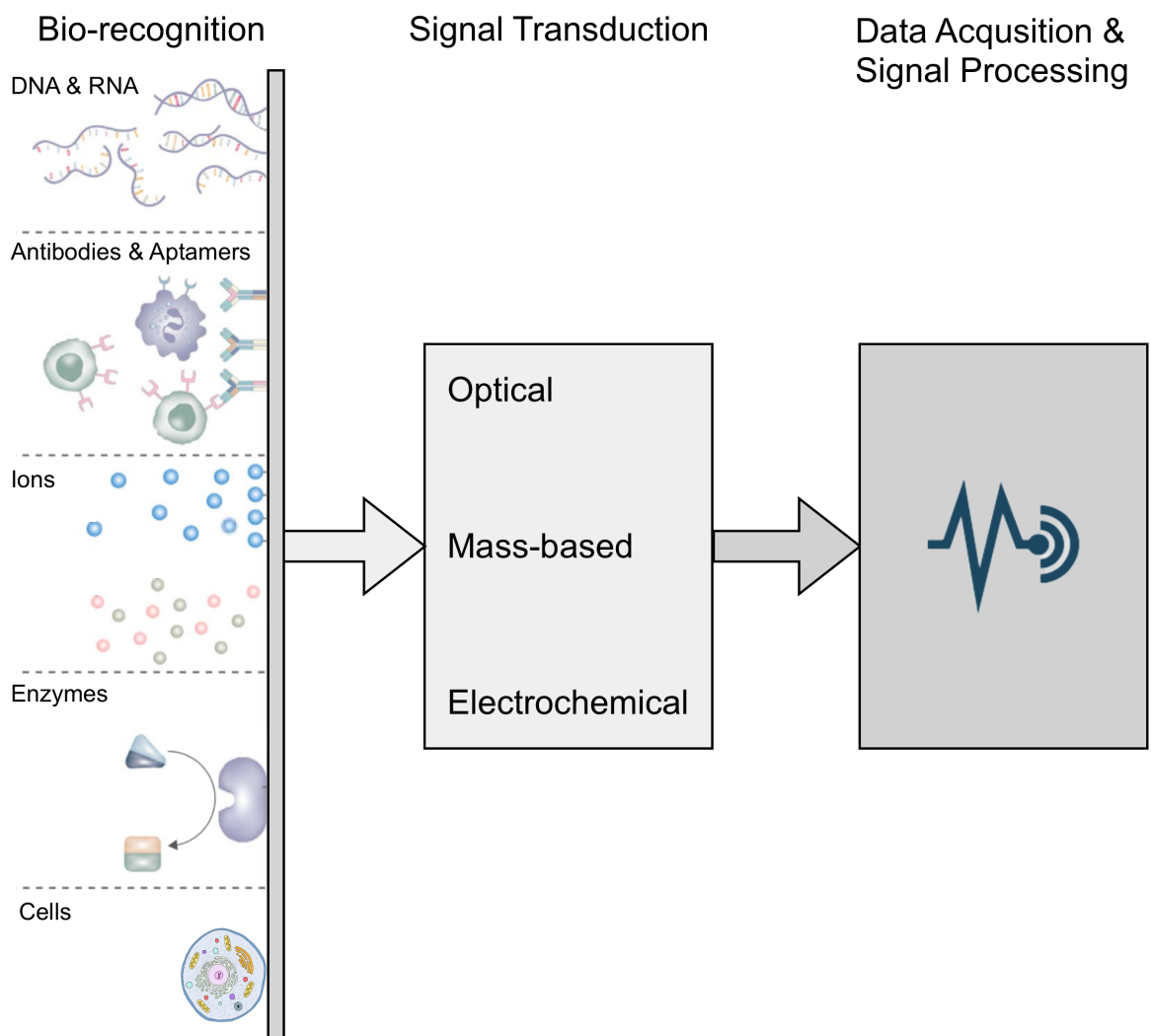


Figure 2.1: General schematic of a biosensor and the range of modalities via which it can operate. Adapted from [10, 11].

There is growing interest in the use of aptamers [15], oligonucleotide sequences that act as artificial chemical antibodies. Once a range of candidate aptamers has been identified, often through a process known as systematic evolution of ligands by exponential enrichment (SELEX) [16], their affinity (K_D) and specificity towards the target can be evaluated. Importantly, these aptamers can be produced artificially without the need for animals, at higher quantities and at lower costs than antibodies. Antibodies and aptamers are both often directly immobilised on the surface of a transducer or nanoparticles using an appropriate surface chemistry such as exposed carboxyl or aldehyde groups.

Nucleic acid based biosensors utilise the strong affinity between base pairs on complementary regions of nucleotide strands for high specificity towards target nucleic acid sequences [17, 18]. The ability to synthesize deoxyribonucleic acid (DNA) strands of increasing length has helped facilitate the growth of this bio-recognition element. Immobilisation of these nucleic acids is often performed using thiols and amine groups.

Enzymatic biosensors rely on an enzyme to catalyse a reaction with the target, where the resulting product such as hydrogen peroxide, protons and other chemical molecules is monitored [19].

Whole cells are also being explored as a form of bio-recognition element, where deviation away from their normal cellular activities can be used to indicate the presence of target analytes, and can again be monitored by a signal transduction element [20].

To ensure specificity and to reduce non-specific binding to the surface from molecules within the sample matrix that are not the target, a broad range of blocking agents are used including bovine serum albumin (BSA), casein, poly-lysine and the developing field of polymer brushes. More information on the importance of blocking within surface bound biosensors can be found in literature [21, 22].

2.1.2 Signal Transduction

The second stage of any biosensor is a form of signal transduction which detects and ideally quantifies the interaction between the bio-recognition element and target. This transducer element transforms the bio-recognition signal into another, via some physico-chemical method, where the three main categories are optical, electrochemical and mass based, although novel approaches exist [10]. As shown in Figure 2.1 each of these categories contains a variety of approaches within.

Optical transduction methods are compatible with most biorecognition methods, can provide low detection limits and are insensitive to electromagnetic noise. The optical signal itself can be detected using several spectroscopic methods, with the most popular being fluorescence and surface plasmon resonance (SPR) based [23]. Within fluorescence biosensors this

fluorescent signal can be inherent to the molecule of interest, or more commonly via a reporting label such as intercalating dyes and fluorophore. SPR utilises a polarised light source, prism and detector to deduce a refractive index change at the sensor surface, as the target molecule binds with an appropriate receptor on its surface.

The two main mass-based techniques are quartz crystal microbalance (QCM) and micro cantilevers, which both fit under the umbrella term of micro-electro-mechanical systems (MEMS) [24, 25]. In QCM, changes in mass occurring as target molecules bind to a piezoelectric sensor are seen as shifts in resonant frequency of its electronically driven oscillations. Micro cantilevers operate via a similar mechanism, where a cantilever is commonly fabricated with one end fixed to a substrate and the other free hanging over a small cavity, with changes in mass altering the oscillating frequency. Both methods allow for quantification, based on knowledge of the bound molecules' structural properties, using the Sauerbrey equation.

Electrochemical transducers are commonly categorised based on the different electronic parameter which they measure, being amperometric, potentiometric, and impedimetric [26, 27]. Amperometric sensors operate via the most widely used mechanism, by monitoring the current produced by the redox activity of an electroactive species. The most well-known example of an amperometric sensor is the blood glucose sensor, which measures the current caused by redox active H_2O_2 , which is produced in quantities proportional to glucose, by glucose oxidase (GOx) enzyme activity [28]. Such amperometric devices measure the current at a constant potential. A variation named voltammetric sensing varies the potential while the current is monitored.

Impedance based devices monitor the capacitive and resistive properties of electron transfer at a working electrode, through analytes and receptors, which are often immobilised on the electrode surface [29, 30]. Potentiometric sensors measure the non-faradaic charge accumulated at the interface of a working electrode, where the field is dominated by ion-selective electrodes (ISE) [31].

In conclusion, the make-up of any biological sensor is focused around the target biomolecule, as this defines the compatible bio-recognition elements and by extension the range of appropriate signal transducers. A wide array of both recognition and transduction elements are under active research, although many do not match the requirements for a point of care (PoC) device outlined in chapter 1.

One promising approach utilises specific enzymes to catalyse reactions involving the target biomarker and the resulting production of protons. In a weakly buffered environment this production of protons will result in acidification of the solution, which can be monitored as a pH change using a pH sensitive transducer. This approach enables flexible detection of any enzyme catalysed reaction that produces a pH change. In order to fully understand a system built around these phenomenon, the underlying theory behind pH must be explored.

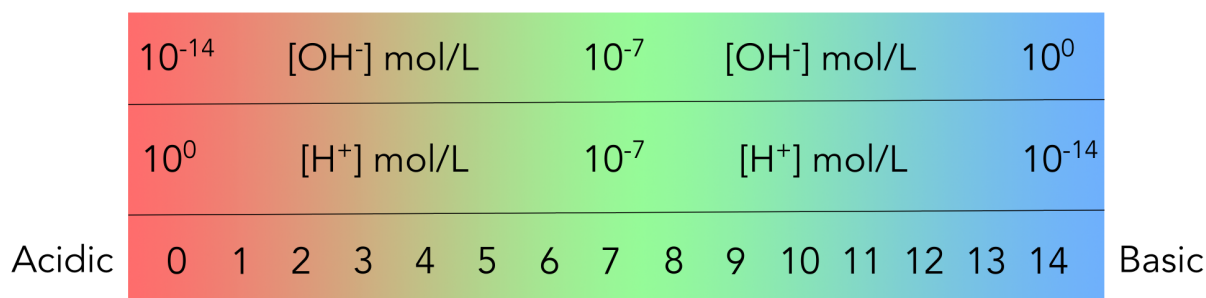


Figure 2.2: pH scale showing H⁺ and OH⁻ concentrations in mol/L.

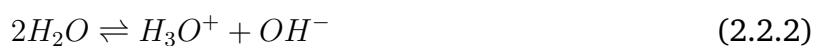
2.2 pH

pH is a characteristic of an aqueous solution, obtaining its name as a shortening of *power of hydrogen*. Specifically, pH represents the activity of positively charged hydrogen ions (protons) within a solution.

At low concentration (below circa 0.1 M) the proton activity is commonly assumed to be equivalent to the proton concentration. At higher concentrations the close proximity of ions results in steric and charge based interactions that restrict the ability for all ions to interact, resulting in an effective lower activity than the concentration present. The relationship for proton concentration is presented in equation 2.2.1.

$$pH = -\log_{10}([H^+]) \quad (2.2.1)$$

Lone hydrogen ions do not persist in aqueous solutions due to a high charge density, where interaction with nearby atoms is more energetically favourable. Instead they form hydronium ions H₃O⁺, where one water molecule donates a H⁺ ion to another as described in equation 2.2.2. This phenomenon is known as the self-ionisation of water and is often assumed to occur in all aqueous solutions, equation 2.2.3 shows this reaction, with the forward and reverse reactions in constant equilibrium.



As seen in equation 2.2.1 the concentration of H⁺ ions can be used to obtain a value for solution pH, where the concentration of hydroxide ions (OH⁻) will be inversely proportional. The pH scale is shown in Figure 2.2 alongside the number of ions present. Pure water at 25°C contains equal concentrations of H⁺ and OH⁻ ions at 10⁻⁷ M, hence the term ‘neutral’ pH.

Equation 2.2.4 is known as the Henderson-Hasselbalch equation, an approximation for the pH of an aqueous acid solution in relation to the acid dissociation constant, pK_a , where $[HA]$ is the concentration of the weak acid species and $[A^-]$ is the concentration of conjugate for that species in a general equation 2.2.5.

$$pH = pk_a + \log_{10} \frac{[A^-]}{[HA]} \quad (2.2.4)$$



The acid dissociation constant quantifies the varying degree to which H^+ ions within specific molecules will dissociate (equation 2.2.6).

$$K_a = \frac{[A^-][H^+]}{[HA]} \quad (2.2.6)$$

$$\log_{10}[H^+] = \log_{10}K_a + \log_{10} \frac{[HA]}{[A^-]} \quad (2.2.7)$$

It is often referred to in the inverse logarithm form (pK_a) given the ability to relate the pH of the surrounding solution as in equation 2.2.7. From this form, using equations 2.2.1 and 2.2.6, the final form as shown in equation 2.2.4 is reached. This equation shows the pK_a value of a molecule is the pH at which half of the protons have dissociated.

I note, this form of the Henderson-Hasselbalch equation is an approximation as it does not consider the self-dissociation of water, which becomes more significant below a molarity of $\approx 10^{-4}$ M and at extremes of pK_a ; < 3 and > 11 . The more precise calculation was not used in this work but detail is available within the literature [32].

2.2.1 Measuring pH

There are a variety of methods for measuring the activity of H^+ ions in solution and determining a value for pH. It is possible to monitor changes using pH-sensitive indicator dyes, where a visual colour change occurs as alterations in the molecular structure result in varying absorption spectra. As shown in Figure 2.3 for the indicator Phenol Red, specific groups on the molecule are amphoteric, where they can both accept and donate H^+ ions, depending on the solution pH, based around their pK_a . A range of indicators are available which each show varying colour changes over a window of ≈ 2 pH units.

In this work Phenol Red is utilised, which shifts from yellow at pH 6.2 to fuchsia at pH 8.2 (Figure 2.3). A change across this range is visible to the naked eye, although quantifying the precise pH is difficult by simple observation, instead requiring an optical system and calibration

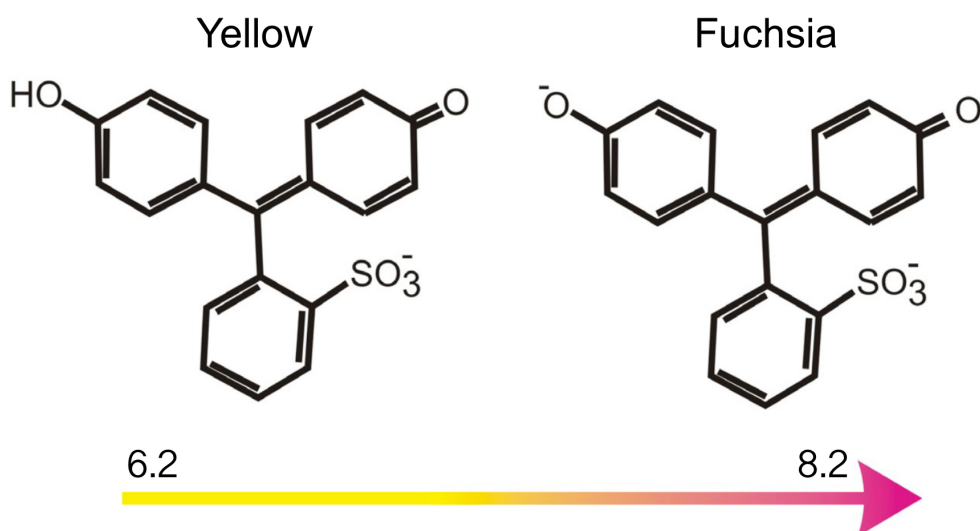


Figure 2.3: Chemical structure of Phenol Red pH indicator dye in response to varying solution pH. Adapted from [33].

information to relate the absorbance to a pH value. This method is also unable to provide information on pH changes beyond the dynamic range of the indicator. Universal indicators combine dyes with overlapping pH ranges to enable monitoring over a larger dynamic range, but again suffer from challenges in quantification of pH.

Electrochemical pH meters can provide a precise pH value and are commonly used in lab settings in the form of a glass bulb pH meter. Figure 2.4 shows the reference electrode, associated internal solutions and porous frits, which result in a stable reference potential (more detail provided in section 2.3.6). A differential measurement is made between this and the potential measured across the H^+ sensitive amorphous silicate glass membrane, to calculate the solution pH. The potential of the internal interface is stable due to the isolated pH buffer in contact with the AgCl coated wire, whereas at the outer-face of the glass membrane, protons displace metal cations originally present within the matrix [34]. Thus the target solution H^+ concentration is reflected as a changing potential at the outer-face of the glass membrane.

Assuming regular calibration with stable solutions of known pH, such meters provide an accurate measure of pH and are simple to use. There are disadvantages to glass bulb pH meters, namely the fragility of the glass probe which is submerged into solution. Due to the time taken for metal cations to diffuse through the glass membrane, providing the necessary small leakage current to measure a potential difference, they also offer a limited rate of response to changes in pH, in the order of tens of seconds [35]. Finally it can be shown the maximum pH sensitivity of these devices is 59.2 mV/pH, which limits the change in pH that can be resolved, this is derived in section 2.3.5.

An alternative electrochemical approach for measuring pH is to utilise an ISFET, which is durable, amenable to miniaturisation and offers a rapid response to changes in pH. For PoC

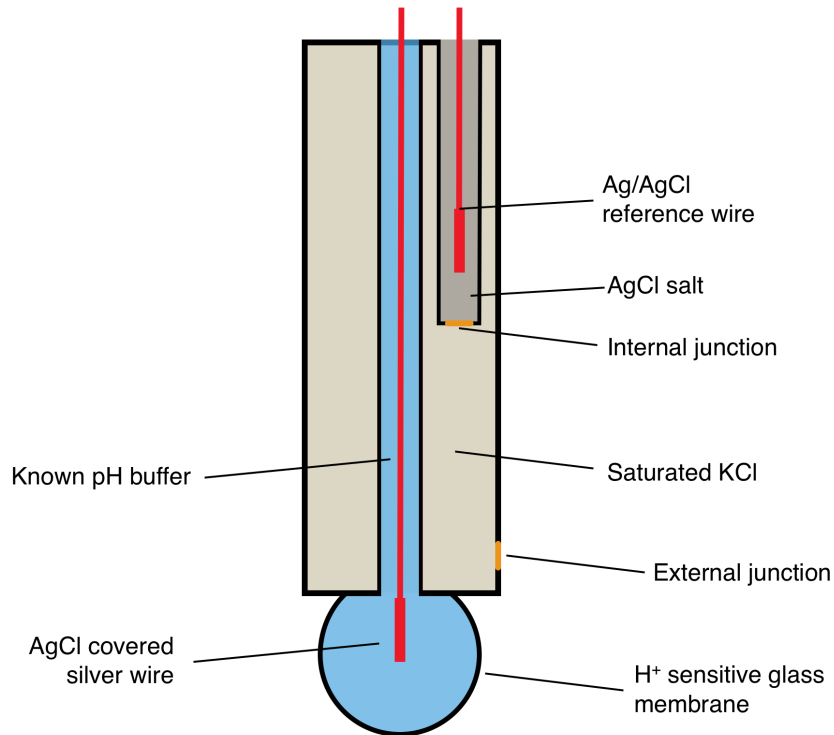


Figure 2.4: Glass pH meter, consisting of a pH sensing electrode and a double junction reference. Adapted from [33].

biosensors these are favourable characteristics and as a consequence ISFET technologies were selected for use within this work.

2.3 ISFET Theory

ISFET devices fundamentally build on the operation of a metal-oxide-semiconductor field effect transistor (MOSFET) which are explained first before modifications are considered.

2.3.1 MOSFET

The schematic structure of a complementary metal-oxide-semiconductor (CMOS) MOSFET is shown in Figure 2.5. The MOSFET is a three electrode device where the voltage applied to the gate electrode determines the conductivity between the source and drain electrodes; power MOSFETs as an exception may have a fourth body electrode connected to the source. Charge carriers can be electrons or holes, named n-channel and p-channel respectively. Different levels of doping within the conduction channel can produce two different forms of device, enhancement and depletion.

Initial operation will be described for a n-channel enhancement mode transistor. Differ-

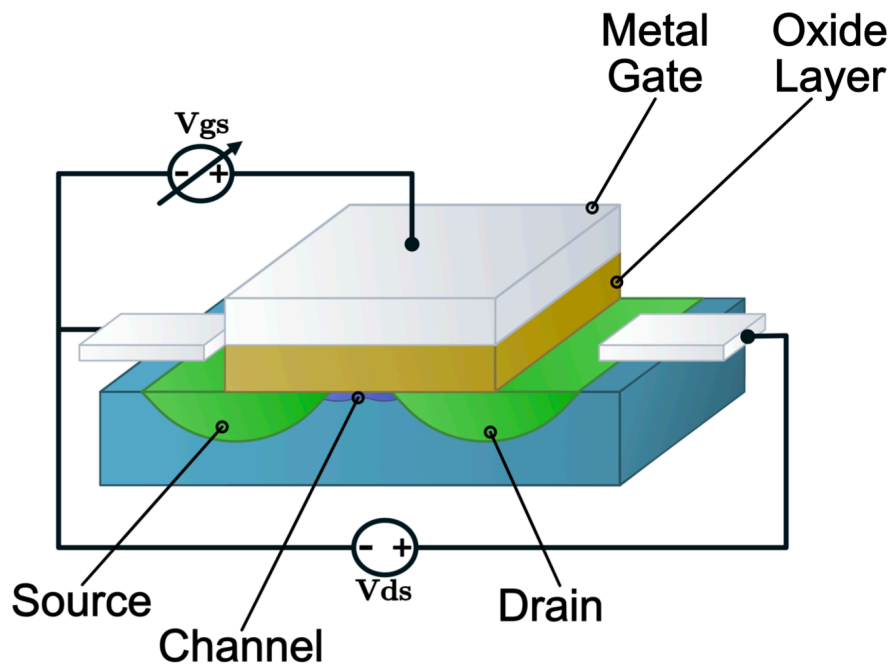


Figure 2.5: Schematic of MOSFET structure, showing three electrodes and regions of doped semiconductor [36].

ences between MOSFET varieties, such as charge carriers and doping will be explained subsequently.

Again referencing Figure 2.5, we see a structure consisting of two heavily doped regions which act as the source and drain of the device, interfaced via metal contact. These two heavily doped regions sit within the body of the device, made up of oppositely doped semiconductor. On top of this structure a thin metal oxide (commonly SiO_2) is deposited, used as an insulator with high dielectric constant, which is capped with a metal gate electrode.

This metal-oxide-semiconductor stack behaves like a capacitor, with a characteristic input resistance of $> 10^{14} \Omega$, resulting in no current flow through the gate. Instead, the build-up of charge carriers at this electrode generates an electric field across the dielectric through polarisation, that effects charge carriers in the semiconductor. Movement of charge carriers towards the semiconductor-oxide interface increases conduction between the two heavily doped regions.

2.3.1.1 MOSFET Varieties

As mentioned previously, there exists heavily doped regions within an oppositely charged body, meaning p-channel and n-channel devices are possible with holes and electrons as charge carriers respectively. There are also two forms beyond this, depletion and enhancement, where the discussed conduction channel at the surface may not be present at fabrication. A total of 4 varieties are available, as shown in Figure 2.6.

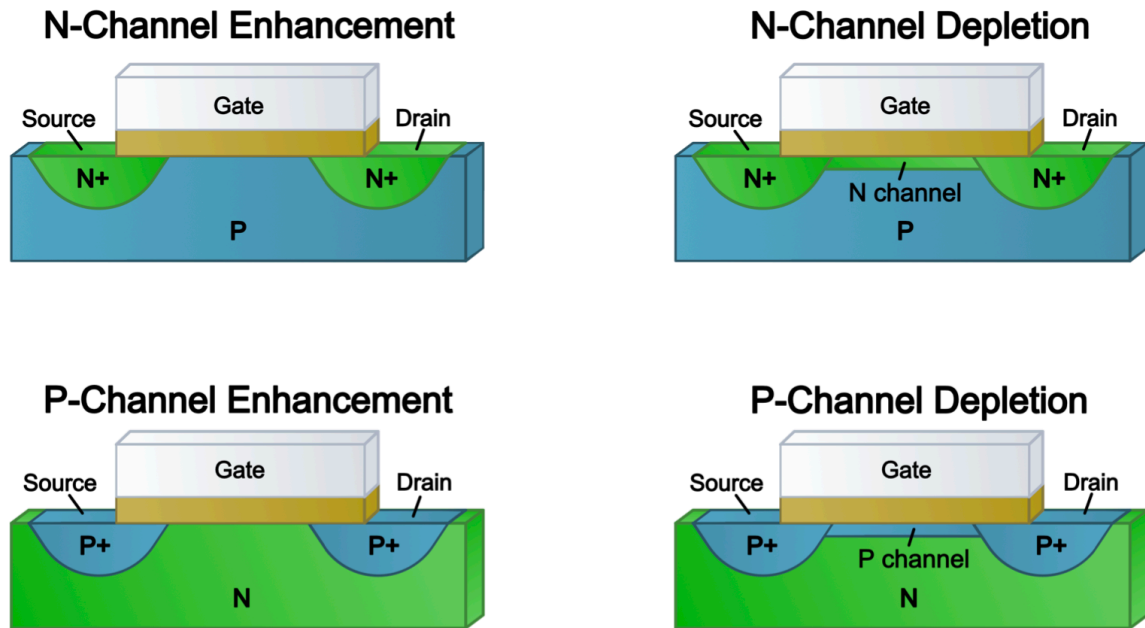


Figure 2.6: Diagrams of 4 MOSFET modes of operation: N-channel enhancement, N-channel depletion, P-channel enhancement, and P-channel depletion [36].

In depletion mode, the conducting channel is present when no gate voltage is applied, to prevent current flow a voltage must be applied. For n-channel devices this is a negative voltage and positive for p-channel. In an enhancement mode device there is no conducting channel with zero voltage applied, to enable conductance a voltage must be applied. A positive bias will attract electron charge carriers in a n-channel device, whereas a negative gate voltage is required to attract holes in p-channel.

Both depletion and enhancement operation possess an equivalent drain-source current I_{DS} versus gate source voltage V_{GS} response, except for a linear offset based on V_{GS} axis as is shown in Figure 2.7. This trend breaks down at large gate source voltages.

Traditionally a MOSFET is used to reflect a 0 or 1 state, making use of the saturation region where the current density within the channel is at saturation. ISFET pH sensors are designed to operate within the linear/triode region, as shown for a n-channel MOSFET in Figure 2.7, where there is a linear relationship between device current and drain-source voltage. A third region where no channel is formed due to an insufficient voltage is possible, where no current will flow; although a small number of charge carriers may pass due to thermal energy, leading to a leakage current.

In conclusion, a changing bias voltage on the gate of a MOSFET is capacitively coupled to alter the current which flows between the source and the drain. When placed in the triode region this relationship is linear, which is key to operation of ISFET devices.

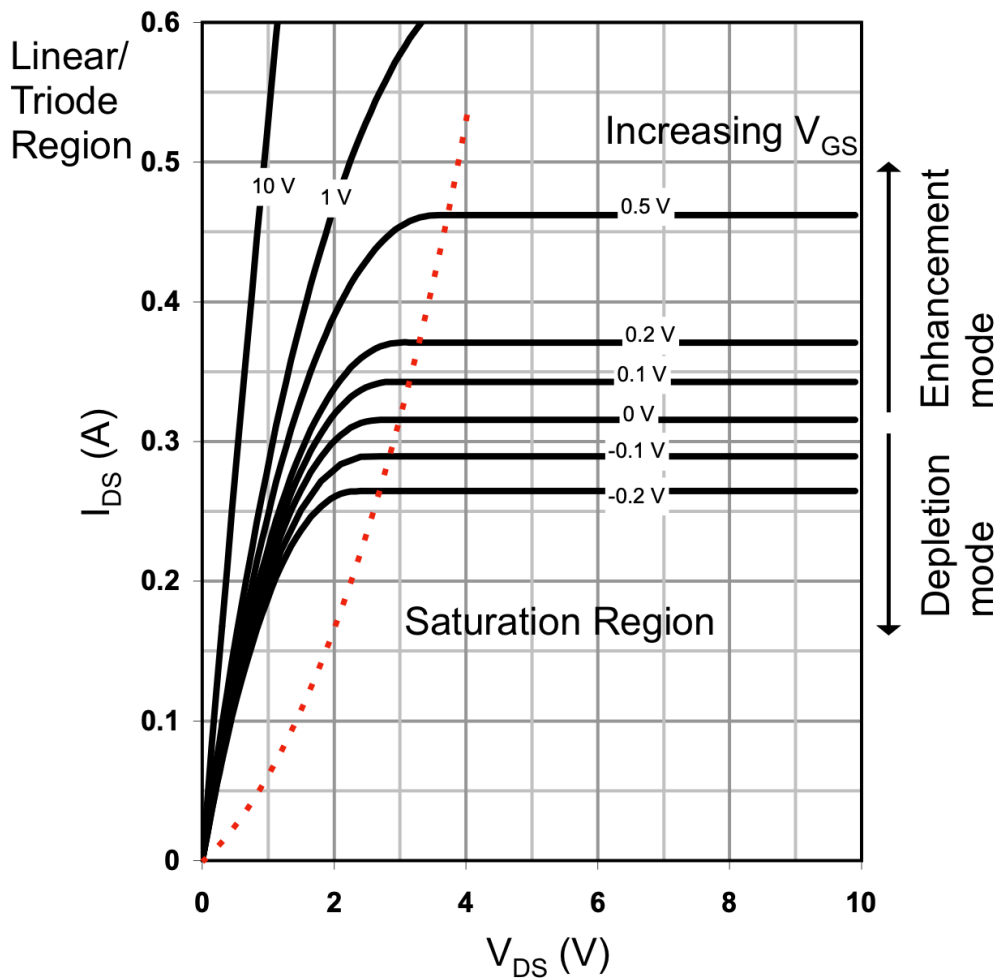


Figure 2.7: Drain-source current as a function of drain-source voltage for the BSS159 n-channel MOSFET, plotted for varying gate-source voltages. Adapted from [37].

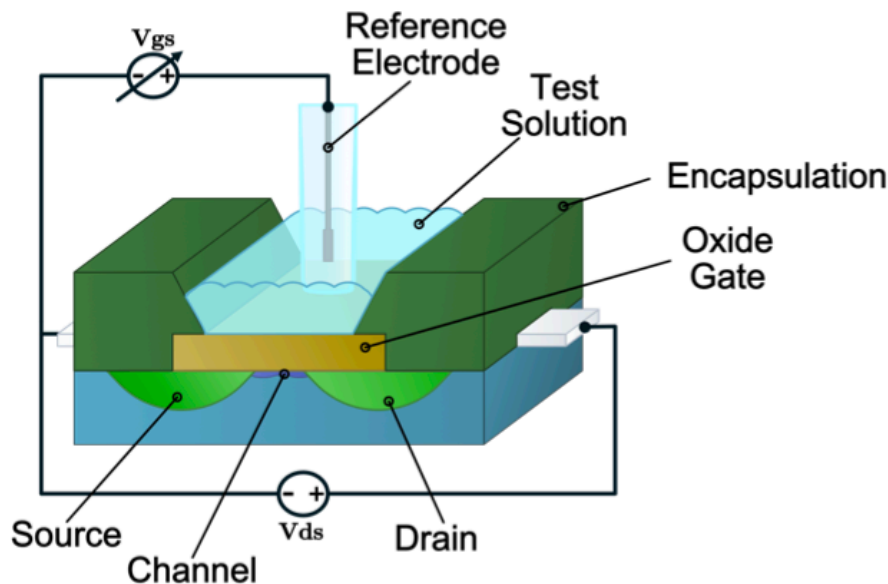


Figure 2.8: Diagram of ISFET structure, showing an ion-sensitive material as the oxide gate, exposed to an electrolytic test solution [36].

2.3.2 ISFET

The voltage at the gate electrode is applied via a connection to external circuitry in a MOSFET. In contrast, the ISFET bias is produced by a build-up of ions at the interface between an electrolyte and an ion-sensitive layer, with a voltage offset applied by a reference electrode to bias the transistor into the linear-triode region. Figure 2.8 shows a diagram of an ISFET, further discussion on the motivation for its use in this work can be found in section 2.4.

2.3.3 Site Binding Model

To fully understand operation of ISFET sensors and its variants, it is key to explore the electrochemical phenomenon occurring at the surface-solution interface. The site binding model [38, 39] describes the properties of an oxide-aqueous electrolyte interface, with a focus on the resulting surface charge. It describes the equilibrium which is obtained between the surface sites and protons in the electrolyte. In a pH sensitive material these sites are amphoteric, meaning they are able to both donate and accept protons [40].

Figure 2.9 shows how proton donors and acceptors are assumed to form at the solution-surface interface for a typical metal-oxide substrate [41]. A neutral site is converted into a proton donor when a H^+ dissociates, leaving a charged O^- at the surface. A proton acceptor is formed when a hydrogen ion in solution associates to a surface molecule and forms OH_2^+ . Equation 2.3.1 shows this represented as an equilibrium reaction for a traditional pH sensitive metal oxide layer [38, 42]. H^+ ions are small and mobile, enabling them to diffuse to the

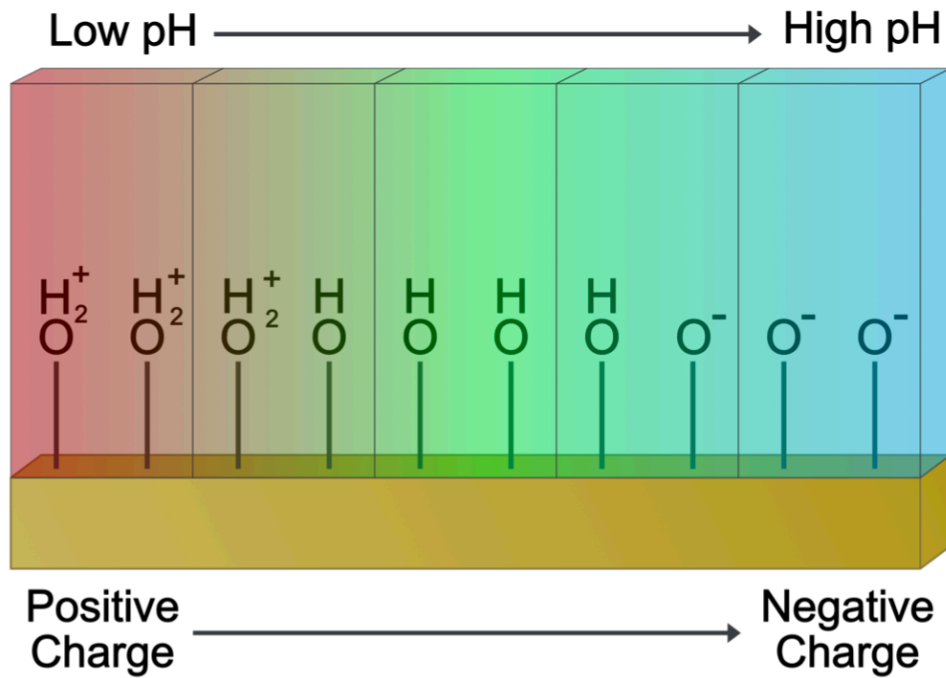
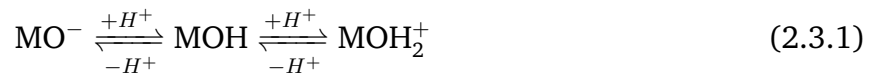


Figure 2.9: Site binding model showing neutral, proton donor and proton acceptor sites. Shown also is the trend between dominant amphoteric site and the solution pH relative to the surface PZC [36].

surface through layers of other charged molecules, relating the surface concentration directly to that observed in the bulk.



The solution pH dictates the number of sites that will be in proton donor or acceptor states, which in turn dictates the surface potential at that pH. At an acidic pH, proton donors will dominate due to increased H^+ ions in solution. At a basic pH, less H^+ ions are in solution, leading to proton acceptor sites dominating. Where amphoteric sites are balanced between proton donor and acceptor sites is the point of zero charge (PZC) [43].

2.3.4 Electrochemical Double Layer (ECDL)

Figure 2.10 shows amphoteric sites at the surface as described by the site binding model. Ionic molecules within solution move towards the surface in order to neutralise surface charge at pH values other than PZC. The sites dictated within the site binding model impact the arrangement of ions in solution to create what is known as the electrochemical double layer (ECDL) at the surface-solution interface.

Over time a number of theories have been developed to explain the ECDL [44]. The first

widely accepted approximation was the Helmholtz model developed in 1879 [45], which made assumptions about an uniform and stable layer of counter-ions moving to the surface to neutralise the surface charge. The Gouy-Chapman model [46] modified this to consider a gradient of charge moving from the surface into the bulk, driven by diffusion and described by the Boltzmann distribution. The model described in this work is a combination of the two theories introduced by Stern in 1924 [47], which additionally provides a more detailed view of the inner layer of molecules, including how the closest approach of molecules will depend on their ionic radius and solvation status; electrostatically shielded by water molecules of a favourable dipole.

Figure 2.10 shows the regions modelled using the Gouy-Chapman-Stern approach, where the surface is in a state dominated by proton donors and the solution is of pH further basic than the PZC; in aqueous phase and with general electrolytes present. Visible are the distinct regions outlined by the model of the inner Helmholtz plane (IHP), outer Helmholtz plane (OHP) and the Gouy-Chapman diffuse layer, leading to bulk solution [48].

The IHP is a charged layer of ions that are adsorbed onto the surface. In Figure 2.10 these are negative adsorbed on a surface dominated by positive charge acceptors. These molecules will be partially solvated, as the adsorption to oppositely charged surface sites via van der Waals or Coulombic interactions dominates over the dipole of water molecules [49]. Water molecules found in this region close to the surface will obtain dipoles based on the local charge.

The OHP is populated by fully solvated ions that approach the surface to neutralise the charge of the remaining amphoteric sites. The distance of their approach is limited by the bound water molecules. I note, the packing of the electrolytic ions is dependent on their relative physical size and charge. These two layers make up the Helmholtz plane, both with a linear potential relationship, although the IHP possessing a steeper gradient.

Extending beyond the Helmholtz plane is the diffusive Gouy-Chapman region, which extends out to the bulk solution. In this region, solvated ions arrange to neutralise the charge created by the surface and inner Helmholtz layers, with the potential across this diffusive layer following a Boltzmann distribution.

The bulk solution contains an even distribution of charge throughout. In an aqueous solution with no additional ions, an ECDL will be formed, but only involving polarised water molecules, where the dipole is oriented to neutralise amphoteric surface sites.

2.3.4.1 ECDL Capacitance

The overall distribution of charge across the layers leads to regions of opposite charge, effectively resulting in the creation of multiple parallel plate capacitors.

The total differential capacitance ($C_{Interface}$) within the ECDL is a combination of the ca-

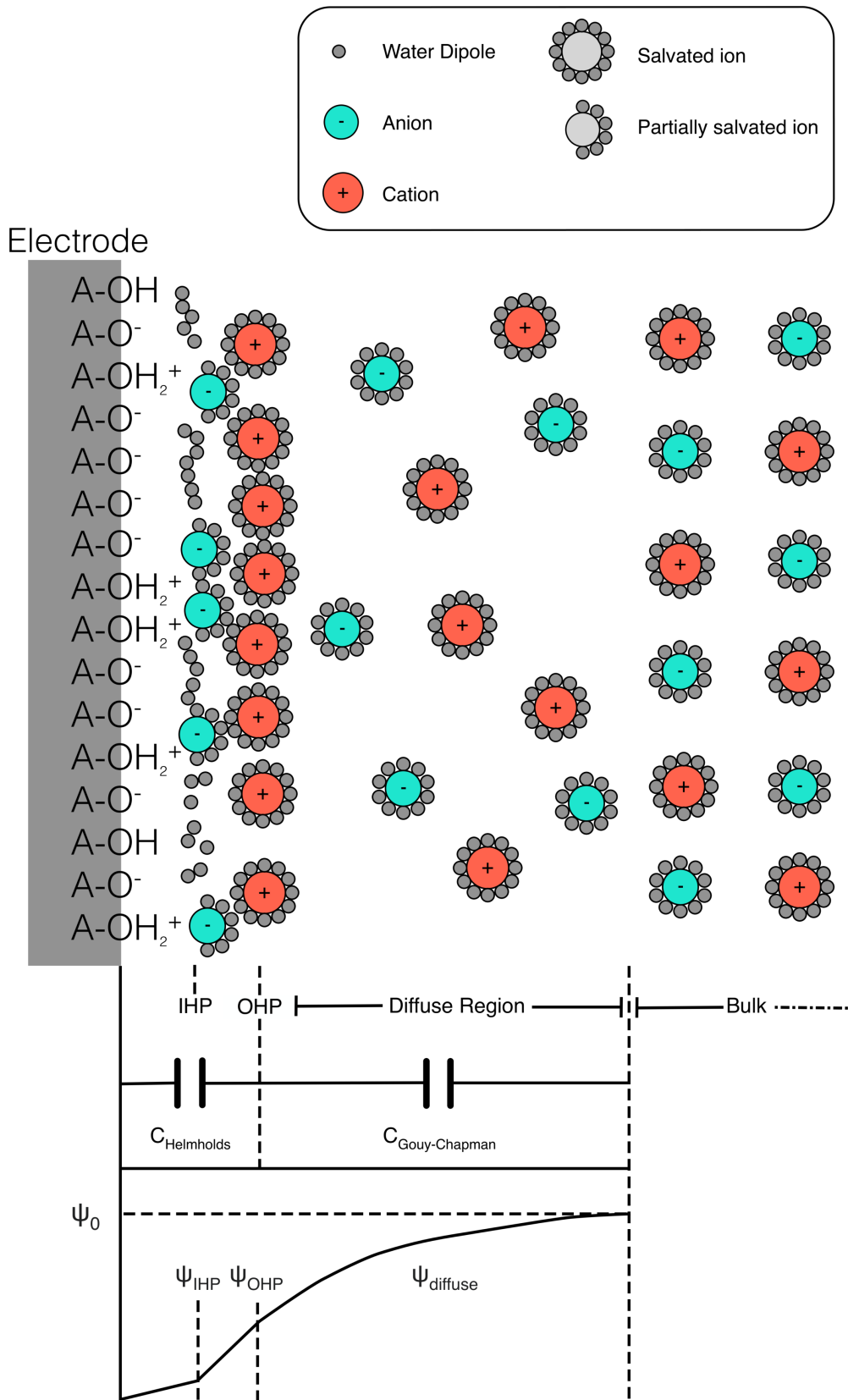


Figure 2.10: Representation of the ECDL combined with site binding model. This is shown for a state where $pH < pH_{pzc}$, which dictates the distribution of amphoteric sites and thus the average surface charge. Potentials and capacitances at the different planes are illustrated.

capacitances from the Helmholtz layer (C_{Helm}) and the Gouy-Chapman layer ($C_{GouyChapman}$) as shown in equation 2.3.2 [11]. In the ISFET, $C_{Interface}$ is coupled capacitively across the transistor gate dielectric and effects ion flow within the MOSFET channel. For other electrochemical models which include a range of other capacitances relevant for CMOS integrated circuit based ISFETs, see [50].

$$\frac{1}{C_{Interface}} = \frac{1}{C_{Helm}} + \frac{1}{C_{GouyChapman}} \quad (2.3.2)$$

Equation 2.3.3 for C_{Helm} is a result of the two parallel planes of charge associated with the IHP and OHP, where A is the surface area of the interface, ϵ_0 is the permittivity of free space, ϵ_r the relative permittivity of electrolyte and L_{OHP} is the distance from the OHP to the solid.

$$C_{Helm} = \frac{A\epsilon_0\epsilon_r}{L_{OHP}} \quad (2.3.3)$$

Equation 2.3.4 for $C_{GouyChapman}$ considers the potential of the diffuse region, where the charge decays exponentially, modelled in differential form [51, 52]. The $\frac{\epsilon_0\epsilon_r}{L_D}$ term is the capacitance of two plates, with the Debye Length L_D a measure of how far an electrostatic effect persists into solution, representing the capacitive plate at the limit of the Gouy-Chapman region. The cosine portion describes the effect of mobile charges, where z is the valence of ions, Ψ_G is the potential over the diffuse layer and V_t is the thermal voltage. Within L_D the bulk concentration of ions is n_0 and q is electron charge. The characteristic thickness of the diffuse layer for a simple salt solution at 25 °C and 100 mM is 9.6 Å [51].

$$C_{GouyChapman} = \frac{\epsilon_0\epsilon_r}{L_D} \cosh\left(\frac{z\Psi_G}{2V_t}\right), L_D = \sqrt{\frac{\epsilon_0\epsilon_r V_t}{2n_0 z^2 q}} \quad (2.3.4)$$

These equations show that the interfacial capacitance within the ECDL, and thus the electric field generated at the ISFET gate, is dependent on the potential at the surface, which itself is influenced by the ion type and concentration, alongside environmental temperature. This is unlike a traditional capacitor where the potential applied would not impact its capacitance.

2.3.4.2 ECDL Potential

After reaching the equation to describe the capacitance of this ECDL, this can be related to the resulting impact on the potential at the electrode interface.

Equation 2.3.5 allows calculation of $\Psi_{Interface}$, which is the total potential dropped across all capacitive regions at the electrode-electrolyte interface, at a specific pH between the surface and bulk solution [52]. pH_{pzc} being the pH at which amphoteric sites alone cause neutral

surface change and pH being the current value. k , T and q are all constants in standard conditions.

$$\Psi_{Interface} = 2.3 \frac{kT}{q} \alpha (pH_{pzc} - pH) \quad (2.3.5)$$

Shown in equation 2.3.6 are two auxiliary equations required for calculating $\Psi_{Interface}$ [53]. α is a dimensionless scaling factor describing the sensitivity and takes a value between 1 (ideal) and 0, where $C_{Interface}$ is the total capacitance of the double layer as obtainable using equation 2.3.2. β_{int} is the intrinsic buffer capacity of the oxide surface (here assuming a silicon oxide dielectric) and describes the efficiency of surface sites to accept H^+ based on small changes in local pH. The β_{int} value is specific for a material and may vary based on the precise structure of that sample, where a poor intrinsic buffer capacity results in a device sensitivity below its theoretical maximum.

$$\alpha = \left(\frac{2.3kTC_{Interface}}{q^2\beta_{int} + 1} \right)^{-1} \quad \beta_{int} = \frac{\delta([AO^-] + [AOH_2^+])}{\delta pH} \quad (2.3.6)$$

$\Psi_{interface}$ is shown to be related to a range of properties of the electrolyte such as pH and temperature, alongside properties of the electrode such as the intrinsic buffer capacity and the PZC pH. I note, changes to the ECDL caused by larger molecules such as enzymes or imperfections in the electrode surface are not considered in this model, further detail can be seen in other published work [51].

2.3.5 Nernst Equation

The response of pH sensitive surface coatings can be determined from the Nernst equation, shown in its original form in equation 2.3.7. Here, E is the electrode potential, E_0 the standard electrode potential and R , T and F are standard constants [54]. Q is the reaction quotient, a term completed from the equilibrium reaction occurring in solution, n is the number of electrons transferred during the reaction.

$$E = E_0 + \frac{RT}{nF} \ln(Q), \quad Q = \frac{[products]}{[reactants]} \quad (2.3.7)$$

Assuming the general reaction shown in equation 2.3.8 for a reversible metal-metal oxide couple, this can be written as equation 2.3.9 [55, 56].



$$E = E_0 - \frac{h}{n} \frac{2.303RT}{F} pH \quad (2.3.9)$$

As can be seen from equation 2.3.9, under constant conditions, the magnitude of the pH response is determined by the stoichiometric coefficient of hydrogen ion activity (h) and the number of electrons transferred during the redox reaction (n), such as those values from reaction 2.3.8.

For all traditional pH-sensitive coatings, h and n are equal [57] leading to a maximum sensitivity of 59.2 mV/pH; the Nernstian limit as calculated in equation 2.3.10. In practice however, the response of pH sensing layers observed experimentally is typically lower than the Nernstian limit.

$$E = E_0 + \frac{1}{n} \frac{2.303RT}{F} pH = 59.2mV/pH \quad (2.3.10)$$

These theoretical concepts are key to understanding pH-sensitive ISFET device operation, section 2.4 will continue to discuss ISFETs and their derivative technologies within literature. Reference electrodes are first discussed as these are required for operation of ISFET.

2.3.6 Reference Electrodes

Reference electrodes are essential in many electrochemical characterisation techniques and sensors, in ISFET systems they enable biasing into the triode region. An ideal reference electrode provides a fixed potential that is independent of solution conditions. In contrast, the potential at a working electrode is often likely to change as a function of solution pH, ion type and concentration, temperature and other molecules within the matrix.

Standard hydrogen electrodes (SHE) are seen as the *gold standard*, which involve bubbling hydrogen gas around a Pt electrode within an acidic electrolyte. This results in a standard potential (E_0) of 0V which remains stable amongst changing solution conditions (with the exception of temperature, which in standard conditions is 25°C). Use of these electrodes is not practical in many applications due to the requirement for consistently passing hydrogen gas [58]. Saturated calomel electrodes (SCE) are solid state and provide a stable potential of +0.242 V vs. SHE, although have fallen out of favour due to the environmental concerns of mercury [54]. Large currents flowing through these reference electrodes will cause the potential to change and should be avoided.

The (Ag/AgCl/Saturated potassium chloride (KCl)) double junction electrode has ultimately become the standard reference electrode with a potential of +0.197 V vs. SHE that remains stable if the internal concentration of Cl⁻ ions is kept constant [54]. These electrodes are suitable across a large dynamic range of pH, use non-toxic components and are inexpensive to manufacture.

Some works utilise quasi-reference electrodes, where inferior stability to changing solu-

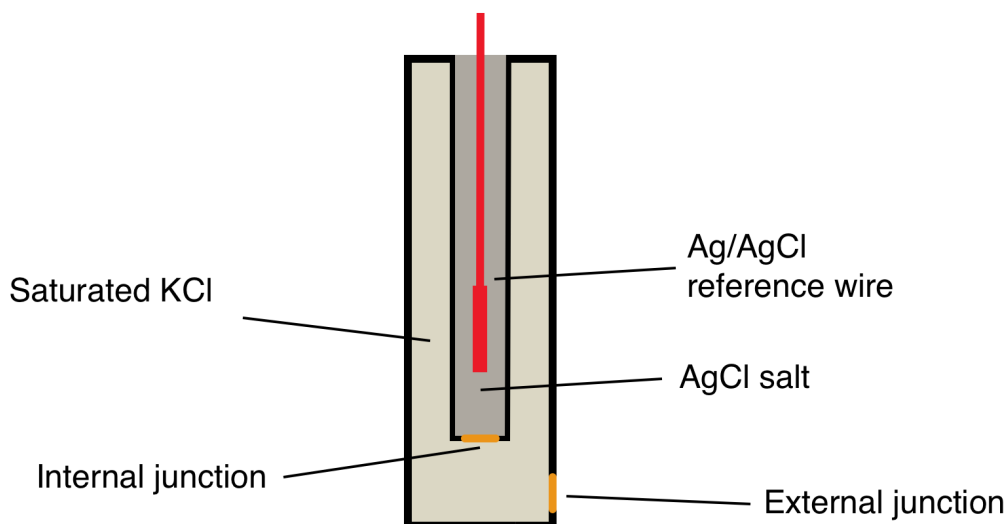


Figure 2.11: Diagram of a double junction Ag/AgCl/Saturated KCl reference electrode. Adapted from [63].

tion conditions (such as pH, temperature, ion type and concentration) are accepted due to improved integration and lack of glass assembly as in Ag/AgCl/KCl electrodes [59, 60, 61].

2.3.6.1 Ag/AgCl/Saturated KCl

In this work, an Ag/AgCl/KCl electrode (RE-1CP, ALS Japan) is used to bias the transistor into the triode region. The same reference electrodes were used in all electrochemical measurements, and ensured any change in potential of the electrochemical cell are a result of ion concentration at the working electrode rather than reference electrode instability [62].

A diagram of an Ag/AgCl/KCl reference electrode is shown in Figure 2.11. It consists of a solid Ag wire coated in insoluble AgCl salt, which is in turn in a sealed environment containing additional AgCl salt. An internal ceramic frit junction separates this from a saturated KCl electrolyte, which is again sealed by a second ceramic frit at the base of the electrode, where it will be in contact with the solution under test. These porous ceramic frits enable mutual ion transfer across the membrane, which does lead to small quantities of KCl leaching into solution over time.

The key reaction occurs at the interface between the Ag wire and AgCl salt, which is outlined in equation 2.3.11. Constant Cl^- ion concentration is required to maintain the electrode half cell reaction in equilibrium and maintain a stable electrode potential. The saturated KCl solution provides these Cl^- ions as they move through the porous internal junction, with saturation being the easiest method of ensuring no change in ion concentration. The almost identical mobility of the K^+ and Cl^- ions (alongside similar concentration) makes this a favourable electrolyte to supply Cl^- ions, as the potential at the interface between the saturated KCl and

test solution is minimised [64].



Alongside the requirement for a constant excess of Cl^- ions, temperature can also influence the electrode potential at the interface, where reaction seen in equation 2.3.11 occurs; the main source of instability in Ag/AgCl reference electrode if not within a temperature controlled system. Separately, current flow through the reference electrode can catalyse the interface reaction, leading to a change in potential.

2.4 pH targeted Ion-sensitive Electrode Literature

This section considers literature on the development of ISFETs, derivative technologies and low-cost pH sensing electrodes, especially printed circuit board (PCB) based potentiometric sensors, or those that utilise a metallic Cu layer on which they deposit a pH sensitive layer.

2.4.1 ISFET

This work focuses on the electrochemical sensing modality of ISFETs, specifically those with H^+ sensitive membranes that function as pH sensors. Originally introduced by Piet Bergveld in 1970 [65], this technology has now been commercialised successfully through the IonTorrent [66] and DNAE [67] next-generation sequencing (NGS) platforms.

ISFETs used in NGS systems are typically realised as bespoke integrated circuits (IC) manufactured using CMOS technology. This enables the fabrication of high-density ISFET arrays to meet the highly multiplexed detection requirements of NGS, utilising a silicon nitride pH sensitive layer [11, 68].

Obtaining a complete CMOS integrated fabrication process is not trivial, with some systems requiring either non-CMOS compatible layer deposition methods [69], or utilising compatible but less sensitive pH layers like silicon oxynitride [70]. Devices with various levels of CMOS integration, including exploitation of back-end-of-the-line (BEOL) fabrication steps have been demonstrated as tools for indirect detection of loop-mediated isothermal amplification (LAMP) amplification, via weakly buffered bulk pH change assays [71, 72] or as ion-sensitive biosensors [73]. More detail is available on CMOS-based ISFET technology, including novel sensing materials in a review article [74].

Non-ideal effects with ISFETs have naturally been the focus of much work, as research has sought to improve the overall performance of sensors for realisation in commercial products.

Mitigation against parasitic capacitances has been explored [74], and external conditions such as temperature and light are known to alter the pH response of some materials [75].

The largest body of research is understanding and addressing drift, and resulting hysteresis within devices, which is accepted to be asymmetric depending on the direction of pH change [76]. The fundamental mechanism that leads to drift is believed to be trapped charges [77, 78] however an universal approach to prevent this phenomenon has not been found.

An approach to reduce drift is the use of a reference field effect transistor (REFET). Instead of the ion-sensitive membrane being exposed to solution as in an ISFET, a REFET uses a surface which is insensitive to changes in pH [79, 80]. If both devices are matched electronically and exposed to the same sample, external environmental effects and non-ideal properties of the sensors will be common to both the ISFET and REFET, allowing for isolation of the pH change.

There are numerous applications for pH measurement where the high multiplexing offered by CMOS ISFETs is not required and instead other characteristics should be prioritised such, as reducing cost and complexity of fabrication.

2.4.2 EGFET & dEGFET

As stated previously, ISFET devices only differ structurally from MOSFETs through the a lack of gate metal, instead an electrolyte under test makes contact with the gate dielectric (Figure 2.8). Extended gate ion-sensitive field effect transistors (EGFET) extend the gate from the transistor via a conducting electrode to force a physical separation, providing simple separation of liquid phase from the electronic components. A device of this nature can be seen in Figure 2.12a and was first published in 1983 by Van Der Spiegel et al. [81] for sensing of ionic species (H^+ , Cl^- and F^-). Since its inception, EGFET fabrication has strived towards highly multiplexed operation, but at reduced cost compared to ISFETs due to the simplified encapsulation [82, 83]. EGFET literature was absent from Bergveld's 30 year review on ISFETs [84], but reviews on the topic are available [85, 86].

Low-cost, single device ISFETs can be realised using commercial off-the-shelf discrete FETs coupled to an extended gate electrode that is rendered pH sensitive. Such discrete extended gate ion-sensitive field effect transistors (dEGFETs) are a further variation on the ISFET concept, with a variety of names across literature such as separative EGFET or ExFET. They were first realised in 2000 [87] and provide further physical separation of the field effect transistors (FETs) from the pH-sensitive layer (Figure 2.12b), simplifying packaging and encapsulation. Moreover, in contrast to CMOS-based ISFET ICs, the dEGFET structure is compatible with a wide range of substrates and sensing layers, which can be selected to balance device cost and ease of manufacture with high pH sensitivity and biological compatibility.

Naturally, due to this flexibility afforded by the dEGFET structure, a large range of extended

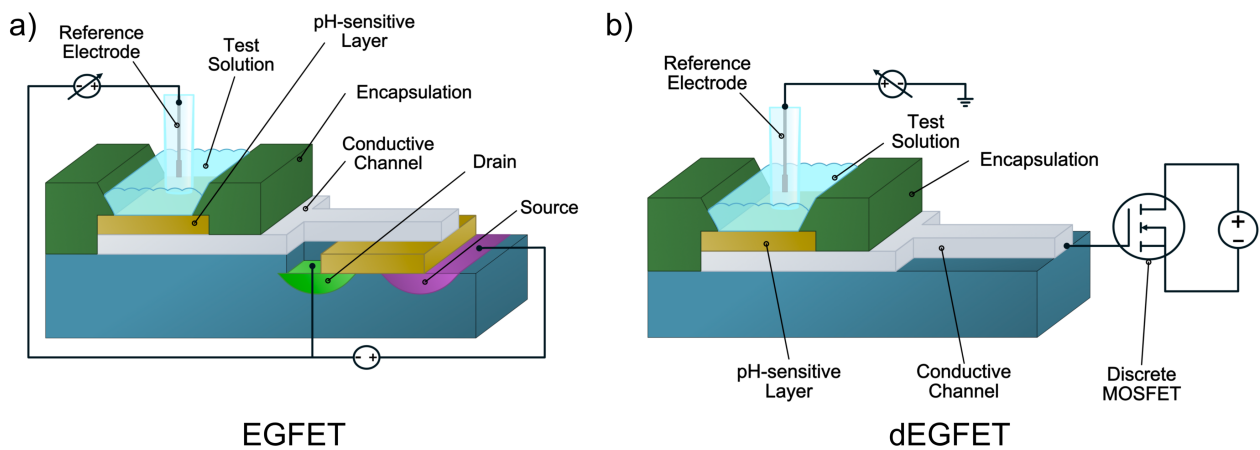


Figure 2.12: Diagrams of a typical EGFET structure a) and that of a dEGFET device b) [36].

gate substrates and pH sensitive layers have been trialled across research. For example, taking inspiration from CMOS ISFETs, Ahmed *et al.* [88] employed a doped silicon substrate that also operated as a pH sensitive layer through etching of the surface with hydrogen fluoride to create a porous layer, with a resulting pH sensitivity of 56 mV/pH. Extended gate electrodes fabricated on glass have also been used widely, due to the established techniques for evaporating the necessary conducting and pH sensitive layers onto the material [89, 90, 91]. Alongside use of commonplace lab substrates, is a group of materials intended to reduce the cost of devices, such as paper, a range of plastics [92, 93] and textiles [94].

2.4.3 dEGFET pH Sensors Based on PCB Substrates

While a range of substrate materials have been explored, PCBs have emerged as a highly compelling choice for the fabrication of extended gate electrodes. As a consequence of being widely used across the consumer electronics industry, the material is readily available at low cost and there exists multiple established approaches for manufacturing patterned PCB substrates at scale.

Moreover, recent research has demonstrated the possibility of integrating microfluidic channels within PCBs, enabling the realisation of lab-on-chip (LoC) or lab-on-PCB devices that combine sensing and fluidics on the same substrate [95, 96]. On chip heating steps such as those required for DNA amplification have also been successfully integrated onto PCB substrates [97, 98]. Chapter 6 provides more examples on current literature around LoC and lab-on-PCB microfluidics.

Despite these advantages, the copper electrodes used in PCBs are inherently weakly pH-sensitive up to a maximum of 28 mV/pH in literature [99, 100]. It is thus necessary to include pH sensing layers with improved sensitivity.

Indium tin oxide (ITO) is an example of a pH sensitive layer commonly deposited on a range of substrate materials, consistently achieving 53 mV/pH sensitivity [101, 93]. SnO₂ [92, 91] has been demonstrated with 58 mV/pH sensitivity, approaching the theoretical limit of 59.2 mV/pH, as has also been shown for TiO₂ [102]. Other research has considered novel sensing materials such as carbon nanotubes (34 mV/pH) [90].

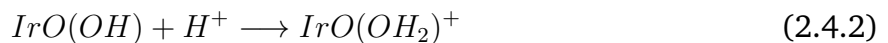
Examples of pH sensing layers deposited on PCB dEGFET devices specifically, exhibit a response well below the traditional Nernstian limit as described in section 2.3.5, these include TiO₂ [103] and Parylene-C [104] exhibiting 22 mV/pH and 16 mV/pH respectively.

2.4.4 Iridium Oxide pH Sensing Layers

Recent attention has focused on metal oxide sensing layers [105] such as iridium oxide (IrOx) that have the potential to offer enhanced pH sensitivity. IrOx can be deposited via a range of processes, some of which have been shown to lead to pH sensitivity beyond the traditional Nernstian limit [106]. Much of the knowledge in the use of IrOx films was originally obtained from IrOx coated electrodes being widely used for neural stimulation and recording [107].

IrOx films deposited by thermal oxidation, sputtering [108, 109] or sol-gel [57] approaches are de-hydrated and offer a maximum sensitivity of 59.2 mV/pH. In contrast, hydrated IrOx films, such as those electrodeposited onto the electrode surface (sometimes referred to as anodic/electrodeposited iridium oxide films (AIROF/EIROF)), offer increased sensitivity up to 88.8 mV/pH.

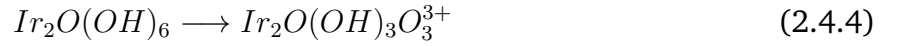
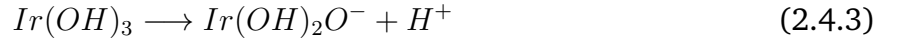
Hydroxide groups at the surface of IrOx layers deposited via all methods protonate and deprotonate in the same manner as traditional pH sensitive materials; as described in section 2.3.3. Possible forms of iridium oxides and oxyhydroxides are shown in Table 2.1, while equations 2.4.1 and 2.4.2 show an example of this deprotonation and protonation respectively, for one specific IrOx complex.



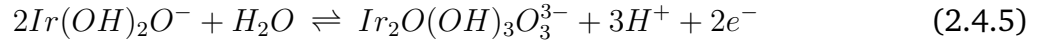
However, in addition to protonation/deprotonation reactions, the increased sensitivity within hydrated IrOx films originates from redox reactions between specific complexes of Ir³⁺ and Ir⁴⁺ oxidation states [106, 110]. If the site binding model is considered for these specific iridium complexes, the resulting half equations for reduction (equation 2.4.3) and oxidation (equation 2.4.4) occur.

Table 2.1: Possible complexes of iridium oxides and oxyhydroxides [106].

Ir^{3+}	Ir^{4+}
$IrO(OH)$	IrO_2
$Ir(OH)_3$	$IrO(OH)_2$
Ir_2O_3	$Ir(OH)_4$
$Ir_2O(OH)_4$	$Ir_2O_3(OH)_2$
	$Ir_2O(OH)_6$



Equation 2.4.5 shows the full equilibrium reaction, where iridium oxide in a specific 3⁺ oxidation state complex transitions to a complex with a 4⁺ state.



Equation 2.4.5 shows an imbalance between h (protons) and n (electrons), resulting in an enhanced theoretical pH sensitivity when substituted into the Nernst equation (equation 2.4.6).

$$E = E_0 + \frac{3}{2} \frac{2.303RT}{F} pH = 88.8 \text{ mV/pH} \quad (2.4.6)$$

It should be noted that while a change in Ir oxidation state is universally agreed to contribute to the enhanced pH sensitivity, consensus has yet to be reached around the mechanism described in equation 2.4.5 [111, 112, 113]. Moreover, the oxidation state of the IrOx layer is linked to the degree of hydration within the film.

Hydrated IrOx films produced by low cost and simple to implement electrodeposition processes are favourable for producing these highly pH-sensitive films [106, 114, 115]. A brief discussion around methodologies for electrodeposition can be found in section 3.4.3.1.

IrOx films have been explored for use as pH sensing electrodes [116, 117, 118] in which the open circuit potential (OCP) of an IrOx coated electrode is used as a measure of pH. In such devices, pH sensitivities of up to 79 mV/pH have been obtained, albeit with slow response times (≈ 10 s) [119]. While ISFET and dEGFET devices provide fast response times which enable characterisation of rapid kinetics [120], ISFETs with IrOx pH-sensitive films have yet to be demonstrated that approach the theoretical maximum pH sensitivity [121, 122].

There exists only a single study that has explored the pH sensitivity of IrOx films deposited on PCB-based electrodes [123]. While this device confirms the possibility of high pH sensitivities (73 mV/pH), the electrodes required both an Au finish during PCB fabrication and an additional Au nanoparticle electrodeposition prior to IrOx film deposition.

This work intends to explore this combination of PCB and a IrOx sensing layer with a discrete EGFET to realise a low-cost pH sensor based on widely available technologies. Although ion-sensitive devices capable of quantifying changes in pH are used across analytical chemistry, environmental monitoring and bioscience, this device will be applied as a biological sensor towards biomarkers of interest via pH change assays.

The pH sensitivity and repeatability of electrodes from this work are compared against other potentiometric pH sensors fabricated using PCB substrates and IrOx sensing layers in Table 2.2 and 2.3 respectively.

Table 2.2: Comparison of state-of-the-art PCB based pH sensors, including ISFET and open circuit potential (OCP) operation. Table also includes literature examples of sensors that use Cu as a substrate or pH sensitive material. Abbreviations: electroless nickel immersion gold (ENIG), polyaniline-dinonylnaphthalene sulfonic acid (PANI-DNNSA), chemical vapor deposition (CVD).

Reference	Modality	Sensitivity (mV/pH)	Substrate	Intermediate Layers	Sensing Layer	Key Fabrication Step(s)	Repeatability - Fabrication of a single design
[123] (Anastasova et al., 2018)	OCP	73.4	PCB	ENIG, Au	IrOx – Electrochemical	ENIG PCB, Au electrodeposition	N/A
[96] (Moschou et al., 2015)	dEGFET	45.8	PCB	Au	ITO	Sputtering	N/A
[103] (Prodromakis et al., 2011)	dEGFET	22.0	PCB	Au	TiO ₂	Au plated PCB, sputtering	N/A
[104] (Trantidou et al., 2013)	dEGFET	16.3	PCB	Au	Parylene C	CVD, photoresist, oxygen plasma	N/A
[99] (Yang et al., 2012)	dEGFET	18.4	Glass	Cu	CuO	DC sputtering, annealing	N/A
[100] (Zaman et al., 2011)	OCP	28.0	Glass	-	CuO	Annealing	(Not Reported) n = 3
Current Work	dEGFET	70.7	PCB	-	IrOx - Electrochemical	Electropolishing	(± 5 mV/pH) n = 56

Table 2.3: Comparison of state-of-the-art pH sensors that employ IrOx as a pH sensitive layer. Abbreviations: open circuit potential (OCP), chemical vapor deposition (CVD), electroless nickel immersion gold (ENIG), complementary metal-oxide semiconductor (CMOS), relative standard deviation (RSD).

Reference	Modality	Sensitivity (mV/pH)	Substrate	Intermediate	Sensing Layer	Key Fabrication Step(s)	Repeatability - Fabrication of a single design
[57] (Huang et al., 2011)	OCP	51.1	Polyimide	Cr + Au	IrOx – so-gel	Photolithography, electron beam evaporator	Single sensor, multiple runs
[106] (Olthuis et al., 1990)	OCP	73.6	Ir wire	-	IrOx – Electrochemical	Ultrasonic bath	N/A
[115] (Kim and Yang, 2014)	OCP	59.0	Glass	Cr, Au	IrOx – Electrochemical	Photolithography, sputtering	($R^2 = 0.999$) n = 2
[116] (Marzouk, 2003)	OCP	73.7	Ti	-	IrOx - Electrochemical	-	(± 1.2 mV/pH) n = 6
[117] (Zea et al., 2019)	OCP	71.3	Polyethylene naphthalate	Pt	IrOx - Electrochemical	Laboratory inkjet printer	(RSD of 0.899%) n = 3
[118] (Gowers et al., 2019)	OCP	58.5	Polycarbonate	Cr, Au, Ag	IrOx - Electrochemical	Sputtering, electron beam evaporator	N/A
[119] (Elsen et al., 2009)	OCP	79	Glass	Cr, Au	IrOx - Electrochemical	Vapor deposition	N/A
[121] (Kim et al., 2003)	dEGFET	62.5	Glass	ITO	IrOx - Electrochemical	ITO deposition	N/A
[123] (Anastasova et al., 2018)	OCP	73.4	PCB	ENIG, Au	IrOx – Electrochemical	ENIG PCB, Au electrodeposition	N/A
[122] (Hendrikse et al., 1997)	EGFET	59.8	Silicon	-	IrOx - Sputtered	CMOS	N/A
Current Work	dEGFET	70.7	PCB	-	IrOx - Electrochemical	Electropolishing	(± 5 mV/pH) n = 56

Chapter 3

Methods & Experimental Techniques

This chapter outlines the methods required to realise this body of work. Working principles of experimental techniques are briefly summarised, with additional detail added where pertinent to operation or data interpretation specific to this work.

3.1 Chemicals

0.05 M potassium phosphate (KPI) buffers were prepared using phosphate monobasic/dibasic (Sigma Aldrich, UK). These ranged from pH 6 to 8 at intervals of 0.5, with pH confirmed to be within 0.01 pH using a commercial Mettler Toledo pH meter (FiveEasy and Inlab Expert Pro). Citric acid solution was prepared at 10% w/v from a powder (Sigma Aldrich, UK). Ultrapure water (18.2 M Ω /cm, MilliQ) was used for preparation of all aqueous solutions.

3.2 PCB Design

The extended gate electrodes were designed using Eagle software and manufactured by a commercial printed circuit board (PCB) supplier (Eurocircuits, Belgium). The Cu electrodes were supplied without surface finish on an improved FR4 substrate (Technolam GmbH, NP-155FR). The Cu layer thickness was measured to be $30 \pm 1.7 \mu\text{m}$ (Bruker DektakXT; $n = 6$). Prior to use, all electrodes were submerged in 10% citric acid (Sigma Aldrich, UK) for 15 minutes to remove visible oxide from the contact pads.

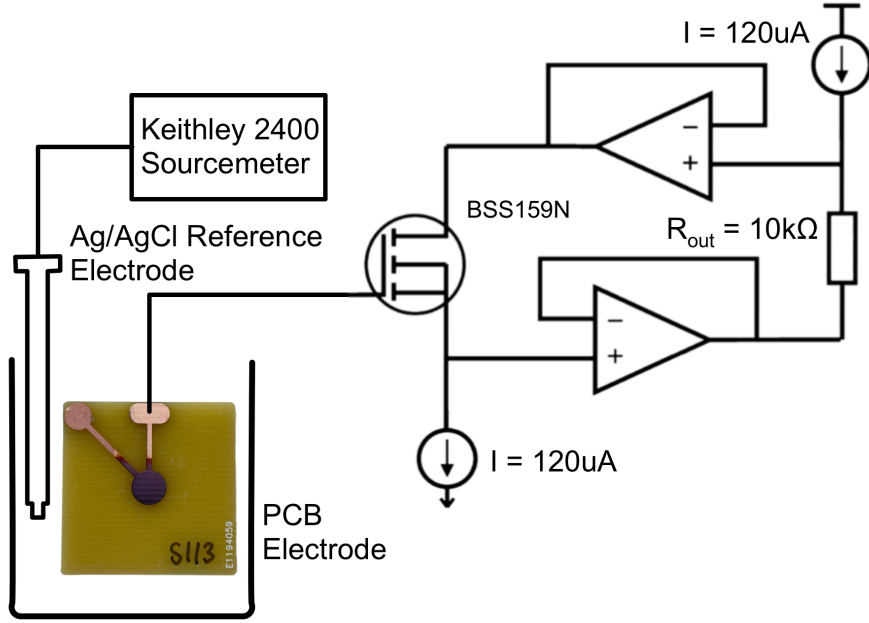


Figure 3.1: System diagram including biasing electrode, readout circuitry and the extended gate PCB electrode. Adapted from [95].

3.3 Discrete EGFET Readout and Bias Circuit

The PCB discrete extended gate ion-sensitive field effect transistor (dEGFET) pH sensor was connected to a biasing and readout circuit, shown in Figure 3.1, that was fabricated in-house based on a previous design [95]. The gate voltage is the sum of the voltage on the double junction Ag/AgCl/Saturated potassium chloride (KCl) bias electrode (ALS, Japan) and the potential across the electrode-electrolyte interface at the PCB electrode, as shown in equation 3.3.1.

$$V_{gate} = V_{bias} + V_{interface} \quad (3.3.1)$$

V_{bias} was fixed for each transistor based on experimental measurement to bias the device into the centre of its linear triode region (see section 2.3.1.1) such that a change in $V_{interface}$ will lead to a linear change in V_{gate} . After sweeping V_{bias} between -0.6 V and -1.4 V, the optimum bias voltage was identified in the centre of the triode region where the dynamic range is the greatest. Further detail on the cause of a potential difference at the surface-solution interface and the role of the bias electrode can be found in section 2.3.2.

The readout circuitry employs a constant-voltage constant-current (CVCC) configuration, such that the source-drain current through the transistor is fixed at 120 μ A. R_{out} , in tandem with a second constant current source, dictates the source-drain voltage which here was fixed at 1.2 V. A change in $V_{interface}$ and thus V_{gate} , results in a change in source voltage (V_{source}) which is mirrored across the operational amplifiers. The electrical isolation enabled by the

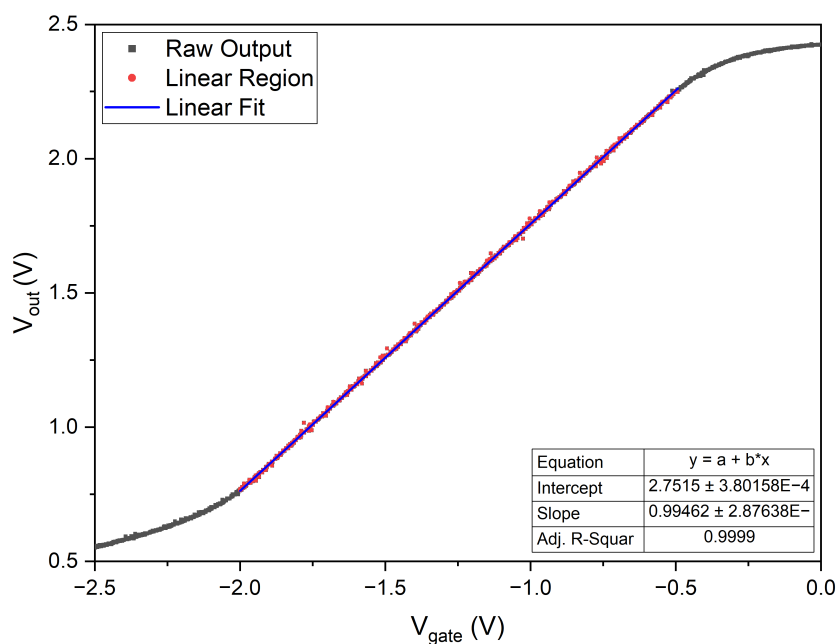


Figure 3.2: Output of the dEGFET readout circuitry in response to a potential sweep between -2.5 and 0 V applied to the transistor gate. Linear fit performed in Origin Pro.

high input impedance of the operational amplifiers prevents loading of the transistor and unwanted changes to the transistor biasing. A PicoLog 1216 12-bit analog-to-digital converter (ADC) (Pico Technology, UK) was used to digitise the resulting output signal, measured with respect to ground, with readings taken every 8 ms and no averaging performed.

All components are discrete surface-mount devices (SMD) including the BSS159N depletion mode n-type metal-oxide-semiconductor field effect transistor (MOSFET), selected due to its low cost and low gate leakage current. LM334M/NOPB was used as a current regulator, LT3045EMSE#PBF-ND as a voltage regulator and LTC6079IGN#PBF as a dual operational amplifier package. DC power was supplied by an external voltage source (GW Instek GPS-4303) while the bias voltage was supplied to the reference electrode using a Keithley 2400 Sourcemeter.

The performance of this readout circuitry was measured by applying a gate bias voltage between 0 and -2.5 V, and monitoring the output voltage. Figure 3.2 shows the response, including a prominent linear region where a linear fit shows a strong adjusted R^2 value over a 1.5 V range.

3.4 Electrochemical Techniques

As discussed in chapter 2, electrochemical phenomena at the surface-solution interface of the PCB electrode are key to the operation of dEGFET devices. Electrochemistry is used more generally in this work to probe the manufactured PCB electrodes, as well as at multiple stages in

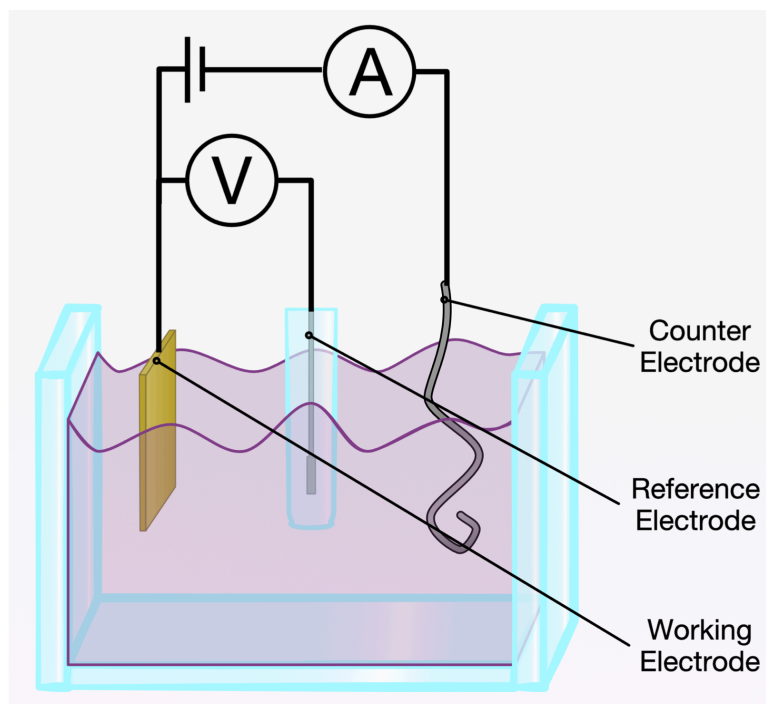


Figure 3.3: Diagram showing a typical three-electrode electrochemical cell, consisting of a Cu working, Pt counter and Ag/AgCl reference electrode [36].

the fabrication of the devices. This section provides information on the utilised electrochemical techniques towards realisation of the dEGFET devices in chapter 4 and electrowetting valves in chapter 6. A SP-300 Biologic potentiostat was used for the electrochemical measurements within this work.

3.4.1 Electrochemical Cells

To perform electrochemical measurements a three-electrode cell (Figure 3.3) was used consisting of a Cu PCB working electrode, a Pt wire counter electrode and an Ag/AgCl/Saturated KCl reference electrode.

In this arrangement, a voltage is applied between the working and reference electrode, where the reference electrode is able to provide a known and stable voltage relative to a working electrode where the electrochemical properties are to be studied. The operating principle of the Ag/AgCl electrode that results in a stable potential is explained in section 2.3.6.

A third electrode is required to enable a current to flow after a potential is applied. Current flow through the reference electrode may alter its potential, introducing additional voltage drops within the system which can not be isolated. In this case a Pt electrode acts as the counter electrode where current flow can be sourced.

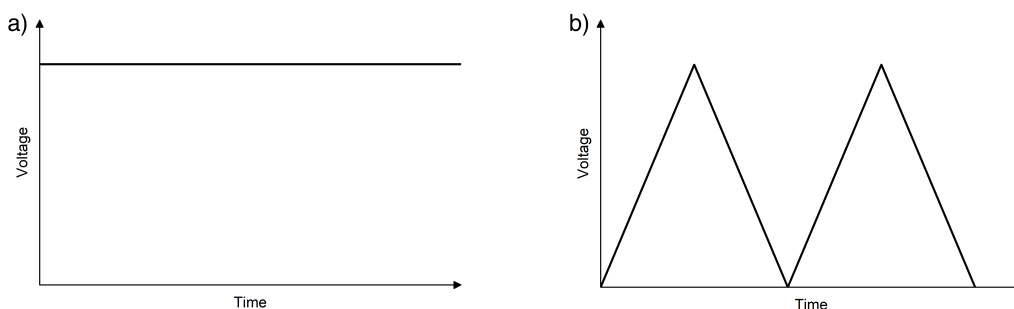


Figure 3.4: Diagram showing input waveforms for Chronoamperometry a) and CV b) electrochemical techniques.

3.4.2 Chronoamperometry

One of the simplest measurements that can be performed using a potentiostat and three electrode cell is the application of a constant voltage between the working and reference electrode (voltage against time shown in Figure 3.4a). The resulting current between the working and counter electrode can be monitored over time, resulting in the technique named chronoamperometry.

This method was used in chapter 6 during the investigation into electrowetting valves for controlled release of reagents around microfluidic channels. The PCB working electrode was coated with a hydrophobic molecule and the measurement performed with KPI as the electrolyte.

3.4.3 Cyclic Voltammetry

Cyclic voltammetry (CV) utilises the same three-electrode chemical cell previously described and was used for two different purposes related to the PCB dEGFET sensors. Firstly, to probe the required potential to catalyse reduction and oxidation (redox) reactions, as a method for monitoring the redox active molecules on surface and in solution. Secondly, the technique was used to electrochemically deposit an iridium oxide (IrOx) layer on PCB dEGFET electrodes from an Iridium Oxalate deposition solution.

The potential is cycled between two voltages at a constant rate (defined in mV/s) as shown in 3.4b and the resulting current between the working and counter electrode monitored. Figure 3.5 shows a typical cyclic voltammogram for a single, reversible redox couple [124].

Redox active molecules are expected to produce peaks at specific voltages (although dependent on the scan rate), where the theoretical separation ($E_{p,a} - E_{p,c}$) for an ideal single electron, reversible reaction is 56.5 mV. Many redox active molecules and reactions are quasi-reversible or non-reversible and exhibit an increased peak separation.

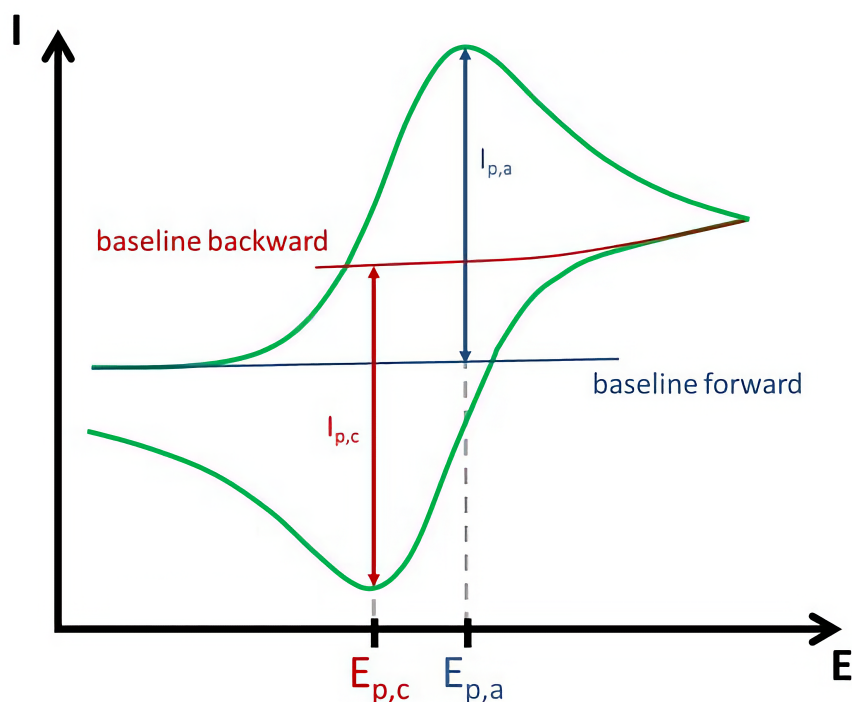


Figure 3.5: Typical cyclic voltammogram obtained for a system containing a single reversible redox couple. Adapted from [125].

The area between the cathodic half of the cycle and the backwards baseline represents the cathodic charge storage capacity (CSCc), which is correlated with the density of redox active groups when adjusted for electrode area [126]. The current value outside of these redox peaks on the positive half cycle can be defined as the non-faradaic capacitance, a physical phenomenon representing the capacitance of the electrochemical double layer (ECDL) at the surface [127].

In this work, multiple electrolytes were used when performing CVs to isolate redox peaks on surface as opposed to those in solution. This includes KPI buffer at pH 7, alongside multiple forms of the iridium oxalate deposition solution introduced subsequently in this work. For this electrochemical characterisation the potential was cycled between -0.5 V and 0.8 V vs. Ag/AgCl at a scan rate of 100 mV/s. CV peak analysis was performed using Origin Pro with a linear baseline fit to the non-Faradaic background current.

3.4.3.1 Electrodeposition of Iridium Oxide

Potential cycling was also used to electrochemically deposit a hydrated IrOx layer onto the surface of the PCB electrodes. Deposition is performed onto a working electrode submerged in an iridium oxalate deposition solution. Yamanaka [128] was the first to prepare a deposition solution, intended to be used in electrochromic displays.

Since Yamanaka's work, research efforts have explored a variety of iridium salts [129, 130] with a view to reduce the stabilisation time. One successful approach is to heat the solution to 90 °C for 10 minutes [116].

The deposition mechanism is now widely accepted to involve IrOx nanoparticles [131] which are electrochemically reduced into IrOx ions and subsequently bind to the electrode when in close proximity. No consensus on the specific species involved in the deposition has been reached [132, 133].

Iridium Oxalate for use in this work was prepared using the following protocol, as outlined initially by Yamanaka [128]:

1. Iridium chloride hydrate ($IrCl_4 \cdot H_2O$: 0.15 g) (Alfa Aesar, UK) was dissolved in 100 mL of water by magnetic stirring for 30 min.
2. 1 mL of aqueous hydrogen peroxide solution (H_2O_2 : 30% wt.) (Sigma Aldrich, UK) was added and stirred for 10 min.
3. Oxalic acid ($(COOH)_2 \cdot 2H_2O$: 0.5 g) (Sigma Aldrich, UK) was added and stirred for 10 min.
4. Anhydrous potassium carbonate (K_2CO_3) (Sigma Aldrich, UK) was finally added to adjust the solution pH to 10.5.
5. The resulting solution was left to stabilise for 3 days, after which it transitions from yellow-green and adopts a dark blue colour (Figure 3.6).

Electrochemical reduction, which drives deposition from the iridium oxalate solution onto an electrode surface, has been demonstrated using constant current, constant voltage, pulsed potential and potential cycling methods [119, 134, 135]. These approaches enable monitoring of the deposition as it progresses, most commonly during potential cycling depositions.

A variety of potential cycling deposition parameters are covered in the literature, varying the range, cycle number [134] and scan rate [131]. Elsen *et al.* [119] performed a study to monitor the impact of deposition parameters on sensitivity and found the Nernstian slope of the pH response is effectively independent of the deposition method.

Deposition conditions used in this work were informed by a protocol from literature [136] which provided layers of consistent mechanical stability (found above 20 potential cycles) and a potential range that was compatible with the electrode surface. All sensors underwent 50 potential cycles between 0.8 and -0.5 V vs. Ag/AgCl at 100 mV/s and at room temperature. A Biologic SP-3000 potentiostat was used in a three electrode configuration, where the CVs obtained during deposition are shown in chapter 4.

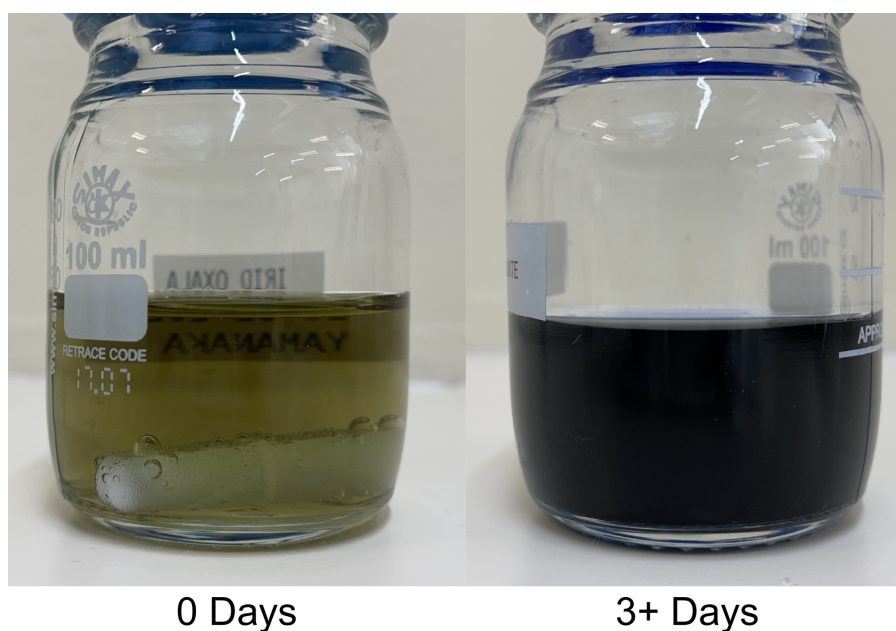


Figure 3.6: Images of the iridium oxalate solution immediately after preparation (0 Days) and after it has stabilised (3+ Days).

A custom 3D printed jig (Figure 3.7) was used to control submersion depth and separation of the three electrodes within the cell, particularly important to ensure consistent Cu working electrode surface area for later analysis of CVs obtained during deposition.

3.4.4 Electrochemical Polishing

Chronoamperometry was utilised to electrochemically polish Cu electrodes, with a 60% dilution of stock 85% Phosphoric Acid (Fluorochem, UK) as the electrolyte. A 1.4 V potential was applied for 6 minutes [137, 138].

Electrochemical polishing focuses on a metallic work-piece which serves as the anode, with a metallic counter electrode as the cathode. As a voltage is applied, surface molecules are oxidised resulting in a current flow. These oxidised molecules subsequently dissociate into the surrounding electrolyte and are reduced at the cathode. Anodic levelling occurs during this electropolishing process, as illustrated in Figure 3.8, where protruding regions are favourably oxidised due to increased current density at these sites. The resulting effect is a reduction in surface contamination and roughness, where the finish often appears visually reflective.

Larger current flowing at protruding regions is accepted across literature, although the precise mechanism is not agreed upon [138]. Recent work [139] further explored the most favourable theories around the development of a viscous region that forms close to the electrode surface during polishing. They probed the rate of water acceptor reactions at varying distances from the surface, monitoring electronic current flow in a water electrolysis reac-

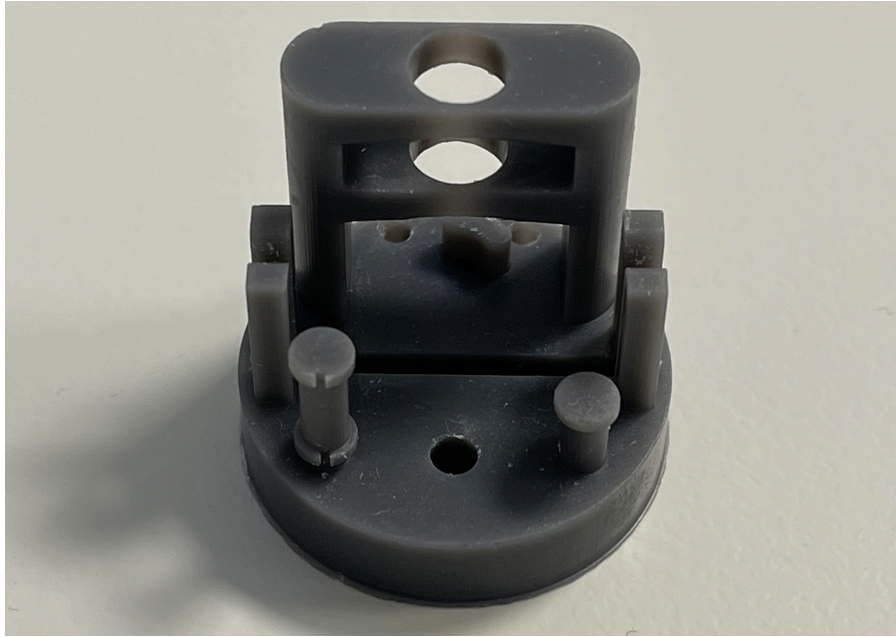


Figure 3.7: Custom 3D printed IrOx electrodeposition jig.

tion to provide additional information on the nature of this viscous layer. This also aids in understanding the cause of preferential current flow and etching at protrusions.

With a potential applied, greater than +0.375 V for Cu but below the potential of significant oxygen evolution (+1.7 V for aqueous phase), the metal ions at the surface dissociate into solution, as per equation 3.4.1 for Cu electrodes deposited on the PCB substrates. A thin initial copper oxide (CuO) layer on the surface reacts in a similar way [140], with an additional O^{2+} molecule moving into solution. This removal of CuO species to reveal bulk Cu was also observed using X-ray photoelectron spectroscopy (XPS) analysis of polished sensors within this work (section 4.2.5).



Figure 3.8a shows the subsequent hydration of these Cu^{2+} ions by water molecules which screen the ionic charge with a negative dipole (δ^{-}) facing inwards. This results in a δ^{+} facing outwards where the solvated ion acts as a positively charged ion available for ionic flow in the system between the anode and cathode.

As shown in Figure 3.8b, this leads to a depletion region with a relative lack of water molecules (termed water acceptors), a relative increase in other molecules such as phosphoric acid and its ions, and a resulting increase in viscosity in this depletion layer. As new Cu^{2+} ions dissociate into solution, the water acceptors that will screen these molecules must diffuse from the bulk solution.

Water acceptors preferentially diffuse to the surface protrusions due to their proximity, for

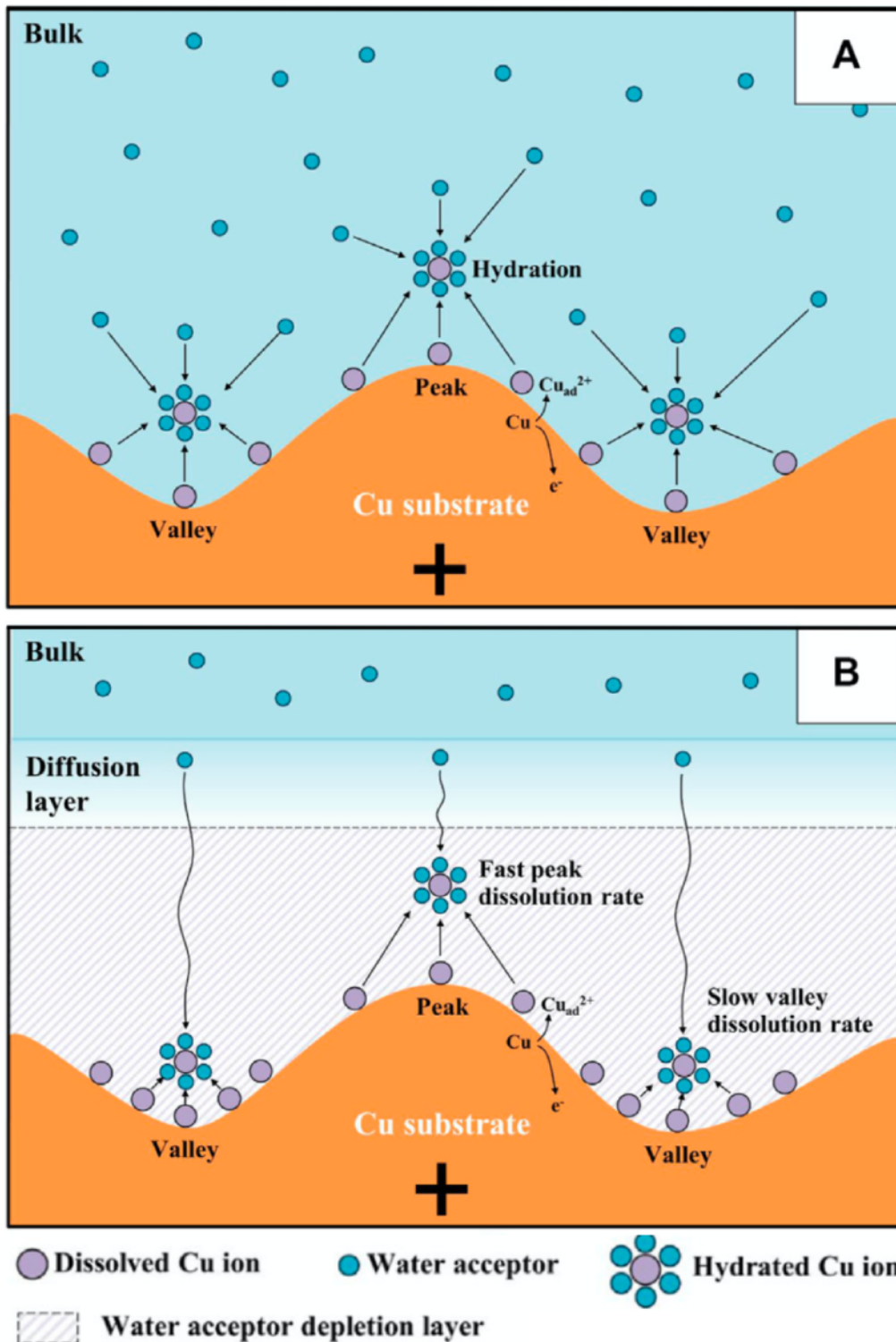


Figure 3.8: Schematic representation showing a Cu surface undergoing electropolishing in an initial state (a) and in steady state (b) [139].

which the viscous depletion layer amplifies the diffusion time between regions of different height on the surface. This leads to increased ion flow of solvated ions away from the area towards the cathode and increased current density at these protruding sites as Cu dissociates into solution.

There is scope for optimization of the electrolyte in which polishing is performed, with a range of literature on the topic for established applications such as electronics, machinery and consumer products. Additives that increase viscosity in this depletion layer such as starch, ethylene glycol [137] and alcohols [141] can be added to phosphoric acid to further reduce prioritise surface protrusions.

Electrolyte selection can also be optimised in relation to its environmental sustainability, considering solutions which are easier to dispose of and safer to handle whilst offering similar polishing capabilities. Ionic liquids are a promising alternative [142, 143], as are deep eutectic solvents (DES) which are biodegradable [144].

Phosphoric acid was ultimately used in this work due to being an established electrolyte within metalworking, enabling proof-of-concept when applied to preparation of the PCB electrodes discussed in chapter 4. Future work could seek to optimise this protocol.

3.5 Physical Characterisation Techniques

3.5.1 Atomic Force Microscopy (AFM)

Atomic force microscopy (AFM) images were obtained using a Bruker Bioscope Resolve in tapping mode with a RTESPA300 tip. Surface roughness analysis was performed using Gwydion. AFM was used to monitor topographical information of the dEGFET sensor surface across various stages in the fabrication process. Figure 3.9 shows the hardware common within an AFM system, involving a micro-electro-mechanical systems (MEMS) cantilever, photo detector, laser source, multi-axis stage and feedback controller.

AFM can be used in multiple imaging modes, the most common being contact, non-contact and intermittent contact [145]. An implementation of intermittent contact mode was used in this work, specifically tapping mode where the MEMS cantilever is piezoelectrically driven to oscillate close to its resonant frequency. As the tip mounted on the underside of the cantilever contacts the surface, repulsive forces decrease the oscillation amplitude, and the z stage moves the tip away from the surface to maintain near resonant oscillations. Reflection of a laser off the back of the cantilever onto the spatially sensitive photo-detector is used to monitor the cantilever oscillation, which combines to create a final height map of the surface. The lag measured between the drive signal and the output of the photo-detector forms a phase map,

which can provide additional information on surface material properties.

This resulting height image provides quantifiable topographical data, reported often as a surface roughness through a range of parameters; in this work often reported as root mean squared (RMS) roughness. Resolution of AFM systems can be greater than 1 nm laterally and 0.025 nm vertically [146].

There are several limitations of AFM relevant to this work, which were considered to ensure validity of the obtained data and subsequent analysis. AFM has a limited scan area, 100 μm on the Bruker Bioscope Resolve used in this work. Multiple images across different regions were used to obtain a representative understanding of surface topography across the sample surface. AFM also has a limited dynamic range for features in the z direction, reported as 15 μm in the system specification. This made it difficult to image dEGFET sensors with IrOx films using AFM, due to features on this surface exceeding this vertical magnitude.

Captured AFM images often required plane fitting, to account for mounted samples not lying perfectly parallel to the sample stage, due to the macro scale roughness of the FR4 substrate in this work. Two areas were selected where their average height is calculated and a linear offset applied to the entire dataset so that these two average heights are set to be equal.

AFM images can also be susceptible to artefacts from non-ideal interactions between the tip and surface [145]. This includes tip convolution where the tip has a large radius with respect to the feature that is to be visualized, artefacts from steep sample topography, and the tip getting stuck and causing spurious oscillation of the cantilever. Due to the samples being hard metallic surfaces and possessing minimal small features these artefacts were not common issues and tip deconvolution was not implemented.

3.5.2 Scanning Electron Microscopy (SEM)

Scanning electron microscopy (SEM) was performed using a JEOL 7800F Prime scanning electron microscope. Images were taken with 5 kV beam energy and a working distance of 10 mm.

SEM utilises a high energy beam of electrons, that act as the source of incident energy, to image a sample [147]. Electrons generated from a source are accelerated to high energies (> 2 kV) using a large potential difference in the column (Figure 3.10). Lenses, either electrostatic or magnetic, collimate and focus the beam of electrons to the sample surface. Much of the complexity in engineering high quality SEMs involves the quality of the focusing in this column, for which literature provides more detail [148]. Due to the electrons being focused to a single collimated point, the beam is raster scanned across the surface to build up an image.

As the sample is imaged, the surface is bombarded with electrons which must be given a path to dissipate, or the sample will become negatively charged and deflect the incoming

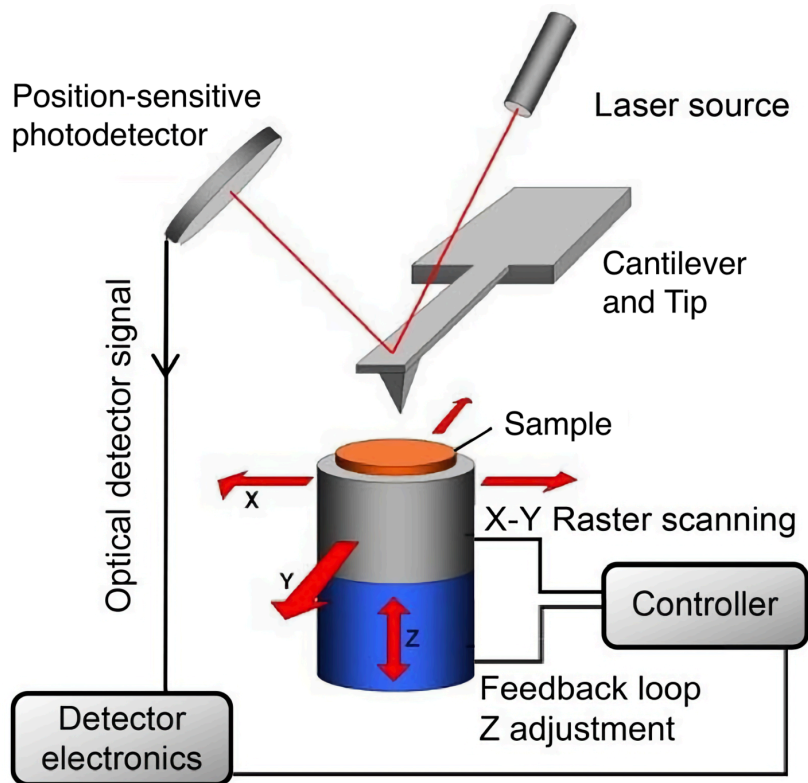


Figure 3.9: Generalized schematic of an atomic force microscope (AFM) with essential hardware components. Adapted from [145].

electrons preventing imaging. For this reason, samples must be grounded to the SEM stage, and be naturally conducting or have a thin metallic layer deposited to act as a charge dissipation layer.

As shown in Figure 3.11 electrons bombarding the surface interact with atoms in the sample to produce an array of different products, which all provide different information about the sample. Images in this work are produced from secondary electrons (SE) which result from inelastic interactions. Due to the low energy of SE, as a result of losses in those collisions, they only escape the sample from near the surface (several nanometres), resulting in SE providing topographical information as the electron yield is higher in topographically rich regions compared to planar surfaces [148].

Detectors capture the ejected SE and provide a signal proportional to the number of secondary electrons as the beam is raster scanned across the imaging area. The images obtained in this work utilised an Everhart-Thornley electron detector, which also collected a lower proportion of back scattered electrons (BSE). These provide atomic information based on elastic collisions between incident electrons and atomic nuclei. Atoms of high atomic number, Z , are stronger scatterers of these incident electrons, meaning the strength of the signal is related to their Z number [148].

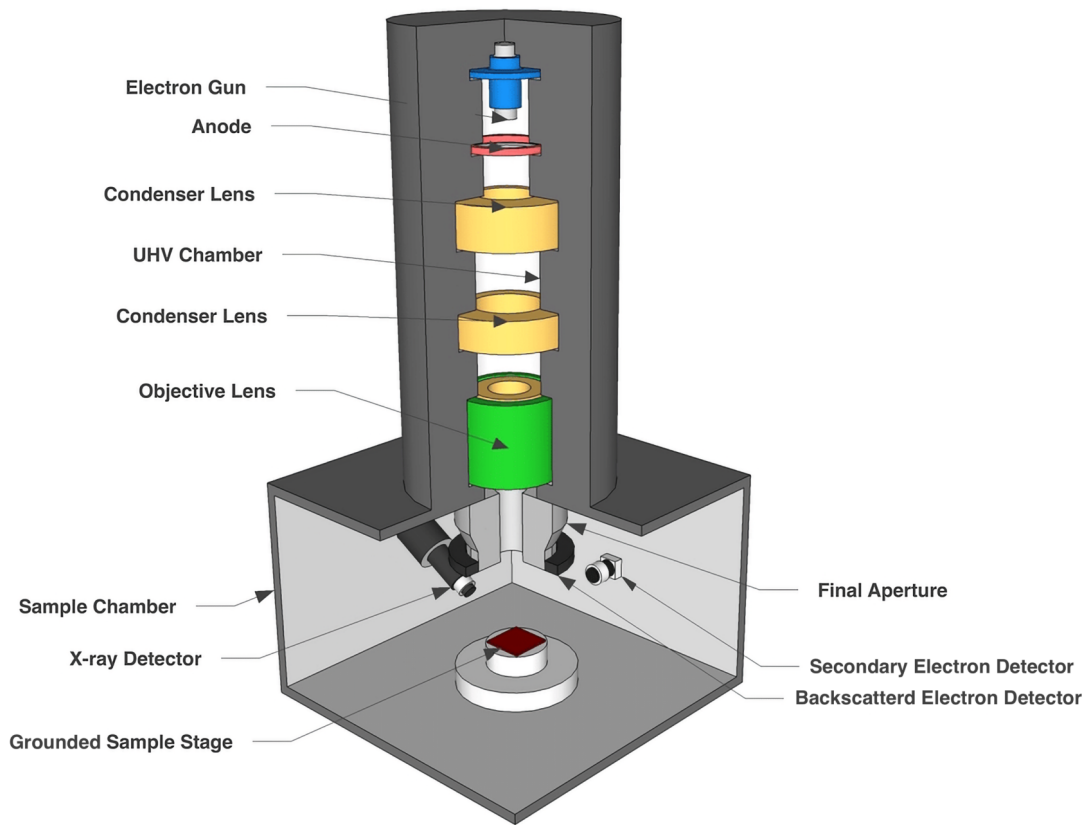


Figure 3.10: Diagram of SEM with key hardware components, including two types of electron detector and a X-ray detector for EDX. Adapted from [149].

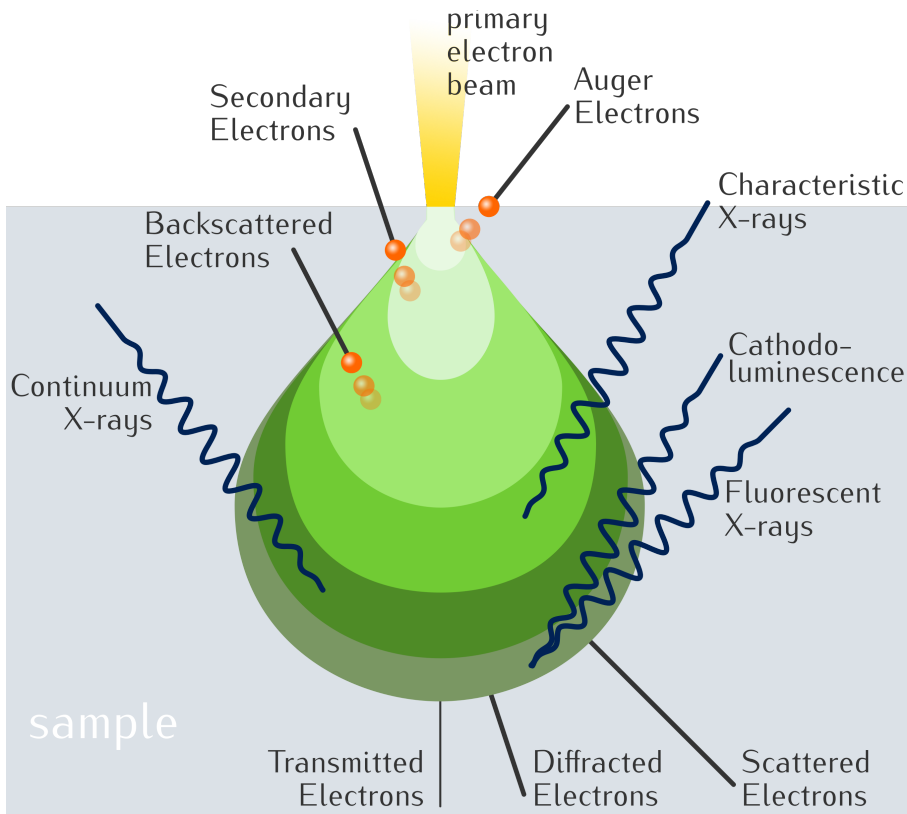


Figure 3.11: Interaction volume of SEM electron beam, various signals generated from the interaction. Adapted from [150].

3.6 Chemical Characterisation Techniques

3.6.1 Energy-dispersive X-ray Spectroscopy (EDX)

An Oxford Instruments AZtec energy-dispersive X-ray spectroscopy (EDX) system containing 2 detectors as part of a JEOL 7800F Prime SEM was used for elemental analysis. EDX maps were collected using a beam energy of 5 keV with fixed acquisition settings ($\times 3,300$ magnification, frame duration of 40 s, frame count of 10, and 50 μs dwell time). EDX analysis was performed using the Oxford Instruments AZtec software.

EDX is a chemical characterisation method often installed as part of a SEM as it requires many of the same components for operation, with the exception of an alternative detector [151]. This integration means traditional topographical SEM images can be overlaid with chemical data derived from EDX images. Instead of monitoring the electrons emitted from interactions with the sample, the characteristic X-rays produced due to atomic excitation by the incident electron beam are detected, as shown in Figure 3.11. The intensity and energy of these characteristic X-rays provide quantifiable elemental information.

Specifically, incident electrons collide with ground state electrons in electron shells around the atomic nucleus, as shown in Figure 3.12 [152]. When a vacancy is created in an inner orbital, an electron in a higher energy state will transfer to this lower energy state with the excess energy emitted in the form of a X-ray. The precise energy of this X-ray is a function of the element of which the orbiting electron collided, and the atomic orbitals from which the electron decayed from and into. The intensity of each wavelength provides quantifiable information on the concentration of atomic species, and the location of the incident beam provides spatial information.

Table 3.1 shows a small selection of energy levels with electron configurations and International Union of Pure and Applied Chemistry (IUPAC) notation, which indicate the initial and final energy level between which an electron transitions [153]. IUPAC notation uses its first character to indicate the shell the electron decays into, and the second the shell the electron originated from. A shortened version of this notation is sometimes used where only the excited state is given, and the subscripts may be dropped when unknown or irrelevant.

Of note for this work, the interaction volume of the incident electrons is related to the incident electron beam energy, with this volume dictating how much of the signal is contributed from the sample surface relative to the bulk [151]. The beam energy must also be large enough to excite electrons to the next energy level for all elements of interest as previously described. 5 keV was used in this work to ensure sufficient energy for detection of all elements of interest, while minimising the contribution of the underlying Cu/FR4 substrate in the detected signal.

The technique provides quantifiable information and is a high throughput analysis method

Table 3.1: Electron energy levels and transitions between them represented using the IUPAC notation [154].

Inner Orbital	Excited Orbitals	IUPAC Notation
$K(1s_{1/2}^{-1})$	$L_3(2p_{3/2}^{-1})$	$K-L_3$
	$L_2(2p_{1/2}^{-1})$	$K-L_2$
	$M_3(3p_{3/2}^{-1})$	$K-M_3$
	$M_2(3p_{1/2}^{-1})$	$K-M_2$
$L_3(2p_{3/2}^{-1})$	$M_5(3d_{5/2}^{-1})$	L_3-M_5
	$M_4(3d_{3/2}^{-1})$	L_3-M_4
$L_2(2p_{1/2}^{-1})$	$M_4(3d_{3/2}^{-1})$	L_2-M_4
$M_5(3d_{5/2}^{-1})$	$N_7(4f_{7/2}^{-1})$	M_5-N_7

due to the minimal sample preparation required and real time results as part of the existing SEM set-up. Limitations of the technique include the previously mentioned penetration depth of the electron beam into the sample, which prevents isolated surface level investigation. Elements H and He are undetectable due to the lack of outer electron shells from which de-excitation can occur. X-rays of light elements ($Z \approx < 10$) are typically difficult to detect due to their low energies which are readily absorbed by the specimen, however the utilised Oxford Instruments system is capable of quantifying elements with an atomic number of Be and above due to the two Ultim Max detectors [152].

Furthermore, the energy of emitted characteristic X-rays is similar across many elements and energy shell transitions. The Oxford Instruments system uses expected compositional information about the sample, alongside detection of decays from multiple energy states and high-performance electronics, to aid element identification.

3.6.2 X-ray Photoelectron Spectroscopy (XPS)

XPS is a highly surface sensitive chemical analysis technique that can provide quantifiable elemental information, including bonding pairs and oxidation states. A system diagram is shown in Figure 3.13. It relies on the photoelectric effect where electrons are ejected from their orbitals due to electromagnetic radiation incident on a sample, if the energy of the incident photons is greater than its binding energy [156]. The energy of the incident photons is determined by the frequency of the X-rays emitted from the source. The energy of the emitted electrons is dependent on the element and specific orbitals from which the electron was ejected. The number of electrons emitted from the sample at any one energy can be used to quantify the relative concentration of each element through the process of peak fitting.

During the peak fitting process, the energies of detected electrons are assigned to the or-

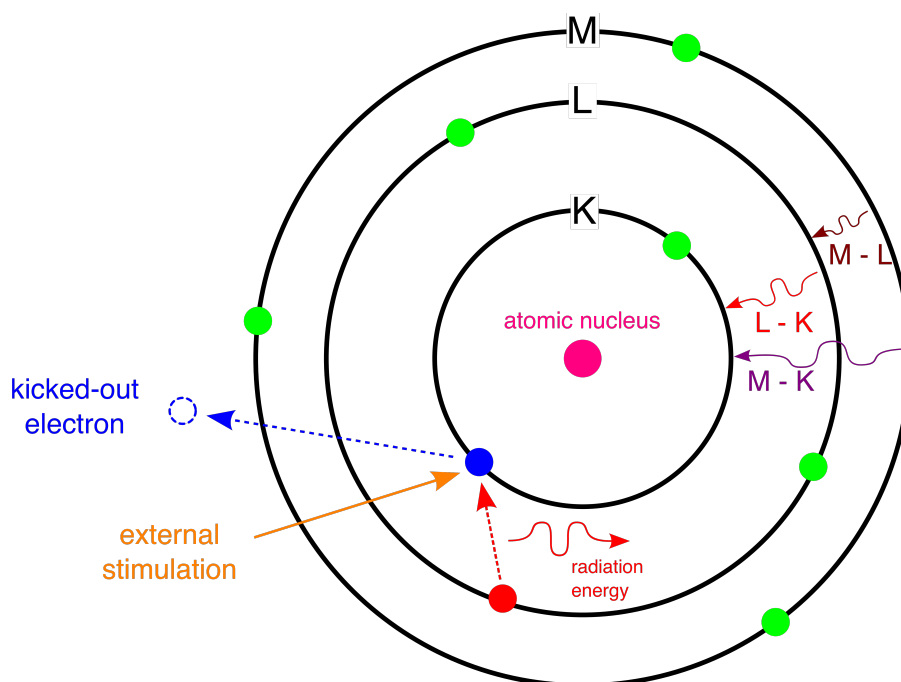


Figure 3.12: Collisions occurring between incident electrons and electrons orbiting atomic nuclei that produce characteristic X-rays. Adapted from [155].

bitals from which they were emitted (e.g. 1s). For orbitals beyond the innermost shell, the spin angular momentum leads to a splitting of the observed energies. This is represented as shown in Table 3.1, by adding the summation of the angular momentum quantum number and the spin angular momentum number [153]. Peak fitting is a complex process, and a mix of expected sample elemental content, alongside reference literature and databases are used to inform the process.

The analytical depth of XPS is typically around 5 - 10 nm, although incident X-rays penetrate deeper into the sample, ejected electrons must leave the specimen without scattering to be detected [157]. In this work, I exploited the low analytical depth of XPS to complement and confirm findings from the higher throughput EDX system. The requirements for XPS sample preparation and high vacuum pressure increase processing times. Additionally, due to the sample being exposed to high energy X-rays, the method is considered to be destructive [158].

XPS data presented in this work was obtained by Dr. Ben Coulson and Dr. Toby Bird on a custom XPS system at the University of York under the supervision of Dr. Andy Pratt. Experiments were performed in an ultrahigh vacuum system with a base pressure of $< 3 \times 10^{-10}$ Millibar, using a monochromated Al $K\alpha$ source at 1486.6 eV (Omicron XM 1000) and a power of 220 W. An aperture diameter of 6 mm was used with the sample normal at 45° to both the X-ray source and the entrance optics of the hemispherical energy analyser (Omicron EA 125). XPS spectra were referenced to adventitious carbon peak at 284.8 eV.

Binding energies were attributed using the National Institute of Standards and Technology (NIST) database [159], with values for Ir oxidation states informed by literature [160,

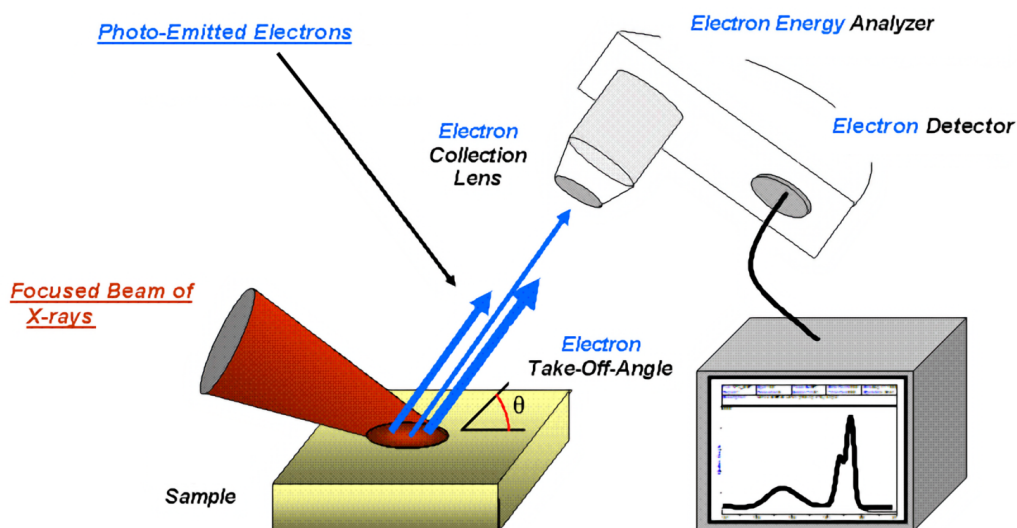


Figure 3.13: Schematic Diagram of XPS system.

161]. Peak deconvolution and fitting were carried out manually in conjunction with Dr. Toby Bird using XPSPEAK 4.1 software. Subsequently, atomic % for elements and species were obtained using the integral of the respective spectra using OriginPro peak find, against a Shirley background, and applying the appropriate correction factors [162].

Chapter 4

PCB ISFET Characterisation

This chapter presents the development and characterisation of a highly sensitive pH sensor based on low-cost and widely available printed circuit board (PCB) substrates.

4.1 Electrode Preparation

The pH-sensitive, discrete extended gate ion-sensitive field effect transistor (dEGFET) platform discussed in section 3.3 consists of a 5 mm diameter Cu electrode fabricated on a PCB, that is electrodeposited with an iridium oxide (IrOx) film. Electrodeposition was performed using a three-electrode cell consisting of a Cu PCB working electrode, Pt wire counter and Ag/AgCl reference electrode immersed in an iridium oxalate solution [128], prepared as described in section 3.4.3.1. Electrodeposition was performed using cyclic voltammetry (CV), allowing the growth of the IrOx film to be monitored. The voltage applied to the Cu working electrode was cycled 50 times between 0.8 and -0.5 V vs. Ag/AgCl at 100 mV/s, more details on the selection of the deposition parameters are found in section 3.4.3.1.

Figure 4.1 shows the resulting cyclic voltammograms (CVs) every 10 cycles. The iridium redox peaks have been attributed using CVs, taken before and after IrOx deposition, in different electrolytes and informed by literature. Peaks caused by other redox active molecules are annotated on Figure 4.3a, with further discussion on the attributing process and supporting CVs presented in section 4.2.2.

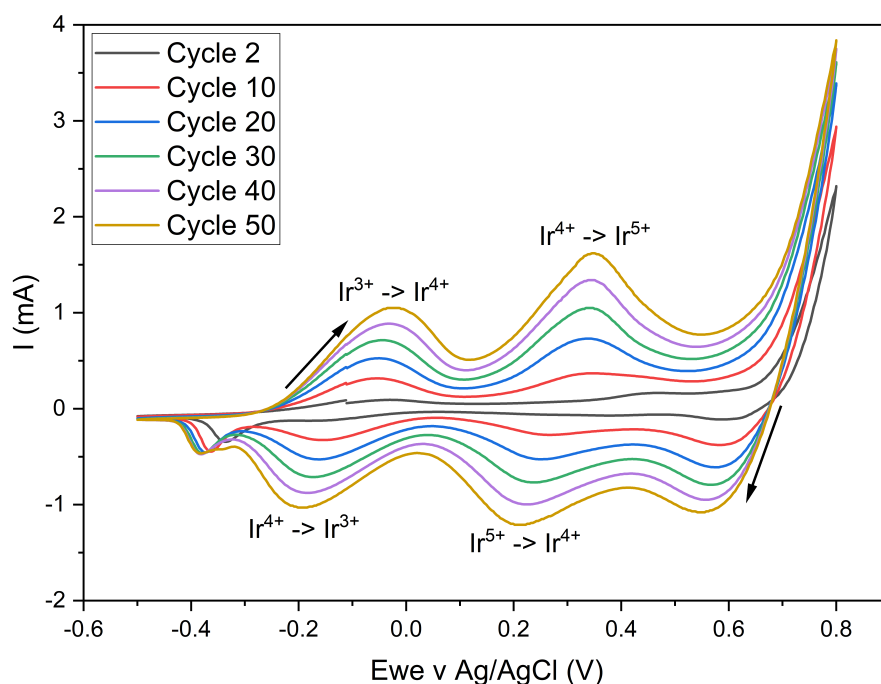


Figure 4.1: Cyclic voltammetry during electrodeposition of an IrOx film on the extended gate Cu PCB electrode, with Ir reduction/oxidation peaks between oxidation states indicated.

4.2 Characterisation

4.2.1 pH Sensitivity of IrOx Coated PCB Electrodes: unpolished vs. polished

The IrOx-coated Cu PCB electrode is connected to the gate electrode of a discrete metal-oxide-semiconductor field effect transistor (MOSFET) mounted on a separate PCB that includes the associated bias and readout circuitry. The pH sensitivity of the IrOx coated electrodes was determined by exposing the IrOx surface to a range of 50 mM KPI buffer solutions of differing pH. Figure 4.2a shows the output voltage of an unpolished, IrOx-coated electrode as a function of solution pH while Figure 4.2b shows the mean voltage recorded at each pH. Here, unpolished refers to those electrodes which were only cleaned by 15 min immersion in citric acid prior to electrodeposition. While the dEGFET clearly showed reversible changes to solution pH, the pH sensitivity, defined as the gradient of the straight line fit to the data in Figure 4.2b, was only 31.4 mV/pH; far below the theoretical limit of 88.8 mV/pH. Moreover, the pH sensitivity of these unpolished electrodes was highly variable, as shown in Figure 4.2c, with a median value of 31.3 mV/pH ($n = 31$ electrodes) and a standard deviation of 14 mV/pH.

In contrast, Figure 4.2a and 4.2b also show the shift in dEGFET output voltage using Cu electrodes that were electropolished prior to IrOx electrodeposition; polishing detailed in section 3.4.4. Here, the dEGFET displayed a pH sensitivity of 73.3 mV/pH; well beyond the traditional Nernstian limit. Moreover, electropolishing of the electrodes markedly improved

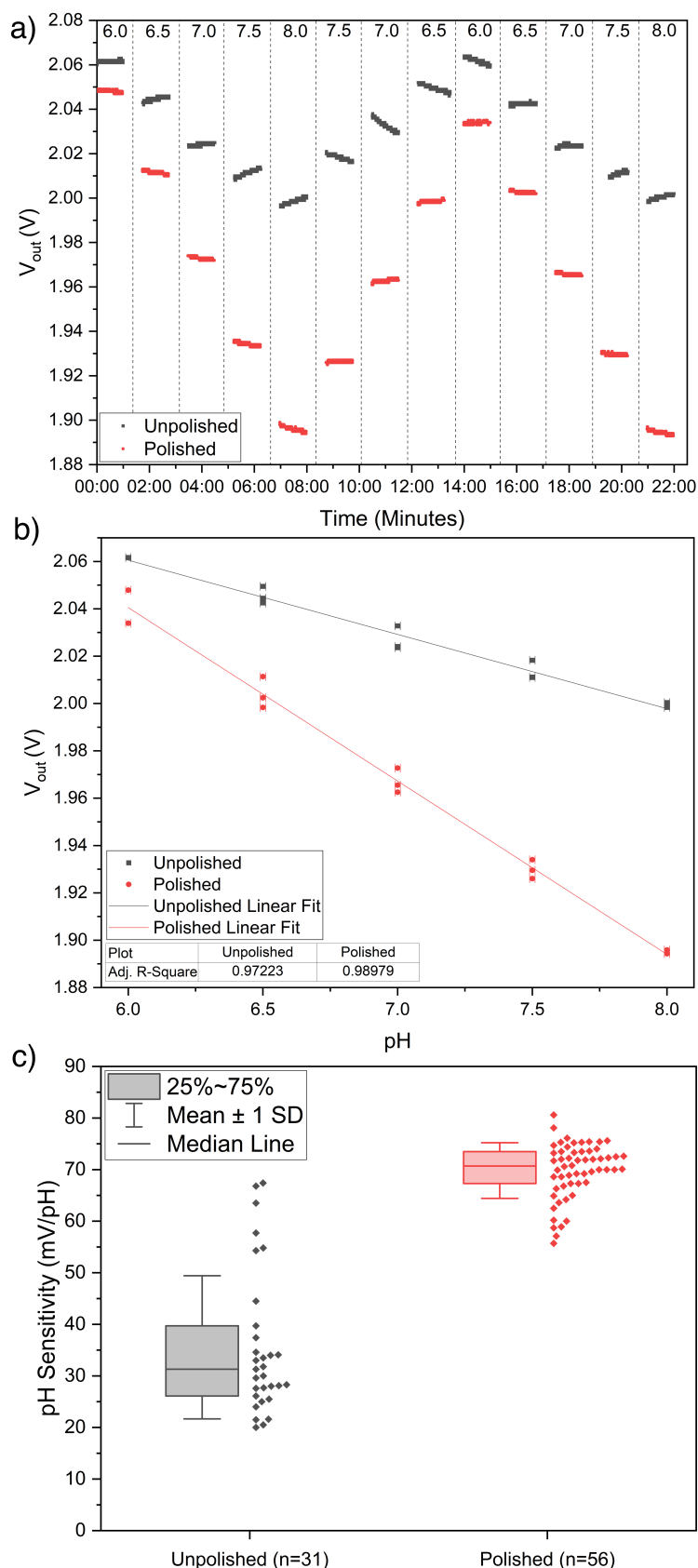


Figure 4.2: a) dEGFET output voltage using IrOx pH sensitive layer electrodeposited on unpolished and polished PCB electrodes. The solution pH is indicated at the top of the graph for each 60 s data collection window. b) Mean voltage of each plateau plotted against pH. c) pH sensitivity of unpolished and polished sensors. Box shows median value, 25th & 75th percentiles, while whiskers show \pm 1 SD. All points are displayed in the half violin plot.

the reproducibility of the pH sensitivity. Specifically, from measurements of a large number ($n = 56$) of nominally identical, polished electrodes exhibited a median pH sensitivity of 70.7 mV/pH and a standard deviation of only 5 mV/pH (Figure 4.2c).

To better understand the origins of the high pH sensitivity and reproducibility of polished Cu electrodes, a detailed study of the physical, chemical and electrochemical characteristics of the IrOx films electrodeposited on unpolished and polished electrodes was conducted.

4.2.2 Electrochemical Analysis of IrOx Deposition

Figure 4.3a shows typical CVs recorded during electrodeposition of IrOx on both unpolished and polished Cu electrodes for the first and final full voltage cycles. All curves are representative with raw data for 3 independent electrodes shown in Figure 4.3b and 4.3c.

Differences between the unpolished and polished samples are observed in the first full voltage cycle of the CV (Figure 4.3a cycle 2). Specifically, the non-faradaic current for the unpolished electrodes is roughly twice that observed for electropolished electrodes. This component is associated with the capacitance of the electrode-electrolyte interface where the larger capacitance of the unpolished electrode can be ascribed to either an increased surface roughness, leading to a larger apparent electrode surface area, or the existence of a thin contamination layer at the electrode surface.

Further analysis of the CVs is performed to identify the origin of redox peaks, as labelled in Figure 4.3a. Figure 4.4 shows CVs of unpolished electrodes in a range of electrolytes, before and after IrOx deposition, used to isolate and identify these peaks. KPI buffer was 50 mM concentration and pH 7. The oxalate solution contained all components of the iridium oxalate deposition solution, excluding the iridium chloride hydrate. This solution was made by adding 1 mL of 30% aqueous hydrogen peroxide and 0.5 g of oxalic acid to 100 mL of de-ionised water. Anhydrous potassium carbonate was used to adjust the solution pH to 10.5 before being left for 3 days, to mimic the protocol used for the iridium containing solution.

Figure 4.4a and 4.4c are CVs taken prior to deposition of IrOx on the sensor surface, enabling the elimination of Ir as a redox active group from both the electrode surface and in solution. This isolates contributions from the Cu electrode and components other than Ir in the oxalate deposition solution. Of note is the reduction peak around -0.3 V vs. Ag/AgCl that is much larger on the unpolished electrodes. This can be ascribed to the reduction of Cu^{2+} to Cu^0 based on results in literature [163, 164, 165], where the adjusted peak shapes in Figure 4.4c are the result of components within the oxalate solution. The presence of Cu^{2+} is believed to be within a native oxide layer at the surface of unpolished electrodes (this is further supported by chemical analysis, see sections 4.2.4 & 4.2.5).

Figure 4.4b and 4.4d are measured with the IrOx film deposited on the surface, enabling

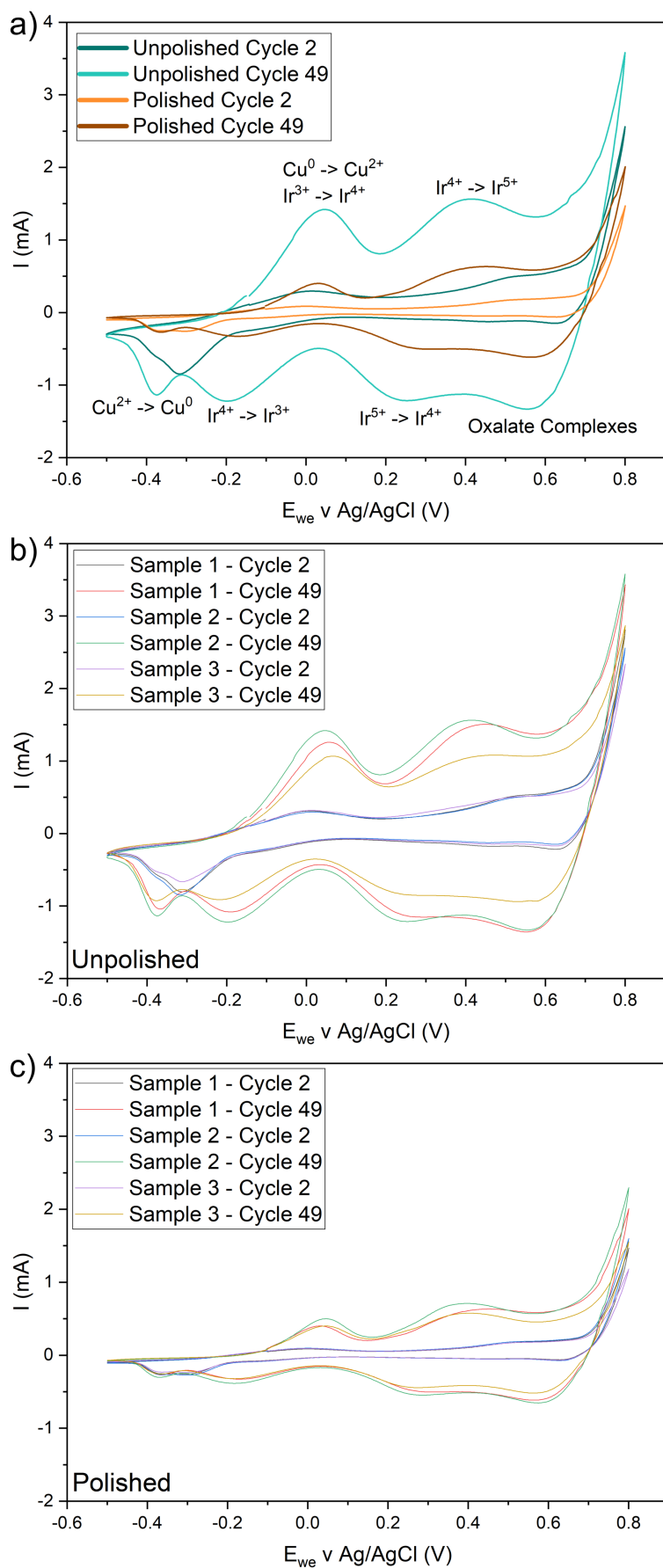


Figure 4.3: CV during deposition of IrOx films compared on both unpolished and polished sensors a), with three repeats for each b) - c) for the first and final full voltage cycles.

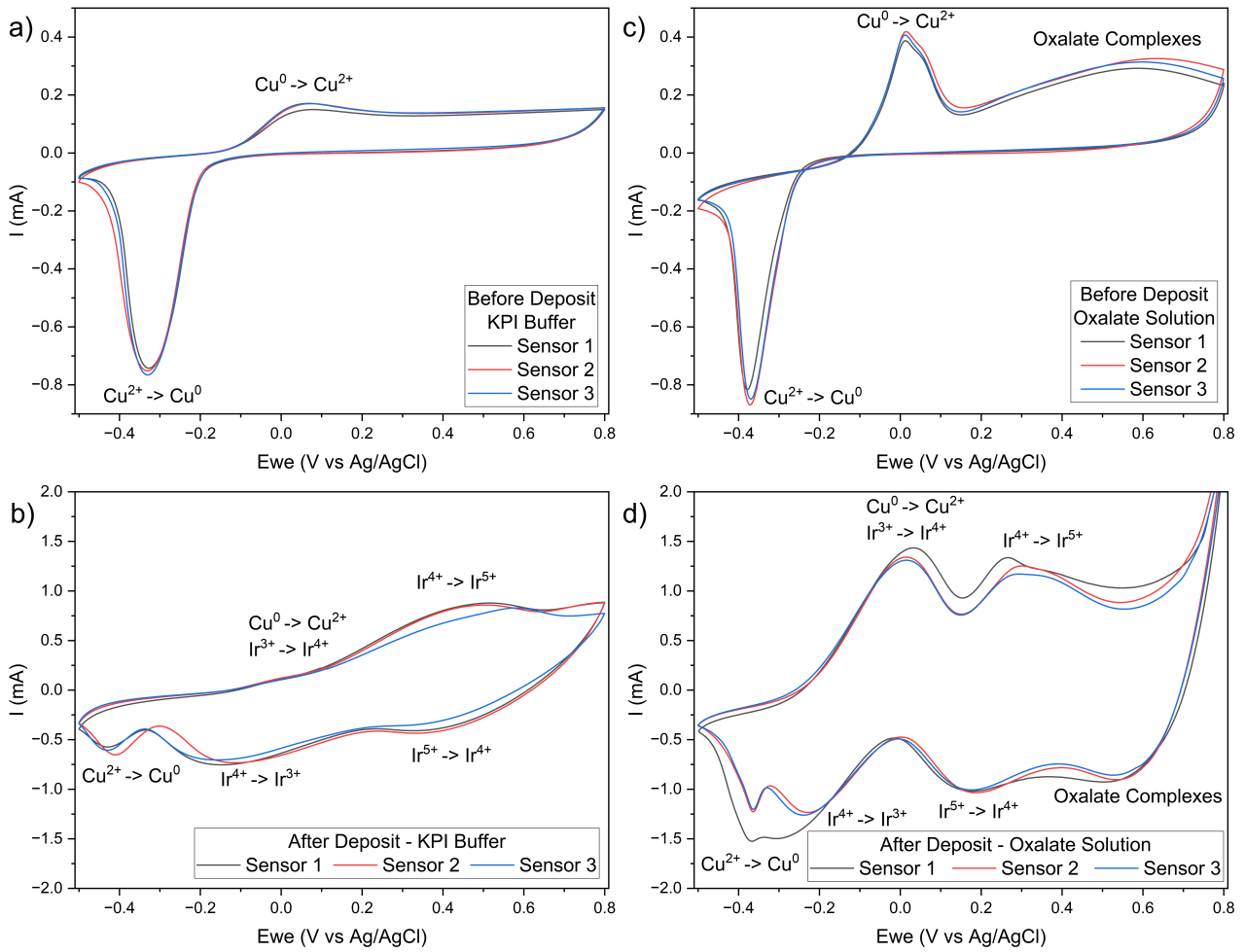


Figure 4.4: Cyclic voltammograms obtained in KPI buffer before a) and after b) deposition of the IrOx layer. CVs obtained in the oxalate solution (i.e. the iridium oxalate deposition solution without addition of the iridium salts) before c) and after d) IrOx deposition.

identification of redox groups associated with IrOx, and were found to be in agreement with those found in literature [166, 129]. Cu peaks remain present in Figure 4.4b, however their magnitude is significantly smaller than the contribution from the IrOx film, seen here as broad peaks. It is also likely the contribution from the Cu electrode has decreased due to reduced electrochemical accessibility following deposition of IrOx. Figure 4.4d shows greater visibility of the Ir oxidation states when performed in the oxalate solution.

As the number of voltage cycles progresses during deposition, reduction and oxidation peaks associated with redox active groups within the IrOx film emerge. Specifically, oxidation peaks associated with the Ir³⁺ - Ir⁴⁺ and Ir⁴⁺ - Ir⁵⁺ transitions are observed at 0.05 V and 0.41 V vs. Ag/AgCl respectively. The cathodic charge storage capacity (CSC_c), which correlates with the density of redox active groups in the IrOx film, can be calculated from the time integral of the CV cathodic current coupled with the electrode area (0.785 cm²) [126]. At the end of deposition, shown in Figure 4.3a, a significantly higher CSC_c is observed, associated with an increased density of redox active groups, on the unpolished electrodes (13.51 ± 2.03 mC/cm²) than on those that had been electrochemically polished (5.13 ± 0.46 mC/cm²). As the high pH-sensitivity of IrOx films is associated with this redox activity, one might naturally assume that unpolished sensors with the greater density of redox active groups would inherently provide higher pH sensitivity. This is contrary to what is observed in this work, where the polished electrodes associated with a lower density of redox active groups display the higher sensitivity.

4.2.3 Physical Characterisation via SEM & AFM

Scanning electron microscopy (SEM) and atomic force microscopy (AFM) were performed to characterise the electrode surface morphology, comparing differences between the electrodes before and after electropolishing, and following IrOx deposition. The difference in surface roughness between unpolished and polished Cu electrodes can be seen clearly in the representative SEM images of Figure 4.5a and 4.5b and in the AFM images of Figure 4.6a and 4.6b respectively. The surface of the unpolished Cu electrode was seen to be covered in a network of deep grooves (Figure 4.5a and 4.6a) and exhibited a root mean squared (RMS) surface roughness of 275 ± 36 nm. After electropolishing, the grooves were seen to have significantly reduced in depth leading to a surface that resembled flat terraces, possibly polycrystalline domains, that extend over areas of 10's μm² (Figure 4.5b & 4.6b). Accordingly, the surface roughness also reduced significantly to 62.7 ± 23 nm. Here, the mean RMS roughness was calculated from AFM images of 4, nominally identical electrodes with each surface being imaged at 3, different 50 μm² scan regions (raw data Figure 4.6c).

SEM images of the IrOx film, electrodeposited on the Cu electrodes reveal individual nanoparticles and clusters of nanoparticles that decorate the surface of both unpolished (Fig-

ure 4.5c) and polished electrodes (Figure 4.5d). The diameters of the individual particles are around 100 - 200 nm while the nanoparticle clusters range between 1 - 20 μm . The clusters are believed to be greater than 15 μm in height, as attempts to obtain AFM images of the IrOx film consistently exceeded the AFM dynamic range of 15 μm .

Particle analysis of SEM images was performed with ImageJ using the Otsu intensity threshold algorithm to quantify nanoparticle size and density [167]. While nanoparticles were observed following IrOx electrodeposition on both unpolished and polished electrodes, particle analysis reveals marked differences in the average nanoparticle diameter (Figure 4.7a) and surface coverage (Figure 4.7b).

On average, the nanoparticle clusters are around $3 \times$ larger in diameter on unpolished compared to polished electrodes and cover a larger area of the unpolished electrode surfaces. The higher surface coverage of IrOx nanoparticle clusters is consistent with CV analysis of the electrodeposition process that revealed a greater density ($2.6 \times$) of redox active groups in IrOx films on unpolished sensors. This data suggests that the high surface roughness and surface contamination associated with unpolished electrodes leads to the preferential deposition of IrOx nanoparticle clusters, likely through field enhancement and local suppression of interfacial charge transport, both of which are reduced following electrochemical polishing of the Cu electrode surface prior to electrodeposition.

4.2.4 Energy-dispersive X-ray Spectroscopy (EDX)

Having confirmed the physical characteristics of the electrodes and associated IrOx films, energy-dispersive X-ray spectroscopy (EDX) was next employed to examine the chemical composition of IrOx films electrodeposited on both unpolished and polished electrodes. EDX analysis of the Cu electrodes prior to IrOx deposition confirms only Cu, C and O are present.

Figure 4.8a compares the elemental ratios between unpolished and polished Cu electrodes prior to IrOx deposition. Polished electrodes show consistently lower C and O contamination (2% combined across the complete surface compared to 7.9% on unpolished electrodes). Notably, oxygen contamination is $4.5 \times$ greater in unpolished devices. This is in agreement with previously presented CV deposition data for unpolished electrodes where a redox peak ascribed to reduction of CuO and a higher interfacial capacitance associated with a thin native oxide at the electrode surface were observed.

The spatial distribution of C and O contamination on blank Cu electrodes was observed from EDX maps. Unpolished surfaces (Figure 4.9a) show broad background contamination across the surface ($\approx 5\%$ C), interestingly there are many regions of elevated contamination (often comprising $> 30\%$ C & $> 5\%$ O). Such areas of high contamination will locally impede the electrodeposition process and thus reduce the uniformity of the resulting IrOx film.

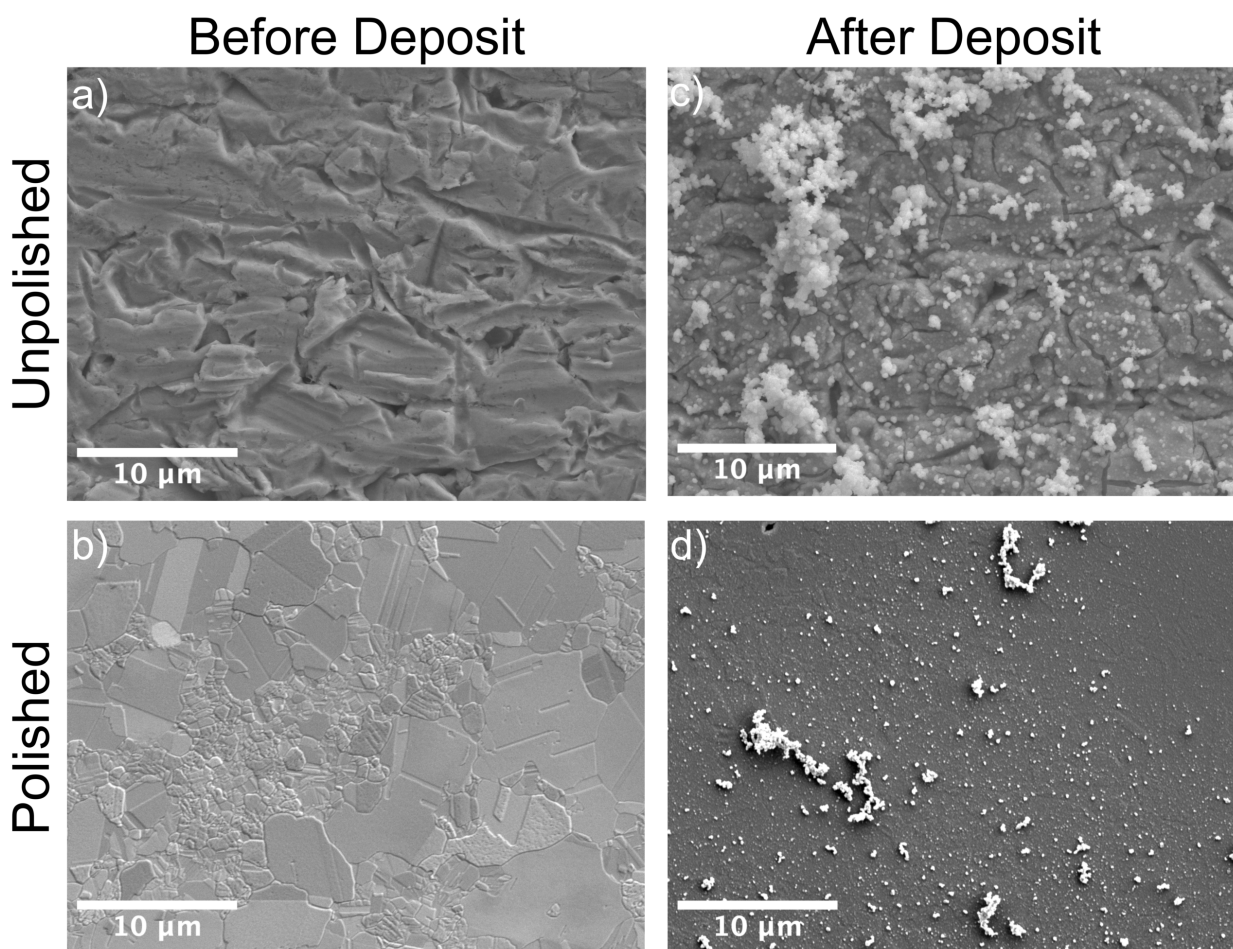


Figure 4.5: SEM images of a) unpolished and b) electrochemically polished Cu electrodes on PCB before deposition of IrOx. SEM images of the IrOx film electrodeposited on c) unpolished and d) polished Cu electrodes.

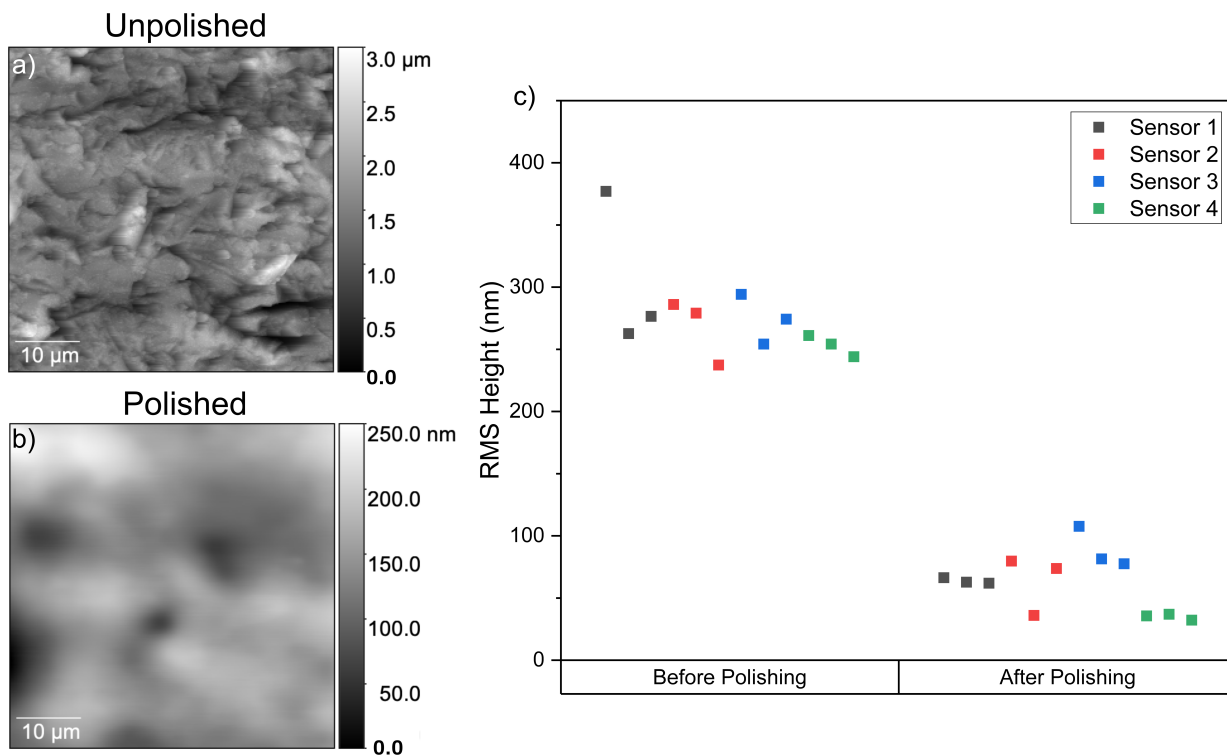


Figure 4.6: AFM images of unpolished a) and polished b) blank Cu electrodes. c) shows mean RMS roughness as calculated using ImageJ from AFM images of four, nominally identical electrodes before and after electropolishing with each surface being imaged at three, different $50 \mu\text{m}^2$ scan regions.

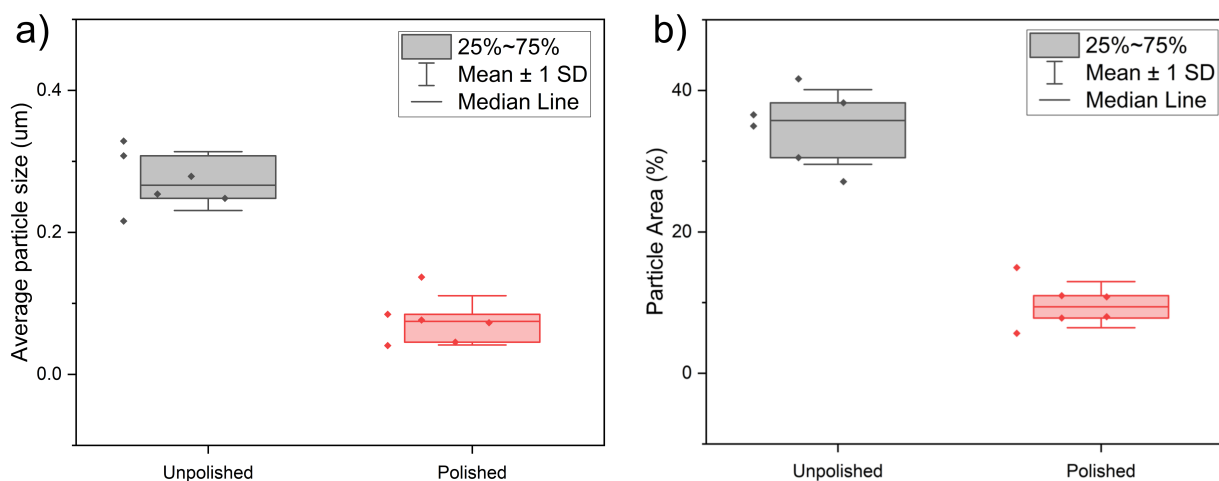


Figure 4.7: Analysis of average nanoparticle diameter a) and particle coverage b) following electrodeposition of IrOx on 6 unpolished and 6 polished Cu electrodes. Data extracted from ImageJ analysis where the Otsu intensity algorithm was used for particle detection. Box shows median value and 25th and 75th percentiles, while whiskers show ± 1 SD from the mean.

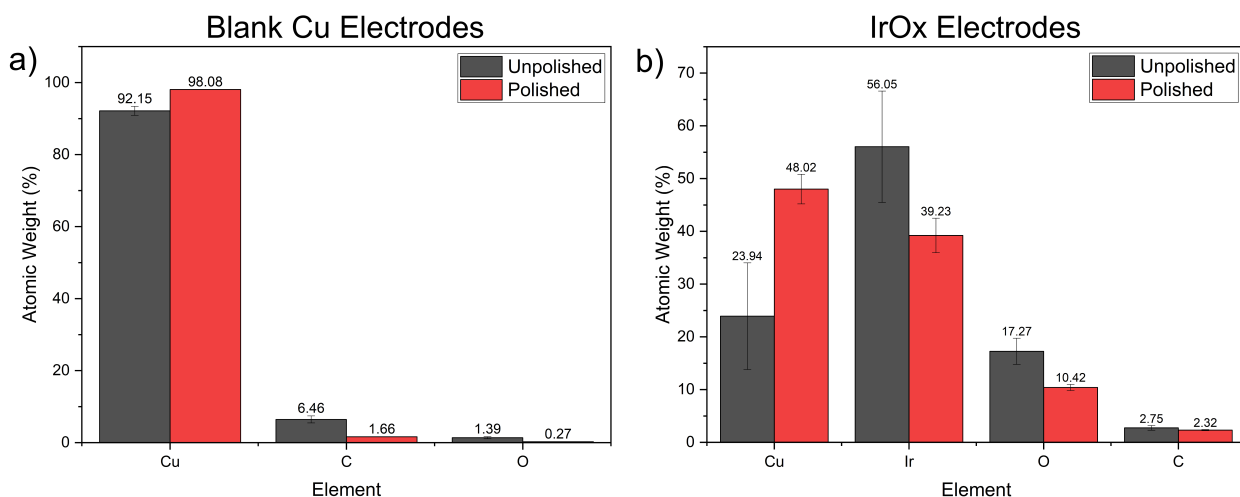


Figure 4.8: a) Relative elemental composition of unpolished and polished Cu electrodes prior to IrOx deposition. The atomic weight % for each element was calculated from the average value across 3 scan regions and 2 samples of each type. Error bars correspond to the standard deviation. b) Relative elemental composition of IrOx film electrodeposited on unpolished and polished Cu electrodes.

In contrast, elemental maps of polished electrodes (Figure 4.9b) show no areas of elevated contamination and background contamination is much reduced ($< 0.5\%$ combined C and O). There is also a reduction in the standard deviation of elemental composition across the surface, suggesting a more consistent and uniform chemical composition of the polished electrode surface.

Figure 4.8b shows EDX analysis of the IrOx films electrodeposited on both polished and unpolished electrodes and confirms the added presence of Ir, and an increase in O concentration. Although Ir and Cu are shown to have broad coverage across both unpolished and polished electrodes, the ratio of Ir to Cu is lower on the polished electrodes (0.82 : 1 in contrast to 2.34 : 1 on unpolished electrodes). Moreover, EDX images (Figure 4.10) confirm the nanoparticles and clusters observed in the SEM images (Figure 4.5c & 4.5d) contain Ir. These findings are in agreement with analysis of CV and SEM data that revealed greater surface coverage of the unpolished electrode surface with Ir containing nanoparticle clusters.

4.2.5 X-ray Photoelectron Spectroscopy (XPS)

EDX provides high throughput and quantifiable chemical analysis, however the incident electron beam penetrates beyond the surface of the sample, to a depth much greater than the IrOx layer thickness. As a result, the EDX signal associated with IrOx deposited samples contains a contribution from the bulk Cu substrate. The low analytical depth (typically around 5 - 10 nm) associated with X-ray photoelectron spectroscopy (XPS) was exploited to better understand the chemical composition of the electrodeposited IrOx film. Initial broad spectrum

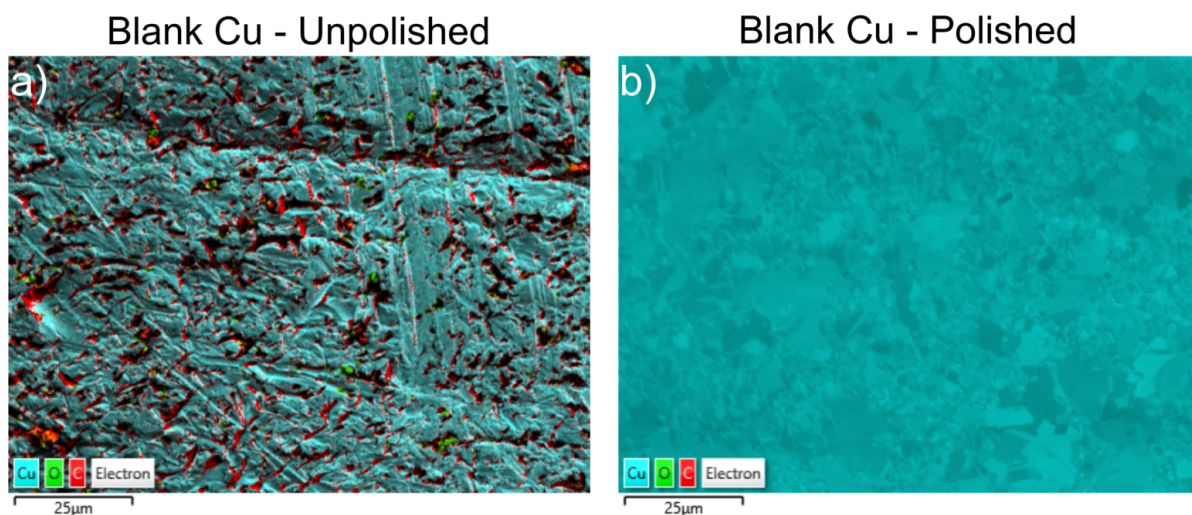


Figure 4.9: EDX elemental maps overlaid on SEM images of unpolished a) and polished b) blank Cu electrodes. All images were obtained with x1000 magnification, 5 kV beam energy and 10 mm WD, with normalised TruMap data based on counts over the imaging duration.

Table 4.1: Extracted XPS elemental atomic % and notable species ratios of unpolished and polished sensors, before and after IrOx film deposition.

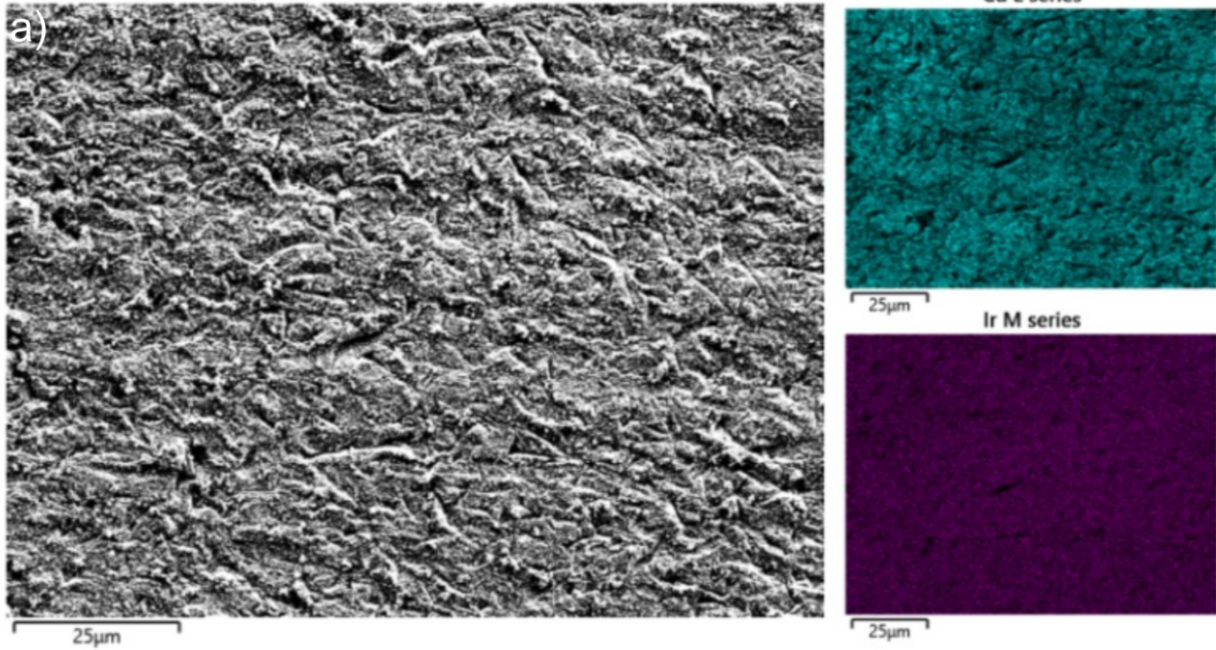
	Cu 2p [At.%]	C 1s [At.%]	O 1s [At.%]	Ir 4f [At.%]	Cu:Ir ratio	$Cu^0\% / Cu^{2+\%}$	Oxide %	$Ir^{3+\%} / Ir^{4+\%}$
Blank - Unpolished	4.8	71.1	24.1	-	-	59.8/40.2	66	-
Blank - Polished	12.0	57.5	30.5	-	-	79.4/20.6	48	-
IrOx Film - Unpolished	1.8	37.3	55.2	5.7	1 : 3.17	27.3/72.7	-	41.5/58.5
IrOx Film - Polished	2.2	39.8	50.9	7.1	1 : 3.23	18.1/81.9	-	45.9/54.1

data for uncoated electrodes and for IrOx films deposited on both unpolished and polished electrodes are shown in Figure 4.11.

As with EDX of the blank unpolished Cu electrodes (Figure 4.9), XPS revealed a higher combined atomic % of carbon and oxygen contaminants adsorbed on the surface, summarised in Table 4.1. Deconvolution of the O 1s region, indicates that 66% of the oxygen on the surface of unpolished electrodes (Figure 4.12e) is associated with a surface oxide compared to only 48% in polished electrodes (Figure 4.12f). Differences in the ratio of copper species also indicate the presence of an oxide layer on the surface of unpolished electrodes compared to the polished electrodes. Specifically, for unpolished electrodes (Figure 4.12a) the bulk Cu^0 signal accounts for 59.8% of the total copper, the remaining (40.2%) being Cu^{2+} associated with cupric oxide (CuO). This contrasts with the polished electrodes (Figure 4.12b) in which the oxide is removed by the process of electropolishing, leading to a reduction in the Cu^{2+} species to 20.6%. The higher fraction of surface Cu in its bulk state (79.4%) is better suited to uniform electrodeposition of IrOx layers.

XPS spectra of IrOx films deposited on unpolished electrodes also show persistently elevated levels of contamination compared to films deposited on electropolished Cu electrodes.

IrOx Film - Unpolished



IrOx Film - Polished

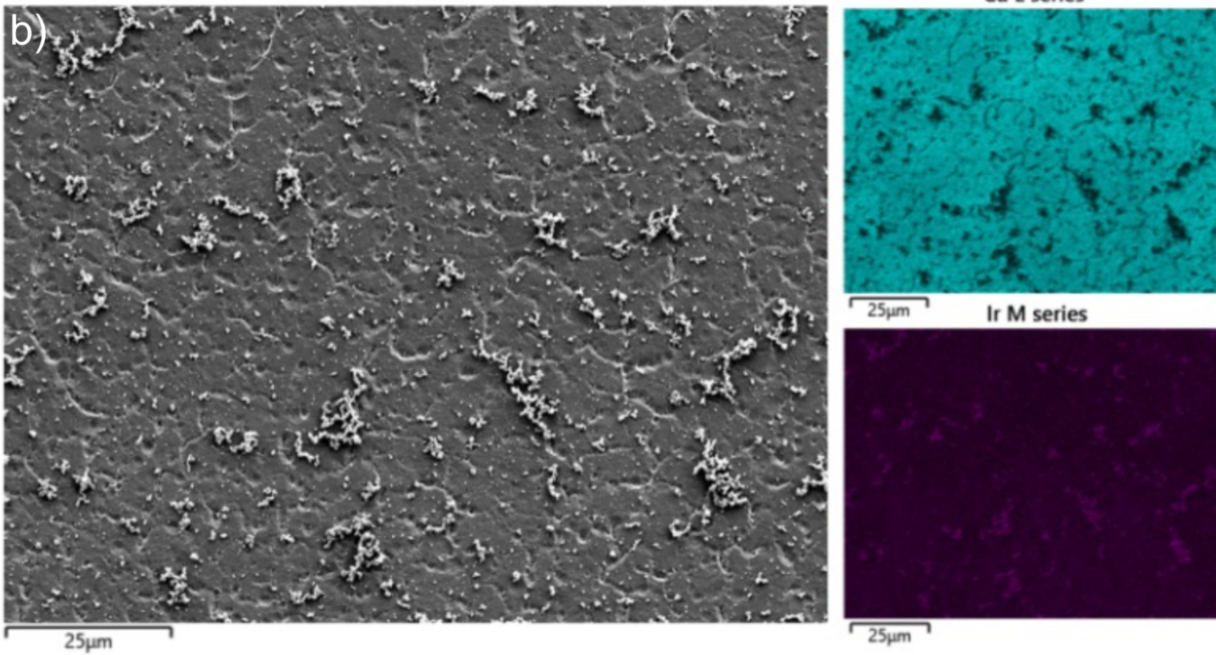


Figure 4.10: Separated SEM and EDX maps for Cu sensors with IrOx deposited are shown for unpolished a) and polished b) sensor surfaces. Only Cu and Ir coverage are shown, detected by X-rays emitted as electrons decay from L and M orbitals respectively, into the ground state. All images were obtained with x1000 magnification, 5 kV beam energy and 10 mm WD, with normalised TruMap data based on counts over the imaging duration.

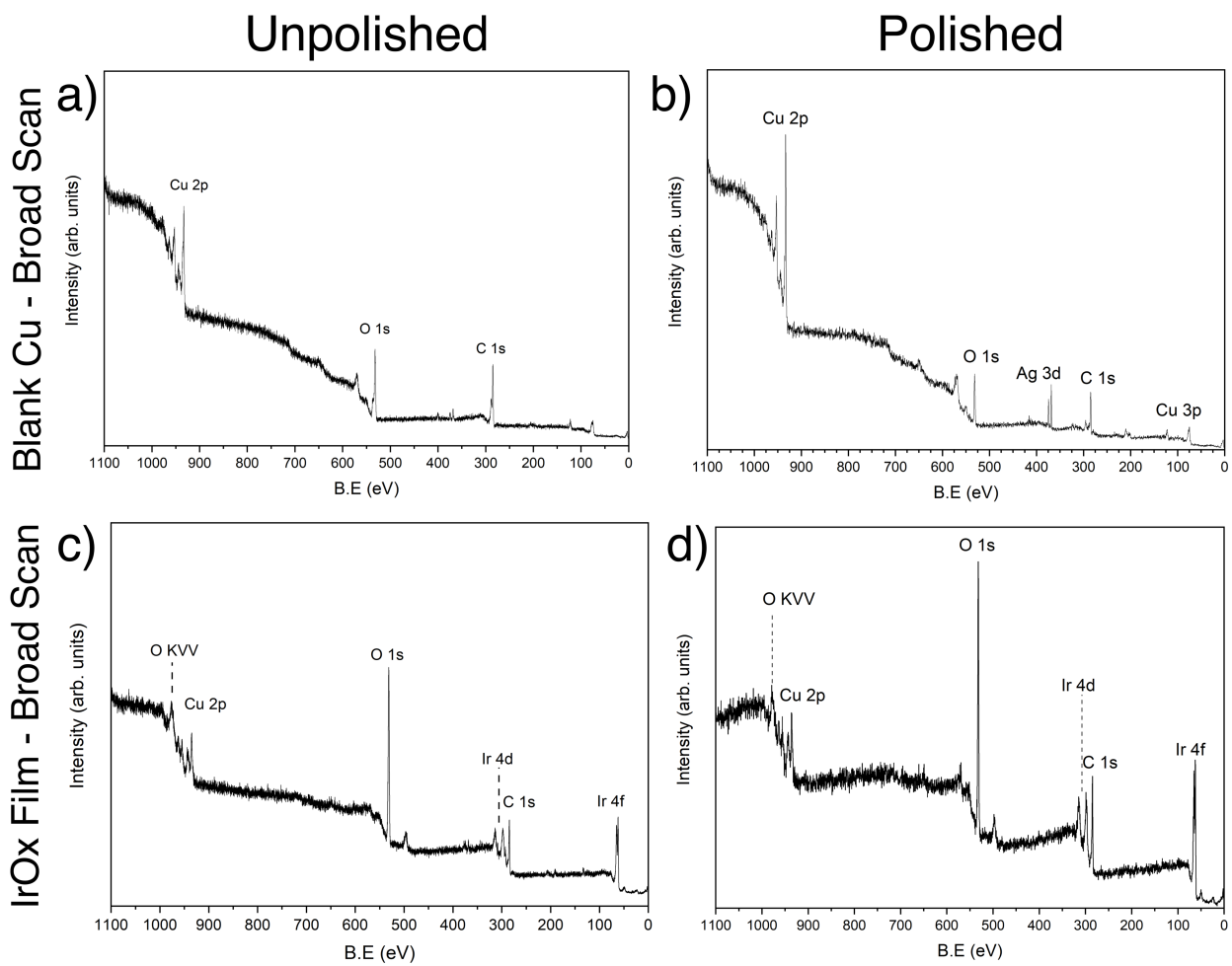


Figure 4.11: XPS broad scan spectra for all 4 imaged sensor types. Indicated are the electron energy levels by which the elemental peaks are attributed.

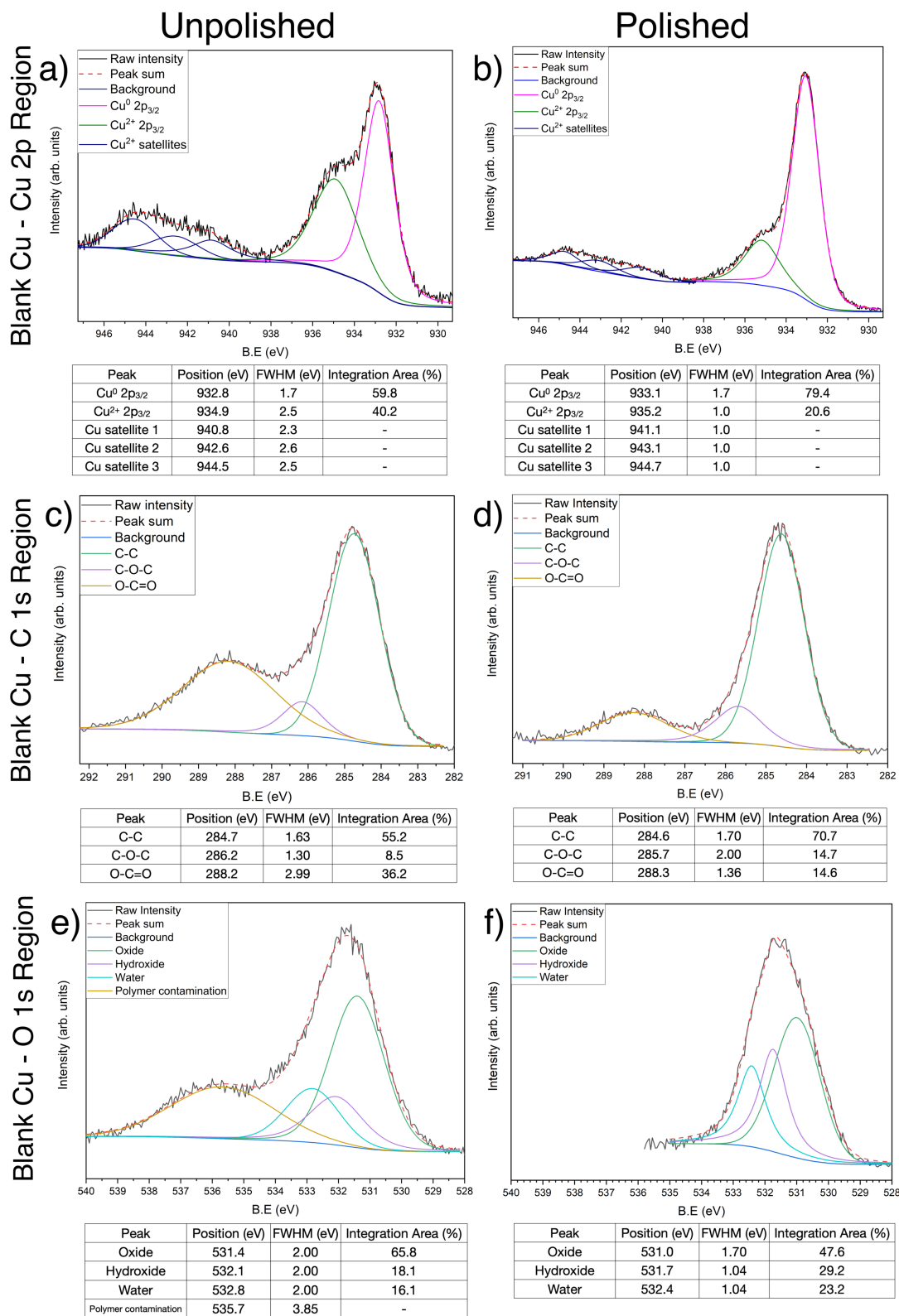


Figure 4.12: Deconvolution and compositional analysis of all elements of interest on blank Cu electrodes, sensors in both unpolished and polished state are shown. The polymer contamination peak g) is believed to be associated with the epoxy and other polymers from the FR4 substrate, a result of the many different oxygen environments found within the FR4 epoxy resin. Integration areas account for the contamination peak via subtraction of the overlapping integration area.

Summarised in Table 4.1 and presented per deconvoluted region in Figure 4.13 and 4.14.

Moreover, Cu, likely associated with the underlying Cu electrodes, is also observed in XPS spectra of IrOx coated electrodes (Figure 4.11c and 4.11d). The thickness of IrOx layers electrodeposited by cyclic voltammetry has been measured at around 40 nm [119, 168]. This is much larger than the analytical depth of XPS suggesting that the IrOx layer (shown in Figure 4.5c and 4.5d SEM images) is not uniform, leading to exposed regions of bulk Cu electrode. It is possible this combined IrOx/Cu surface directly leads to the observed pH sensitivity of the layer, and their ratio is proportional to the resulting pH response. The non-linear trend displayed in Figure 4.15 could be due to additional effect of the exposed Cu.

Notably, given the accepted dependence between pH sensitivity of IrOx films and the Ir oxidation state [169], the increased pH sensitivity observed in polished samples could in part be ascribed to the oxidation state of the Ir. However, deconvolution of the Ir 4f region (Figure 4.13c and 4.13d) shows a marginally higher fraction of Ir⁴⁺ with respect to Ir³⁺ in unpolished (58.5%), compared to polished sensors (54.1%). Given that the IrOx film deposited on polished electrodes show a greater pH sensitivity, it is clear that factors additional to the Ir oxidation state play a role in determining the observed improvement in pH sensitivity.

4.2.6 Discussion

From the comprehensive physical and chemical analysis, it can be concluded that high median pH sensitivity and repeatability associated with IrOx films electrodeposited on polished Cu electrodes relates to the improved uniformity of the IrOx films. Specifically, localised regions of high oxide and carbonaceous contamination (as observed on unpolished electrodes) impede faradaic transport of electrons across the electrode-solution interface, leading to preferential formation of IrOx nano-structures at local surface regions (Figure 4.5c) rather than electrodeposition of an uniform film. These contaminants are removed effectively by electropolishing, as shown by both EDX (Figure 4.8a) and XPS analysis (Figure 4.12a & Figure 4.12b), enabling electrodeposition of IrOx to occur more uniformly across the electrode surface (Figure 4.5d), although a reduced number of nanoparticle clusters are still observed.

In addition, the high surface roughness associated with the unpolished sensors (Figure 4.5a) would also lead to an electric field that varies locally at the surface, further reducing uniformity of the IrOx electrodeposition process. In contrast, the largely smooth copper surface following electropolishing of the Cu electrodes (Figure 4.5b) supports the growth of a more uniform IrOx film leading to the high reproducibility in pH sensitivity observed for polished sensors.

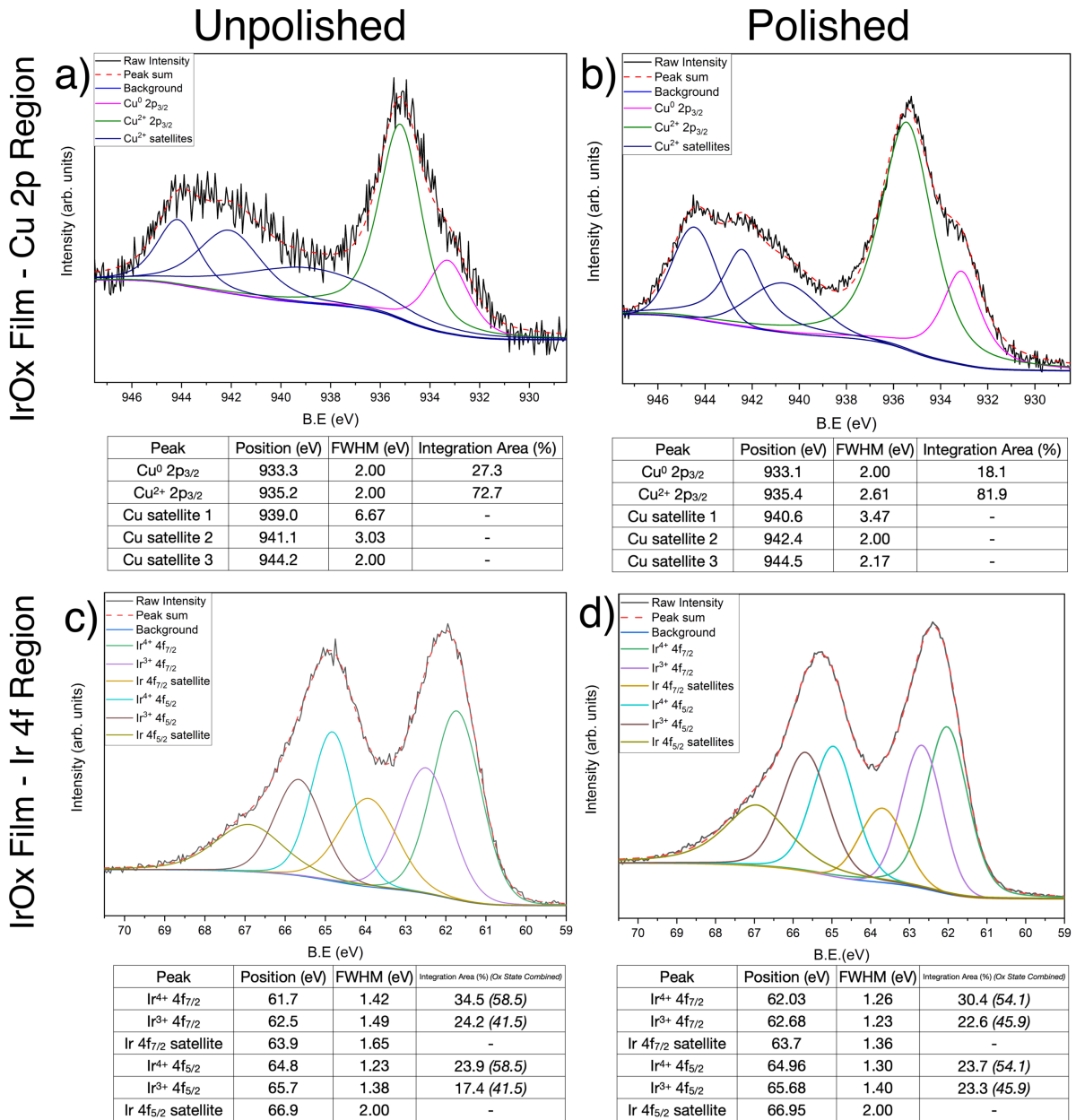


Figure 4.13: Deconvolution and compositional analysis of unpolished and polished electrodes after deposition of an IrOx film. Here, the unpolished electrode displayed a pH sensitivity of 37.8 mV/pH while the polished sensor was measured to have a pH sensitivity of 73.2 mV/pH.

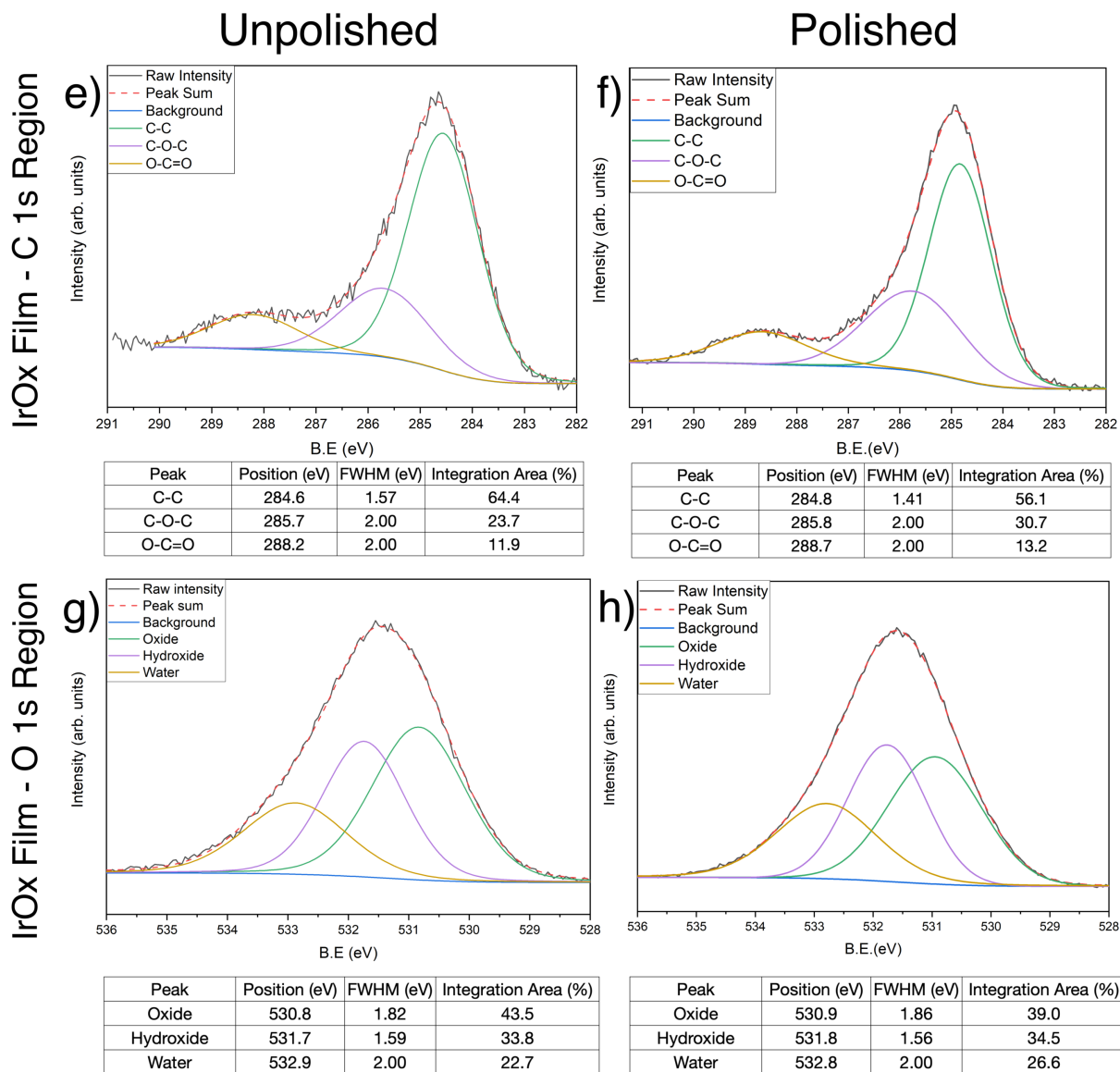


Figure 4.14: Deconvolution and compositional analysis of unpolished and polished electrodes after deposition of an IrOx film. Here, the unpolished electrode displayed a pH sensitivity of 37.8 mV/pH while the polished sensor was measured to have a pH sensitivity of 73.2 mV/pH.

4.2.7 pH Sensitivity within Polished Sensors

While this analysis reveals the importance of IrOx uniformity, the redox activity of the Ir complexes within the hydrated IrOx film also influences the observed pH-sensitivity of devices. Additional analysis was performed of deposition cyclic voltammograms for 5 independent IrOx films on polished Cu electrodes. These voltammograms are shown in the inset of Figure 4.15.

The magnitude of the Ir³⁺ to Ir⁴⁺ oxidation peak for each of these sensors is plotted in Figure 4.15 as a function of the measured pH sensitivity; there is also contribution in this peak region from oxidation of Cu⁰. The area under this peak is a measure of the number of Ir³⁺ molecules in complexes that can transition to the Ir⁴⁺ oxidation state. As discussed in section 2.4.4, it is these oxidation state changes that provide beyond Nernstian pH sensitivity associated with IrOx.

A direct correlation is revealed between the measured pH sensitivity and surface concentration of redox active Ir³⁺ complexes. This indicates an IrOx layer consisting of a greater surface concentration of Ir³⁺ complexes that can be oxidised to Ir⁴⁺ will result in increased pH response of the electrode, in agreement with literature. This remaining trend explains the small device-to-device variability observed for polished Cu electrodes (± 5 mV/pH) and this understanding could be used to further improve repeatability, but was not explored in this work.

4.3 Conclusion

A low-cost and simple to manufacture pH sensor has been demonstrated, that comprises a discrete transistor, coupled to an extended gate Cu electrode manufactured on PCB that is rendered pH-sensitive through an electrodeposited IrOx film. In contrast to previous dEGFETs on PCB, the sensors displayed beyond-Nernstian pH responses with very low device-to-device variability. These excellent performance characteristics arise from the improved uniformity of the IrOx film achieved by electropolishing the Cu electrodes prior to IrOx deposition, which not only removes oxides and adventitious carbon contamination but also reduces the electrode surface roughness leading to IrOx films of increased uniformity.

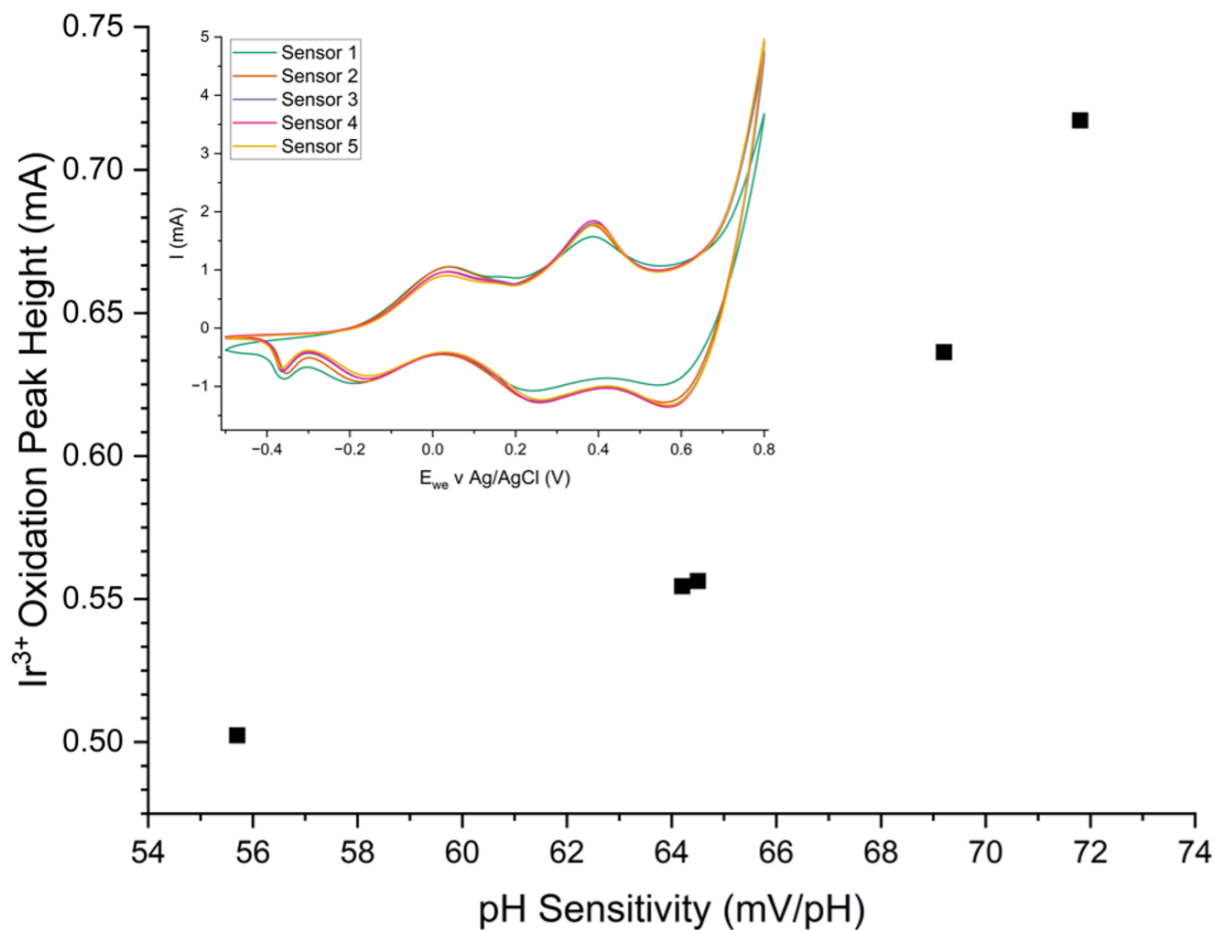


Figure 4.15: (Inset) IrOx deposition CVs within polished sensors, final cycle shown for each sensor. (Main) Extracted Ir³⁺ peak current versus measured device pH sensitivity; where peak current is adjusted to the oxidation non-faradaic background current.

Chapter 5

Biological Assay & Detection

This chapter briefly introduces recent literature and novel approaches for antibiotic susceptibility assays, before detailing the detection of β -lactamase enzymatic turnover of penicillin antibiotic. Under appropriate buffer conditions, this turnover results in acidification of the local environment which was used to detect and quantify ampicillin concentration using the printed circuit board (PCB) discrete extended gate ion-sensitive field effect transistor (dEGFET) sensors developed in chapter 4, through both a kinetic and endpoint analysis approach.

5.1 Introduction & Literature

As mentioned in section 1.1.1, antimicrobial resistance (AMR) is already challenging our ability to deal with routine infections and the impact of drug resistant infections (DRI) will continue to grow in the short term. A key part of the solution to AMR are new diagnostic technologies that can be used at the point of care (PoC), to rapidly profile the antimicrobial susceptibility of an infection and reduce prescription of inappropriate or ineffective treatments.

A broad range of antibiotics exist [170], which can be categorised by the mechanism by which they inhibit bacterial processes [171]. The most commonly prescribed class are β -lactam antibiotics [172, 173] which inhibit formation of the bacterial cell wall. The widespread use of these antibiotics has naturally lead to the evolution of multiple mechanisms of resistance [174, 175, 176]. The assay presented in this chapter focuses on detection of bacterial resistance to β -lactam antibiotics where the mechanism is the production of enzymes that modify the active component on the antibiotic structure, rendering them ineffective.

Current antimicrobial susceptibility tests (AST) rely on bacterial growth to evaluate resistance to specific antimicrobials. For example, the disk diffusion assay uses an agar plate inoculated with bacteria from a clinical sample, on which paper discs containing potential antibiotic treatments are placed [177]. The growth, or inhibition of growth, around each disk is

subsequently measured after a period of incubation to identify bacterial susceptibility. While well-established and inexpensive, such AST are typically slow, requiring two bacterial culturing steps of approximately 24 hours each [178]. This often leads to the test not being utilised, as healthcare systems and patient expectations are not compatible with this delay. While genomic methods which detect and amplify genes associated with AMR have been demonstrated [179, 180], these methods typically require preparation in a laboratory setting by trained professionals, and often still rely on culturing of clinical isolates, not meeting PoC requirements.

These examples emphasise the need for AST that can be performed rapidly and be used at the PoC to inform antibiotic susceptibility at the point antibiotics are prescribed [181]. This has led to a range of novel AST that do not require time consuming and lab-bound culturing steps but instead determine resistance to specific classes of antibiotics or mechanisms of resistance. Many of these technologies focus on the most prevalent antibiotics and associated resistance mechanisms, such as degradation of β -lactam antibiotics by β -lactamase enzymes.

Multiple optical transduction approaches to detect enzymatic degradation of β -lactam antibiotics have been demonstrated, such as fluorescence [182] and colourimetric [183]. These commonly utilise optically active β -lactam-mimics such as nitrocefin which changes absorption spectra when hydrolysed by β -lactamases, enabling detection via a spectrophotometer at 490 nm. The NDP test [184], named after the three scientists credited with its origin, instead uses a pH sensitive dye for colourimetric readout. Rather than use of an optically active β -lactam-mimic, the hydrolysis of an antibiotic by bacterial β -lactamases is exploited. The NDP assay is performed in a weakly buffered solution, where the bulk pH changes as cefotaxime molecules are hydrolysed, pH indicator Phenol Red then undergoes a visible colour change. The initial study showed its efficacy on 255 different bacterial strains, with a sensitivity of 92.6% and specificity of 100%, where the test also completes in under 2 hours. Its disadvantage lies in the need for a bulky spectrophotometer for optical readout, and the remaining need for growth of bacterial colonies or blood cultures before the test can be started.

The pH change of a weakly buffered solution due to β -lactamase activity can also be detected and more accurately quantified electrochemically. Recently, ion-sensitive field effect transistor (ISFET) sensors have been exploited to detect this pH change in work by Kotsakis *et al.* [185]. Specifically, imipenem hydrolysis by free carbapenemases were detected using a commercial ISFET flow cell and external double junction Ag/AgCl reference electrode. They found it was important, when the testing bacterial suspensions, to normalise against a control of the suspension alone, due to pH instability in an un-buffered environment and intact bacterial cells disturbing the electrochemical double layer (ECDL). The limit of detection (LoD) was dependent on the specific enzyme produced by the *Enterobacterale*, with greater activity resulting in an increased pH change. For example, New Delhi metallo-beta-lactamase (NDM) resulted in a LoD of 0.4 nM and Verona integron-encoded metallo-beta-lactamase (VIM) a value of 130 nM. Kotsakis' *et al.* work, serves as a proof of concept for electrochemically detecting

the solution pH change caused by enzymatic hydrolysis of antibiotics. Commercially available complementary metal-oxide-semiconductor (CMOS) ISFETs are however used, which are currently a specialist device, limiting widespread deployment of the technology due to cost when compared to discrete field effect transistors (FETs).

The work presented in this chapter seeks to explore the suitability of low cost dEGFET systems based on PCB extended gate electrodes towards β -lactam susceptibility testing. These devices, which can be fabricated with facile methods accessible in developing countries, are used to detect and quantify ampicillin concentration in the presence of β -lactamase enzymes, as would be produced by resistant bacteria.

5.2 Assay Theory

The assay is designed to monitor β -lactamase mediated hydrolysis of the penicillin class β -lactam antibiotic ampicillin. β -lactam antibiotics contain a 4 membered ring structure named the β -lactam ring, which acts as the active portion of the molecule, visible in Figure 5.1a and highlighted in blue. Bacteria that are resistant to β -lactam antibiotics commonly produce enzymes, known as β -lactamases, which can hydrolyse the β -lactam ring rendering it ineffective.

Hydrolysis of the β -lactam ring leads to the production of an additional carboxylic acid and an amine group, which both remain part of the hydrolysed penicillin module shown in Figure 5.1. At appropriate pH values, this carboxylic acid deprotonates, changing to the overall solution pH. If the solution pH is not within the appropriate range, based on the pK_a of the resulting hydrolysed penicillin molecule, then the solution pH will not change.

Previous pK_a simulations [36] explored to what extent the carboxylic acid groups on both intact and hydrolysed penicillin groups deprotonate, as a function of the pH of the surrounding solution. These simulations, shown in Figure 5.2, revealed that above pH 5.2, the hydrolysed β -lactam deprotonates to a greater extent than the original penicillin molecule such that at pH 7, 54% greater H^+ ions are donated from the hydrolysed form compared to the intact molecule. Below a pH of 5.2, the amine groups on the molecule become protonated. I note, it is not expected the β -lactamase enzyme will remain active at this pH.

5.3 Determining Suitable Assay Buffer

An appropriate buffer was selected, such that deprotonation of the hydrolysed β -lactam would lead to measurable change in the pH of the solution, while simultaneously maintaining activity of the β -lactamase.

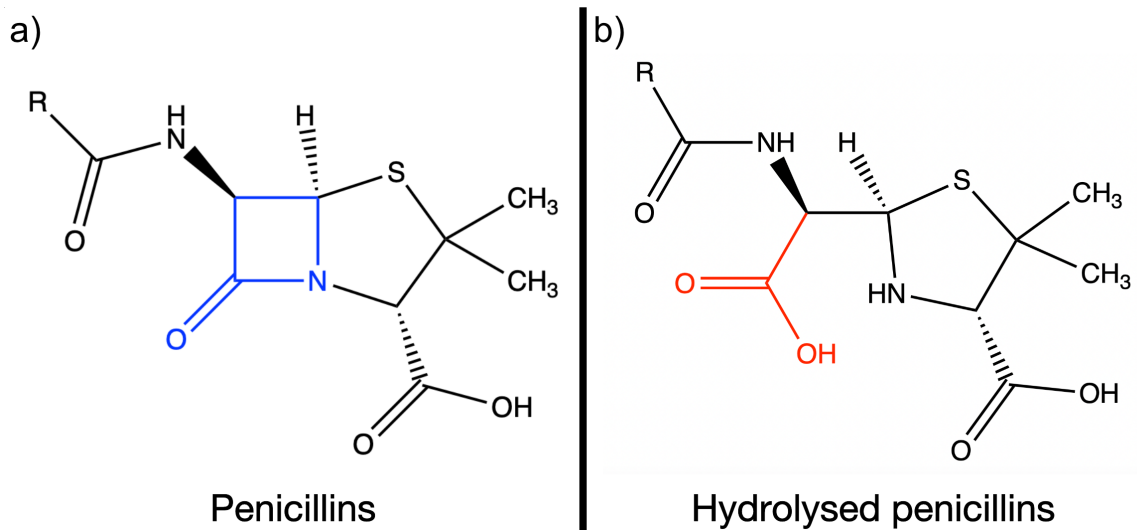


Figure 5.1: Schematic structure showing both intact penicillin β -lactam antibiotic a) and its hydrolysed form b). The β -lactam ring is highlighted in blue. Following hydrolysis by β -lactamase, an additional carboxylic acid (highlighted in red) is produced within the molecular structure [36].

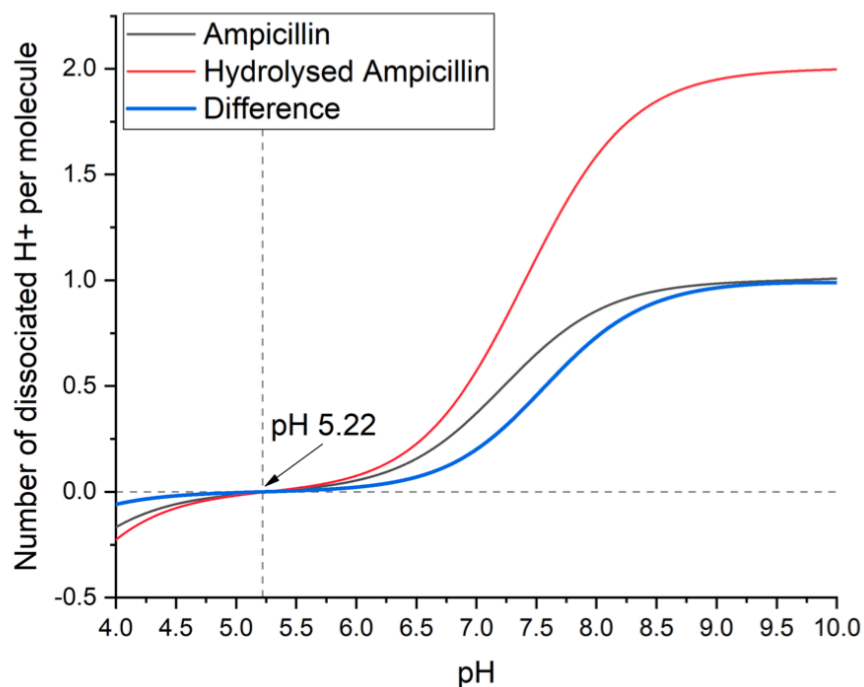


Figure 5.2: Calculated number of dissociated H^+ ions per molecule of intact (black) and hydrolysed (red) ampicillin between pH 4 and 10. The blue trace shows the number of H^+ ions added into solution for each ampicillin molecule that is hydrolysed [36].

5.3.1 pH Buffer Theory

pH buffer solutions pair a weak acid with its conjugate base (or the inverse), to maintain a stable pH when a strong acid or base is added. Consider the Henderson-Hasselbalch equation 5.3.1 and the dissociation of a weak acid and conjugate salt as in the general equation 5.3.2.

$$pH = pK_a + \log_{10} \frac{[A^-]}{[HA]} \quad (5.3.1)$$



It can be shown that at a pH equal to the acid dissociation constant pK_a , there are an equal number of proton donors and acceptors. A buffer has the greatest ability to resist pH change at values close to its pK_a , known as its buffer capacity (β). The useful pH range of a buffer is often considered to be $pK_a \pm 1$ pH unit, where its ability to buffer is deemed to have fallen significantly [35].

Equation 5.3.3 can be used to obtain buffer capacity, where ΔC_a is the concentration of H^+ ions added in M, and ΔpH is the change that occurs. Using ± 1 pH unit as the accepted useful pH range, Figure 5.3 simulates the relationship between moles of strong acid added and the resulting pH delta for 500 mM KPI buffer with a pK_a of 7.21; negative concentrations of acid are the addition of OH^- dominant base [36].

$$\beta = \frac{\Delta C_a}{\Delta pH} \quad (5.3.3)$$

5.3.2 Buffer Calculations

For this work, the buffer capacity was set to enable initial operation of the enzyme, while low enough so that the subsequent production of H^+ ions will result in a pH change of the surrounding environment.

The optimal pH for the β -lactamases used in this work is pH 7 for β -lactamase I, and pH 6.6 - 7.25 for β -lactamase II [186, 187]. For this reason, a buffer with an initial pH value of 7 was selected for this work. Moreover, potassium phosphate (KPI) buffer was selected due to its pK_a of 7.21.

To ensure efficient operation of the enzyme within the assay, the addition of clinically relevant levels of ampicillin (44.3 - 177.6 $\mu\text{g}/\text{ml}$) should not drastically shift the initial buffer pH [188]. In this work, a value of < 0.75 pH units was used as the designed maximum shift in pH, following addition of ampicillin at the upper range of clinically relevant concentrations.

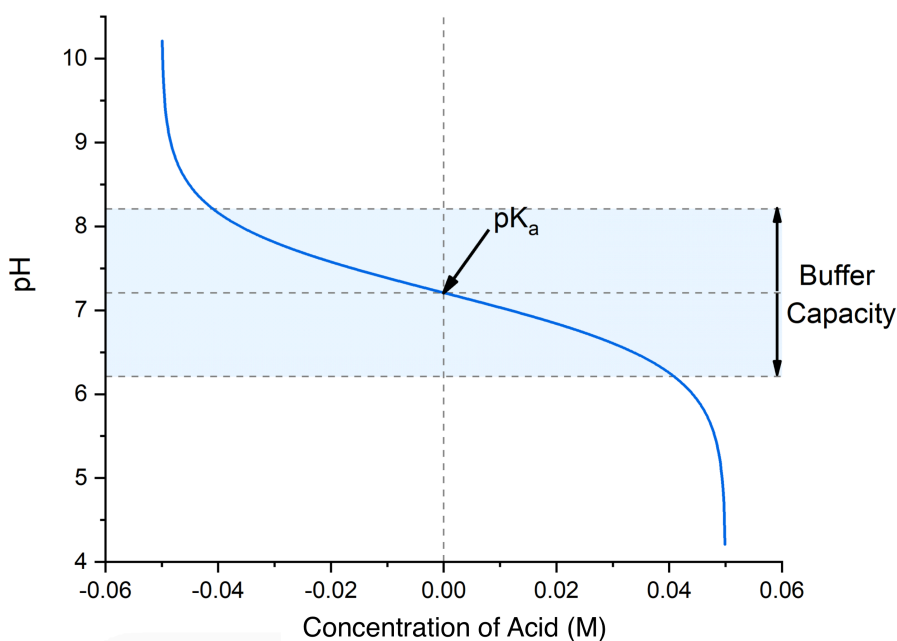


Figure 5.3: Response of KPI buffer pH ($pK_a = 7.21$) to addition of strong base or acid, used as a measure of buffer capacity [36].

This value was chosen to maintain enzyme activity and to keep the buffer capacity within the linear region during this initial phase.

Simulations presented in Figure 5.2 were used to estimate to what extent the overall ampicillin molecule would deprotonate and contribute to a pH change based on the complex interaction between multiple amphoteric sites and the molecule pK_a . This shows a maximum estimated deprotonation of 37% for addition of intact Ampicillin at pH 7.

Utilising equation 5.3.3, a value for the required buffer capacity can be calculated. Here delta pH is 0.75 and the concentration of ampicillin was assumed to be 200 $\mu\text{g}/\text{ml}$, corresponding to a molarity of 572.39 μM (ampicillin molecular weight = 349.41 Da). Finally, the maximum simulated deprotonation of 37% is used to normalise the H^+ ions released into solution, resulting in a buffer capacity of $282.4 \times 10^{-6} \text{ M} / \Delta \text{pH}$.

Equation 5.3.4 is used to calculate the corresponding buffer concentration which describes the relationship between buffer capacity (β) and buffer molar concentration (T_{HA}), for a specific buffer based on the dissociation constant (K_a) and pH (via the concentration of H^+ ions [H^+]). For the pH 7 KPI buffer in this work, H^+ is $0.1 \times 10^{-6} \text{ M}$ and K_a is 6.3×10^{-8} . I note, the full definition for buffer capacity includes two additional terms, however these dominate separately at extreme pH values < 2 and > 12 , which are conditions this assay will not enter [189].

$$\beta \approx 2.303 \frac{T_{HA} K_a [H^+]}{(K_a + [H^+])^2} \quad (5.3.4)$$

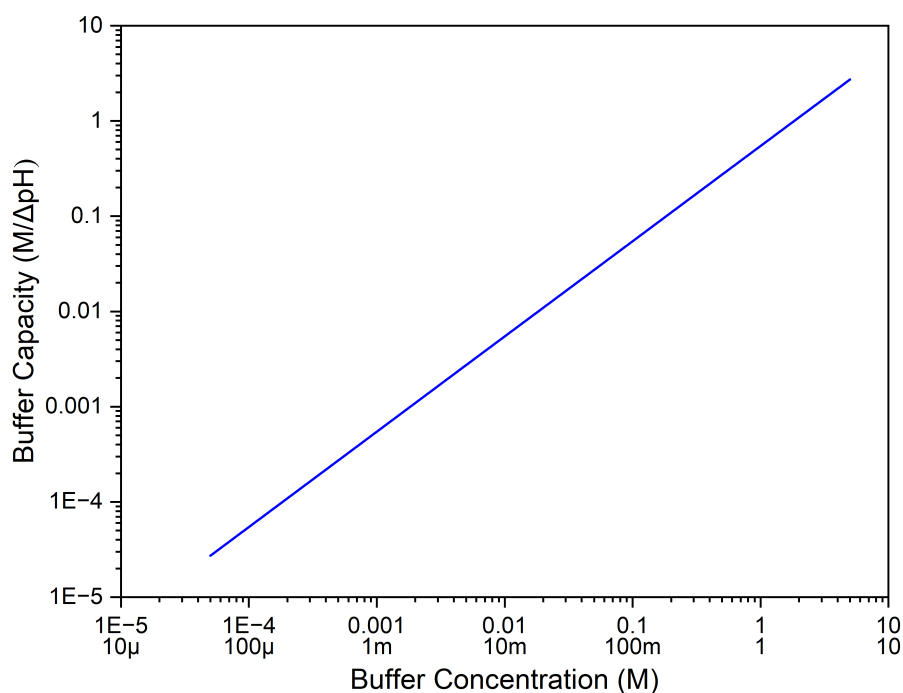


Figure 5.4: Calculated buffer capacity of pH 7 KPI buffer across a range of concentrations.

The relationship between buffer capacity and concentration is shown in Figure 5.4. At the required capacity for this assay, calculated to be $282.4 \times 10^{-6} \text{ M}/\Delta \text{pH}$, the buffer concentration should be $517 \mu\text{M}$. In this work, a rounded $500 \mu\text{M}$ was selected for ease of preparation, and due to previous assumptions made that overestimate the required buffering capacity.

Potassium sulphate was also added to the buffer to provide additional ions for transfer in the dEGFET system, where 50 mM concentration shifted the solution pH by less than 0.1 due to being a neutral salt.

A commercial pH meter was used to measure the change in pH of the $500 \mu\text{M}$ pH 7 KPI buffer after addition of varying concentrations of ampicillin and to confirm the pH did not shift > 0.75 units beyond the initial pH 7. Figure 5.5 shows the change in pH reaches around 0.5 pH units with the addition of $200 \mu\text{g}/\text{ml}$ of ampicillin. Using these experimental results and equation 5.3.3 for buffer capacity, a value for the deprotonation of ampicillin within this system was calculated, resulting in a value of 24% as opposed to the simulated 37%. The experimental pH shift caused by addition of ampicillin to the low molarity buffer was smaller than that calculated, but was still used within this work. Further work could further optimise this β -lactam assay pH buffer.

In conclusion, this assay has been designed to operate with a low molarity (0.5 mM) pH 7 KPI buffer with additional 50 mM potassium sulphate for increased conductivity. At this pH it is favourable for the carboxylic acid of the hydrolysed penicillin molecule to deprotonate based on its pK_a alongside providing an optimal region for enzyme activity. The buffer capacity has been set at this value to absorb initial changes which may be caused by the weak acid

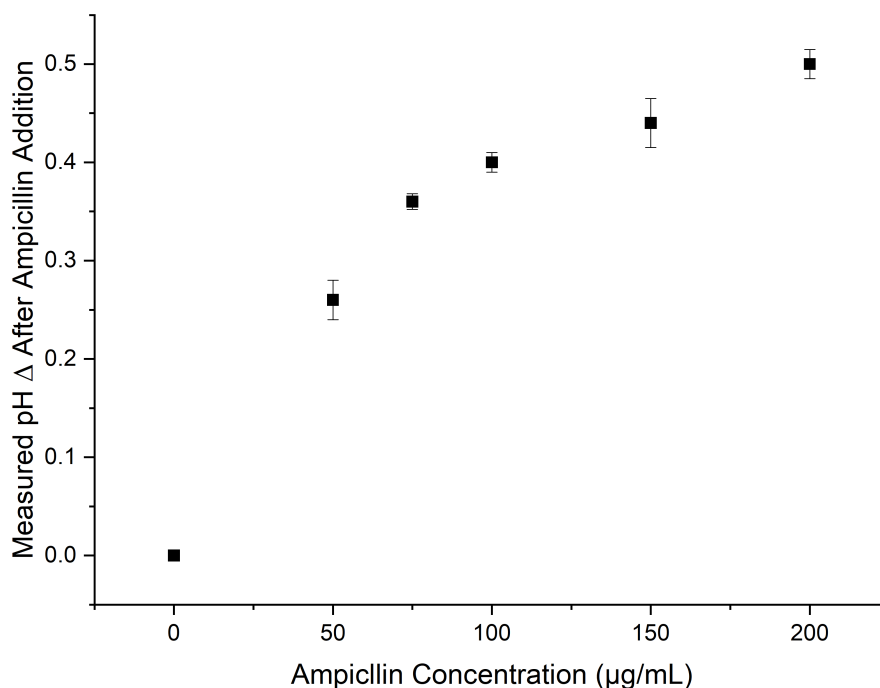


Figure 5.5: The pH delta as measured using a commercial pH meter between the assay buffer and the pH value after spiking with a range of ampicillin concentrations. Error is the SD across three measurements per concentration.

properties of intact ampicillin, but to result in a pH change as hydrolysis of the ampicillin molecule progresses.

5.4 Assay Method

Stock solutions of a β -lactamase blend (Sigma Aldrich, UK, L7920) of recombinant enzymes expressed in *Escherichia coli* were prepared by dissolving in 50 mM KPI (pH 7) buffer, stored at $-20\text{ }^{\circ}\text{C}$, and used without further dilution. Each aliquot contained 40-70 IU β -lactamase I and 6-10 IU β -lactamase II. Solutions of anhydrous ampicillin (Sigma Aldrich, UK, 271861) were made in 0.5 mM KPI (pH 7) buffer with 50 mM potassium sulphate (Sigma Aldrich, UK).

5.5 Kinetic Assay

The assay was performed, and the resulting pH change monitored via the output voltage of the PCB dEGFET sensors developed in chapter 4. ISFET sensors were exposed to solutions of different ampicillin concentration (up to 200 $\mu\text{g/ml}$) in KPI buffer. 100 μL of the aliquoted β -lactamase blend was subsequently added to 15 ml of the ampicillin solution and a datapoint was recorded every 8 ms.

The theoretical response shape of dEGFET output against time, after challenge with the β -lactamase enzyme blend is expected to be the combination of three effects. The response of a weak buffer to pH change, which depends on the distance between current pH and the pK_a as shown in Figure 5.3, expected to be small relative to the other two effects.

Enzymatic activity will initially drive a linear pH change while the ampicillin is in excess, as the concentration of ampicillin reduces, the rate of reaction will decrease as their interactions are limited by diffusion. Enzyme activity is also dependent on solution pH, although its response shape is not provided by the supplier due to blend batch-to-batch variation and dependence on the substrate. Both the reduction in ampicillin concentration and change in enzyme activity are expected to reduce the rate of pH change in a non-linear fashion after this initial linear region.

The current solution pH also impacts the proportion of H^+ ions which dissociate from hydrolysed ampicillin molecules, due to behaving as a weak acid as discussed and simulated in section 5.2. This effect will also reduce the rate of pH change in a non linear fashion, with greater impact for higher concentrations of ampicillin due to a larger expected pH delta.

5.5.1 Kinetic Raw Data Response

Figure 5.6 grey) shows representative responses of kinetic measurements on a PCB dEGFET sensor, where a rapid change in the device output voltage can be seen that occurs shortly after injection of the β -lactamase enzyme. It is interesting to explore the shape of this response, in context with the response of experiments performed at multiple ampicillin concentrations and control experiments in the same figure.

Measurements containing both ampicillin and active enzyme show an immediate increase in output voltage, associated with a shift towards more acidic pH. The magnitude of the pH shift is related to the concentration of ampicillin in the analyte, as expected due to the production of H^+ ions caused by hydrolysis of the ampicillin by the β -lactamase enzyme. The relationship between ampicillin concentration and maximum pH change is explored in section 5.5.3.

Control experiments were performed to ensure the observed response was due to the enzymatic turnover of ampicillin. With no enzyme present in solution, the dEGFET response does not deviate from the same linear drift seen prior to injection (Figure 5.6 purple). Interestingly, an immediate change in dEGFET response is observed (blue) when enzyme is added to an ampicillin-free solution, although in the opposite direction to when both ampicillin and β -lactamase are present, suggesting a more basic solution pH. Additional control measurements were performed to confirm the cause of this pH change observed in the enzyme-only, no ampicillin control.

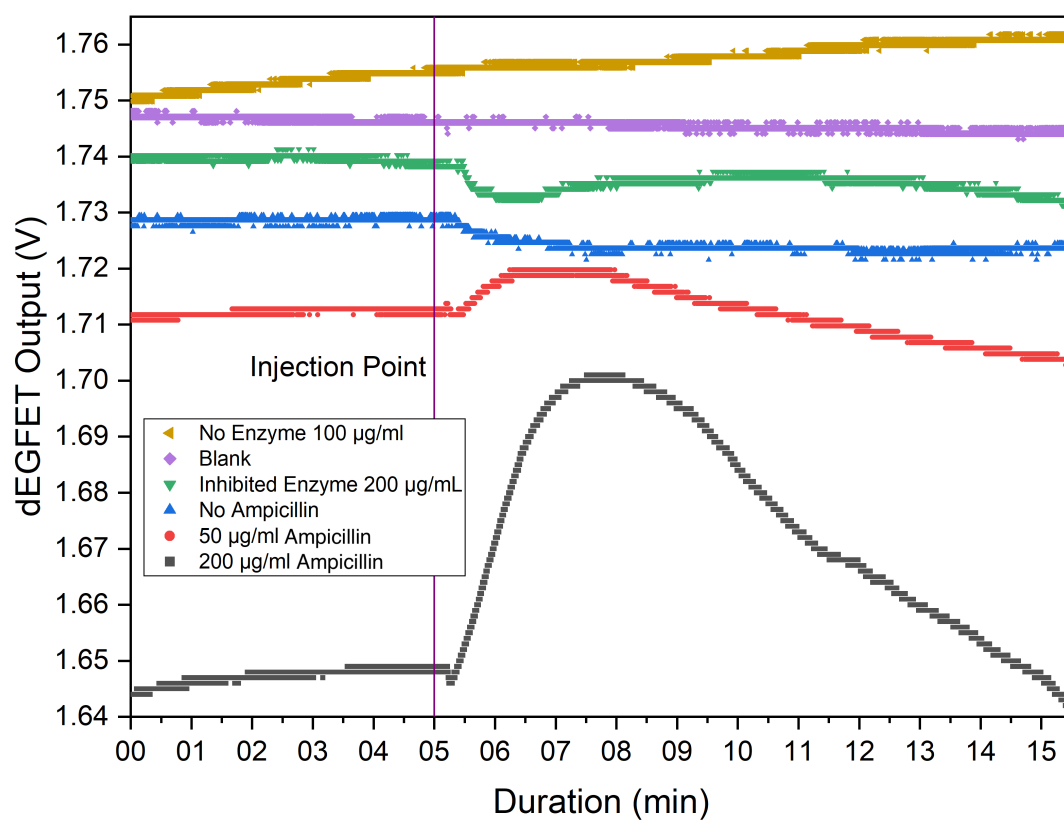


Figure 5.6: Raw output traces from PCB dEGFET devices, measuring a change in output voltage across a range of ampicillin concentrations and control measurements of the β -lactam assay.

Firstly the pH of the aliquoted β -lactamase blend was measured using a commercial pH meter, to a value of $\text{pH } 7.15 \pm 0.2$ ($n=5$). To separate the impact of this pH change alone on the no-ampicillin control, from any effects caused by the presence of β -lactamase enzyme within the buffer. An additional measurement was performed on the dEGFET system.

100 μL of blank KPI buffer at $\text{pH } 7.15$ was injected to 15 ml of blank KPI buffer $\text{pH } 7$, where the overall pH delta as measured by the dEGFET was 0.078 ± 0.024 ($n=5$). Extracting this same delta from no ampicillin controls, where the injected aliquot contained enzyme, a pH delta of 0.064 ± 0.011 ($n=4$) was calculated. This shows the majority of the pH shift observed upon injection of the enzyme is caused by the pH of the injected solution. The discrepancy is potentially caused by the enzyme by nature being a charged molecule that may absorb H^+ ions into protonation sites within its structure, which would reduce the pH of the solution.

A control was also performed (Figure 5.6 green) with addition of inhibited enzyme, intended to confirm that the observed dEGFET response was due to hydrolysis of ampicillin by the β -lactamase enzyme. For these measurements, the β -lactamase enzyme was inhibited by incubating the stock solution with 10 mM sulbactam (Alfa Aesar, J66235) which binds to the active site of the enzyme and prevents its ability to hydrolyse the ampicillin [190]. I note, the enzyme blend includes a range of enzymes, including metalloenzymes that are not inhibited by sulbactam and thus some activity is expected to remain, albeit significantly reduced. This inhibited enzyme was subsequently injected into a 200 $\mu\text{g}/\text{ml}$ ampicillin solution. At the point of injection, I observed the same trend seen with the ampicillin-free control, namely an immediate fall in output voltage caused by the pH of the injected solution.

These measurements and controls suggest this initial pH change is caused by ampicillin hydrolysis by the β -lactamase enzyme. When the enzyme is injected but no hydrolysis occurs, this is due to the lack of ampicillin or inhibition of the enzyme. In these cases a small pH change occurs in the opposite direction due to the pH of the injected enzyme in the low buffer capacity analyte.

5.5.2 Kinetic Secondary Trends

Here, the dEGFET response after the initial region is considered. Measurements without enzyme injection exhibit the same linear sensor drift across the whole 15-minute measurement window (Figure 5.6 yellow and purple). In contrast, with both ampicillin and enzyme present, (Figure 5.6 red and grey), a secondary effect begins to dominate the response after 6-10 minutes of the reaction proceeding, this manifests as the dEGFET output voltage plateauing and then trending downwards. This is contrary to the theoretical response outlined in section 5.5.

Additional understanding is obtained when these responses are compared to measurements taken with a dEGFET sensor using an iridium oxide (IrOx) pH sensing layer, deposited

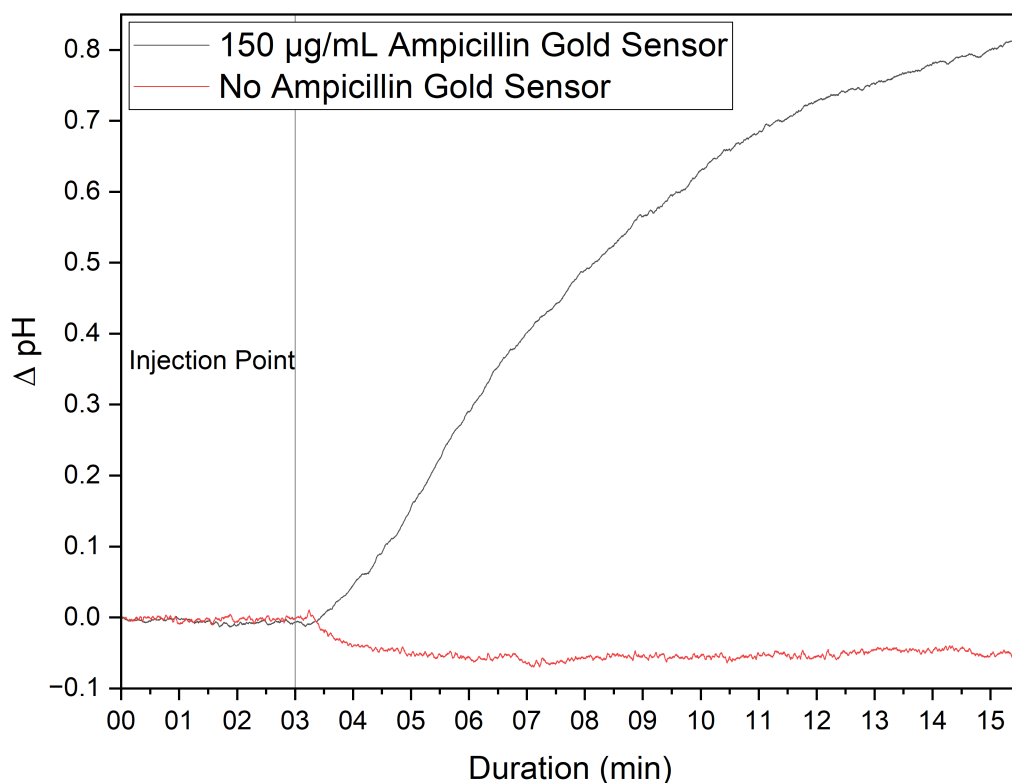


Figure 5.7: Output traces from gold dEGFET devices with ampicillin present at 150 $\mu\text{g}/\text{ml}$ and without ampicillin present [36]. Output traces have been smoothed with a rolling average filter.

onto an Au/Cr electrode on a glass substrate, performed by Dr. Callum Silver [36]. Figure 5.7 shows the differing response where the pH gradient changes after an initial linear region, as expected from discussion in section 5.5.

An additional control type is presented in Figure 5.8 to further isolate the origin of the secondary response observed on Cu electrodes. For these experiments, 200 $\mu\text{g}/\text{ml}$ ampicillin in the standard buffer was incubated with the enzyme blend for 45 minutes at 37 $^{\circ}\text{C}$ without exposure to the Cu sensor. The enzyme was subsequently removed using 10 kDa Amicon spin columns (Sigma-Aldrich, UK, UFC5010).

Figure 5.8 shows the dEGFET output response after exposure to the pre-hydrolysed ampicillin, where the output signal reduces a similar magnitude to that seen after sufficient hydrolysis has occurred when in contact with the sensor. At the injection point, the expected small bulk pH change due to the pH of the injected enzyme blend is seen, after which the response is flat indicating no further interactions.

This suggests that the negative slope in the output signal after plateauing, only occurs when the IrOx coated Cu electrode is exposed to hydrolysed ampicillin. This is further supported by the dEGFET response at various ampicillin concentrations (raw data Figure 5.9), that show a relationship between the magnitude of this secondary signal decay and the ampi-

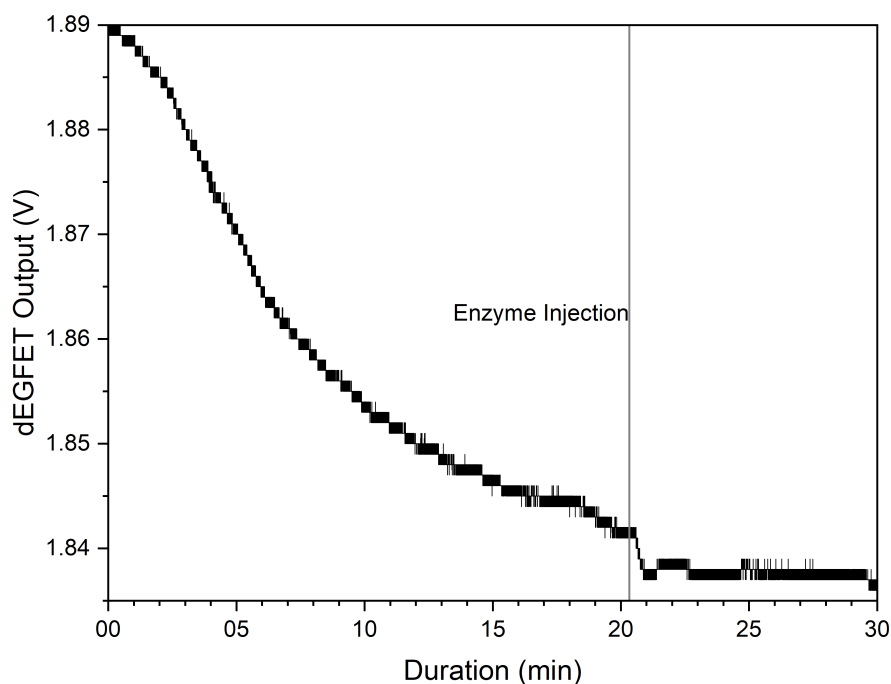


Figure 5.8: Measurement performed by exposing the Cu dEGFET sensor to 0.5 mM KPI buffer containing pre-hydrolysed ampicillin at a concentration of 200 $\mu\text{g}/\text{ml}$. The initial slope is a consequence of this exposure to pre-hydrolysed ampicillin.

cillin concentration as shown in Figure 5.10. Here Δ pH was calculated between the peak and a point after 5 minutes has elapsed.

Finally, an inhibited form of the enzyme, injected into 200 $\mu\text{g}/\text{ml}$ ampicillin (Figure 5.6 green), shows a heavily reduced peak height caused by hydrolysis when compared to the same concentration of ampicillin with uninhibited enzyme. This remaining peak is suspected to be caused by specific enzymes within the utilised blend operating via different mechanisms, of which metalloenzymes are not inhibited by sulbactam. This peak is elongated due to the effective lower concentration of enzymes. The drastic inhibition of the enzyme observed using this method served to show that heavily reducing enzymatic activity leads to reduced hydrolysis.

Although the secondary reduction of the dEGFET output voltage has been isolated and is known to only occur with the presence of hydrolysed ampicillin and when using Cu electrodes, the precise mechanism is not known. Additional investigation would be required to understand the deviation of Cu sensors from the theoretically expected response (section 5.5) shown on gold electrode sensors. It may be caused by Cu ions leaching into solution from the electrode surface, which interact with the hydrolysed ampicillin molecule. The presence of Cu ions in solution changes the ability of groups on the hydrolysed molecule to protonate/deprotonate, which is already a known capacity of the molecule as discussed earlier in section 5.2. Zaworotko *et al.* shows the potential for Cu ions to interact with sites on the ampicillin molecule and alter its pK_a [191], supporting this theory.

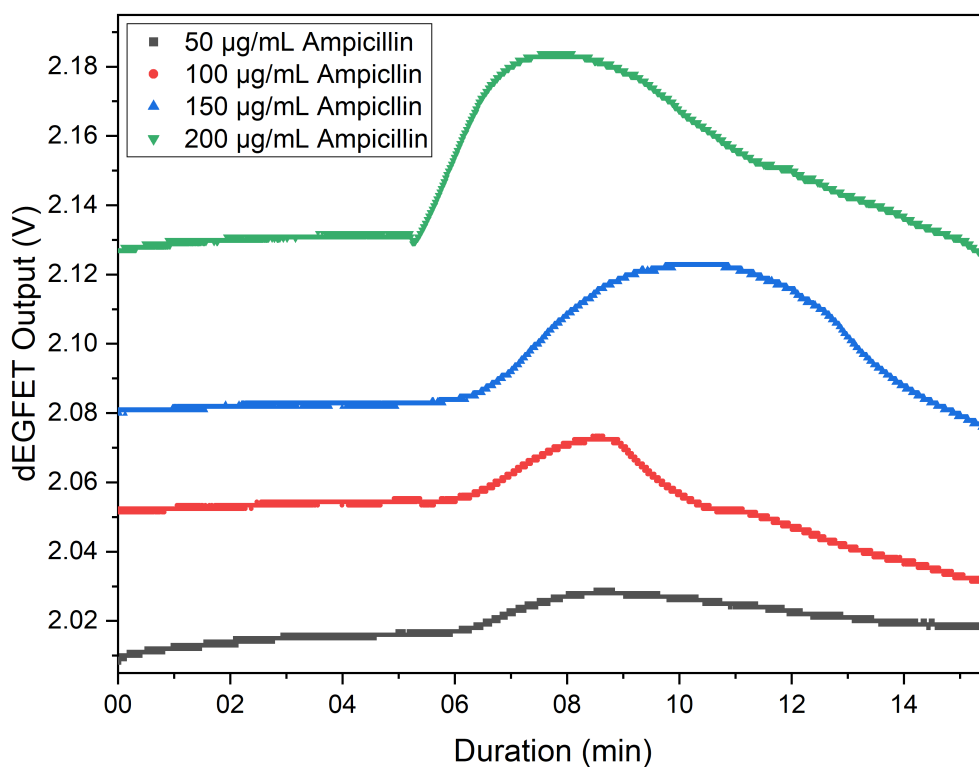


Figure 5.9: Raw dEGFET output traces obtained on PCB electrodes, across 4 ampicillin concentrations.

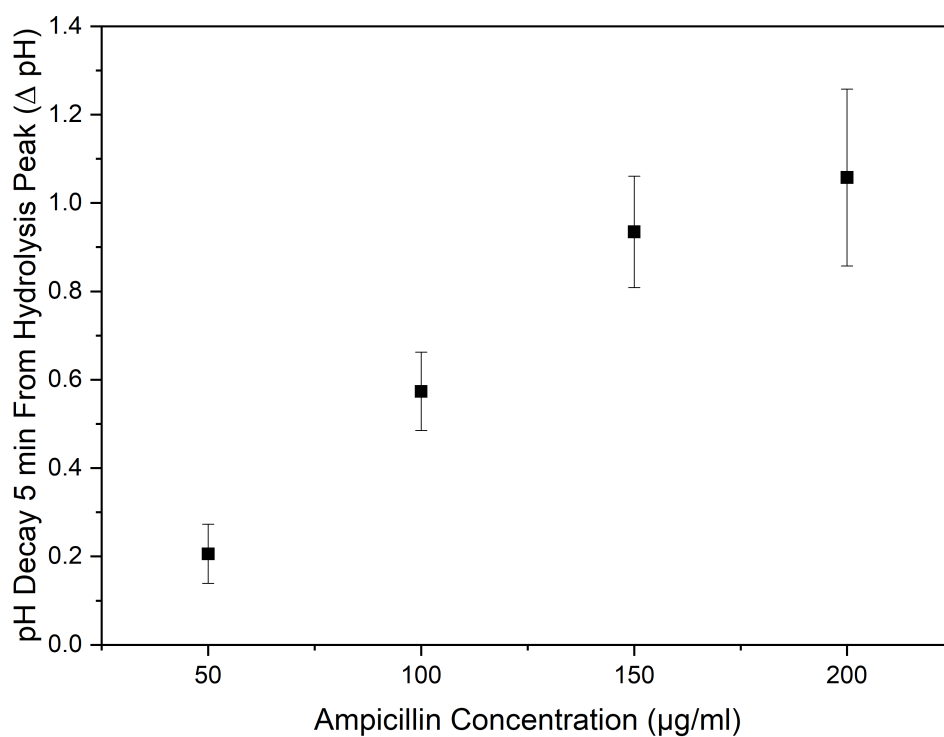


Figure 5.10: Reduction in pH measured 5 minutes from the peak for raw data across 4 ampicillin concentrations. Error bars represent ± 1 SD across 3 repeats at each concentration.

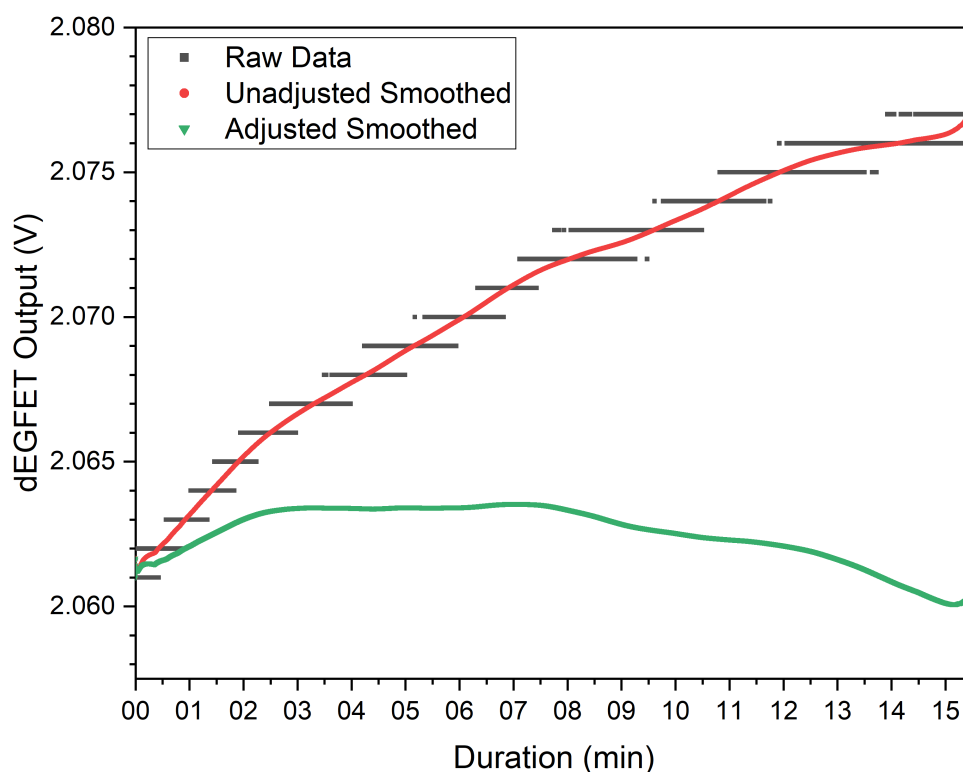


Figure 5.11: dEGFET output trace (black), with smoothing (red) and linear adjustment (green), applied as described in section 5.5.3.

5.5.3 Kinetic Analysis

After considering raw kinetic data obtained using the dEGFET in the β -lactamase assay, the results and associated control measurements, the ability to detect the change in pH caused by hydrolysis of ampicillin by β -lactam enzyme is confirmed. The rate at which the dEGFET output changes upon injection of the enzyme, compared to the consistent rate with no enzyme present, was exploited to quantify the initial ampicillin concentration.

Measurements were first corrected for the slow, linear drift, sometimes present and a common characteristic of extended gate ion-sensitive field effect transistors (EGFET) sensors. Linear correction was applied based on the gradient of the 90 second period prior to injection. The linear fit was performed on weighted adjacent-averaged data which removes errors in fitting caused by quantisation of the dEGFET output data from the Picoscope analog-to-digital converter (ADC).

Figure 5.11 shows a complete raw trace with quantisation and linear slope, alongside the smoothed data and the resulting trace after smoothing and linear drift correction have been applied. These provide a flat linear response at the point of injection. It is accepted this only partially accounts for sensor drift due to the non-linear response over longer time periods, however the subsequent results in this section show these are insignificant compared to the pH change seen when ampicillin hydrolysis occurs, over the reaction time-frame.

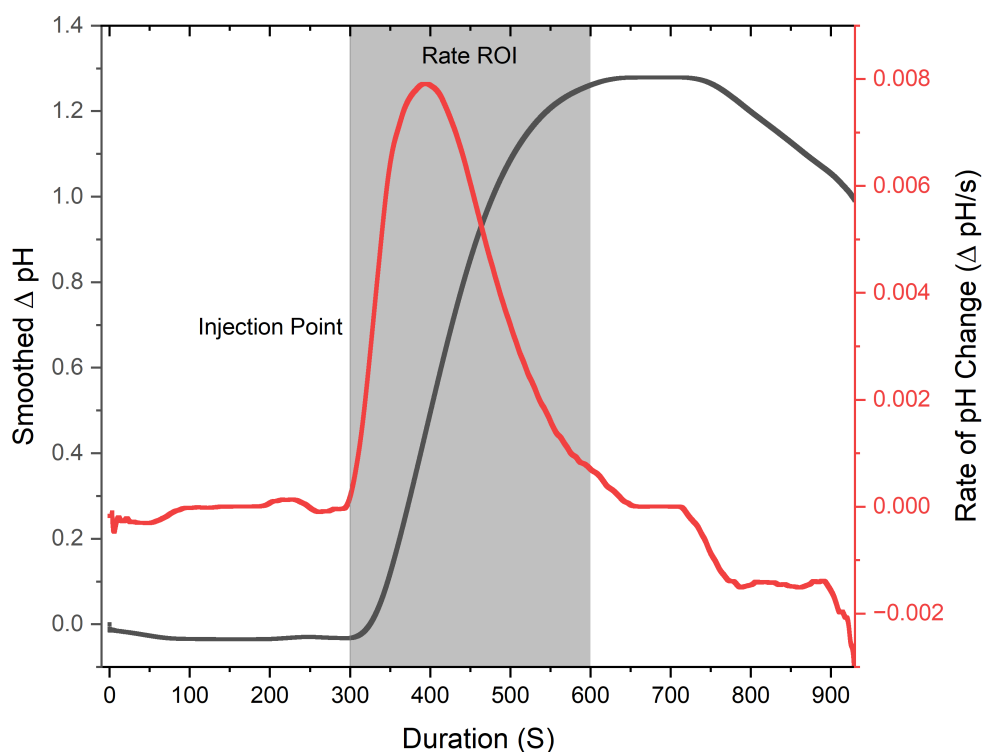


Figure 5.12: pH change calculated from the dEGFET output and calibrated with sensor performance for 200 $\mu\text{g}/\text{ml}$ ampicillin (grey), including smoothing and linear correction. Rate of pH change obtained using the first derivative of the pH change (red).

After drift correction, the rate of pH change for all relevant sensors was calculated by obtaining the first differential of the pH change with respect to time, as is shown in Figure 5.12 for 200 $\mu\text{g}/\text{ml}$ ampicillin. The highest magnitude rate in the 5 - 10 minutes (300 - 600 s) window was selected, this was the period after injection over which the signal took the longest to plateau. The pH change observed after enzyme injection is seen alongside the increased rate seen during this period, calculated to the value of $0.0079 \Delta \text{pH}/\text{s} \pm 0.0010$.

The resulting maximum rate of pH change is presented in Figure 5.13 for ampicillin concentrations between 0 and 200 $\mu\text{g}/\text{ml}$. This calibration curve shows a linear relationship between the ampicillin concentration and the maximum rate of pH change, which differs from the logistic response expected as outlined in section 5.2, where trends from overcoming the buffer capacity and production of H^+ from enzymatic turnover combine. This change in response is potentially due to the interaction with Cu discussed in section 5.5.2.

The LoD of the kinetic assay was calculated using the method described in [192]. A limit of blank (LoB) was first calculated using the mean and standard deviation (SD) of blank samples ($n=3$) as in equation 5.5.1.

$$LoB = blank_{mean} + (1.645 \times blank_{SD}) \quad (5.5.1)$$

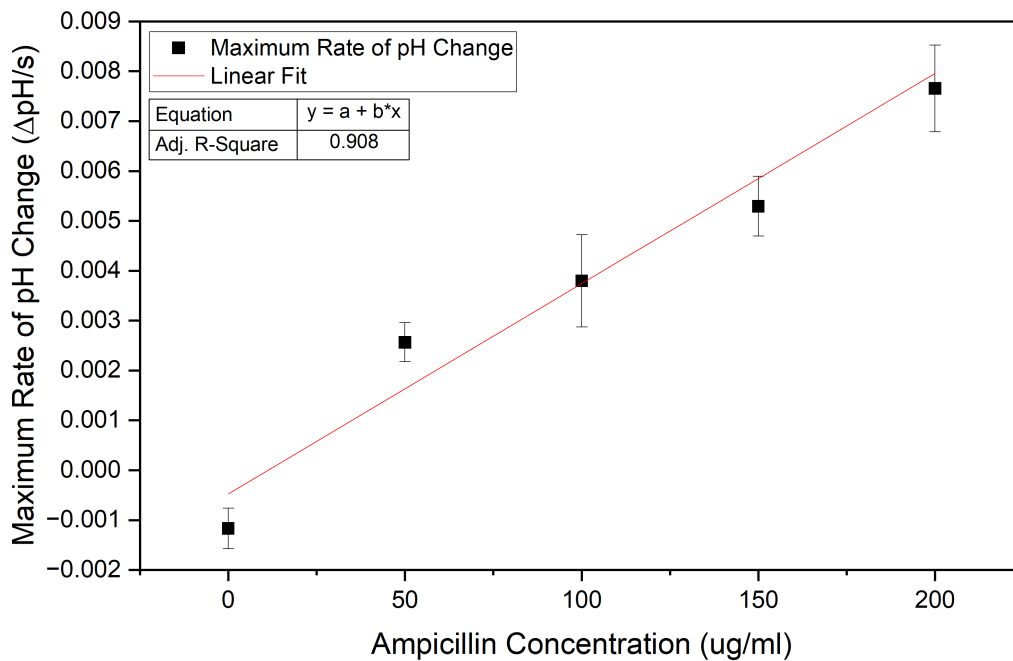


Figure 5.13: Calibration curve for kinetic β -lactam assay between 0 and 200 $\mu\text{g/ml}$.

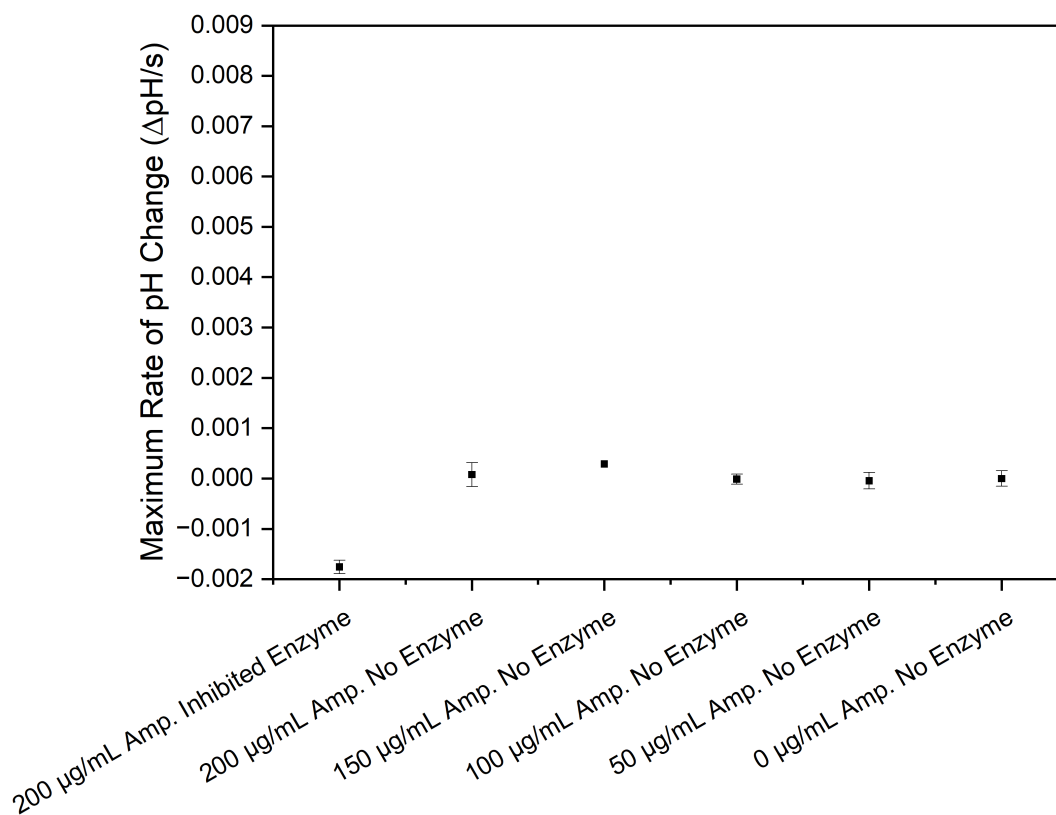


Figure 5.14: Control experiments for kinetic β -lactam assay, showing response with ampicillin present is a result of enzymatic hydrolysis.

Subsequently the LoD was calculated using the SD at the lowest measured ampicillin concentration according to equation 5.5.2. For this assay, the LoD was found to be 44.61 µg/ml of ampicillin.

$$LoD = LoB + (1.645 \times low\ ampicillin_{SD}) \quad (5.5.2)$$

For completeness, the same kinetic analysis was also performed for all control measurements, as shown in Figure 5.14. Of note, it was not expected to observe hydrolysis of the ampicillin without the enzyme present, as at room temperature, pH 7 and acetate/borate buffers, the half-life of ampicillin is 27 days [193].

5.5.4 Kinetic Conclusions

In the presence of the β -lactamase enzyme, a linear relationship is seen between the ampicillin concentration and the maximum rate of change of the dEGFET output caused by the ampicillin hydrolysis. There could be multiple effects which cause deviation away from the expected sigmoidal response. Firstly, the downward reduction in dEGFET output in the presence of hydrolysed ampicillin, enzyme and Cu is expected to have an impact. Although this has been seen to dominate hydrolysis in a 5-10 minute time frame, it is expected the phenomena will also occur as soon as the ampicillin begins to be hydrolysed. Secondly, the change in pH is measured over a short time period (< 5 minutes), where the pH change may not have exceeded the buffer capacity. The pH response of the buffer to addition of acid should be slowly varying and linear within the buffer capacity region. The interaction between these phenomena and resulting expected trend was not explored further.

5.6 Endpoint Methodology

Due to interactions between the Cu electrode and assay components, an endpoint measurement approach was explored that significantly reduces the interaction time between the Cu electrode, enzyme and hydrolysed ampicillin. The endpoint measurement consisted of immersing the sensor for 10 seconds in the ampicillin containing solution while the output voltage was recorded. The β -lactamase enzyme is then injected at 100 µl per 15 ml using a pipette and three aspiration-dispense cycles completed before incubating for 45 minutes. After incubation, the IrOx coated PCB electrode is again placed into the solution and the output voltage recorded for a 10 second duration. Raw data resulting from these measurements is shown in Figure 5.15.

Some sensors (typical examples shown in Figure 5.16) were seen to show significant mea-

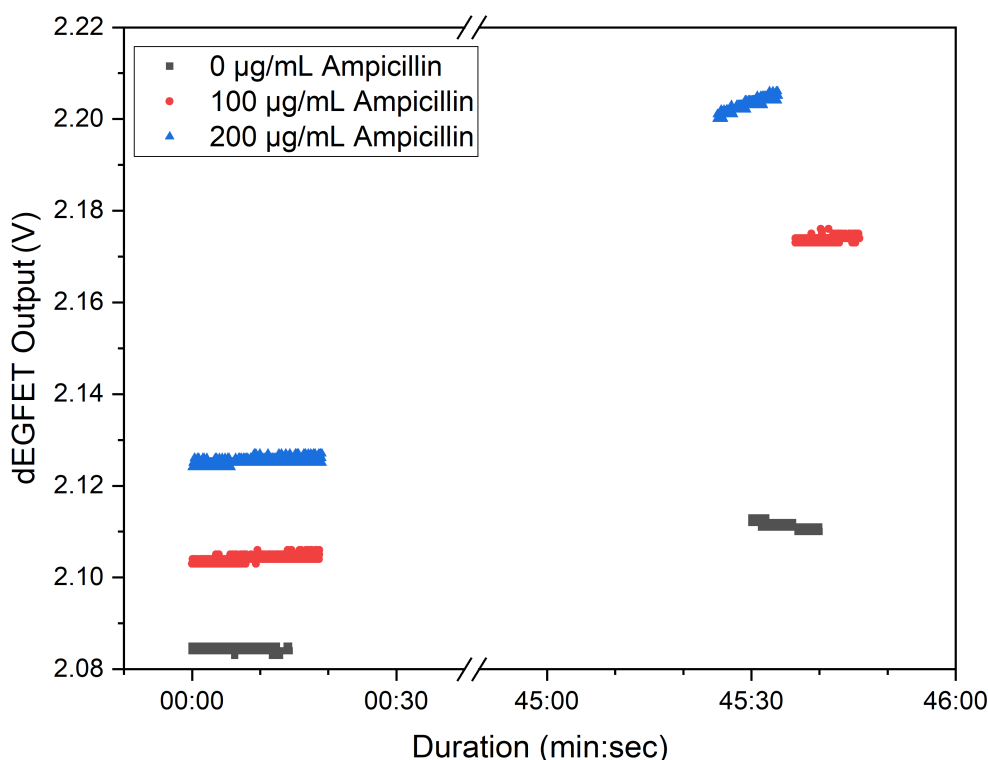


Figure 5.15: Change in dEGFET output voltage as a result of the bulk pH change caused in solution by ampicillin turnover after 45 minutes. An x-axis break is added to account for the 45 minute incubation.

surement drift upon re-submersion after the 45 minute incubation period. The cause of this drift is believed to be caused by the same interaction seen in kinetic measurements between hydrolysed ampicillin and Cu ions that have leached into solution, as the effect was never observed on control measurements without hydrolysed ampicillin present.

It is suspected, this effect is not present on all measurements due to differing extent to which the Cu substrate is covered in IrOx. On sensors with an uniform coating of IrOx, the short exposure time between sensor and solution in endpoint measurements does not allow enough time for sufficient Cu to leach into solution, for the effect to be observed. Whereas in kinetic measurements the exposure time between sensor and solution is greater, leading to consistent Cu ion leaching, including on electrodes with a highly uniform IrOx coating. A linear slope was fitted to this region, measurements which exhibited a drift with an absolute slope greater than 100 V/s at re-submersion were discounted.

I note, variation in the timing of the measurement step after initial injection will add error to the results. Improving the timing as part of a manual system is challenging. To obtain higher accuracy, an automated system is required, such as through the use of a microfluidic system with electronically actuated valves as discussed in chapter 6.

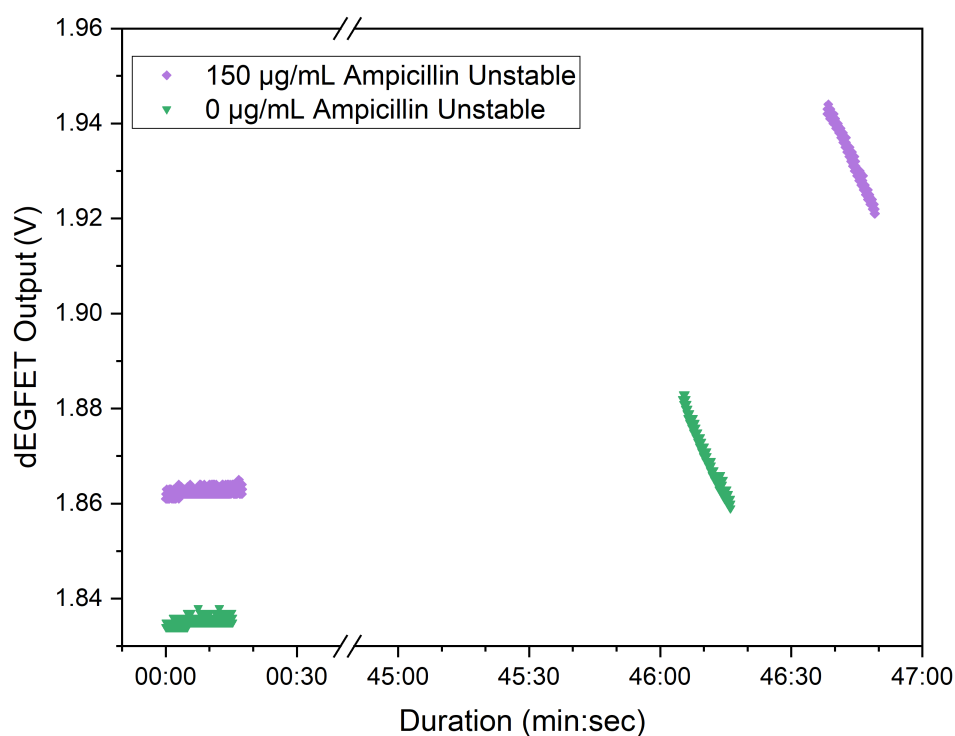


Figure 5.16: dEGFET output for sensors which demonstrate a rapidly changing response at re-submersion after 45 minute incubation. A gradient magnitude > 100 V/s was considered a rapidly changing response and measurements over this threshold are discounted due to the error introduced.

5.6.1 Endpoint Calibration Curve without pH Calibration

The change in dEGFET output voltage after 45 minute incubation with β -lactamase blend plotted against an ampicillin concentration between 0 and 200 $\mu\text{g/ml}$ is shown in Figure 5.17. The mean value is reported at each concentration, with the error bars representing the SD across three repeats.

A sigmoidal fit was used for the pH change response against increasing concentration of ampicillin, influenced by the three effects discussed in section 5.5 and their dependence on starting concentration of ampicillin.

The point at which the dEGFET output becomes non-linear depends on the ampicillin concentration. As the magnitude of solution pH change varies based on ampicillin concentration, it is effected to different extents by the dissociation of hydrolysed ampicillin molecules, which is non-linearly proportional to the H^+ ions produced by hydrolysis. Differing ampicillin concentrations change solution pH to varying extents, which will also impact the enzyme activity.

The adjusted R^2 value of the fitted sigmoidal response curve suggests a strong fit, despite the fact that multiple sensors of differing pH sensitivity were used to generate the data. This highlights the high reliability of the IrOx coated Cu PCB electrode fabrication process presented in chapter 4.

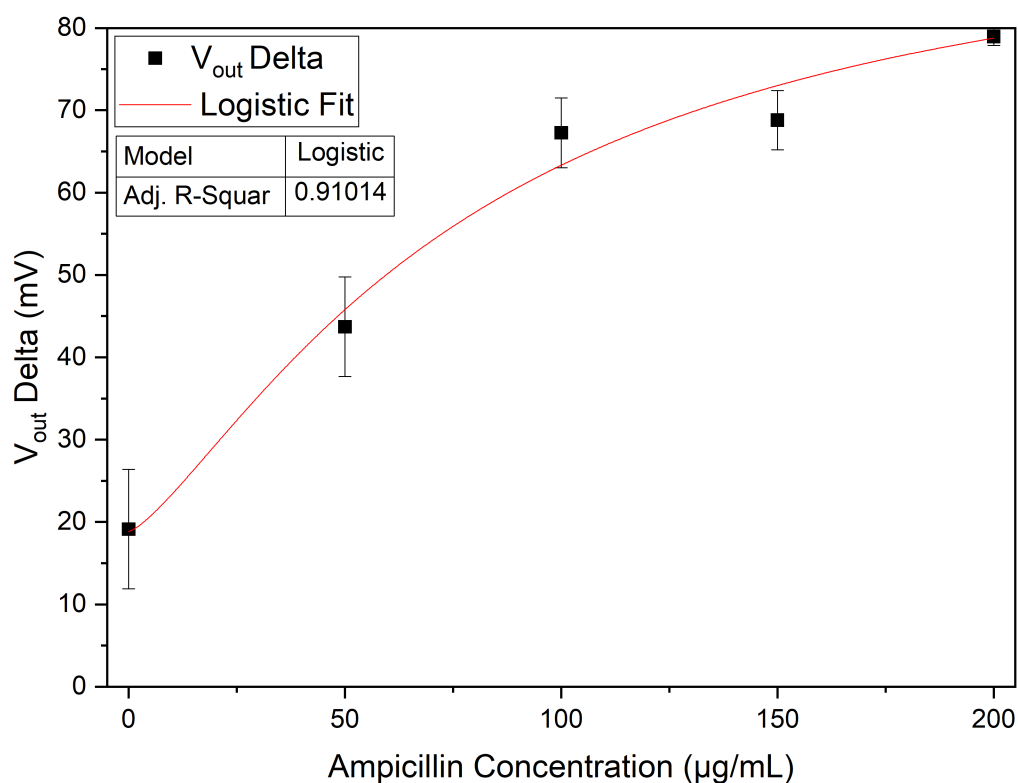


Figure 5.17: Concentration curve showing change in output voltage from un-calibrated dEGFET PCB sensors as a function of ampicillin concentration, after incubation with β -lactamase enzyme. Error bars represent the standard deviation of repeat measurements.

5.6.2 Endpoint Calibration Curve

In order to further improve the quality of the fit, and thus enhance the accuracy of ampicillin quantification, the data was calibrated to account for small variations in pH sensitivity between sensors, as is common with all commercial pH meters that must be routinely calibrated using solutions of known pH before use. Figure 5.18 shows the same data from Figure 5.17 but here calibrated for using the measured sensitivity for each sensor.

As can be seen from the adjusted R^2 value of the sigmoidal fit to the calibrated data, calibration significantly improves the quality of the fit. Figure 5.18 also shows the LoD for the endpoint form of the assay, calculated using the same method as presented in section 5.5.3. The LoD was found to be 31.0 $\mu\text{g/ml}$ of ampicillin which compares well with levels found clinically in urine (ranging between 44.3 - 177.6 $\mu\text{g/ml}$ [188]).

5.6.3 Endpoint Conclusion

In conclusion, this work has shown the suitability of PCB dEGFETs to detect and accurately quantify the concentration of β -lactam antibiotic, through the pH change that occurs due to the action of a β -lactamase enzyme blend. The highest precision was demonstrated using

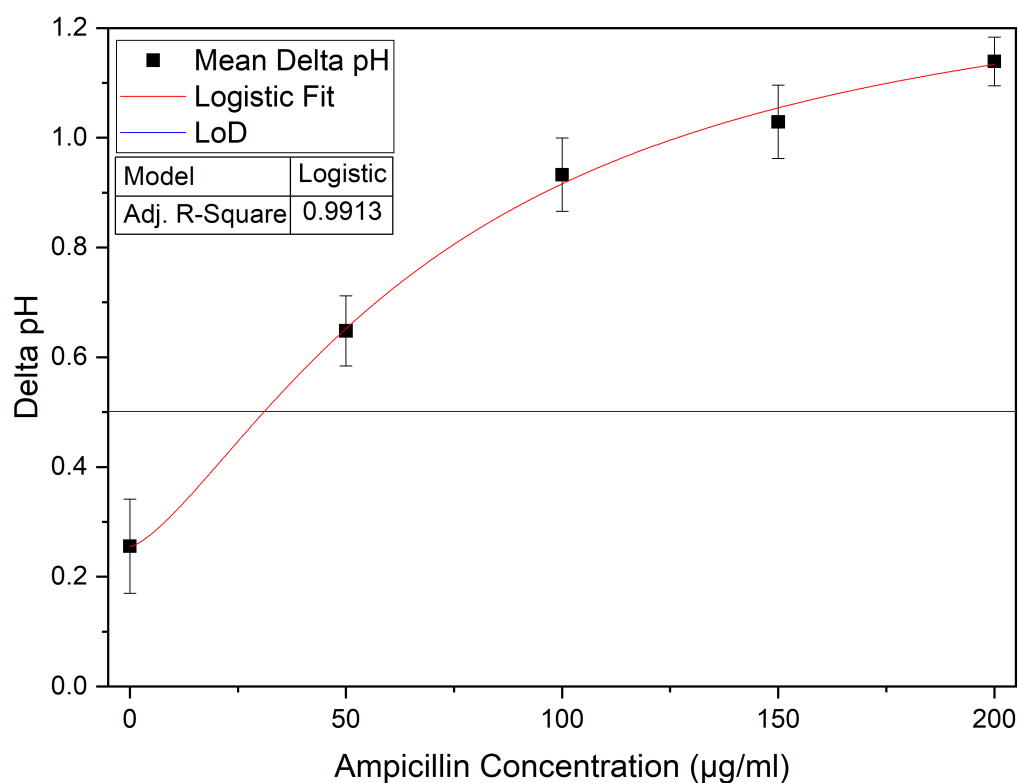


Figure 5.18: Concentration curve showing change in pH measured using sensitivity calibrated dEGFET PCB sensors as a function of ampicillin concentration. Horizontal line as 0.5 pH indicates the limit of detection. All error bars are the standard deviation of repeat measurements.

endpoint analysis using calibrated sensors, where the response matches the expected logistic response and a clinically relevant LoD of 31.0 µg/ml.

There remains potential to use kinetic analysis to provide a faster time to result, beneficial for real world PoC applications and to potentially improve the LoD by reducing the impact of sensor drift. Although, more work is required to understand the impact of Cu ions on enzyme catalysed reactions.

Ultimately, the same low-cost PCB dEGFET devices could be used to monitor a range of other enzyme-catalysed reactions relevant across a range of global challenges. One such example is the detection of deoxyribonucleic acid (DNA) amplification reactions which can be used to detect specific nucleic acid sequences. Chapter 7 shows initial work to realise the Cu PCB dEGFET devices to quantify isothermal DNA amplification.

Chapter 6

Electrowetting Valves

This chapter briefly provides the motivations behind development of electronically controlled electrowetting valves on printed circuit board (PCB) substrates. It then discusses the technologies used for this development process and the underlying theories which enable such a device. Experimental data is presented throughout development of the fluidic device.

6.1 Introduction & Literature

To enable widespread deployment of novel diagnostic technologies, such as those presented in chapter 4, the sensors must not only be low-cost and facile to fabricate, but also ideally be simple and safe to use at the point of care (PoC), often by untrained users.

A lab-on-chip (LoC) approach integrates multiple essential components e.g. sample storage, processing, handling and analysis, onto a single chip, to achieve high levels of automation. This not only reduces assay complexity but can also improve performance through increased consistency. Manufacture of LoC devices remains a challenge, as multiple processes that may not be compatible or are not commonly integrated can increase fabrication complexity and cost.

Lab-on-PCB systems seek to address these challenges by using the well-established PCB materials and fabrication processes developed by the consumer electronics industry, to create highly integrated and low-cost LoC devices. Moreover, electronic components for control, signal processing and readout can be easily integrated, alongside microcontrollers and a broad range of communication technologies to create complete standalone lab-on-PCB systems [194].

A critical component of LoC systems is the inclusion of fluidic components to allow the controlled movement and processing of liquid samples and reagents. Microfluidic channels have been realised with a range of device structures and materials [195], including with PCB

substrates [196]. Fluidic channels can be plasma etched directly into the FR4 substrate of a 2 layer PCB and sealed with polyimide tape [97] or glass [197]. Polymer tapes overlaid onto the PCB are often patterned with channels themselves [198] and sealed with another biologically compatible polymer. Similarly, polydimethylsiloxane (PDMS) is a flexible and optically transparent polymer that can be easily patterned using soft-lithography to create microfluidic channels [199], with feature sizes down to 30 nm [200].

In addition to transporting fluids, there are applications where controlling the order of reagent movement is essential, such as deoxyribonucleic acid (DNA) amplification which requires the mixing of multiple reagents in a well-defined order [67]. This can be achieved through user input, for example by breaking blister packs or manual pipetting of solutions. However, such user intervention is not suitable for assays that require precise timing of reagent handling steps. For these assays, entire device automation is essential. A range of valves have been demonstrated for use within LoC devices that operate in combination with fluidic pumps to control fluid flow through a microfluidic network [195]. These can be interfaced electronically to automate operation, but the pumps are bulky and expensive, and their mechanical nature adds noise to the system.

A range of alternative non-mechanical approaches to control fluid transport have been investigated, including pumps based on pressurised chambers, electro-osmotic flow [201] and capillary flow, or solid-state valves such as grooves with specific geometries [202]. In the context of lab-on-PCB systems, approaches based on capillary flow for fluid transport coupled with electrowetting valves are particularly relevant.

This chapter reports initial work towards a fluidic system that employs capillary flow channels and electrowetting valves fabricated on PCB. The concept is shown schematically in Figure 6.1. Microfluidic channels constructed here using PDMS, are mounted on a PCB substrate, the channel dimensions and surface charge properties are optimised to enable passive fluid flow via capillary action. A Cu electrode placed perpendicular to capillary flow and functionalised with a hydrophobic molecular layer (here 1H,1H,2H,2H-Perfluorodecanethiol (PFDT)), changes the system dynamics so as to inhibit capillary flow beyond the electrode. When a potential difference is applied between the functionalised electrode and a second Cu electrode exposed to the same capillary channel, the properties and/or structure of the hydrophobic layer change, enabling capillary flow to resume.

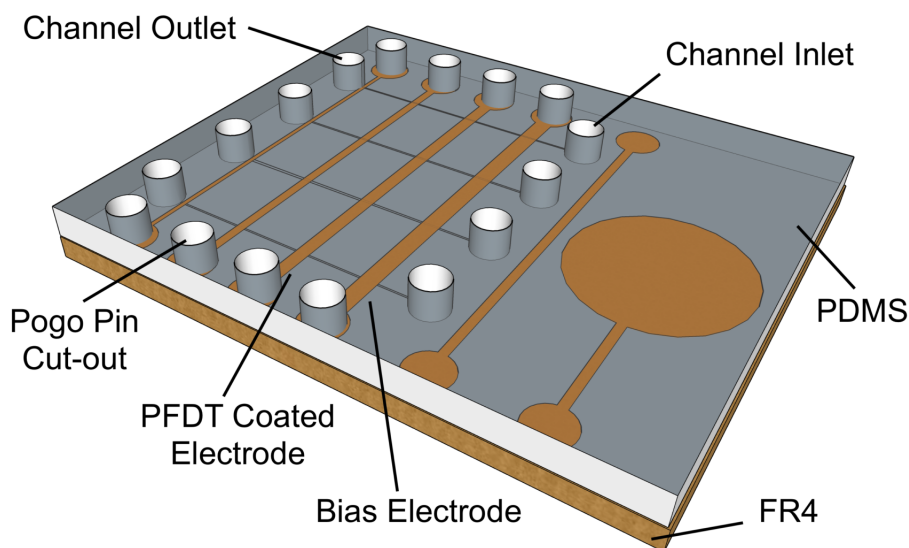


Figure 6.1: Schematic of PCB electrode and PDMS flow channel layout.

6.2 Methods

6.2.1 Surface Wettability Modification

Controlling surface wettability of materials used within the PCB fluidic system is critical to balance capillary flow and inhibition of fluid flow at the functionalised, valve electrode.

The contact angle (CA), θ_C , is a common parameter used to quantify the wettability of a surface, defined as the geometric angle of the liquid-vapor interface generated at the liquid-solid interface of interest. Figure 6.2 shows a schematic diagram for a droplet on an idealised surface with no roughness. θ_C can be calculated with Young–Dupré equation and the relationship between the interfacial energy at the three interfaces, solid-liquid (γ_{SL}), solid-gas (γ_{SG}) and liquid-gas (γ_{LG}) at thermodynamic equilibrium [203].

A FTA-100 series goniometer produced by 'First Ten Angstroms, UK' and the sessile drop method were used to measure CA values. Figure 6.3 shows images obtained using the system, for a CA of 0° on plasma treated FR4 a) and 97° on PDMS b). The contrast algorithm with spherical fit in *Drop Shape Analysis* (First Ten Angstroms, UK) is unable to generate an angle for super hydrophilic surfaces like treated FR4, as the droplet blends into the substrate. A surface can be referred to as hydrophobic (non-wettable) and hydrophilic (wettable) in relation to aqueous solutions with which it makes contact.

The surface CA can be adjusted in a variety of ways, such as the deposition of thin material films such as Teflon that lead to highly hydrophobic surfaces [205], or chemical modification such as doping of polyethylene glycol (PEG) co-polymer into PDMS [206]. In this work, ultraviolet ozone (UV-ozone) and oxygen plasma (Ox-plasma) methods were used to modify surface chemistry and enable a range of CA to be achieved.

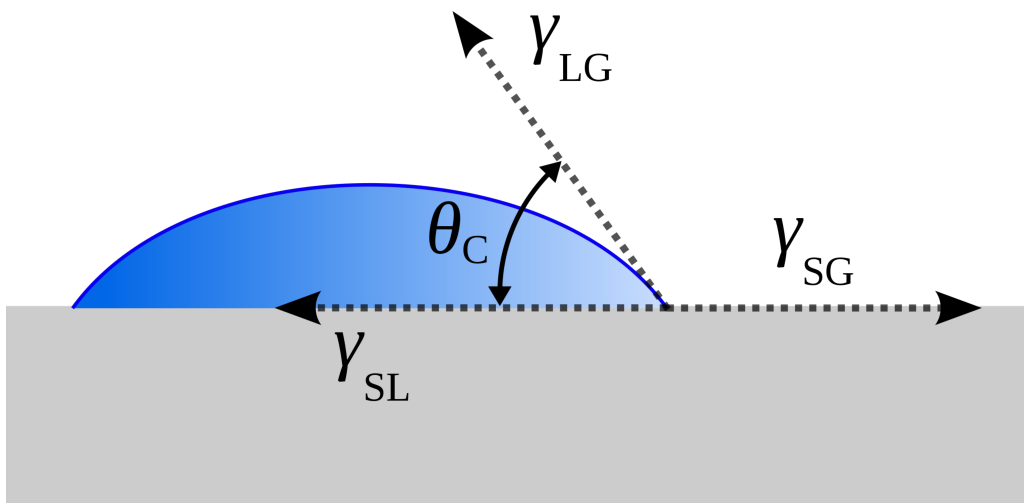


Figure 6.2: Schematic diagram of a droplet on a flat surface, showing relationship of interfacial energy between the three phases, and the location of the reported CA. Adapted from [204].

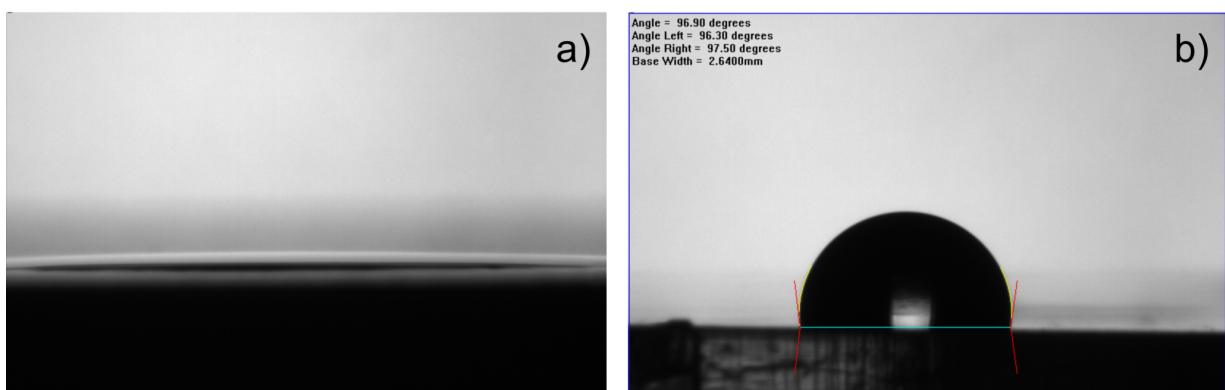


Figure 6.3: Images from CA goniometer showing a CA of 0° on plasma treated FR4 a) and 97° on PDMS b), as calculated using *Drop Shape Analysis* contrast based algorithm.

6.2.2 UV Ozone

UV-ozone treatment is often employed as a surface cleaning method capable of removing organic contaminants. The mechanism of action (photo-oxidation) also changes the chemical moieties at the surface of a material, which can in turn change the surface energy and wettability. Atoms in the bulk of a material are commonly stable, due to balanced bonds in all directions within the lattice, whereas surface atoms on a virgin surface are not bonded on their outer face leading to a high surface energy (high wettability). These atoms are stabilised by bonding to different species, often oxygen found in the atmosphere, which reduces the surface energy (reduced wettability).

A UV-ozone system contains a high-intensity UV light source, which has strong emission peaks at both ≈ 185 nm and ≈ 254 nm which interact differently with the surface (Figure 6.4a). The shorter wavelength of light dissociates molecular oxygen in the air, forming two oxygen radicals. These are unstable in this lone state and highly reactive, subsequently forming O_3 . Simultaneously, the longer wavelength of light excites organic contaminants present on the surface, increasing the chance of a reaction when interacting with ozone. As a result, volatile species such as carbon dioxide (CO_2), water (H_2O) and nitrogen (N_2) are formed which can readily desorb from the surface [207].

The removal of these contaminants from the surface ultimately alters the surface energy, while creating a more chemically uniform surface. Hydroxyl (OH) functional groups are also formed at the surface of the material, caused by irradiation of water molecules with ≈ 254 nm light producing OH and O radicals [208]. If irradiated, OH groups near the surface do not react with ozone, they will instead react with the surface producing oxide and hydroxide bonds which have a high bonding energy (Figure 6.4b).

In this work, it is expected that under UV-ozone treatment, bulk Cu bonds at the surface are replaced with Cu-OH and Cu=O bonds. It is accepted this effect is not permanent as contaminants return to the surface, however UV-ozone offers flexibility in the surface energy achieved by varying the treatment duration. This alters what portion of surface molecules undergo the change to high surface energy functional groups. A short discussion on methods for longer term alteration of surface energy is included at the end of section 6.3.1.

6.2.3 Plasma Treatment

Plasma treatment is also commonly used to remove surface contamination and alter the surface energy. In this work Ox-plasma was utilised, where a vacuum chamber is used to evacuate the atmosphere and replaced by oxygen gas. This is subsequently ionised by a radio frequency (RF) voltage which forms a plasma that is highly reactive [210]. As electrons orbiting oxygen atoms, previously excited to a higher energy state by this RF voltage, decay to lower state, they

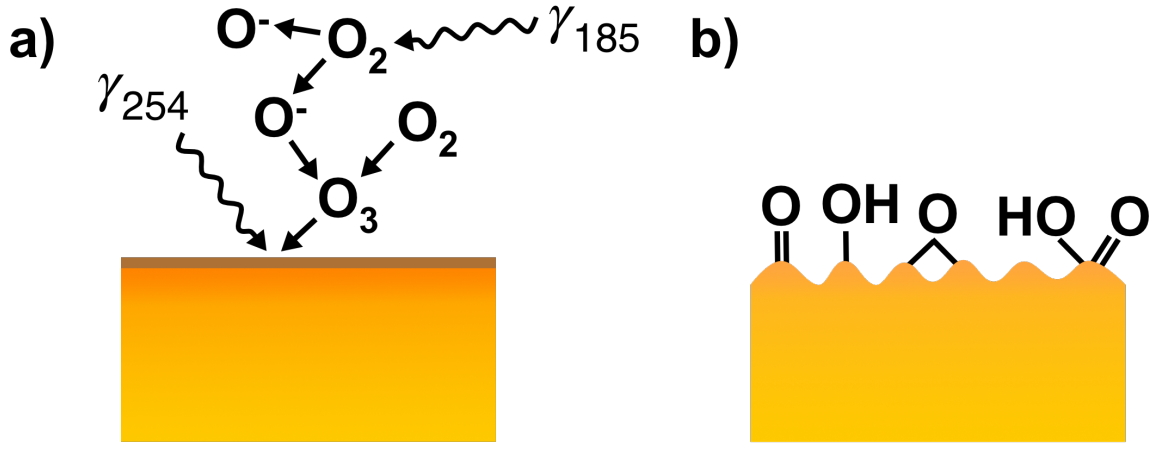


Figure 6.4: a) Surface bombarded with high energy UV photons and species generated from UV interaction with the air. b) Polar surface groups generate after UV irradiation. Adapted from [209].

release a photon with a wavelength in the UV spectrum which results in the characteristic *glow*.

There are multiple mechanisms by which the gas molecules, free radicals and electrons within this plasma interact with surfaces [210, 211]. As with UV-ozone treatment these lead to the removal of surface contaminants and formation of high surface energy functional groups.

6.2.4 Washburn Equation Theory

This work exploits capillary flow to move fluid through channels without the need for bulky and expensive mechanical pumps. The Washburn equation is used to describe capillary flow within a range of systems including porous materials and channels. A modified version of the Washburn equation [212] is shown in equation 6.2.1, which describes capillary flow in a channel of rectangular cross-section, where 3 walls are PDMS and one is FR4 of a PCB substrate. This also assumes static contact angles as opposed to dynamic without the introduction of significant errors [212].

$$\dot{x} = \frac{\gamma_{LV}}{8\eta x} \left(\frac{hw}{h+w} \right)^2 \left[\frac{2\cos(\theta_{PDMS})}{w} + \frac{\cos(\theta_{PDMS}) + \cos(\theta_{FRA})}{h} \right] \quad (6.2.1)$$

The contact angles of channel wall materials (θ_{PDMS} & θ_{FRA}), and channel dimensions (height (h) & width (w)) are the variables that dictate if capillary flow will occur. The portion of equation 6.2.1 within the square brackets, can return a positive flow velocity (\dot{x}), where capillary flow will occur or a negative value where no flow will occur. The other variables; interfacial tension (γ_{LV}), liquid viscosity (η), and distance of the meniscus from the inlet (x), dictate the precise flow velocity as shown in the first portion of equation 6.2.1 which always remains positive.

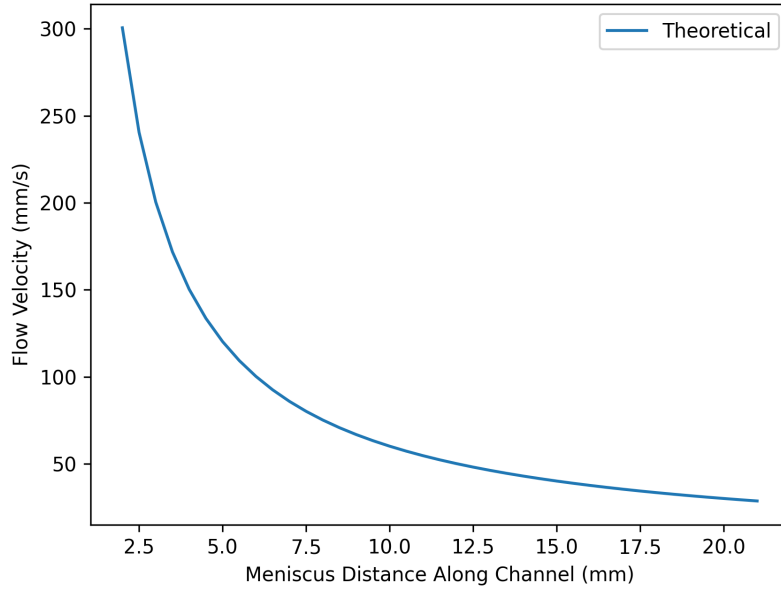


Figure 6.5: Simulated flow velocity based on distance of the fluid along the microfluidic channel. Parameters utilised are detailed in section 6.2.4.1.

The Washburn equation is used here to balance the system parameters, so that capillary flow transports the liquid through the channel on the FR4 substrate but flow is impeded at the valve electrode functionalised with the hydrophobic molecule; and capillary flow is subsequently resumed after biasing of the valve electrode. To satisfy this combination of requirements, certain parameters will be measured and others will be guided by literature and validated later.

6.2.4.1 Flow Velocity Dependence on Channel Meniscus Distance

Notably, the distance of the meniscus along the channel heavily influences the flow velocity. The simulated flow velocity at distances along the channel (total length 21 mm) is plotted in Figure 6.5 with all other variables fixed to illustrate this dependence. The water-PDMS interfacial tension value is assumed to be 41.1 ± 6.54 mN/m based on literature [213], which itself notes low confidence based on assumptions required from an indirect calculation of the value, alongside the expected impact of surface roughness. Other assumed parameters for this simulation are $\eta = 0.98$, $h = 200$ nm, $w = 370$ nm, $\theta_{PDMS} = 80$ & $\theta_{FRA} = 2$.

Figure 6.5 shows the flow velocity decreases in a non-linear fashion as the distance along the channel increases, trending towards a constant none zero value. To enable calculation of channel and material characteristics that will enable capillary flow, the velocity at the point halfway along the channel (10.5 mm) is considered for subsequent work; this is the location the electrowetting valve will be placed later in device development. Section 6.3.8 compares

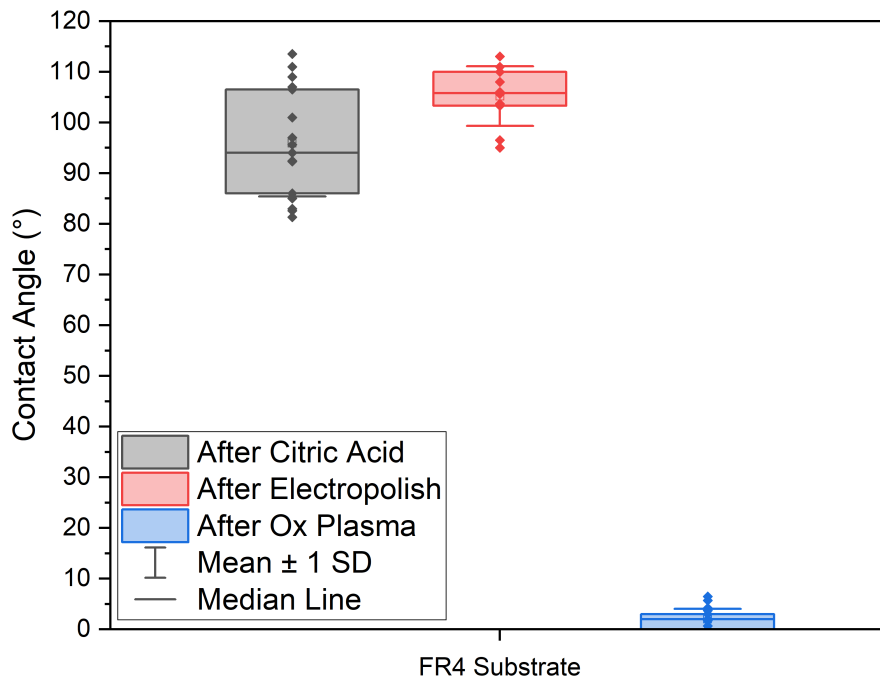


Figure 6.6: Contact angle of FR4 substrate after various treatment steps used on PCB sensors for ISFET and electrowetting valves fabrication.

this theoretical dependence of meniscus distances to flow velocity against practical measurements.

6.3 Capillary Flow

This section follows the process to obtain capillary flow in fabricated devices, including measuring CA of key materials to compare theoretical results to empirical data.

6.3.1 FR4 Contact Angle

The CA of the FR4 is presented (Figure 6.6) after exposure to citric and phosphoric acid, included to mimic the cleaning procedures used in preparation of the pH-sensitive electrodes, as discussed in chapter 4. In both cases, the CA for FR4 was above 90° . The CA of FR4 should be maintained close to zero to support capillary flow across the FR4 surface. Initial work thus focussed on approaches to reduce the CA of FR4. While UV-ozone treatment has been shown to moderately reduce the CA of FR4 to below 25° [214], Ox-plasma treatment can reduce the CA of FR4 to 0° [215]. The FR4 substrate was thus exposed to oxygen plasma using a HPT-200 system (Henniker Plasma) set to 20 standard cubic centimetres per minute (SCCM) oxygen flow, 100 W for 20 minutes. The CA after oxygen plasma is also shown in Figure 6.6 which revealed a significant reduction in CA to a mean of $2 \pm 2^\circ$.

This treatment was subsequently used for all PCBs. I did not explore the long-term stability of this hydrophilisation, but it has been reported that CAs below 10° can be maintained for at least two weeks [215]. It is also known that storage in dehumidified or vacuum conditions can be used to extend this duration, although more a complete study is required to optimise this process [216]. Alternatively PEG coatings can be used to reduce the CA to 0° for 80 days [217].

6.3.2 PDMS Flow Channels

PDMS (Sylgard 184, Dow Corning) is made from two liquid components; a base elastomer and a curing agent. When these are mixed and left to cure, a solid elastomer is formed. When the curing process is performed within a master mould containing the complementary shape to the desired channel design, the shape of the mould becomes imprinted in the cured PDMS. This mould can be re-used to form multiple microfluidic devices.

The mould is often created in silicon, which is patterned using UV lithography and etching [218]. Recent work with affordable 3D printers has demonstrated resin-based moulds can also be used [219]. While 3D printed moulds offer rapid prototyping during development, issues of inhibited PDMS curing have been reported when 3D printed moulds are not themselves cured completely [220]. Keeping with the vision of low-cost and widely available fabrication processes, here I investigated fabrication of the PDMS moulds via 3D printing using a Formlabs Form-3⁺ and Tough-2000 resin.

Figure 6.7a shows a PDMS mould consisting of 4 flow channels and other features for alignment and electrical contact which will be used later in this work. Figure 6.7b shows a closed form of the mould, which is secured with bolts and an inlet for the liquid PDMS.

6.3.3 PDMS Contact Angle vs. UV-ozone Duration

The Washburn equation also highlights the importance of the PDMS contact angle for enabling capillary flow within the system. A series of measurements were performed to characterise the CA of PDMS when exposed to varying durations of UV-ozone, which was selected over Ox-plasma due to the finer control offered by the reduced rate of surface modification. This would enable selection of a CA that will not only support capillary flow, but also that places the system in a state where capillary flow can be stopped at the valve electrode.

Figure 6.8a shows the CA measured at multiple regions across 3 different samples of PDMS. Prior to UV-ozone treatment, the mean CA for the three samples ranges from 92.6° to 104.3° , with an average standard deviation of $\pm 4.0^\circ$. This variation in CA between samples and across the surface is suspected to be caused by varying surface roughness of the cast PDMS

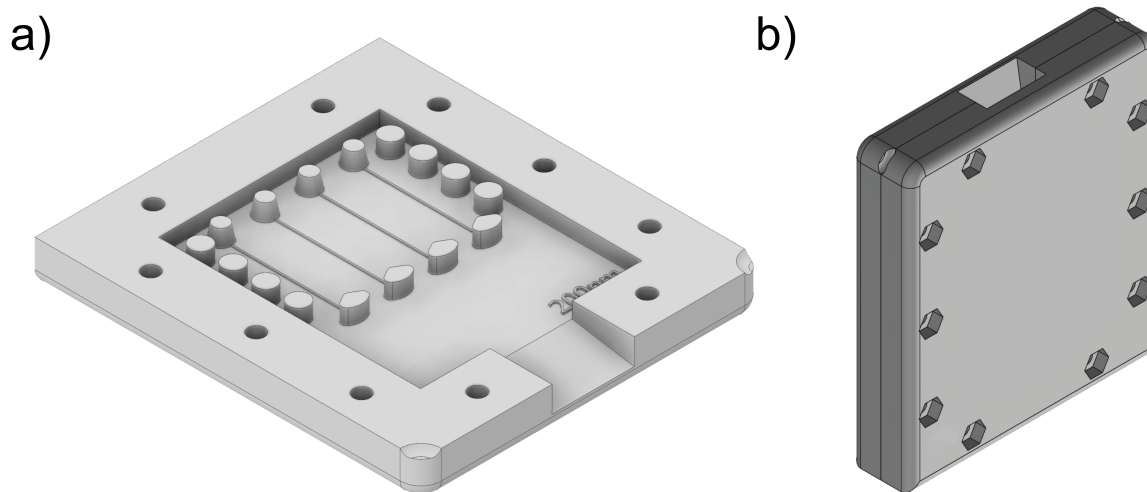


Figure 6.7: a) Base of 3D Printed mould, consisting of protrusions to create 4 flow channels, a sloped inlet and an outlet. b) closed form of the mould, ensuring consistency of device thickness.

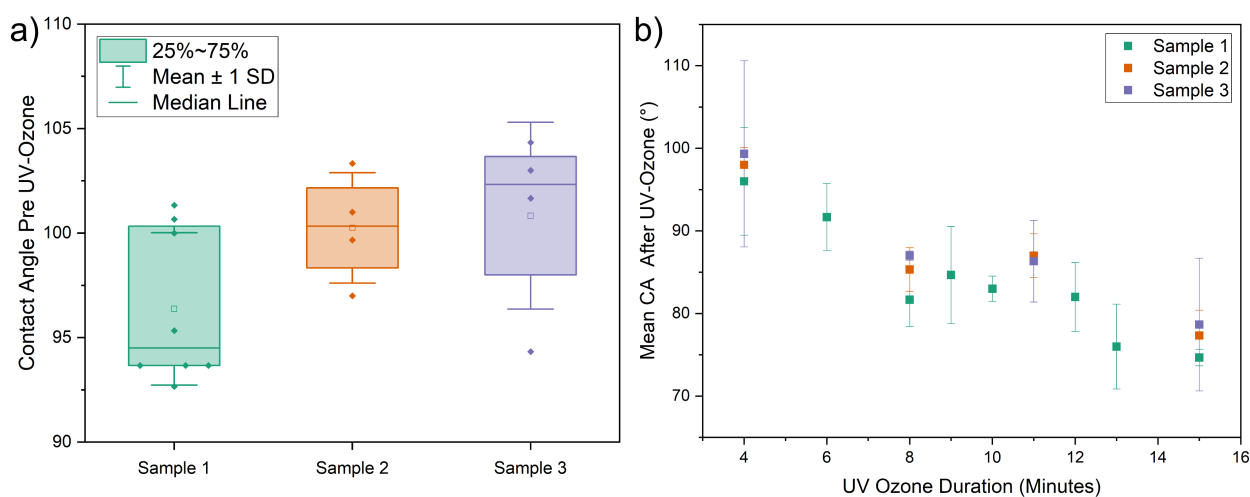


Figure 6.8: a) CA of three PDMS samples directly after casting and prior to any additional treatment. b) CA of the same 3 samples after varying durations of exposure to UV-ozone. Error bars show are across 4 regions on each PDMS sample.

(see section 6.3.4.3) and variation in dosage across the stage in the UV-ozone system.

Figure 6.8b displays the relationship between UV-ozone treatment duration and CA, showing the ability to tune the CA. I note, high precision of the PDMS CA was not essential for device operation, so no further effort was committed to reducing sample variability or the precision of CA tuning.

6.3.4 PDMS 3D Master Mould Characterisation

As described by the Washburn equation, the channel dimensions impact the capillary flow rate. The accuracy and consistency of the printed moulds were compared to the designed dimensions, to understand the techniques applicability for this stage of development. Surface roughness of the cast PDMS was also explored due to the known impact on material CA. Alternative fabrication methods could be utilised after a future final device layout has been decided, such as injection moulding if performance beyond that displayed here is required.

Initial channel heights and widths were selected based on literature precedent, whilst also considering the spatial resolution of the 3D printed master moulds. The channel width was fixed at 300 μm for all channels [212]. Much of the literature on electrowetting valves utilises channels formed using adhesive tape which leads to channel heights below 100 μm [198, 221]. Features of this size are not recommended by the manufacturer of the 3D printer in use. Instead, to better fit the capabilities of the 3D printer channels, varying between 100 and 300 μm were used. Section 6.3.5 includes simulations of capillary flow rates in channels of these dimensions.

6.3.4.1 Master Height

Moulds featuring channels of 5 different heights, with two channels of each height per design, were printed to measure the accuracy and precision of the 3D printed mould compared to the computer-aided design (CAD) files. Figure 6.9a shows raw data (DektakXT, Bruker) obtained from 4 measurements of a 100 μm channel fabricated on a single mould, with scans taken at 5 mm intervals. A step height function (Figure 6.9b) was applied (Gwyddion) to obtain a value for the measured height on each scan. For any one channel on a sample, the heights are reproducible with an average SD of 1.97 μm . Although the mean across 4 samples (100.69 μm) matched the intended height, the SD in channel height between samples was 5.65 μm , showing there is a high level of precision, but lower accuracy.

This trend continues (Figure 6.10) as channel height increases, with high precision across features of the same height on a single sample, but with reduced accuracy between different moulds. The magnitude of intra- and inter-sample SD was also found to increase with

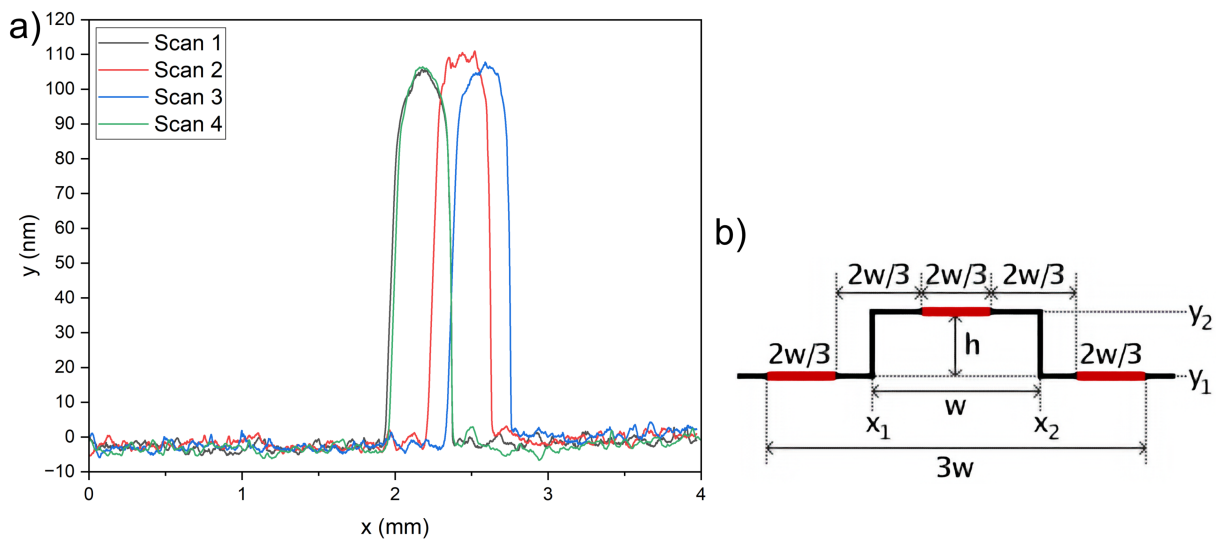


Figure 6.9: a) 4 raw scans of 100 μm high and 300 μm wide channel in 3D printed mould, taken 5 mm apart. b) Step height function used to extract feature height (h) and width (w), performed in Gwydion [222].

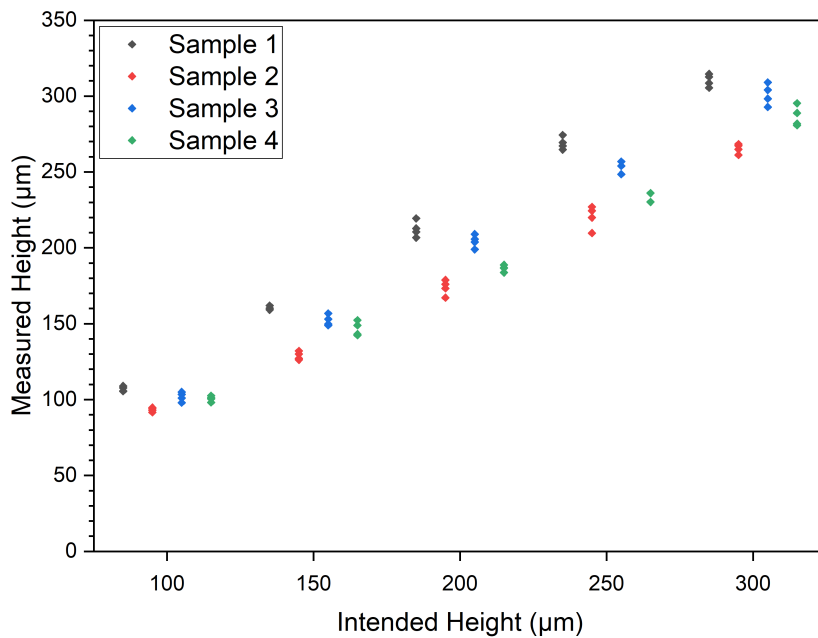


Figure 6.10: Measured height of 3D printed channels at 4 locations on 4 samples, across a range of channel heights.

Table 6.1: Tabulated data as shown in Figure 6.10, showing inter- and intra-mould trends of channel height.

Channel Height (μm)	Sample 1 (Mean \pm SD)	Sample 2 (Mean \pm SD)	Sample 3 (Mean \pm SD)	Sample 4 (Mean \pm SD)	Average (Mean \pm SD)
100	106.99 \pm 1.65	93.31 \pm 1.31	101.89 \pm 1.82	100.57 \pm 1.26	100.69 \pm 5.64
150	160.11 \pm 1.26	128.85 \pm 2.67	152.12 \pm 3.53	146.71 \pm 4.75	146.95 \pm 13.26
200	212.33 \pm 5.31	173.86 \pm 5.00	204.40 \pm 4.18	186.50 \pm 2.11	194.27 \pm 17.35
250	268.87 \pm 4.08	220.26 \pm 7.60	253.34 \pm 3.48	233.14 \pm 3.38	243.90 \pm 21.50
300	310.33 \pm 4.09	265.42 \pm 3.16	301.00 \pm 7.04	286.65 \pm 6.74	290.85 \pm 19.55

Table 6.2: Width of channel at three heights, as a percentage of the feature height, as calculated using the Gwyddion step height function.

Distance up channel height	Sample 1	Sample 2	Sample 3	Sample 4	Mean \pm SD
0 %	451	456	460	452	454.8 \pm 4.1
50 %	380	369	371	376	374.0 \pm 5.0
90 %	283	288	284	282	284.3 \pm 2.6
% Variation 0 – 90%	63	63	62	62	-
Gwyddion step function width	372.9	353.1	356.8	364.7	361.9 \pm 8.8

increasing sample height as show in Table 6.1.

Given the limited accuracy of the 3D printed moulds, each new mould was measured prior to use to confirm the channel heights were within 10 μm of the intended height. Moulds outside of this accepted variance were rejected.

6.3.4.2 Mould Width

The precision and accuracy of 3D printed mould channel widths were also measured using a DektakXT step profiler, compared to the designed 300 μm width. Channel width was extracted at three points along the height of the channel (0%, 50% and 90%) to understand how the width changes at different heights. These were calculated with using the Gwyddion step height function [222], the results are shown in Table 6.2.

If a 100 μm high channel is taken as an example, at its base the channel width average is 454 μm , compared to 284 μm at 90% of its height. This shows a lack of accuracy in achieving the designed 300 μm width, as its width varies an average of 63% between the channel base and top. Channel width was measured to vary in a similar manner for all channel heights, as shown in Figure 6.11.

To move forwards with device simulations for optimising capillary flow, an average width

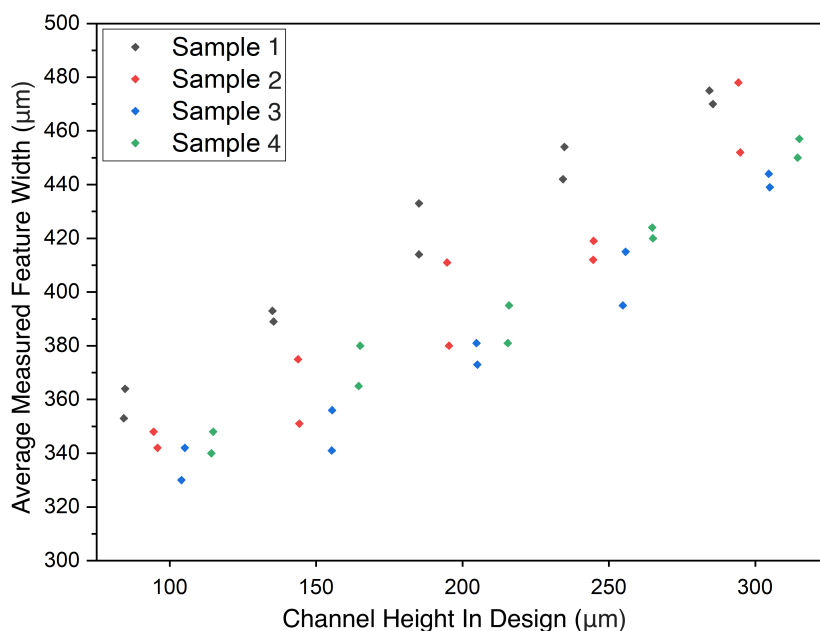


Figure 6.11: Average channel width for a range of designed channel heights as calculated using Gwyddion. All widths designed to be 300 µm.

was used, calculated along its height using the Gwyddion step height function. It was accepted this variation will affect the accuracy of the Washburn equation when applied to the system. The average width is 345, 368, 396, 423 and 458 µm for channels of respective design heights 100, 150, 200, 250 and 300 µm.

6.3.4.3 Mould Surface Roughness

Surface roughness of the base of these 3D printed moulds was also quantified as root mean squared (RMS) roughness (R_{rms}) using Gwyddion, showing a value of 6.04 ± 4.56 µm across 4 samples. This large SD relative to the mean R_{rms} shows the high variability in surface roughness between samples, those with visibly damaged surfaces, such as distinct scratches, were not used as PDMS moulds.

6.3.5 Washburn Simulations of Capillary Flow Channels

Simulations were performed to explore the balance between capillary flow through the channel and inhibition of fluid flow at the valve electrode coated with a hydrophobic molecule. Parameters used in the simulations are outlined in Table 6.3.

Of note, the contact angle of the hydrophobic coatings to be deposited on the valve electrode are reported in section 6.4.2, but are required for these simulations. The mean CA of these deposited hydrophobic layers on Cu in this work ranged from 99.6° - 102.1° depending on the deposition method, with the lowest value used for simulations, as this is the hardest

Table 6.3: Values used within the Washburn equation to simulate flow velocity halfway along the fluidic channel across a range of PDMS contact angles.

Parameter	Value/Range	Source
Interfacial Tension (γ_{LV})	41.1 ± 6.54 mN/m	[213]
Liquid Viscosity (η)	0.98 mPa s	[212]
Location of electrode valve (x)	10.5 mm	Measured
FR4 Contact Angle (θ_{FR4})	$2 \pm 2^\circ$	Measured
PDMS CA (θ_{PDMS})	75 - 100°	Measured
Channel Height (h)	100 – 300 μm	Measured
Channel Width (w)	330 – 480 μm	Measured
PFDT CA (θ_{PFDT})	99.6°	Measured

system to optimise for capillary flow whilst stopping at the valve electrode. These PFDT CA values are lower than values reported in literature on ink-jet printed silver electrodes (138 - 114°) [221, 223] or gold electrodes (125°) [224].

The resulting simulated flow velocities on both FR4 regions and PFDT deposited gate electrodes are shown in Figure 6.12, where the ideal range of PDMS contact angles is highlighted and determined by the region in which the flow velocity is positive on FR4 substrate, but negative on the PFDT coated electrode. For a channel height of 250 μm and 423 μm width, this requires PDMS with a CA between 85.4 - 117.3°.

In contrast, for a reduced channel height of 100 μm and width of 345 μm , shown in Figure 6.13, the ideal range of PDMS contact angles is 83.7 - 129.2°.

These simulations show that larger channel heights have a reduced range of acceptable PDMS contact angles and therefore the target PDMS CA must be above 85.4° to enable flow for all channel heights considered in this work, with targeted upper limit of 90° to encourage faster flow and aim for consistent flow rate. According to Figure 6.8, this equates to an approximate UV-ozone duration of 8 - 10 minutes. Microfluidic devices were to be fabricated using the parameters obtained using initial measurements and these simulations.

6.3.6 Device Assembly & Clamping

Attachment of the fabricated PDMS channels to the surfaces is typically achieved either using a form of chemical bonding or by using a physical clamping device. Approaches have been shown that are suitable for bonding PDMS to a range of polymers, such as the use of silane chemistry [225] or Norland Optical Adhesive [226] although these are not compatible with PCBs. Approaches designed specifically for PCBs are available [227, 228], but add complexity to the fabrication process due to the need to only bond the PDMS to selective regions of the

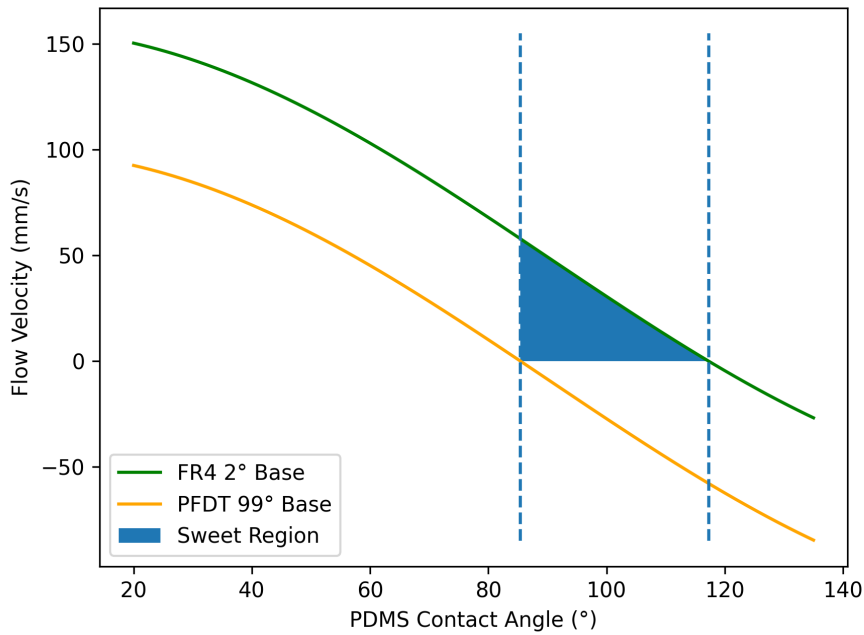


Figure 6.12: Python simulation showing the velocity 12.5 mm along a 250 μm high flow channel, as calculated using the Washburn equation. The velocity in regions of FR4 base material and PFDT coated Cu electrodes are plotted for a range of PDMS CA values. Optimal CA values are calculated to be in the region 85.4 - 117.3°.

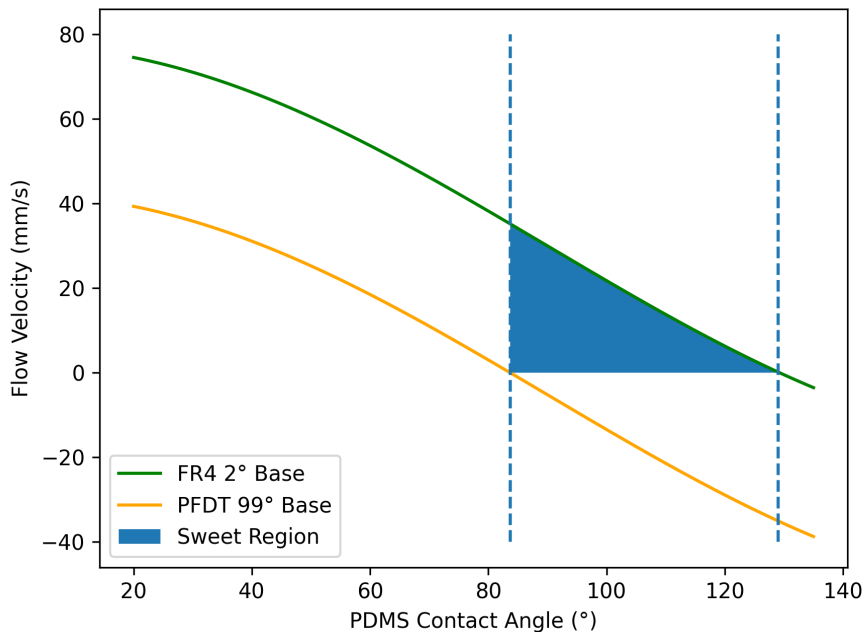


Figure 6.13: Python simulation showing the velocity 12.5 mm along a 100 μm high flow channel using the Washburn equation. The velocity in regions of FR4 base material and PFDT coated Cu electrodes are plotted for a range of PDMS CA values. Optimal CA values are calculated to be in the region 83.7 - 129.2°.

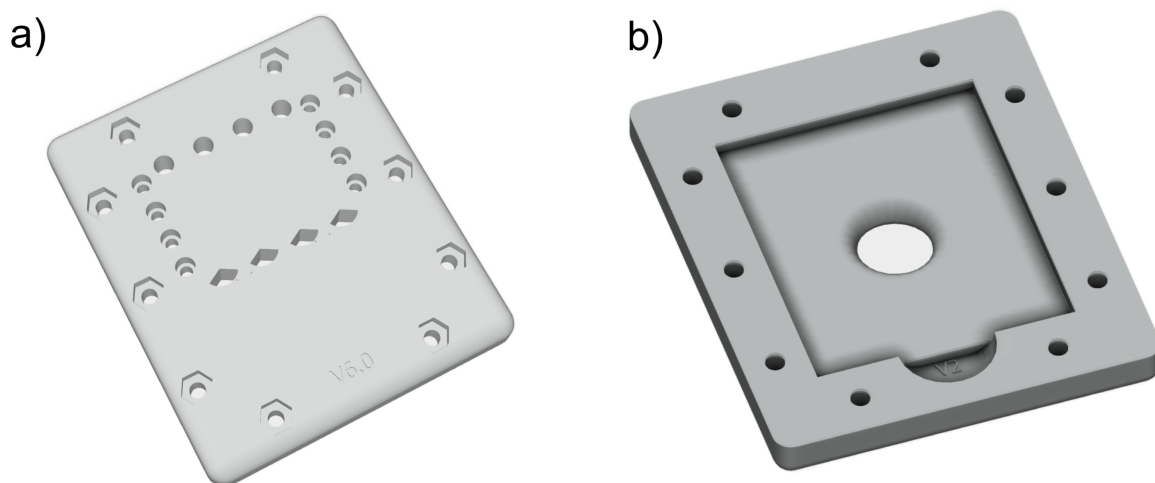


Figure 6.14: Final clamp design used for all testing of flow channels within this work, showing top a) and bottom b) sections, fastened with nuts and bolts to 0.05 N/m.

PCB surface. It was thus decided to physically clamp the PDMS the PCB substrate.

Devices were assembled using a 3D printed clamp, which was designed to apply adjustable but uniform force across the PDMS device, as well as ensuring the flow channels were visible. The clamp also included access to the PDMS fluidic inlet and outlets ports. The design also incorporated ledges for pogo pins to enable electrical contact with the valve electrodes. The PCB clamp was designed in collaboration with an undergraduate student, Alex Pembury, under my supervision.

Initial versions of the device used both a top and bottom plate with a recess for the PDMS and PCB respectively, alongside cut-outs above the channels. Leaking was prominent, believed to be due to a lack of uniform pressure around the cut-out viewing windows. It was thus decided to remove the recess in the top plate to ensure more even clamping force across the PDMS, similar to the design used in [218]. Rather than include an opening for viewing the channels, the viewing area was replaced with a solid section of 3D printed clear resin, that was polished to an optical transparency. The final design of the clamp top section is shown in Figure 6.14a. The base plate shown in Figure 6.14b is clamped using 10 nuts and bolts at the perimeter, tightened to 5.0 mN/m of torque.

6.3.7 FR4 Capillary Flow

To evaluate and confirm capillary flow, a device consisting of a FR4 substrate and PDMS fluidic channels of 300 μm diameter and heights ranging from 100, 150, 200 and 250 μm was assembled using the 3D printed clamp. The FR4 had undergone Ox-plasma treatment for 20 minutes (CA of 0°) as described in section 6.3.1 and PDMS was UV-ozone exposed for 10 minutes (CA of 85°) prior to assembly. 30 μl of solution, here de-ionised (DI) water containing a

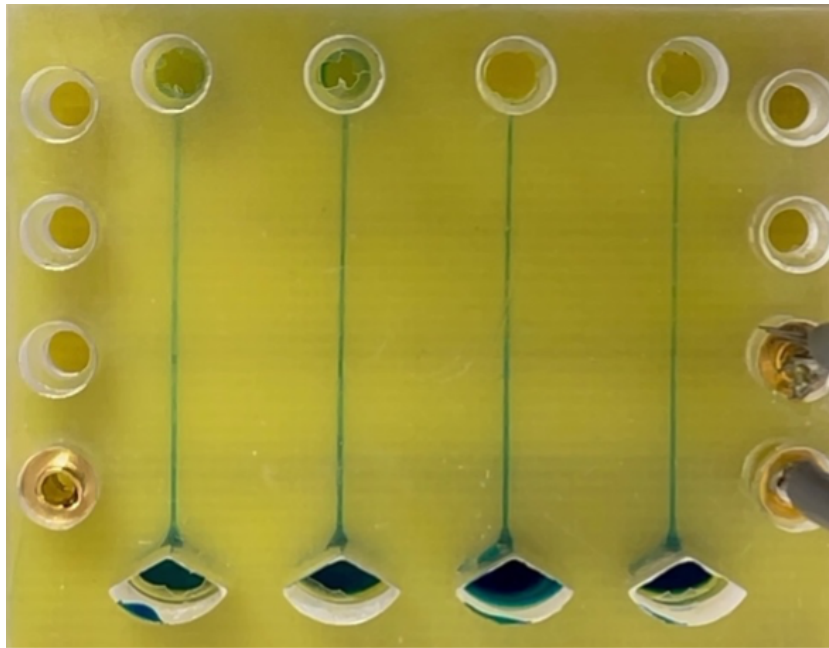


Figure 6.15: PDMS flow channels on FR4 substrate, with channel heights of 150 μm (inner) and 100 μm (outer). Successful capillary flow was observed through the full length of all 4 channels.

dye (Phenol Red) was pipetted into each inlet and the fluid flow imaged using an iPhone 12 Pro (Apple, US). Capillary flow was observed across the full length (21 mm) of all channels. An image taken of 100 μm and 150 μm high flow channels are shown in Figure 6.15.

This confirms capillary flow is possible across FR4 with UV-ozone treated PDMS, across a range of channel heights up to 250 μm using the surface properties deemed suitable using the Washburn equation.

6.3.8 Flow Rate Empirical Analysis

A system consisting of 4, independent channels of 100 μm height, with an average channel width of 345 μm and measured CA of 85° and 0° for the PDMS and FR4 respectively, was fabricated. The flow rates at varying distance along the channel were measured and compared to the theoretical result from the Washburn equation obtained in section 6.3.5.

A video was recorded at 240 frames per second (fps) and split into its individual frames, which are known to be at 4.16 ms intervals. These images were imported into ImageJ and the scale per pixel set to allow the distance of capillary flow to be measured. The capillary flow velocity can then be calculated as a function of distance through the channel, results shown in Figure 6.16.

The measured flow velocity decreases from around 115 mm/s at the fluid inlet to 20 mm/s as the meniscus of the moving fluid column approaches the outlet. This decrease in capillary

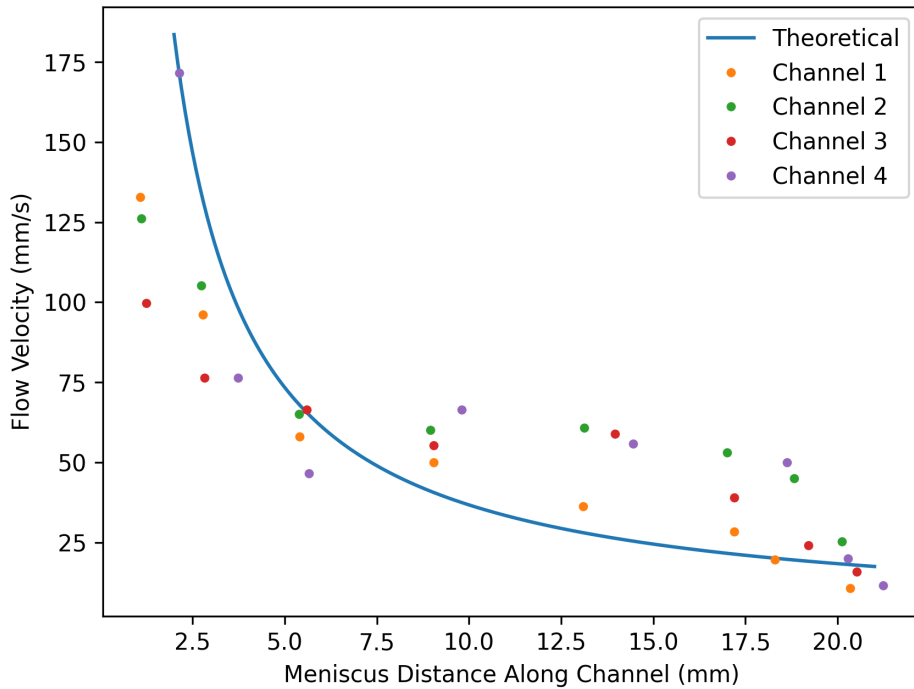


Figure 6.16: Flow velocity as a function of distance of the meniscus along the channel, comparing simulation obtained using the Washburn equation and measurements on 4 flow channels.

flow velocity as a function of distance through a channel agrees with theoretical predictions, although with inconsistencies, particularly after the meniscus moves > 10 mm from the inlet. However, the Washburn equation is a very simplified model of a real capillary flow channel that does not account for all physical phenomena e.g. momentum of the moving column of fluid or surface roughness.

6.3.9 Blank Cu Impeding Flow

Having confirmed capillary flow through a PDMS channel clamped onto a FR4 substrate, I next evaluated capillary flow across a Cu track fabricated on a FR4 PCB substrate. This was to investigate whether capillary flow could be established over a valve electrode after complete removal of the hydrophobic PFDT layer.

Figure 6.17 shows capillary channels of 200 and 250 μm height in PDMS that had undergone a 10 minute UV-ozone treatment. This is mounted on a FR4 PCB that includes 0.4, 0.8, 1.2 and 1.6 mm diameter Cu electrodes that are aligned perpendicular to the flow channels. The FR4 substrate and Cu electrodes were treated with Ox-plasma for 20 minutes prior to clamping to the PDMS channels. The image shows that 1.6 mm Cu electrodes impede capillary flow within these channels, where the same was observed at all channel heights tested in this work.

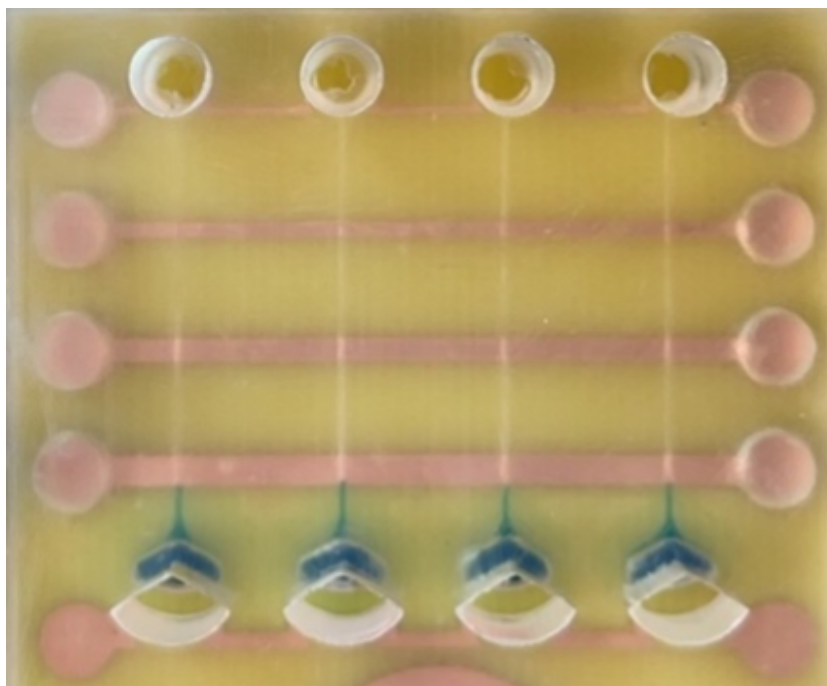


Figure 6.17: Blank unpolished Cu electrodes perpendicular to the flow channels, preventing capillary flow on 250 μm (inner) and 200 μm (outer) height channels.

CA measurements of these Ox-plasma treated unpolished electrodes (performed on large PCB pads shown in Figure 6.18a and 6.18b), reveal a CA of $26.8 \pm 5.2^\circ$ (see Figure 6.18c). This CA has effectively inhibited wetting of the Cu surface and thus impeded capillary flow. Electropolishing of the electrode surface prior to Ox-plasma, using the protocol in section 3.4.4, was thus performed and was found to reduce the electrode CA to $3.4 \pm 2.4^\circ$ (Figure 6.18c).

Capillary flow measurements were subsequently performed using polished Cu electrodes as shown in Figure 6.19, again with 200 and 250 μm high channels. These results show that with electropolishing, the CA of Cu is significantly reduced to permit capillary flow within the UV-ozone modified PDMS. I note, capillary flow was also seen with 100 and 150 μm high channels.

Notably, it was observed that fluid would flow over electrodes < 1 mm in width, which had not been treated by electrochemical polishing. This highlights the high experimental variability in both the device dimensions and contact angle. However, polishing was essential to consistently allow flow by capillary action over electrodes greater than 1 mm in width. This additionally highlights a limitation of the Washburn equation, which does not consider the role electrode width plays on stopping capillary flow.

In conclusion, it has been shown that capillary flow is possible using Ox-plasma and UV-ozone to modify the wettability of the FR4 and PDMS surfaces. Electrochemical polishing is required for Cu valve electrodes of over 1 mm in width.

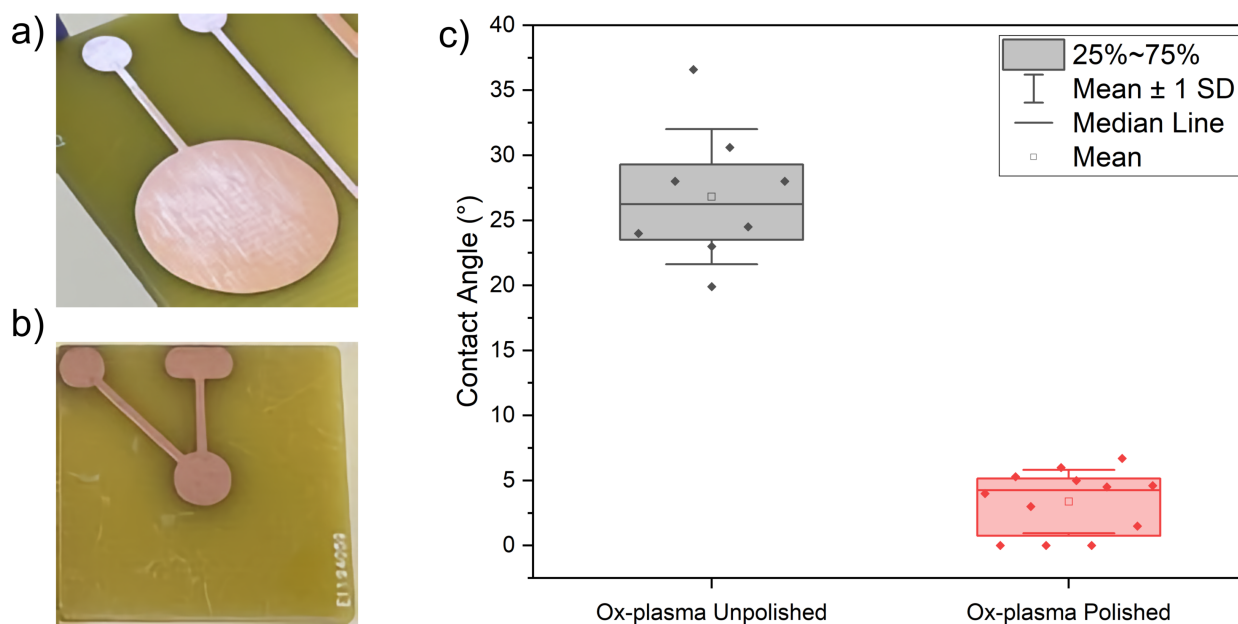


Figure 6.18: a) & b) Cu pads used to perform CA measurements. c) CA measured of unpolished and polished Cu electrodes.

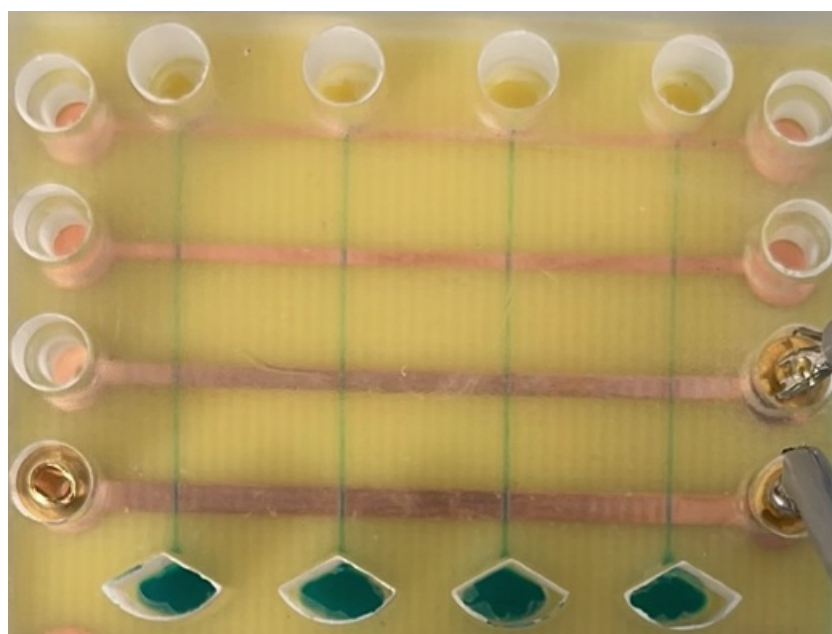


Figure 6.19: Capillary flow occurring over perpendicular polished Cu electrodes due to the reduced CA compared to unpolished electrodes.

6.4 Investigating PFDT Deposition

The next step in the development of electronically actuated electrowetting valves is to introduce a hydrophobic layer capable of stopping capillary flow at the Cu electrode. In the phenomenon electrowetting on dielectric (EWOD), an electric field is applied between an electrolyte and a surface coated in a dielectric layer, where the CA changes under the applied field. This occurs as molecules within the dielectric are polarised by the field, resulting in a redistribution of water molecule dipoles at the dielectric-electrolyte interface and a consequential change in the surface energy.

The Nugen research group [198] exploited an alternative, non-reversible approach to the actuation of electrowetting valves based on CA change induced by removal of surface oxides [212]. Research has since prioritised reducing the bias required to change the surface CA. A promising development towards this goal is the use of thin, hydrophobic monolayers [198, 224] that are attached to an electrode surface via thiol bond, and which can be electrochemically reduced by biasing of the electrode leading to cleavage of the hydrophobic monolayer.

A range of thiolated molecules which can form monolayers and alter surface wettability have been explored, such as alkanethiols e.g. 1-dodecanethiol (1DT) and 4-fluorothiophenol (FTP) [224, 229]. PFDT remains the most established for use within electrowetting valves. I note, PFDT has been shown to assemble on Cu surfaces [230], but not in the context of electrowetting valves.

This work aimed to 1) identify a PFDT deposition protocol suitable for Cu electrodes on PCB, 2) evaluate its effectiveness to prevent capillary flow in a perpendicular channel, and 3) assess subsequent modification of the CA of the PFDT coated electrode through an external bias. Stamping, immersion and dropcasting deposition processes were investigated, and then performed on Ox-plasma treated, polished Cu samples as required for capillary flow once the PFDT layer has been removed.

Cyclic voltammograms (CVs) have been used to investigate the assembly and density of self-assembled monolayers (SAM) [231]. This requires redox active molecules, either directly bound within the SAM or added to the supporting electrolyte [232], or exploiting the redox activity of the electrode material itself [233]. Here, the redox accessibility of the Cu electrode with/without the PFDT deposited layer is used to characterise the integrity of the SAM by monitoring electron transfer at key redox potentials [231].

Initial work sought to identify a suitable potential scan region that would probe the surface, without driving an electrochemical reaction that would lead to an irreversible change to the surface or solution. Cu working electrodes were used with a Pt wire counter and Ag/AgCl reference electrode within pH 7 KPI buffer, which would be used as the electrolyte for all future CV measurements (100 mV/s scan rate). When the applied potential vs. Ag/AgCl reached

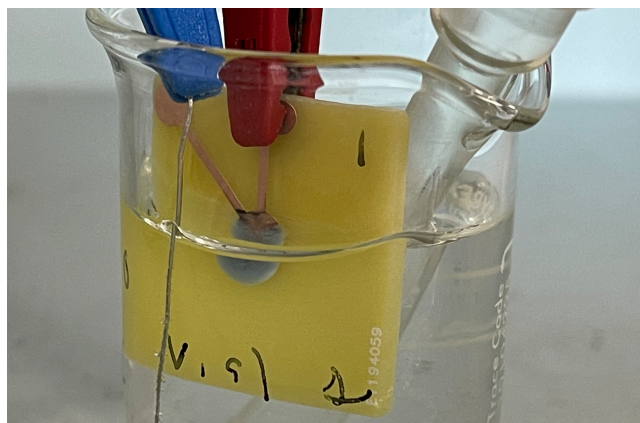


Figure 6.20: Image of white precipitate forming around the working electrode during applied potentials above +1.2 V.

above +1.2 V on blank Cu electrodes, a white precipitate was observed in solution alongside a permanent change to the CVs; this same precipitate was also observed on PFDT coated electrodes under the same conditions. Figure 6.20 shows this precipitate formed around the blank Cu working electrode after 1 cycle.

Formation of white precipitate is believed to be due to the removal of Cu ions from the electrode surface, surrounded by an electrolyte in which they are not soluble. The phenomenon was not investigated further, instead a maximum applied potential below this threshold was set of +0.9 V. At negative potentials beyond -1.1 V, the magnitude of suspected water hydrolysis increases significantly, resulting in an usable potential range of +0.9 V to -1.1 V.

6.4.1 Polished Electrode CV & CA Repeatability

CVs of Cu electrodes following electrochemical polishing and Ox-plasma surface treatment are shown in Figure 6.21. 4 independent samples were measured, each consisting of a 5 mm diameter Cu electrode fabricated on a FR4 substrate, measured to be $2.9 \pm 2.5^\circ$.

The oxidative peak position and magnitude are -0.328 ± 0.013 V and -0.470 ± 0.025 mA respectively, with the non-faradaic background current measured to be 0.051 ± 0.006 mA at 0.4 V. These peak characteristics provides a comparison for the CV properties after cleavage of the PFDT layer. While the CV traces are similar, the small variation in Cu redox peak magnitude is likely caused by inconsistency of the submerged electrode area, from imprecise mounting and small variations in surface roughness, which could be improved by optimising the electropolishing process and controlling submersion of the working electrode using a custom jig. Peak position shifting could be caused by slight contamination or impurities in the test electrolyte, or by changing electrode separation [124].

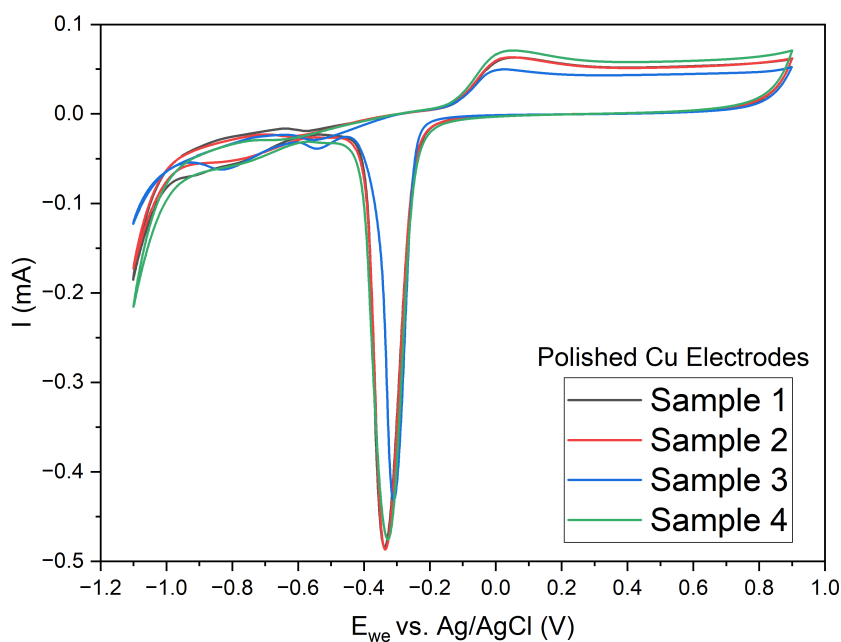


Figure 6.21: CV of 4 separate Cu electrodes after polishing, showing a consistent response.

6.4.2 PFDT Deposition Methods CV & CA

Having established the expected CV for a blank Cu electrode, the hydrophobic PFDT molecule was deposited on the Cu electrode and further CVs obtained. The measured redox activity of the PFDT coated Cu electrode, and the resulting CAs were used to quantify the impact on the surface wettability.

Deposition was performed via three methods common in the literature; dropcasting [223], stamping [224] and submersion [234]. The dropcasting protocol consisted of pipetting a solution of 1 μL PFDT in 50 μL of ethanol (EtOH) (70 mM), onto the electrode surface and allowing the solution to evaporate for 5 minutes. Electrode functionalisation via submersion was achieved by immersing the Cu electrode in a 100 mM PFDT in EtOH solution for 2 hours. Finally, stamping was performed by first drying a 70 mM solution of PFDT, with EtOH as the solvent, onto a section of PDMS for 10 minutes. This was subsequently pressed against the electrode surface for 2 minutes to transfer the PFDT. A final rinse in EtOH and DI water was applied to all deposition methods.

Figure 6.22 show CVs of Cu electrodes before and after deposition of the PFDT layer via stamping a), dropcasting b) and submersion c), with two repeats shown for each. Mean oxidative peak heights are reported per deposition method as $-258 \pm 9 \mu\text{A}$ (stamping), $-223 \pm 24 \mu\text{A}$ (dropcast) and $-222 \pm 9 \mu\text{A}$ (submersion), showing changing redox accessibility to the Cu electrode across the deposition methods, although with relative consistency between each type of deposition method. Non faradaic currents at 0.4 V were measured to be $27 \pm 6 \mu\text{A}$, $20 \pm 8 \mu\text{A}$ and $8 \pm 1 \mu\text{A}$, indicative of a change in capacitance of the PFDT layer.

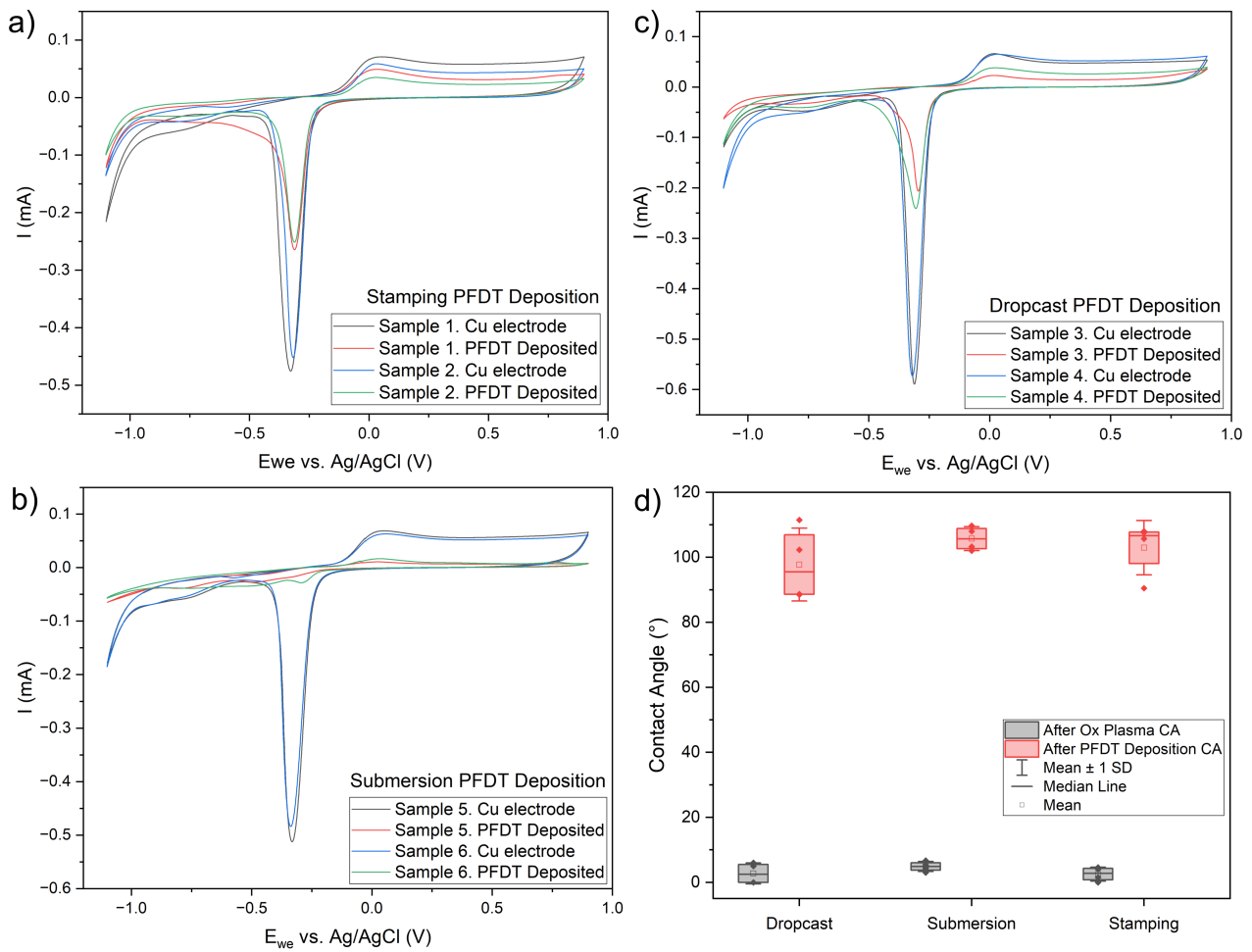


Figure 6.22: CV before and after deposition of the PFDT layer via stamping a), dropcasting b) and submersion c), with two repeats shown for each. d) CA before and after deposition of PFDT using 3 methods ($n = 4$ for each).

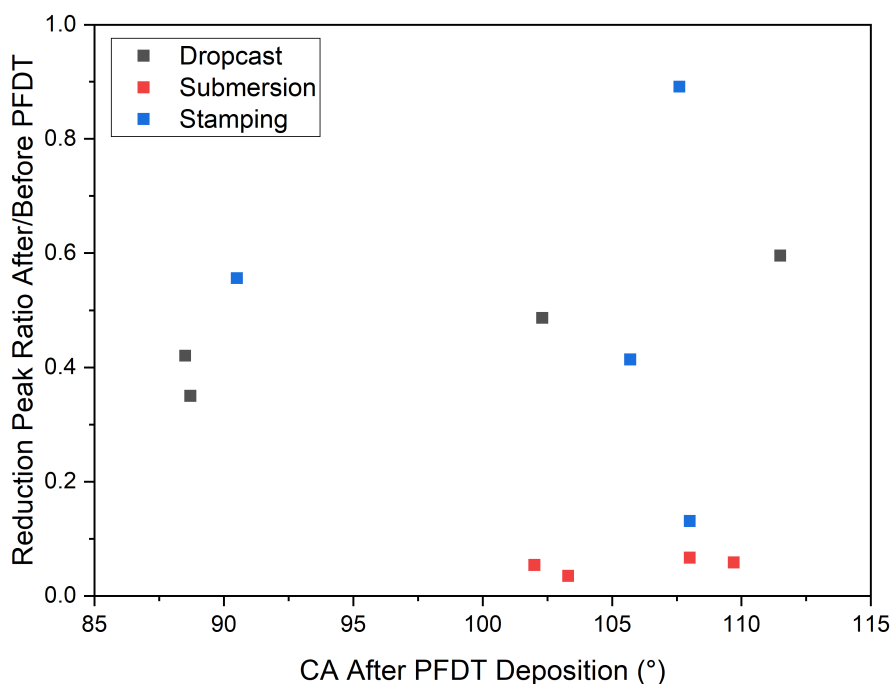


Figure 6.23: Ratio of Cu reduction peak after PFDT deposition vs. before deposition, across the three deposition methods.

Figure 6.22d shows the CA of the Cu electrodes before and after PFDT deposition for each method ($n=4$ for each deposition method). The CA of PFDT deposited via dropcasting was 97.8° , by submersion 105.8° and by stamping 103.0° . The highest consistency was observed for samples functionalised via submersion, with a SD of 3.7° compared to 11.2 and 8.4° for dropcast and stamping deposition methods respectively.

The CV traces (Figure 6.22a-c) were further analysed for any relationship between the redox accessibility of the Cu electrode and the CA of the PFDT layer. Figure 6.23 plots the CA against the ratio of peak height after and before deposition. No clear trends are seen across the deposition methods. Although, the ratio for submersion deposition is shown to be repeatable compared to the other deposition methods, which could be related to the increased CA consistency as presented in Figure 6.22d. A relationship was expected between the reduction in Cu redox peak magnitude, caused by PFDT deposition, and the CA of the PFDT layer. It is believed, improved consistency of electrode area submerged in the electrolyte, more consistent surface roughness and increased CA averaging across each single Cu sample would reveal this trend.

6.4.3 Sonication After PFDT Deposition

Sonication of the PCB sensors in EtOH for 10 minutes followed by a rinse in DI water was explored as a method to improve repeatability of the CA of the PFDT films.

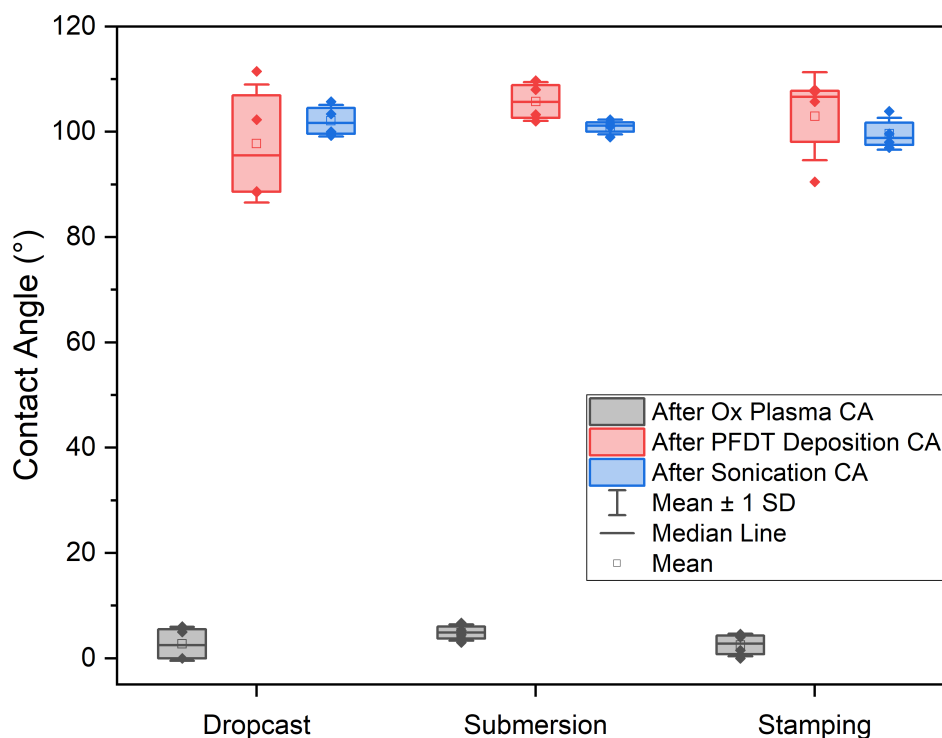


Figure 6.24: CA of Ox-plasma treated electrodes after PFDT deposition and after sonication across 3 methods (n = 4 for each).

The resulting impact on the CA for each method of PFDT deposition (n=4) is shown in Figure 6.24. The spread of CAs after sonication are reduced across all deposition methods, albeit with a moderate reduction on average in the CA; submersion $100.9 \pm 1.4^\circ$, dropcast $102.1 \pm 3.0^\circ$ and stamping $99.6 \pm 3.0^\circ$. It is believed sonication removes excess molecules that are non-specifically bound, perhaps part of a multilayer system.

Despite the moderate reduction in CA, the improved repeatability following sonication was deemed beneficial for investigating cleavage of the PFDT and was thus included as part of the standard protocol moving forward.

6.4.4 FR4 Contact Angle

Data suggests that deposition of PFDT on the Cu electrodes also impacts the CA of the FR4 substrate, as shown in Figure 6.25. An increase in CA was observed on the FR4 substrate after PFDT deposition for all deposition methods, that does not return to the previous state after sonication. Given the requirement for a low CA on the FR4 to support capillary flow, this was explored further.

Both submersion and dropcasting result in a significant increase in CA on the FR4 $105.8 \pm 3.7^\circ$ and $97.8 \pm 11.2^\circ$ respectively. This is believed to be non-specific adsorption of the PFDT molecule that occurs as the deposition solution contacts the FR4; perhaps to exposed surface

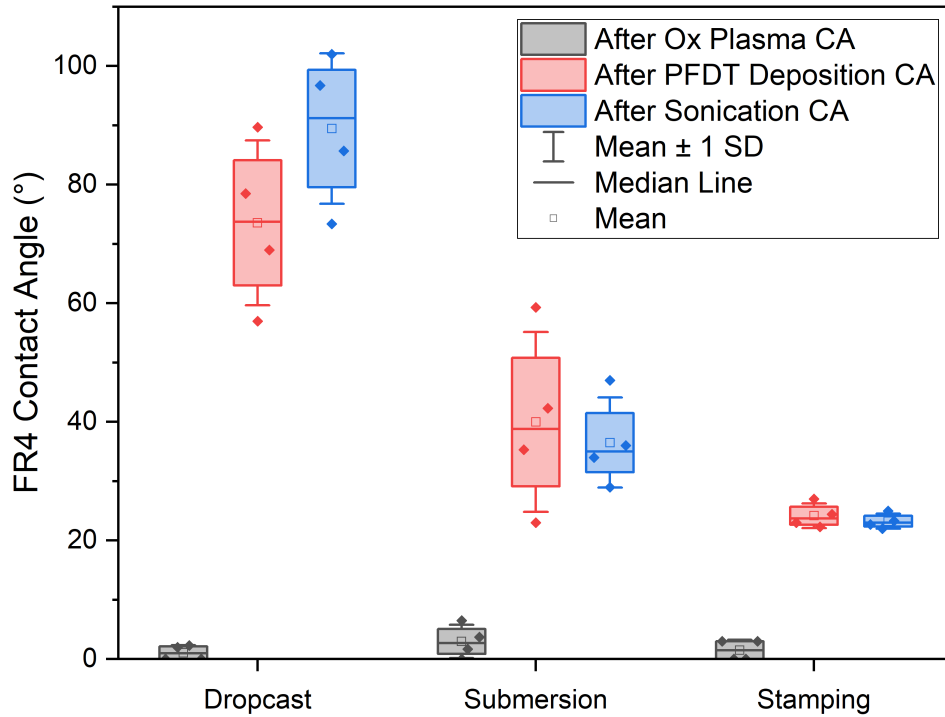


Figure 6.25: Unintended impact of PFDT deposition method on the FR4 contact angle, including impact of sonication as performed on the whole PCB electrode (n = 4 for each).

epoxide groups. The higher CA from dropcasting is suspected to be due to the higher local concentration as a result of EtOH evaporation.

In contrast, stamping minimises contact between the FR4 and the PFDT dried onto the PDMS stamp leading to only a moderate increase in CA from $1.5 \pm 1.7^\circ$, to $23.3 \pm 1.3^\circ$. Any increase is surprising given the stamp is designed to contact the Cu electrode only, localising PFDT deposition to the electrodes. It is believed this increase in CA arises from exposure of the FR4 substrate to EtOH and DI water during the various rinsing steps. This is confirmed by experiments, shown in Figure 6.26, in which the CA of FR4 was measured following multiple EtOH and DI water washes, without any PFDT.

Additional plasma treatment through a shadow mask could be used to selectively return the FR4 CA to near 0° , however based on subsequent experiments in section 6.4.5, capillary flow successfully occurred under the conditions with a DI rinse after deposition step.

In conclusion, deposition of PFDT by submersion leads to deposition across the entire PCB surface, including the FR4 and secondary electrode required for activation of the electrowetting valves. Dropcast deposition also suffers from similar problems due to the inability to constrain the PFDT solution to the electrode due to the high hydrophilicity of the FR4 surface following oxygen plasma treatment. For this reason a protocol consisting of deposition via stamping and subsequent sonication in EtOH with DI rinse was selected.

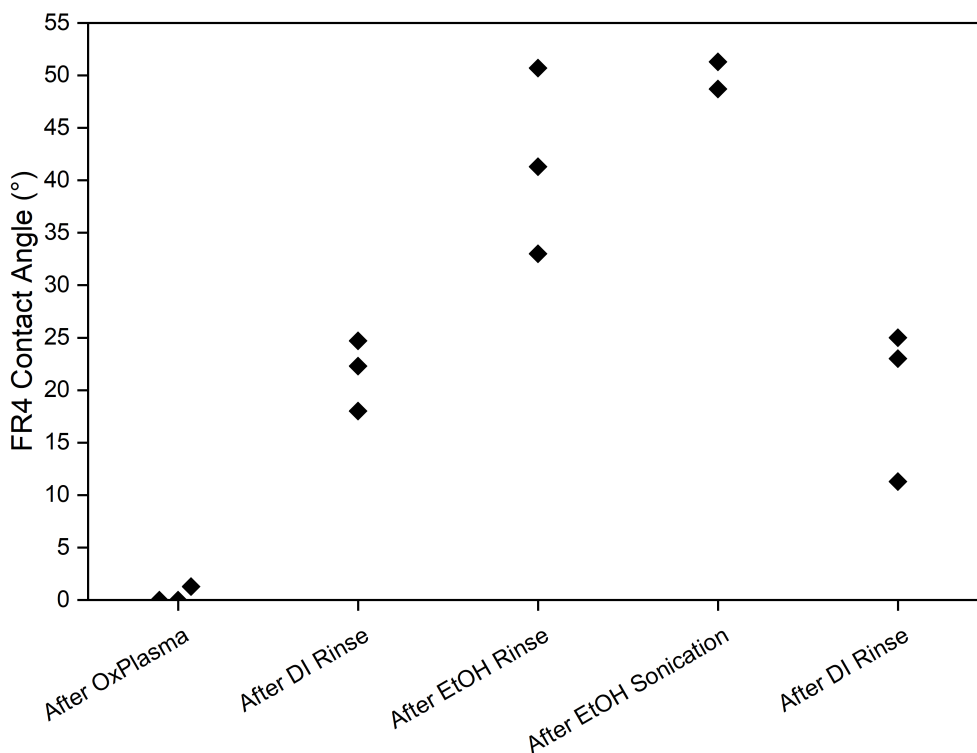


Figure 6.26: Control measurements to decouple impact of PFDT exposure on FR4 CA change, showing impact of treatment and wash steps. Steps are performed in sequence on 3 samples.

6.4.5 Stopping Capillary Flow Using PFDT electrodes

Figure 6.27 shows four PDMS channels (300 μm in width and height) that are intersected by Cu electrodes. E2 in the two fluidic channels on the right of the image have been functionalised with PFDT via the stamping method, while those on the left remain bare Cu. The image was captured 70 seconds after injection of liquid into the flow channel inlet. This image clearly shows capillary flow can occur over the unfunctionalised, Cu electrodes while the PFDT coated electrodes prevent fluid flow.

6.5 PFDT Electrochemical Cleaving

Literature suggests it is possible to cleave (electrochemically desorb) a thiolated SAM by applying specific potentials to the electrode which target the thiol bond. For thiol-gold bonds this is widely accepted to be at -0.9 V relative to Ag/AgCl reference electrodes [235, 236], although this value is dependent on the electrolyte. For Cu-thiol bonds, values between -1 and 1.3 V are reported as the potential at which desorption dominates over reduction of Cu oxides [237, 238].

In contrast, literature associated with PFDT as the thiolated SAM have reported modification of the hydrophobicity of the SAM using positive voltages ranging between $+4.5\text{ V}$ [234]

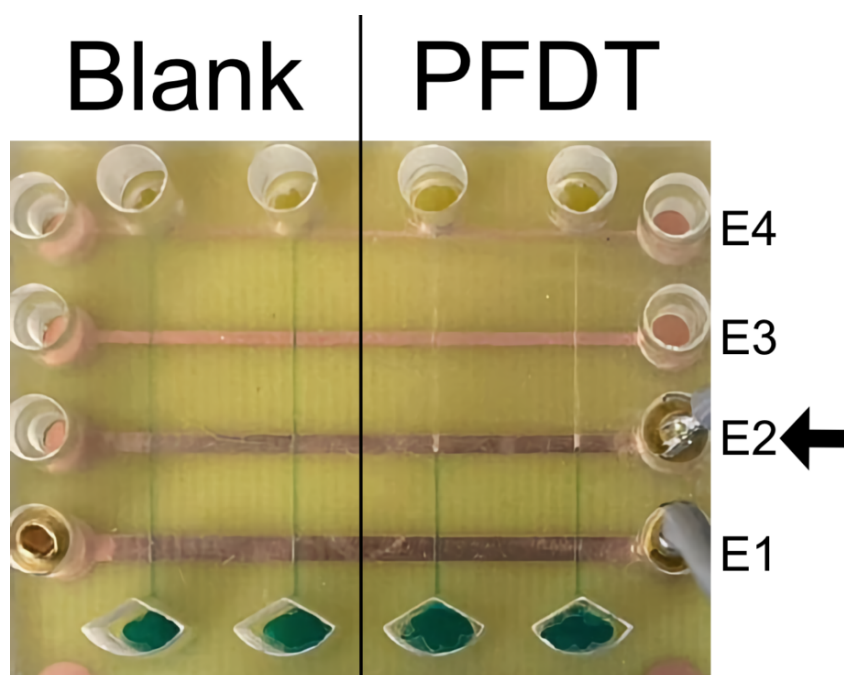


Figure 6.27: (Left two channels) Flow cell showing capillary flow along the full length of the channel when E2 is blank. (Right two channels) Halting of capillary flow at electrode 2 (E2) with PFDT functionalised.

and +2 V [198, 221]. These studies also report a relationship between the change in CA and the applied potential, duration of application, and electrode separation, where a faster and more consistent response time can be traded for reduced potential.

Initial measurements are performed on electrode pads submerged in bulk solution of 50 mM potassium phosphate (KPI) pH 7 to enable measurement of CA changes not possible directly in the flow cells.

6.5.1 PFDT Thiol Desorption at -1.3 V

Electrochemical cleaving at a potential of -1.3 V was attempted to specifically target the Cu-thiol bond between the electrode and PFDT, however no change in hydrophobicity was observed, with the CA remaining at $102.0 \pm 1.7^\circ$ ($n=3$). Figure 6.28 shows a representative CV of a PFDT functionalised Cu electrode after electrochemical cleavage at -1.3 V. While there is an increase in the magnitude of the Cu redox peak after application of -1.3 V, the peak current remains well above the level observed on the bare Cu electrode prior to PFDT deposition.

While electrochemical desorption of thiolated SAM has been previously demonstrated, it was not possible here to cleave the PFDT from the Cu electrode. This was not investigated further but I note, multilayer molecular assemblies have been reported on Cu [239] and could be prevent desorption of the surface bound molecules.

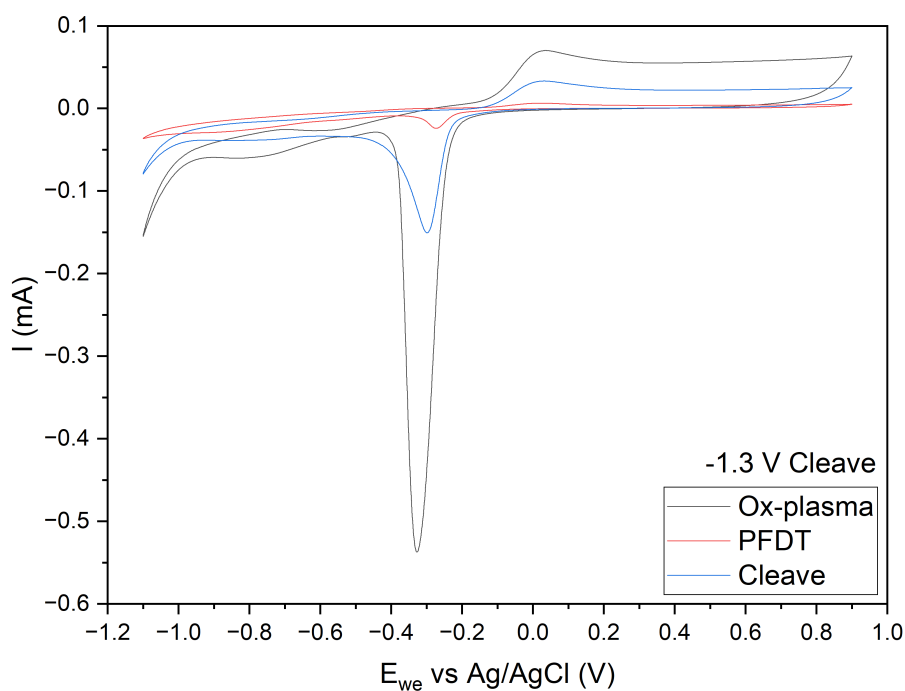


Figure 6.28: CVs measured after application of a -1.3 V potential, attempting to cleave the PFDT layer.

6.5.2 Disruption of PFDT Layers Using Positive Potentials

Informed by previous research, I investigated disruption of a PFDT layer printed on an electrode using a potential of +2 V [198, 221]. The potential was applied for 6 second between the PFDT coated Cu electrode and a platinum counter with approximately 1 cm of separation. The length of the Pt counter immersed in a 50 mM KPI 7 buffer electrolyte was 4 cm.

CVs of the Cu electrode before stamped deposition of the PFDT layer and after application of the +2 V bias are shown in Figure 6.29. For clarity, CVs are only shown for a single sensor. The Cu reduction peak increases in magnitude after PFDT cleaving, beyond that at the Ox-plasma stage (this was also observed on repeat experiments). Measurements of the CA of the electrode surface also revealed changes, decreasing to $11 \pm 0^\circ$ after cleaving, compared to $100 \pm 1^\circ$ for the PFDT coated electrode. These results suggest successful cleaving of the PFDT layer.

6.5.3 PFDT Disruption in Flow Channels

Given a +2 V constant voltage applied to the PFDT coated electrodes for 6 seconds successfully reduced the CA of the electrode surface, the same protocol was attempted within the capillary flow channels. Electrical connection to the PFDT coated electrowetting valve electrodes and the bare Cu counter electrode was made via pogo pins embedded within the 3D printed clamp.

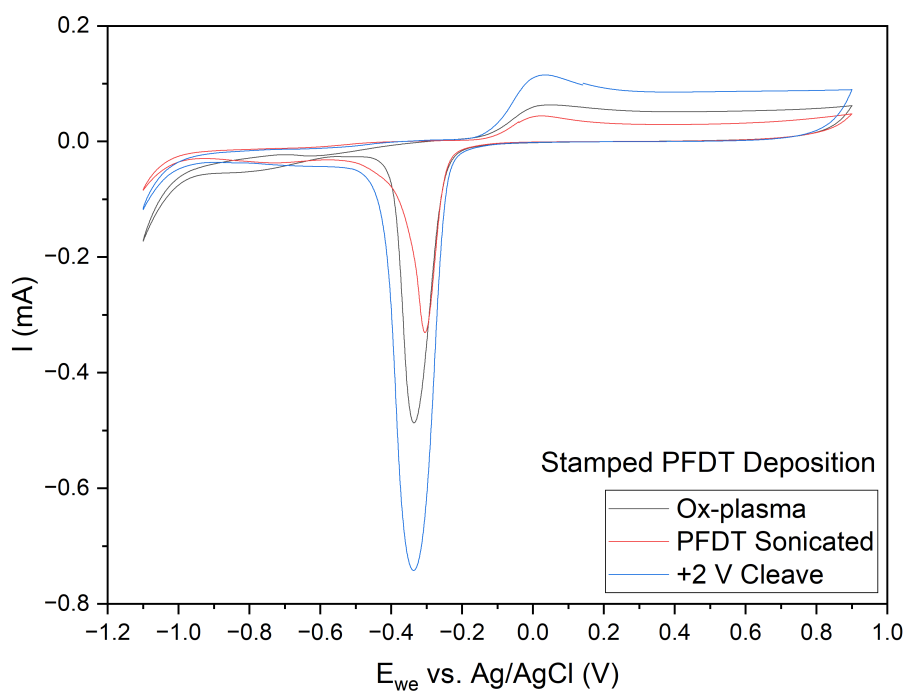


Figure 6.29: CVs measured after application of a +2 V potential, successfully cleaving a PFDT layer in bulk solution.

Capillary flow (of the 50 mM KPI 7 buffer) through the fluidic channels, over the uncoated, Cu auxiliary electrode and halting of capillary flow at PFDT coated electrode were implemented as discussed previously. However, fluid flow did not resume after application of a +2 V potential difference between the PFDT coated electrode and Cu counter electrode.

6.5.4 Conclusion

The widespread deployment of novel diagnostics requires technologies that are low cost, able to be manufactured at scale and simple to use. Lab-on-PCB devices aim to achieve this by integrating and automating multiple stages of an analytical technology (including sample handling and sensing stages) on a single, low-cost substrate. This chapter presented preliminary investigations into the creation of passive and active fluidic components on PCB.

Capillary flow within PDMS channels mounted on a FR4 substrate has been demonstrated, along with the ability to arrest flow via deposition of PFDT on an electrode via a stamping method. While modifying the hydrophobicity of a PFDT electrode following application of +2 V bias was demonstrated in an excess of electrolyte, the same conditions did not lead to the resumption of capillary flow within the PDMS channels. Further work focussed on optimising the electrochemical set-up, e.g. electrode spacing within the PDMS capillary flow channels, and on characterising the structure of the PFDT layer may help identify optimal conditions for PFDT cleave within the flow cell.

Chapter 7

Conclusions & Future Work

7.1 Summary

This thesis has described the development, characterisation and optimisation of a discrete extended gate ion-sensitive field effect transistor (dEGFET), based on printed circuit board (PCB) electrodes, modified with an electrodeposited iridium oxide (IrOx) pH sensitive layer. The pH sensor has been applied towards detection of an enzyme catalysed reaction, here the hydrolysis of a β -lactam antibiotic by a β -lactamase enzyme, where in low molarity buffer environments a bulk pH change occurs. Additionally, initial research into the development of electronically controllable electrowetting valves on the PCB substrate was presented, working towards a complete low-cost lab-on-PCB biosensor for enzyme catalysed reactions.

Diagnostic technologies will play a critical role in resolving a range of current and future healthcare issues. For many of these challenges, the greatest impact will require implementation of the diagnostic technology at the point of care (PoC), without sacrificing performance. Moreover, for truly widespread deployment, technologies should be low-cost and suitable for mass manufacture, even in resource limited settings. The implementation of pH sensitive ion-sensitive field effect transistor (ISFET) sensors, using discrete transistors coupled with PCB substrates, such as those used widely in the consumer electronics industry, has the potential to meet these requirements.

Chapter 4 presented the development of such a dEGFET sensor, in which the extended gate is fabricated on PCB and modified by electrodeposition of IrOx. Critically, this work showed that a facile electrochemical polishing treatment prior to electrodeposition drastically increases median pH sensitivity and significantly enhances reproducibility (from 31.3 ± 14 mV/pH for IrOx on unpolished electrodes to 73.3 mV/pH after electropolishing). A combination of complimentary surface analysis techniques were used to understand the electrochemical, physical and chemical properties, which show the high pH sensitivity and repeatability of the dEGFETs are dependent on both the chemical composition and critically the uniformity

of the IrOx film. The IrOx oxidation state still influences the ultimate pH sensitivity, but this is secondary to the uniformity of the film, as enabled by the removal of surface contaminants and oxides.

Having demonstrated an approach to reliably fabricate a PCB based dEGFET, chapter 5 presented application of the pH sensor for detection and quantification of β -lactamase activity via turnover of β -lactamase antibiotics. The buffering capacity of the assay was set to enable acidification of the local environment at clinically relevant antibiotic concentrations. Despite interference associated with the Cu electrodes, kinetic measurements demonstrated the ability to detect and quantify ampicillin concentration, with a limit of detection (LoD) of 44.61 $\mu\text{g/ml}$. An endpoint form of the assay that eliminates these interferences was also demonstrated showing a LoD of 31.0 $\mu\text{g/ml}$.

Finally, chapter 6 presented research towards the integration of electrowetting valves onto the PCB substrate. Such valves have the potential to enable electronic control of reagents within an automated system, which is suitable for deployment at the PoC. Passive capillary flow through polydimethylsiloxane (PDMS) channels mounted on the PCB substrate was realised using manipulation of surface wettability. Moreover, I demonstrated the ability to inhibit capillary action using a hydrophobic 1H,1H,2H,2H-Perfluorodecanethiol (PFDT) layer, coated onto an electrode surface. Electronic cleavage of this layer on Cu electrodes was shown, but not realised within flow cells.

Below, I present further research required in order to realise full electrowetting valve operation on PCB. I also discuss future work on the β -lactamase assay and the development of an additional enzymatic assay to detect and quantify deoxyribonucleic acid (DNA) amplification that demonstrates the wide applicability of the PCB dEGFET platform.

7.2 Electrowetting Valves Future Work

Greater understanding of the deposited PFDT layer, through chemical and physical analysis methods such as atomic force microscopy (AFM), scanning electron microscopy (SEM) and energy-dispersive X-ray spectroscopy (EDX) would be beneficial for optimisation of the deposition methods and cleaving process. Layer uniformity and thickness are beneficial to quantify, associating trends between deposition protocols, cyclic voltammograms (CVs) and the impact on contact angle (CA).

As mentioned in section 6.4, a white precipitate was formed during CVs of the blank Cu electrodes, when a potential above +1.2 V vs. Ag/AgCl was applied for probing the redox properties of the system. It was also found this precipitate was produced during +2 V constant voltage cleaves longer than 6 seconds, intended to remove the PFDT layer.

Formation of this precipitate may hint at the mechanism for which a +2 V cleave successfully alters the CA, possibly removing Cu molecules from the electrode surface, with PFDT molecules remaining bound as opposed to electrochemical desorption the PFDT molecule specifically via the thiol bond. It is believed, when this occurs in an electrolyte that the Cu is not soluble, the precipitate forms. Future work would investigate these beliefs to confirm the mechanism for disruption of the PFDT layer by positive potentials.

A greater understanding of these two aspects would assist in identifying solutions towards resuming capillary flow within flow channels, after a potential has been applied to a PFDT coated electrode. Steps could be taken to make transport of cleaved PFDT molecules away from the valve electrode more favourable, either by increasing channel dimensions, altering the electrolyte or minimising the PFDT concentration. Parameters of electrode spacing and electrolyte conductivity could also be considered. Additionally, compatibility of the electrowetting valves with clinical samples and reagents should be explored.

7.3 β -lactamase Assay Future Work

Future work could both, better understand and optimise the β -lactamase assay, and begin to translate the assay and related technologies towards real world application.

The assay LoD could be improved through boosting magnitude of the pH change induced by enzymatic hydrolysis of ampicillin, through optimising the buffer capacity and starting pH. Further research to understand the observed kinetic response and the interaction between Cu, enzyme and ampicillin could enable use of kinetic readout to reduce the assay time to result.

Timed delivery of reagents to the surface to increase accuracy of the measurement would further improve the LoD, alongside providing automation essential for PoC applications. For susceptibility testing, it would be necessary to *flip* the assay i.e. use the dEGFET response to quantify the concentration and activity of β -lactamase at a constant concentration of antimicrobial; including testing on clinical samples such as blood or plasma.

7.4 DNA Amplification Assay

Complementary metal-oxide-semiconductor (CMOS) ISFETs have been commercialised through the IonTorrent [66] and DNAe [67] next-generation sequencing (NGS) platforms. While these and related technologies have been developed for a range of applications, their primary use has been indirect detection of DNA amplification through localised change in H⁺ ion concentration [71, 72]. Inspired by this, an interesting avenue for future research would be the use of the PCB dEGFET platform to detect and quantify nucleic acid (NA) sequences of interest.

Below I present preliminary data towards this goal, focussing on the detection of NA sequences specific for *Escherichia coli* (*E. coli*), as an indicator species for faecal contamination of water.

7.4.1 DNA

Figure 7.1 shows the DNA double helix structure; two polynucleotides coiled around one another, storing genetic information encoded as four bases, cytosine [C], guanine [G], adenine [A] and thymine [T]. The backbone between these bases is formed by covalent bonds between the deoxyribose sugar of one nucleotide and the phosphate of another, to create a sugar-phosphate structure. The deoxyribose binds one phosphate group on a 3' carbon, and the other to its 5' carbon. Two polynucleotides form into the double helix structure, with hydrogen bonds between associated bases, also shown in Figure 7.1. C with G and A with T, known as base pairs.

7.4.2 pH Change by Nucleotide Incorporation

Quantitative polymerase chain reaction (qPCR) [241] was invented in 1991 as a technique to amplify and thus detect specific DNA sequences, and has since become the standard for detection of pathogens [242]. Traditionally, real-time monitoring of PCR has relied on the inclusion of fluorescent molecules or dyes, leading to a change in light intensity or colour. This allows quantification of the initial template concentration by monitoring the kinetics of the reaction with a known rate of amplification.

An alternative method of readout can be employed, based on chemical products released at the point of nucleotide incorporation into the DNA backbone by the polymerase [243]. Figure 7.2 shows the mechanism, where nucleophilic attack on the α -phosphate group of a nucleotide from the terminal 3'-hydroxy group of the growing DNA strand, leads to replacement of the proton on this terminal hydroxyl group by the nucleotide base to be incorporated. This liberation of the proton to solution for each new base added to the backbone, alters the solution pH that can be detected using pH sensitive dyes or as proposed here, using a pH sensitive ISFET.

7.4.3 Loop Mediated DNA Amplification (LAMP)

While qPCR remains the gold standard approach to DNA amplification, the amplification reaction requires tightly controlled cycling of the temperature. This complicates the instrumentation required to perform qPCR and potentially precludes its application at PoC or in resource limited settings. Research has thus been directed towards alternative DNA amplification methods with simpler temperature profiles [244].

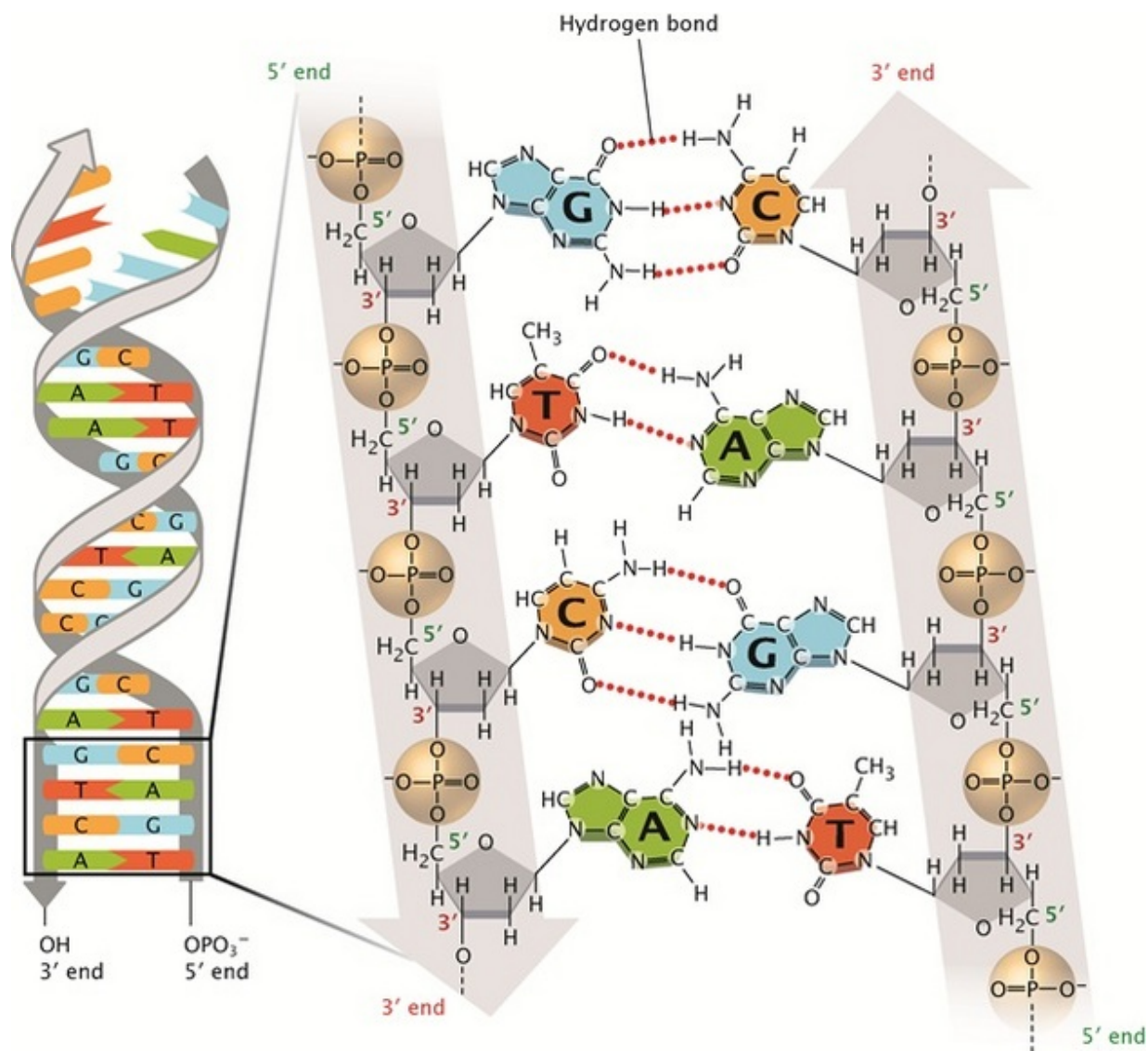


Figure 7.1: DNA molecular structure, with base pairing between nucleotides seen through hydrogen bonds. The sugar-phosphate backbone joins these bases into a polymer, the deoxyribose sugar is seen in grey and the phosphate group in gold [240].

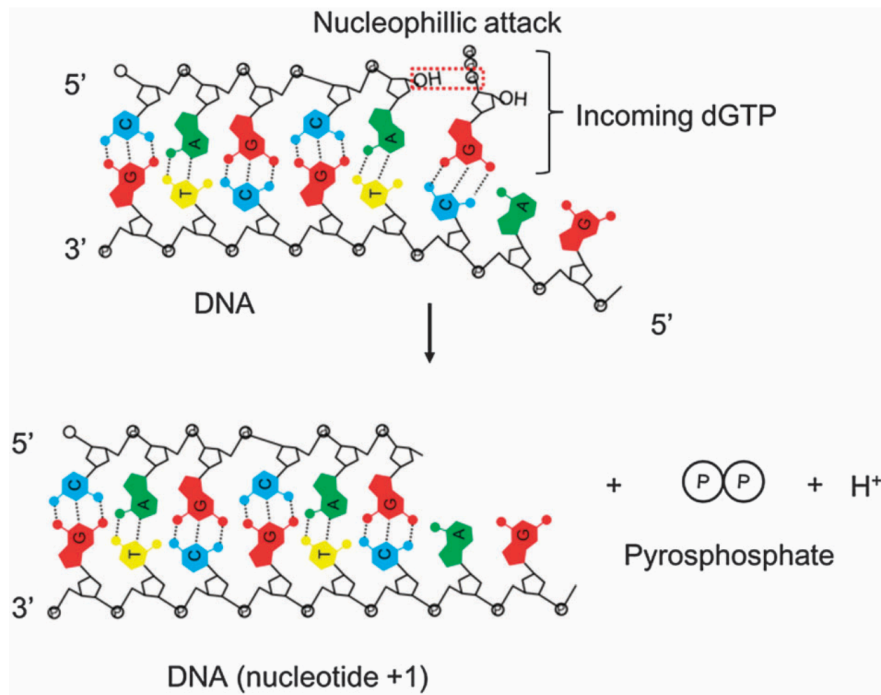


Figure 7.2: Mechanism of H^+ ion production at the point of nucleotide incorporation into the DNA backbone [243].

Loop-mediated isothermal amplification (LAMP) is an example of an isothermal DNA amplification reaction, first published in 2000 by Notomi *et al.* [245]. Figure 7.3a outlines the LAMP components with 4 primers, an outer and inner for each direction, and the target double stranded DNA (dsDNA).

The polymerase used in a LAMP reaction (commonly *Bacillus stearothermophilus* (Bst) polymerase or a modified form with improved characteristics) is able to not only amplify DNA but also displace dsDNA, removing the need for thermal dissociation required by traditional PCR. This allows LAMP to be an isothermal process; the system is maintained at 65 °C where dsDNA is in dynamic equilibrium.

Considering the forward direction in Figure 7.3a, a pair of primers will bind to the top strand of DNA. There is an outer primer named F3 (forward, binding site 3) and a FIP (forward Inner primer) that is made of two component parts, one being a binding site to F2 (forward 2) and another F1c (forward 1 complimentary). A set of primers do the same in the backward direction, hybridising with the bottom target DNA strand.

As shown in Figure 7.3b, the F2 region of the FIP binds with its complementary via strand invasion and the strand displacing polymerase extends the primer and separates the target DNA duplex, leading to step 2. During this time the outer F3 primer will have bound to its complimentary region that was left exposed, and synthesis from upstream target region will subsequently displace the first product, seen displaced in step 3. As it is displaced, the end of the product forms a self-hybridising loop structure due to inclusion of a reverse complimentary

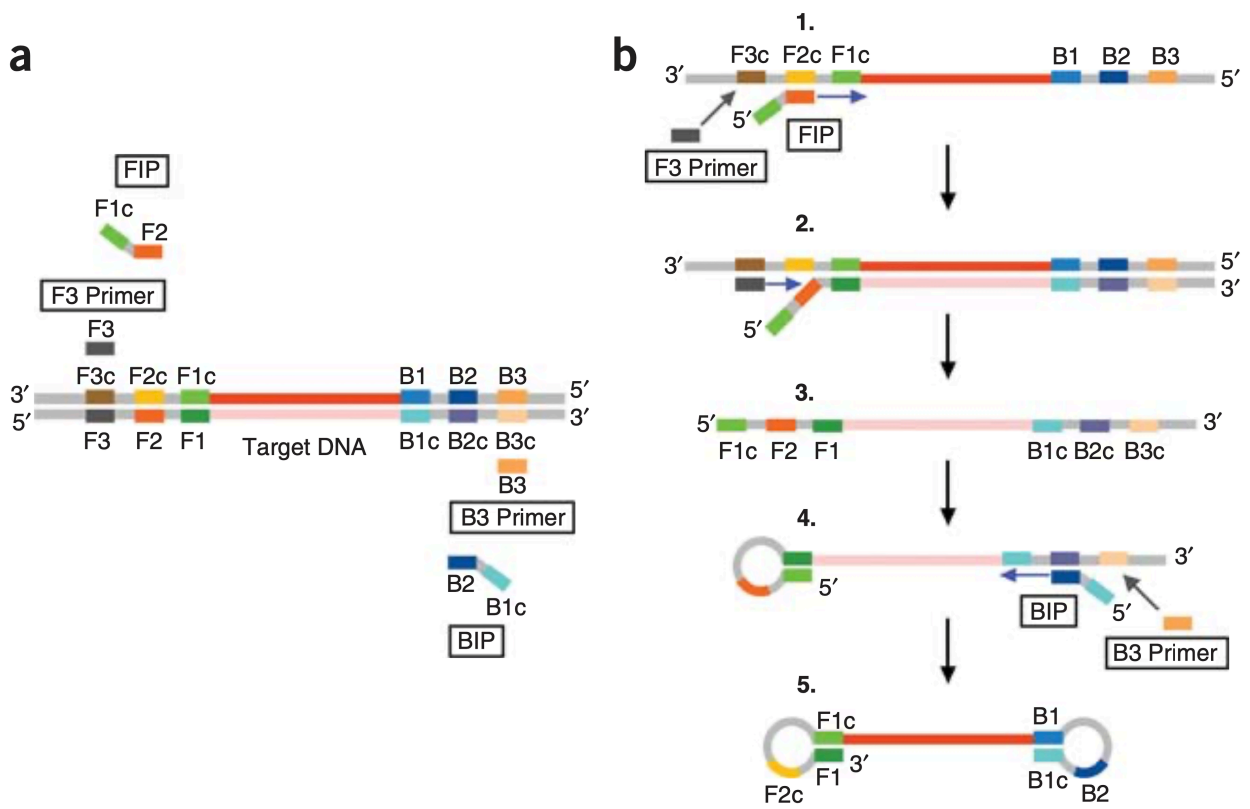


Figure 7.3: a) The target DNA alongside the four primers required for its amplification, FIP, F3, BIP and B3. b) LAMP amplification steps to reach stem-loop structures, further explained in the text [246].

sequence in the FIP.

In step 4, the two backward primers B3 (backward, binding site 3) and BIP (backwards inner primer), result in this annealing and displacement cycle repeating on the opposite end of the target sequence. This stem-loop (or dumbbell) structure, shown in step 5, is the seed which allows for factorial amplification in LAMP. From this stem-loop there are multiple locations from which amplification can be initiated. This can occur from the exposed 3' end or from the location of the inner primer.

It is also possible to use LAMP with 6 primers, where a loop primer is added for each direction [247]. These primers reside in the loops of the stem-loop structures and offer additional sites from which further amplification can be initiated. Initiation from different points allows for a variety of different products, as depicted in Figure 7.4. These concatemers contain multiple copies of the same DNA sequence linked in series. These numerous sites for initiation, that grow with increasing concatemer length, results in the factorial amplification. A greater number of primers theoretically makes LAMP reactions more tolerant to non-specific amplification [245, 248], although the rapid amplification can result in non-specific amplification occurring at a delayed point in the assay, meaning obtaining kinetic data is essential.

Much like other DNA amplification methods, readout of LAMP reactions has been performed by a range of methods, traditionally optically via fluorescence [249] or turbidity [250]. A pH change produced by nucleotide incorporation has also been used as a LAMP detection mechanism via pH sensitive dyes [251, 252, 253]. Here, I propose the pH change will be measured using the PCB dEGFET.

7.5 LAMP Towards *E. coli*

7.5.1 Methods

Work by *Tanner et al.*, linked to New England Biolabs (NEB), was used as the basis of the LAMP assay in this work [251, 253]. Assay components and their concentrations are shown in Table 7.1.

As mentioned *E. coli*, was the target in this work, specifically the *uidA* gene [254] due to its almost universal presence across strains. Primers were used from within literature [249], with the DNA sequences shown in Table 7.2.

Of note for assay operation, is the use of hot-start polymerase which controls enzyme activity below a threshold temperature. Above this temperature the protective aptamer is released [255], allowing for better timing of reaction start points by reducing amplification during assay setup, caused by high primer and Mg^{2+} concentrations.

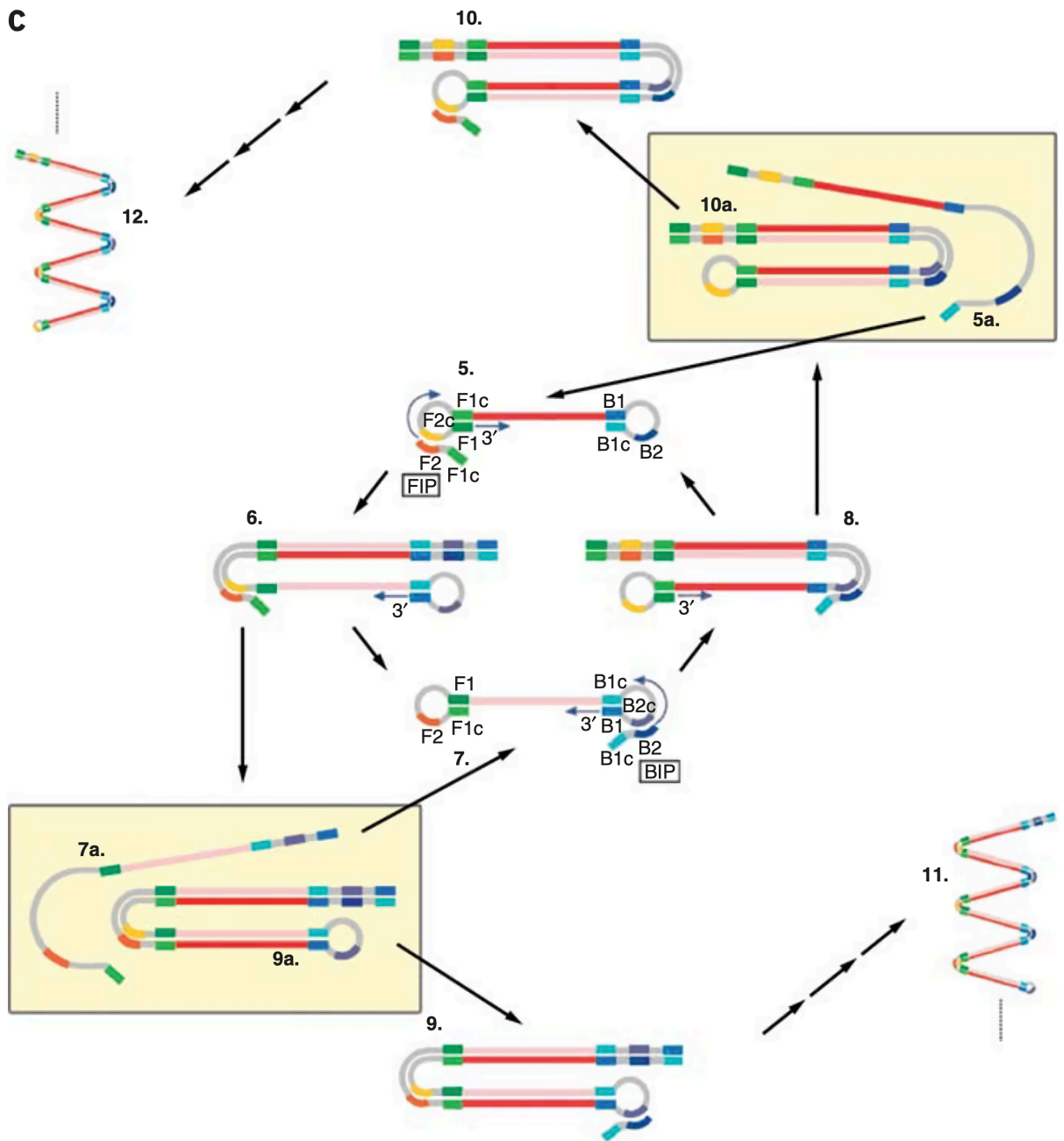


Figure 7.4: LAMP amplification steps beyond the stem-loop structure, producing a range of concatemers [246].

Table 7.1: LAMP assay reagents in a 25 μ l reaction.

Reagent	Stock Concentration	Final Concentration	Volume in 25 μ l	Intermediate Solution
<i>MgSO</i> ₄	100 mM	8 mM	2 μ l	Amplification Mix
(<i>NH</i> ₄) ₂ <i>SO</i> ₄		10 mM	1 μ l	
KCl		50 mM	5 μ l	
dNTP	10 mM	1.4 mM	3.5 μ l	
Phenol Red	50 mM	0.10 mM	1 μ l	
DI Water			7 μ l	
KOH (pH adjustment)				
FIP/BIP	100 μ M	1.6 μ M		Primer Mix
F3/B3	100 μ M	0.2 μ M	2.5 μ l	
FLP/BLP	100 μ M	0.4 μ M		
Template DNA	-	-	2 μ l	
Warmstart Bst 2.0	120 U/ μ l	120 U/ μ l	1 μ l	

Table 7.2: 6 LAMP Primer sequences used in this work [249].

Primer Name	Sequence (5' - 3')
F3	GTGGACGATATCACCGTG
B3	TGGTTAATCAGGAACTGTTGG
FIP	CCGCTAGTGCCTTGTCCAGGGTGATGTCAGCGTTGAA
BIP	GAATCCGCACCTCTGGCAAATCACACTCTGTCTGGCT
LoopF	CCACCTGTTGATCCGCAT
LoopB	TCTCTATGAACTGTGCGTCAC

The *amplification mix* is set to pH 8.8 - 9.0, which after addition of the remaining reagents and sample, places the starting assay pH at approximately 8.2. This aligns with the colour change region of the Phenol Red indicator [253] and a region of high polymerase activity. Only buffer carry over from the stock polymerase storage solution contributes to the overall assay buffering capacity of 26 μM .

Potassium ions in potassium chloride (KCl) act to neutralise the charge present on the DNA backbone, enabling association between the primers and target. Ammonium sulphate helps prevent primers binding to mis-matched regions on the target by destabilising weak hydrogen bonds during these interactions. Mg^{2+} is a key cofactor for polymerase extension and must be present in a higher ratio than deoxynucleotide triphosphates (dNTPs) and oligonucleotides as phosphate groups on these molecules will also bind Mg^{2+} ions. Higher concentrations provide a higher rate of polymerase activity, although fidelity will reduce at excessive concentrations.

Other additives could be considered, such as Betaine to reduce secondary structure formation in GC-rich regions, caused by base stacking and may also assist Bst polymerase in strand displacement [256]. Tween-20 at 0.1% v/v can also be added to stop non-specific binding to the test tube walls; as a non-ionic detergent it is not expected to interfere with DNA binding at these concentrations.

7.5.2 Target

Target DNA would reside within the structure of an *E. coli* cell in a real-world sample, although in the development of this assay it was decided to target extracted DNA. This removes the need to perform cell lysis within the assay and creates a simpler matrix for initial testing. Cell lysis in this situation could be performed using a non-ionic surfactant like Tween-20 or Triton-100, or through heating.

DNA purification was performed by Hannah Walker (Department of Biology, University of York) using a QIAamp UCP Pathogen Mini (Quiagen) from a W3110 *E. coli* culture. Figure 7.5 shows gel electrophoresis of the extracted DNA, compared against a GeneRuler 1 kb ladder. The gel contained 0.5% agarose, with the expected *E. coli* genome length of 24 kbp. A potential difference of 110 V was applied for 5 minutes and a subsequent 70 V for 2 hours.

Figure 7.5 shows a top band of 10,000 base pairs on the DNA ladder. The extracted DNA sits above this band, in agreement with the expected 24 kbp of the *E. coli* genome. A single broad band is present, which may indicate some fragmentation.

Nanodrop was used to quantify the concentration of DNA in the extracted sample, with a resulting value of 170 ng/ml for the extracted sample. The Nanodrop collimates a 2 μl droplet, measuring absorption at 260 nm to quantify the concentration using beer-lamberts law, while removing contamination from proteins by simultaneously probing at 280 nm.

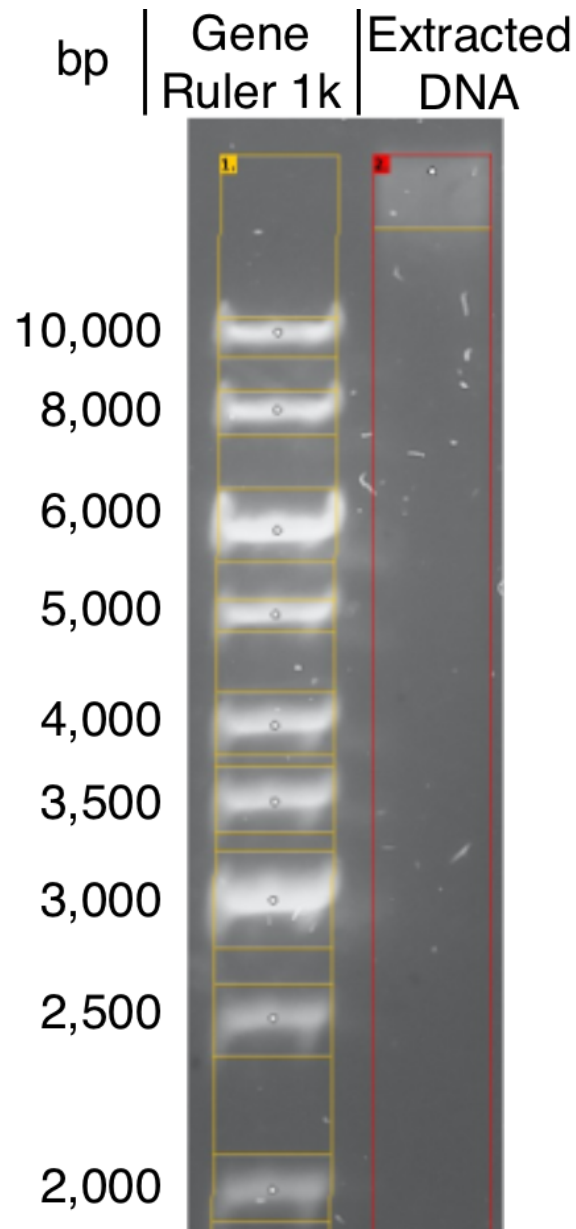


Figure 7.5: Gel electrophoresis performed in house, showing extracted DNA sample alongside 1 kb GeneRuler. Band detection performed using GelAnalyzer V19.1 [257].

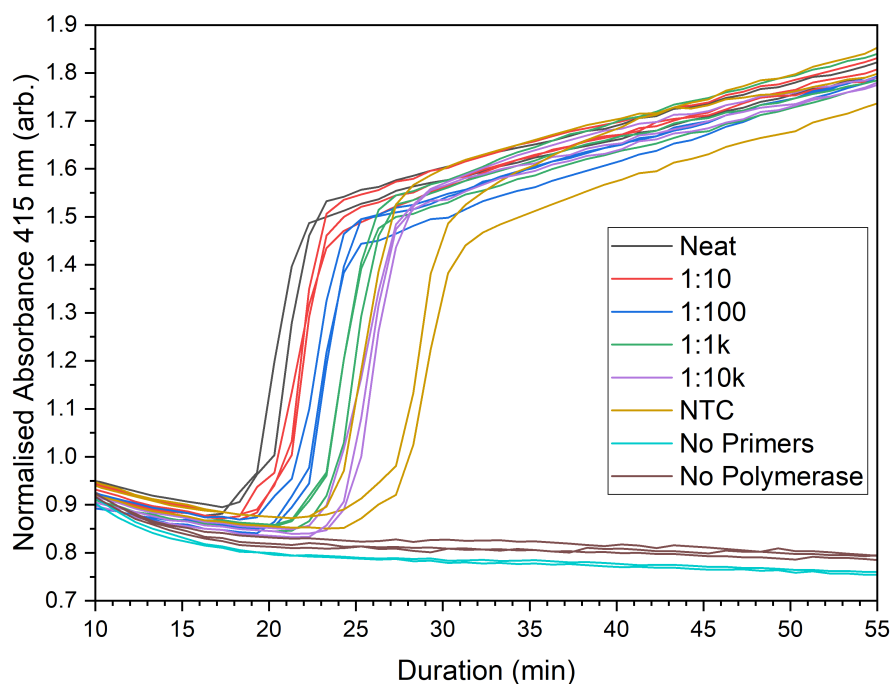


Figure 7.6: Absorbance at 415 nm as measured using a 96 well plate spectrophotometer. Extracted DNA is used as the target, ranging from neat concentration to a 5 fold serial dilution in DI water. No template control (NTC) was measured alongside two further controls with no primers or polymerase present.

7.5.3 Optical Assay Development

Firstly, the assay was developed and characterised using an established system, in this case with a pH sensitive dye, Phenol Red. It shows a colour change from yellow at pH 6.2 to red at pH 8.2, beyond 8.2 it is a bright fusicha colour. The colour can be detected and quantified using a spectrophotometer [258], typically measuring at 560 and/or 415 nm [259] [258] where 560 nm corresponds to the yellow colour as the solution pH becomes acidic, while 415 nm is violet and is absorbed to a greater extent at more basic (red) pH values. Absorbance at 415 nm, normalised against blank amplification mix background, was selected for analysis of this optical assay. At this wavelength, a large change in absorption occurs at the point of amplification.

Figure 7.6 shows raw data obtained on a 96-well plate, with three repeats across a 5 fold serial dilution of template DNA and multiple of controls. Measurements are taken at 1 minute intervals. These results show a clear change in absorbance for all spiked samples, caused by acidification of the local environment by base-pair sugar-phosphate backbone addition during DNA amplification. The colour change occurs between strong red pH \approx 8.2 and yellow (pH \approx 6.2), suggesting a pH change of between 1.5 - 2.5 units.

Control measurements without the primers or polymerase, do not exhibit a change in absorbance, confirming the change seen in template runs is a result of DNA amplification. No

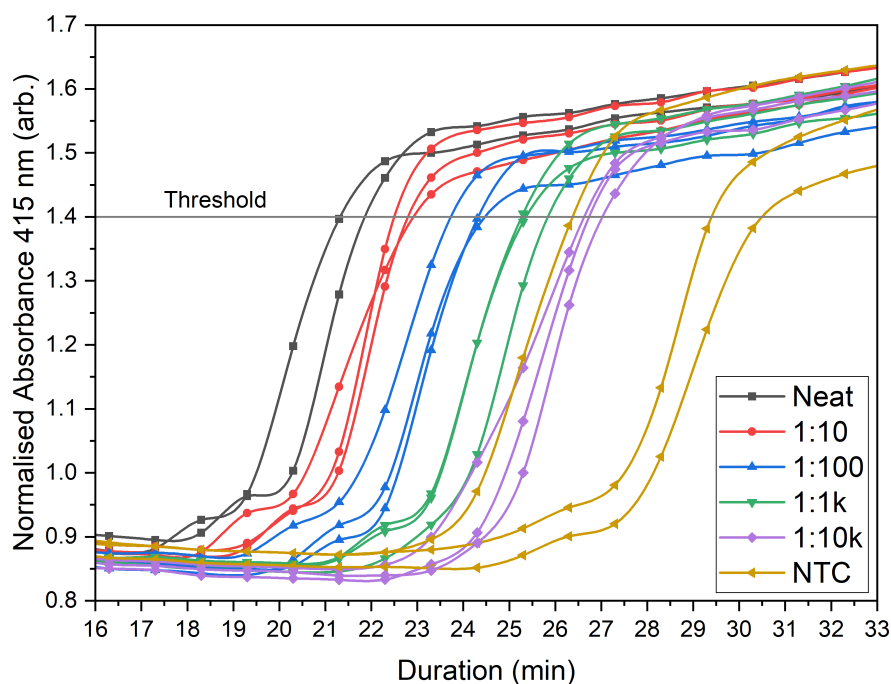


Figure 7.7: Region of greatest absorbance change in the optical LAMP assay, showing the selected threshold for confirmation of DNA amplification.

template control (NTC) measurements do not contain target DNA and therefore are expected to exhibit no amplification. However, due to the rapid amplification rate fundamental to LAMP, non-specific amplification occurs where primers bind to any DNA present in the reaction, irrespective of a mismatched sequence with the designed primers [260]. It is believed the high concentration of polymerase used in the reaction to ensure vivid colour change, further increases the rate of non-specific amplification [261].

Figure 7.7 shows only wells containing all assay components for enhanced visibility of the DNA amplification window. A conventional spline interpolation was applied as calculated using OriginPro. A normalised absorbance threshold was defined at 1.4, for which colour change of the assay was seen to be stabilising, suggesting a significant reduction in the rate of pH change as the assay runs to completion. The cause for this could be a bulk pH shift to a region where the polymerase has become inactive, or alternatively exhaustion of a key reagent.

A calibration curve was produced, relating the defined threshold to the copy number of template DNA and is shown in Figure 7.8. Copy number was calculated based on the 170 ng/ml concentration of template DNA as measured with the Nanodrop. With 2 μ l of DNA spiked into the assay, undiluted stock equates to 0.34 ng of template DNA per reaction. Equation 7.5.1 shows the translation between this weight of target DNA in ng (x) and the number of copies [262]. The weight of the oligonucleotide was approximated using the average mass of 1 bp of single stranded DNA (ssDNA) (bp_{mass}), 330 g/mol, and the length of the *E. coli* genome (n) consisting of approximately 4.64 million ssDNA bases [263]. Avogadro's constant

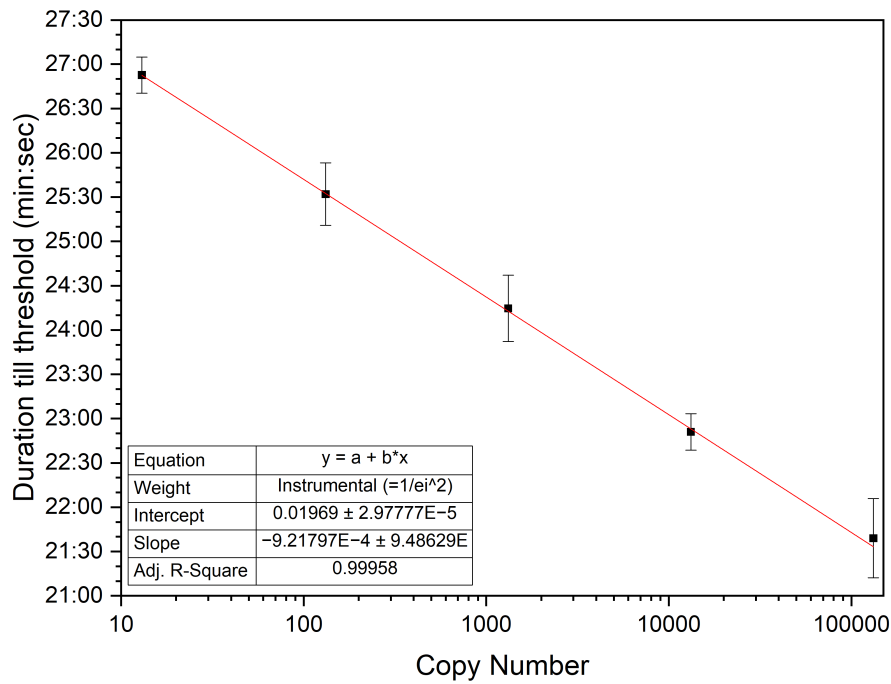


Figure 7.8: Calibration curve relating target DNA copy number to threshold time, showing a strong linear relationship.

(N_A) 6.022×10^{23} is the number of molecules per mole, alongside a conversion factor (c) of 1×10^9 . The result for the neat template DNA stocks used is 133,400 copies.

$$copy\# = \frac{x \times N_A}{bp_{mass} \times n \times c} \quad (7.5.1)$$

In conclusion, optical characterisation of this LAMP assay shows detection of samples spiked with *E. coli* DNA is possible down to a copy number of 13. Non-specific amplification does occur, but at a delayed time point which can be disregarded using the kinetic nature of these measurements. Future work could consider the applicability of additives to reduce the effect of non-specific binding [260] such as Pulluan [264] or tetramethylammonium chloride [265]. Alternative mechanisms to improve non-specific amplification would be to reduce the number of polymerase units (to as low as 0.5 Units (U) as recommended by NEB), to optimise the DNA primer sequence, or temperature [261].

7.6 LAMP on PCB dEGFET

Having demonstrated optical detection of LAMP, the assay was subsequently translated onto the PCB ISFET. Issues were faced when using the system to detect and quantify the target *E. coli* DNA, this section discusses the issues and presents suggestions for future work.

7.6.1 Dri-Ref Electrode & Fluidics

To perform measurements with small sample volumes as required with the LAMP assay, the set-up required a chamber with small sample volume and by extension, a smaller reference electrode interface that remains capable of biasing the transistor gate.

A World Precision Instruments (WPI) Dri-Ref 2SH was used as a reference, as opposed to a traditional double junction Ag/AgCl/Saturated KCl electrode. As well as a smaller footprint, a Vycor frit with 40 Å pore size results in reduced leakage of Ag and Cl ions into the test solution.

The stability and potential of Dri-Ref electrodes were briefly compared to a master Ag/AgCl reference electrode, which has not been subjected to solutions other than its storage in saturated KCl. With both reference electrodes immersed in saturated KCl filling solution, the open circuit potential (OCP) between them is ideally zero. This would show they both are in equilibrium at the same potential, although a small shift in $OCP \pm \approx 5$ mV is accepted for real world devices, as long as this potential remains consistent with no oscillations [266]. Figure 7.9 shows the OCP for three reference electrodes, a second Ag/AgCl/Saturated KCl, a functioning Dri-Ref and a faulty Dri-Ref electrode, compared to the *master* Ag/AgCl/Saturated KCl reference. The Ag/AgCl/Saturated KCl electrode shows a small offset of 0.65 mV, with high stability. Notably, the Dri-Ref electrode shows a stable response and an offset of around 5 mV, showing acceptable real world performance. For comparison, the trace of an unsuitable reference is shown, in this case a faulty Dri-Ref electrode, with oscillation in the OCP.

A fluidic manifold was designed and 3D printed, with a top and bottom component which are clamped together as in Figure 7.10a. The base is printed from a thermally tolerant resin, with a thermal deformation temperature above the 65 °C required to perform this assay. A hotplate was used as a source of thermal energy set at a constant temperature, measurements were performed with a thermocouple to obtain the offset inside the reaction chamber. The top piece was printed in clear resin to monitor the reaction and alignment within the cell. Figure 7.10b shows the top piece inverted, with a 25 µl chamber for the reaction. Visible also are mounts for pogo pins, outer protective o-ring, and a recess for a square gasket at the base of the chamber which creates a seal to prevent liquid leaking out of the chamber.

7.6.2 Kinetic Assay

Initial measurements to detect and quantify target nucleic acids via pH change caused by DNA amplification on the dEGFET devices were performed kinetically, where time-varying data is collected. This continuous data acquisition improves quantification of the assay but can also be beneficial to understand the behaviour of the sensors, which is particularly applicable due the effects seen between the Cu surface and hydrolysed ampicillin in chapter 5.

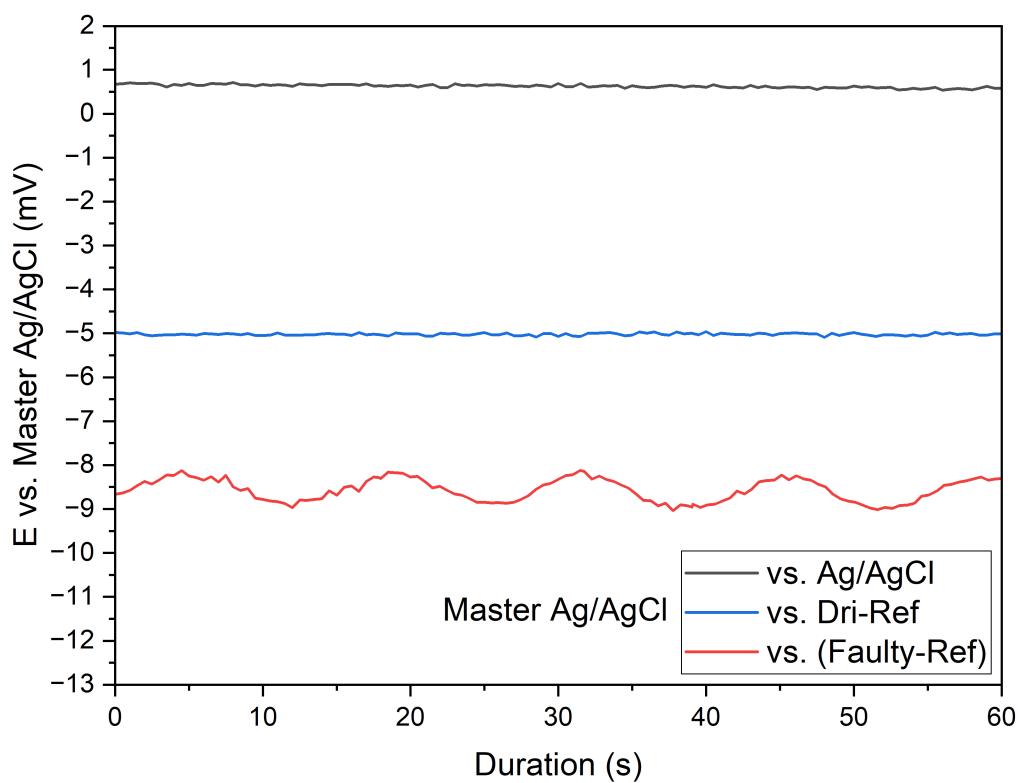


Figure 7.9: OCP stability of double junction Ag/AgCl/Sat. KCl and Dri-Ref reference electrodes to a known *master* double junction Ag/AgCl/Sat. KCl reference.

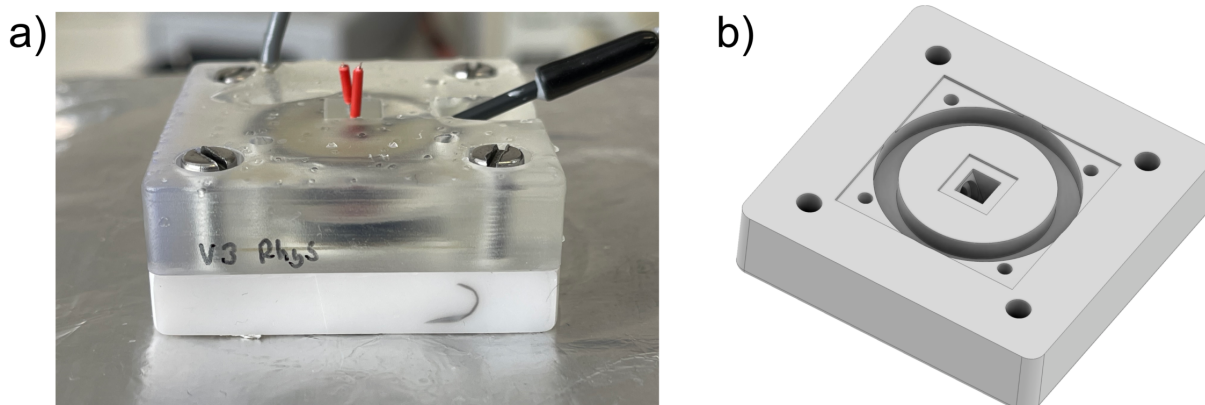


Figure 7.10: a) Assembled fluidic manifold for use with low volume LAMP assay. b) Underside of the top component showing the solution chamber.

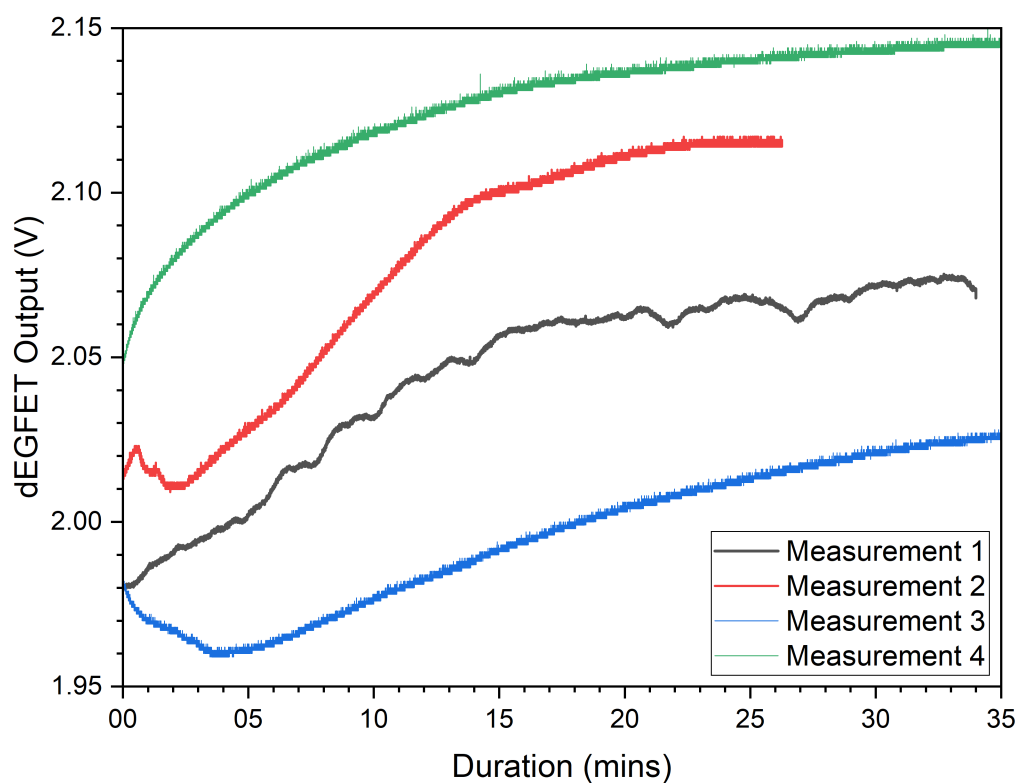


Figure 7.11: Kinetic LAMP assay measurements, showing a range of different responses.

Figure 7.11 shows a range of kinetic responses that were measured when performing the LAMP assay on the dEGFET sensor, all with a template DNA dilution of 1:20. The traces show a lack of consistency with some exhibiting two distinct linear regions with different rates, while others show an exponential or logarithmic response.

There is also inconsistency in control experiments performed using the dEGFET sensor, as shown in Figure 7.12, across a range of control assays. Amplification mix only controls show the expected minimal change in output voltage, however NTC samples exhibit a positive linear drift after an initial decay, although with inconsistent magnitudes. The response of a control (purple) that includes all reagents but without heating shows the same kinetics as the measurements in Figure 7.11, raising concerns this response shape is not caused by DNA amplification.

IrOx coated Cu sensors exposed to the LAMP solutions intermittently show signs of adverse reactions occurring at the surface, such as shown in the images of Figure 7.13. Changes are observed on the area of the Cu pad exposed to solution in the chamber fluidics. Such tarnishing of the electrode surface could clearly impact on the pH sensitivity of the device.

Further work is required to understand the link between measurement kinetics and surface tarnishing on Cu electrodes. This would involve a range of control experiments, alongside exploration into the resulting surface physical and chemical composition using SEM and EDX.

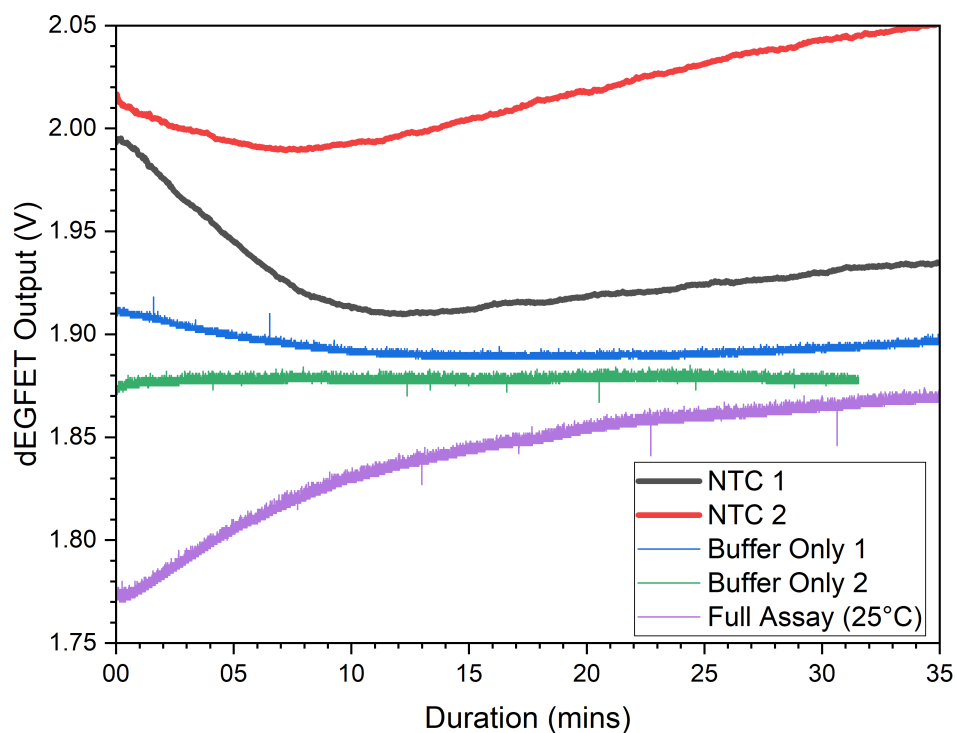


Figure 7.12: Kinetic LAMP control measurements, showing unexpected responses.

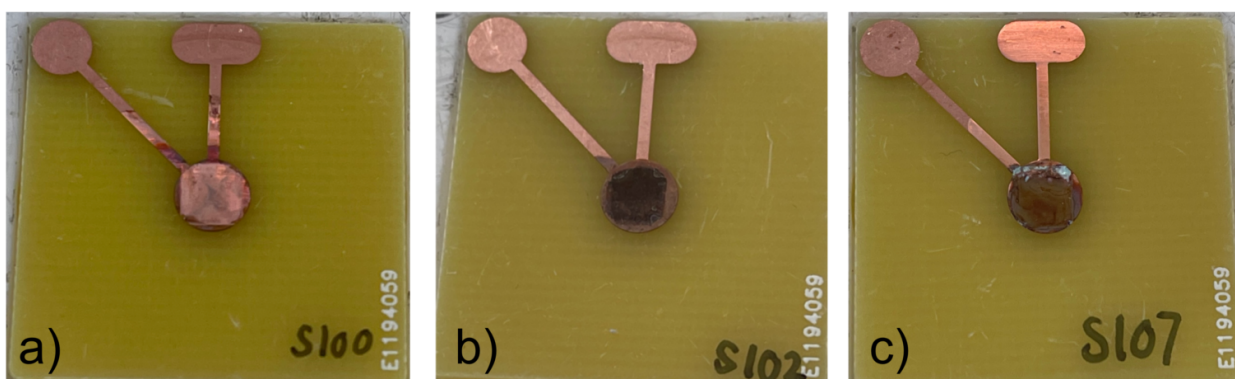


Figure 7.13: PCB electrodes after running LAMP assay, showing surface tarnishing in liquid exposed areas.

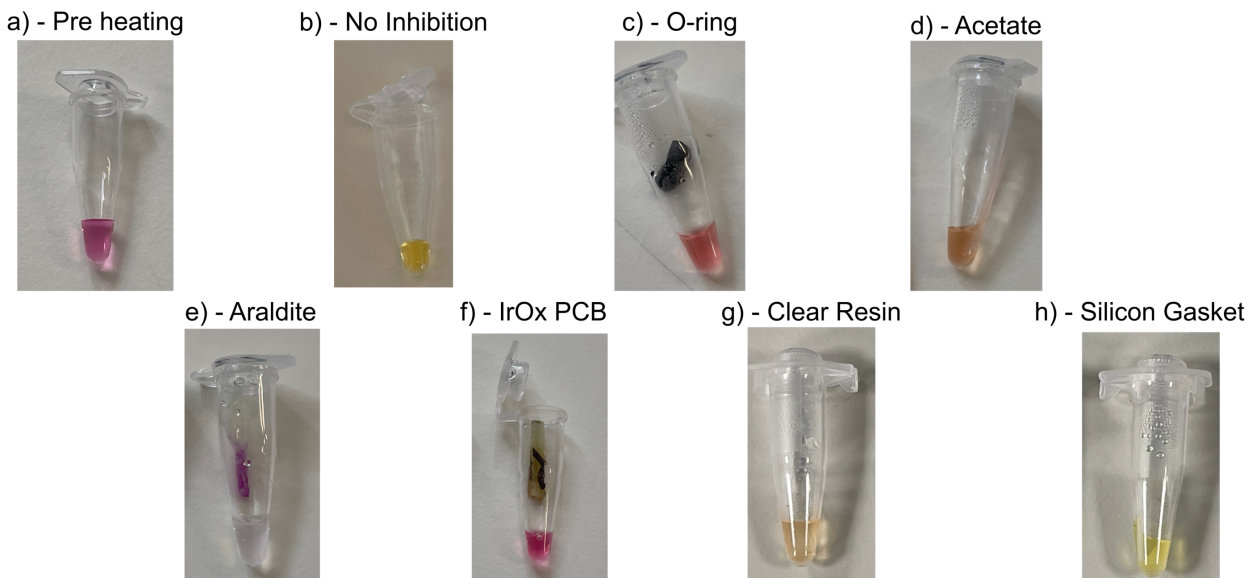


Figure 7.14: Colourmetric LAMP assay performed in a thermocycler prior to assay start a) and after 60 minutes b). c)-g) are the same LAMP assay, including a range of materials that are used in the chamber fluidics or earlier versions of the system.

7.6.2.1 Material Inhibition

The pH sensitive dye was also included in the assay through this development stage to confirm successful DNA amplification. The colour change expected as a result of amplification was not always observed, although at this stage no trends between response shape and assay colour change could be determined.

To understand possible causes for this lack of colour change, the assay was performed in a 200 μ l PCR tube and heated to 65 $^{\circ}$ C using a thermal-cycler, with the tube spiked with materials used in the PCB dEGFET and associated fluidic assembly. It is accepted these measurements are only a proxy to the real assay but do provide a starting point for investigation.

Figure 7.14a shows the initial solution colour at the point of enzyme addition while Figure 7.14b shows the colour change after 60 minutes for an assay in which LAMP-based DNA amplification has occurred successfully. Figure 7.14 c-g show the same LAMP assay after 60 minute incubation, in which a range of contaminant materials used in the assembly of the dEGFET hardware have been added. It is clear that for many of the materials the expected colour change has not occurred, suggesting inhibition of the LAMP assay.

7.6.3 Conclusions

Further experiments are required to understand inhibition of the LAMP assay on the dEGFET measurement system. Literature is widespread when considering inhibitors for PCR. Although

less common for LAMP, many of the same principles are expected to apply due to the similarities between the methods [267, 268].

Inhibitors can be found across numerous categories and operate via a broad range of mechanisms, such as metal ions, enzymes, polymers and acids, of which more detail is provided in literature [268, 269, 270]. Future work would prioritise investigation into fluidic materials [271] and metal ions [272], with alternative materials or inclusion of additional assay reagents considered to mitigate the impact of potential inhibitors to DNA amplification.

Cu ions from the underlying electrode are one potential inhibitor of the LAMP reaction, and there is evidence of Cu^{2+} leaching into solution at a surface-liquid interface [273, 274]. Divalent metal-ion chelators such as EDTA [275] or EGTA which have a high affinity for Cu^{2+} over Mg^{2+} [276], may prevent Cu^{2+} ions aggregating around the DNA, causing conformational changes [273], or favourably binding to the polymerase active region in place of the Mg^{2+} cofactor.

Abbreviations

ADC analog-to-digital converter.

AFM atomic force microscopy.

AIROF anodic iridium oxide films.

AMR antimicrobial resistance.

AST antimicrobial susceptibility tests.

BEOL back-end-of-the-line.

BSA bovine serum albumin.

BSE back scattered electrons.

CA contact angle.

CAD computer-aided design.

CMOS complementary metal-oxide-semiconductor.

CSCc cathodic charge storage capacity.

CV cyclic voltammetry.

CVCC constant-voltage constant-current.

CVD chemical vapor deposition.

dEGFET discrete extended gate ion-sensitive field effect transistor.

DES deep eutectic solvents.

DI de-ionised.

DNA deoxyribonucleic acid.

dNTPs deoxynucleotide triphosphates.

DRI drug resistant infections.

dsDNA double stranded DNA.

ECDL electrochemical double layer.

EDX energy-dispersive X-ray spectroscopy.

EGFET extended gate ion-sensitive field effect transistors.

EIROF electrodeposited iridium oxide films.

ENIG electroless nickel immersion gold.

EWOD electrowetting on dielectric.

FETs field effect transistors.

GOx glucose oxidase.

IC integrated circuits.

IrOx iridium oxide.

ISE ion-selective electrodes.

ISFET ion-sensitive field effect transistor.

ITO indium tin oxide.

IUPAC International Union of Pure and Applied Chemistry.

KCl potassium chloride.

LAMP loop-mediated isothermal amplification.

LFD lateral flow device.

LMICs low- and middle-income countries.

LoC lab-on-chip.

LoD limit of detection.

MEMS micro-electro-mechanical systems.

MOSFET metal-oxide-semiconductor field effect transistor.

NA nucleic acid.

NDM New Delhi metallo-beta-lactamase.

NGS next-generation sequencing.

NIST National Institute of Standards and Technology.

NTC no-template control.

OCP open circuit potential.

Ox-plasma oxygen plasma.

PCB printed circuit board.

PCR polymerase chain reaction.

PDMS polydimethylsiloxane.

PFDT 1H,1H,2H,2H-Perfluorodecanethiol.

PoC point of care.

PZC point of zero charge.

QCM quartz crystal microbalance.

qPCR quantitative polymerase chain reaction.

REFET reference field effect transistor.

RMS root mean squared.

RSD relative standard deviation.

SAM self-assembled monolayers.

SCCM standard cubic centimetres per minute.

SCE saturated calomel electrodes.

SD standard deviation.

SE secondary electrons.

SELEX systematic evolution of ligands by exponential enrichment.

SEM scanning electron microscopy.

SHE standard hydrogen electrodes.

SMD surface-mount devices.

SPR surface plasmon resonance.

ssDNA single stranded DNA.

UV-ozone ultraviolet ozone.

VIM Verona integron-encoded metallo-beta-lactamase.

XPS X-ray photoelectron spectroscopy.

Bibliography

- [1] Edmond J. Safra, “Roadmap To Pandemic Resilience,” Harvard University, 2020, pp. 1–56, [Online]. Available: https://ethics.harvard.edu/files/center-for-ethics/files/roadmaptopandemicresilience_updated_4.20.20_1.pdf (Accessed: 1/6/2023).
- [2] J. O’Neill, “Tackling Drug-Resistant Infections Globally: Final Report and Recommendations,” Review on Antimicrobial Resistance, 2016, pp. 1–81, [Online]. Available: https://amr-review.org/sites/default/files/AMR%20Review%20Paper%20-%20Tackling%20a%20crisis%20for%20the%20health%20and%20wealth%20of%20nations_1.pdf (Accessed: 1/6/2023).
- [3] M. E. A. De Kraker *et al.*, “Will 10 Million People Die a Year due to Antimicrobial Resistance by 2050?” *PLOS Medicine*, vol. 13, no. 11, e1002184, Nov. 29, 2016, ISSN: 1549-1676, DOI: 10.1371/journal.pmed.1002184.
- [4] H. W. Boucher *et al.*, “Bad Bugs, No Drugs: No ESKAPE! An Update from the Infectious Diseases Society of America,” *Clinical Infectious Diseases*, vol. 48, no. 1, pp. 1–12, Jan. 2009, ISSN: 1058-4838, 1537-6591, DOI: 10.1086/595011.
- [5] HM Government, “Tackling antimicrobial resistance 2019–2024 – The UK’s five-year national action plan,” 2019, pp. 1–98, [Online]. Available: https://assets.publishing.service.gov.uk/government/uploads/system/uploads/attachment_data/file/784894/UK_AMR_5_year_national_action_plan.pdf (Accessed: 3/6/2023).
- [6] C. Troeger *et al.*, “Estimates of global, regional, and national morbidity, mortality, and aetiologies of diarrhoeal diseases: A systematic analysis for the Global Burden of Disease Study 2015,” *The Lancet Infectious Diseases*, vol. 17, no. 9, pp. 909–948, Sep. 2017, ISSN: 14733099, DOI: 10.1016/S1473-3099(17)30276-1.
- [7] H. Pennington, “E. coli O157 outbreaks in the United Kingdom: Past, present, and future,” *Infection and Drug Resistance*, p. 211, Aug. 2014, ISSN: 1178-6973, DOI: 10.2147/IDR.S49081.
- [8] T. Saxena *et al.*, “Prevalence of E. coli O157:H7 in water sources: An overview on associated diseases, outbreaks and detection methods,” *Diagnostic Microbiology and*

- Infectious Disease*, vol. 82, no. 3, pp. 249–264, Jul. 2015, ISSN: 07328893, DOI: 10.1016/j.diagmicrobio.2015.03.015.
- [9] R. Bain *et al.*, “Fecal Contamination of Drinking-Water in Low- and Middle-Income Countries: A Systematic Review and Meta-Analysis,” *PLoS Medicine*, vol. 11, no. 5, P. R. Hunter, Ed., e1001644, May 6, 2014, ISSN: 1549-1676, DOI: 10.1371/journal.pmed.1001644.
- [10] B. Srinivasan and S. Tung, “Development and Applications of Portable Biosensors,” *SLAS Technology*, vol. 20, no. 4, pp. 365–389, Aug. 2015, ISSN: 24726303, DOI: 10.1177/2211068215581349.
- [11] M. Kaisti, “Detection principles of biological and chemical FET sensors,” *Biosensors and Bioelectronics*, vol. 98, pp. 437–448, Dec. 2017, ISSN: 09565663, DOI: 10.1016/j.bios.2017.07.010.
- [12] K. Strimbu and J. A. Tavel, “What are biomarkers?” *Current Opinion in HIV and AIDS*, vol. 5, no. 6, pp. 463–466, Nov. 2010, ISSN: 1746-630X, DOI: 10.1097/COH.0b013e32833ed177.
- [13] Z. Farka *et al.*, “Nanoparticle-Based Immunochemical Biosensors and Assays: Recent Advances and Challenges,” *Chemical Reviews*, vol. 117, no. 15, pp. 9973–10 042, Aug. 9, 2017, ISSN: 0009-2665, 1520-6890, DOI: 10.1021/acs.chemrev.7b00037.
- [14] E. Engvall and P. Perlmann, “Enzyme-Linked Immunosorbent Assay, Elisa,” *The Journal of Immunology*, vol. 109, no. 1, pp. 129–135, Jul. 1, 1972, ISSN: 0022-1767, 1550-6606, DOI: 10.4049/jimmunol.109.1.129.
- [15] E. T. S. G. da Silva *et al.*, “Electrochemical Biosensors in Point-of-Care Devices: Recent Advances and Future Trends,” *ChemElectroChem*, vol. 4, no. 4, pp. 778–794, Apr. 2017, ISSN: 21960216, DOI: 10.1002/ce1c.201600758.
- [16] C. Tuerk and L. Gold, “Systematic Evolution of Ligands by Exponential Enrichment: RNA Ligands to Bacteriophage T4 DNA Polymerase,” *Science*, vol. 249, no. 4968, pp. 505–510, Aug. 3, 1990, ISSN: 0036-8075, DOI: 10.1126/science.2200121.
- [17] L. Zhang *et al.*, “Point-of-care-testing of nucleic acids by microfluidics,” *TrAC Trends in Analytical Chemistry*, vol. 94, pp. 106–116, Sep. 2017, ISSN: 01659936, DOI: 10.1016/j.trac.2017.07.013.
- [18] H. Zhang *et al.*, “Gene detection: An essential process to precision medicine,” *Biosensors and Bioelectronics*, vol. 99, pp. 625–636, Jan. 2018, ISSN: 09565663, DOI: 10.1016/j.bios.2017.08.033.
- [19] H. H. Nguyen *et al.*, “Immobilized Enzymes in Biosensor Applications,” *Materials*, vol. 12, no. 1, p. 121, Jan. 2, 2019, ISSN: 1996-1944, DOI: 10.3390/ma12010121.

- [20] A. Ahmed *et al.*, “Biosensors for Whole-Cell Bacterial Detection,” *Clinical Microbiology Reviews*, vol. 27, no. 3, pp. 631–646, Jul. 2014, ISSN: 0893-8512, 1098-6618, DOI: 10.1128/CMR.00120-13.
- [21] J. Y. Lichtenberg *et al.*, “Non-Specific Adsorption Reduction Methods in Biosensing,” *Sensors*, vol. 19, no. 11, p. 2488, May 31, 2019, ISSN: 1424-8220, DOI: 10.3390/s19112488.
- [22] A. Frutiger *et al.*, “Nonspecific Binding—Fundamental Concepts and Consequences for Biosensing Applications,” *Chemical Reviews*, vol. 121, no. 13, pp. 8095–8160, Jul. 14, 2021, ISSN: 0009-2665, 1520-6890, DOI: 10.1021/acs.chemrev.1c00044.
- [23] J. Homola, “Present and future of surface plasmon resonance biosensors,” *Analytical and Bioanalytical Chemistry*, vol. 377, no. 3, pp. 528–539, Oct. 1, 2003, ISSN: 1618-2642, 1618-2650, DOI: 10.1007/s00216-003-2101-0.
- [24] D. Dell’Atti *et al.*, “Development of combined DNA-based piezoelectric biosensors for the simultaneous detection and genotyping of high risk Human Papilloma Virus strains,” *Clinica Chimica Acta*, vol. 383, no. 1-2, pp. 140–146, Aug. 2007, ISSN: 00098981, DOI: 10.1016/j.cca.2007.05.009.
- [25] F. Zhang *et al.*, “Hierarchically imprinted polymer substrates for enhanced attachment of *Escherichia coli*,” *Journal of Colloid and Interface Science*, vol. 343, no. 1, pp. 109–114, Mar. 2010, ISSN: 00219797, DOI: 10.1016/j.jcis.2009.11.038.
- [26] J. Wu *et al.*, “Device integration of electrochemical biosensors,” *Nature Reviews Bioengineering*, vol. 1, no. 5, pp. 346–360, Feb. 24, 2023, ISSN: 2731-6092, DOI: 10.1038/s44222-023-00032-w.
- [27] D. Grieshaber *et al.*, “Electrochemical Biosensors - Sensor Principles and Architectures,” *Sensors*, vol. 8, no. 3, pp. 1400–1458, Mar. 7, 2008, ISSN: 1424-8220, DOI: 10.3390/s80314000.
- [28] G. S. Wilson and R. Gifford, “Biosensors for real-time in vivo measurements,” *Biosensors and Bioelectronics*, vol. 20, no. 12, pp. 2388–2403, Jun. 2005, ISSN: 09565663, DOI: 10.1016/j.bios.2004.12.003.
- [29] M. Xu *et al.*, “The label free picomolar detection of insulin in blood serum,” *Biosensors and Bioelectronics*, vol. 39, no. 1, pp. 21–25, Jan. 2013, ISSN: 09565663, DOI: 10.1016/j.bios.2012.06.014.
- [30] R. Sharma *et al.*, “Label-free electrochemical impedance biosensor to detect human interleukin-8 in serum with sub-pg/ml sensitivity,” *Biosensors and Bioelectronics*, vol. 80, pp. 607–613, Jun. 2016, ISSN: 09565663, DOI: 10.1016/j.bios.2016.02.028.

- [31] J. Ding and W. Qin, "Recent advances in potentiometric biosensors," *TrAC Trends in Analytical Chemistry*, vol. 124, p. 115 803, Mar. 2020, ISSN: 01659936, DOI: 10.1016/j.trac.2019.115803.
- [32] H. N. Po and N. M. Senozan, "The Henderson–Hasselbalch Equation: Its History and Limitations," Oregon State, Nov. 2011, [Online]. Available: <https://sites.science.oregonstate.edu/chemistry/courses/ch421/Previous%20pages/Course%20Docs%20Fall%202006/Henderson.pdf>.
- [33] P. Held, "Using Phenol Red to Assess pH in Tissue Culture Media," Agilent, 2022, [Online]. Available: <https://www.agilent.com/cs/library/applications/phenol-red-to-assess-ph-in-tissue-culture-media-5994-3391EN-agilent.pdf>.
- [34] Mettler Toledo, *A Guide to pH Measurement - the Theory and Practice of pH Applications*, 2013, [Online]. Available: https://www.mt.com/dam/non-indexed/po/pro/Brochures/IB_pH_Theory_Guide_EN_230113.pdf (Accessed: 29/8/2023).
- [35] D. C. Harris and C. A. Lucy, *Quantitative Chemical Analysis*, 9. ed. New York, NY: Freeman, 2016, ISBN: 978-1-4641-3538-5.
- [36] C. Silver, "Development and implementation of an extended-gate ion-sensitive field-effect-transistor (EGFET) biosensor for the detection of β -lactamase activity," University of York, 2021, [Online]. Available: <https://etheses.whiterose.ac.uk/29368/>.
- [37] Infineon Technologies, *BSS159N - Small-Signal-Transistor*, 2006, [Online]. Available: <https://www.farnell.com/datasheets/12522.pdf> (Accessed: 15/6/2023).
- [38] D. E. Yates *et al.*, "Site-binding model of the electrical double layer at the oxide/water interface," *Journal of the Chemical Society, Faraday Transactions 1: Physical Chemistry in Condensed Phases*, vol. 70, no. 0, p. 1807, 1974, ISSN: 0300-9599, DOI: 10.1039/f19747001807.
- [39] J. A. Davis and J. O. Leckie, "Surface ionization and complexation at the oxide/water interface II. Surface properties of amorphous iron oxyhydroxide and adsorption of metal ions," *Journal of Colloid and Interface Science*, vol. 67, no. 1, pp. 90–107, Oct. 1978, ISSN: 00219797, DOI: 10.1016/0021-9797(78)90217-5.
- [40] L. Knijff *et al.*, "Electric double layer at the metal-oxide/electrolyte interface," in *Encyclopedia of Solid-Liquid Interfaces*, Elsevier, 2024, pp. 567–575, ISBN: 978-0-323-85670-6, [Online]. Available: <https://linkinghub.elsevier.com/retrieve/pii/B978032385669000012X> (Accessed: 24/9/2023).
- [41] L. Bousse *et al.*, "Operation of chemically sensitive field-effect sensors as a function of the insulator-electrolyte interface," *IEEE Transactions on Electron Devices*, vol. 30, no. 10, pp. 1263–1270, Oct. 1983, ISSN: 0018-9383, DOI: 10.1109/T-ED.1983.21284.

- [42] T. W. Healy and L. R. White, "Ionizable surface group models of aqueous interfaces," *Advances in Colloid and Interface Science*, vol. 9, no. 4, pp. 303–345, Jun. 1978, ISSN: 00018686, DOI: 10.1016/0001-8686(78)85002-7.
- [43] A. Hutin, "Difference between Isoelectric point (IEP), Point of zero charge (PZC), and Isoionic point (IIP)," Mar. 16, 2022, DOI: 10.5281/ZENODO.6346860.
- [44] B. B. Damaskin and O. A. Petrii, "Historical development of theories of the electrochemical double layer," *Journal of Solid State Electrochemistry*, vol. 15, no. 7-8, pp. 1317–1334, Jul. 2011, ISSN: 1432-8488, DOI: 10.1007/s10008-011-1294-y.
- [45] H. Helmholtz, "Studien über elektrische grenzschichten," *Annalen der Physik*, vol. 243, no. 7, pp. 337–382, 1879, DOI: 10.1002/andp.18792430702.
- [46] D. L. Chapman, "A contribution to the theory of electrocapillarity," *The London, Edinburgh, and Dublin Philosophical Magazine and Journal of Science*, vol. 25, no. 148, pp. 475–481, 1913, DOI: 10.1080/14786440408634187.
- [47] O. Stern, "Zur theorie der elektrolytischen doppelschicht," *Zeitschrift für Elektrochemie und angewandte physikalische Chemie*, vol. 30, no. 21-22, pp. 508–516, 1924, DOI: 10.1002/bbpc.192400182.
- [48] R. Van Hal *et al.*, "A novel description of ISFET sensitivity with the buffer capacity and double-layer capacitance as key parameters," *Sensors and Actuators B: Chemical*, vol. 24, no. 1-3, pp. 201–205, Mar. 1995, ISSN: 09254005, DOI: 10.1016/0925-4005(95)85043-0.
- [49] H. Yang *et al.*, "Towards understanding the effects of van der Waals strengths on the electric double-layer structures and capacitive behaviors," *Journal of Power Sources*, vol. 366, pp. 218–225, Oct. 2017, ISSN: 03787753, DOI: 10.1016/j.jpowsour.2017.09.036.
- [50] Yuanqi Hu and P. Georgiou, "A Robust ISFET pH-Measuring Front-End for Chemical Reaction Monitoring," *IEEE Transactions on Biomedical Circuits and Systems*, vol. 8, no. 2, pp. 177–185, Apr. 2014, ISSN: 1932-4545, 1940-9990, DOI: 10.1109/TBCAS.2014.2313512.
- [51] D. A. Borkholder, "Cell Based Biosensors Using Microelectrodes," Stanford University, 1998, [Online]. Available: <https://digitalarchive.rit.edu/xmlui/bitstream/handle/1850/5746/DBorkholderDissertation11-1998.pdf> (Accessed: 17/9/2023).
- [52] Y. Hu, "Advanced sensing and processing methodologies for ISFET based DNA sequencing," Imperial College of Science, Technology and Medicine, 2015, [Online]. Available: <https://spiral.imperial.ac.uk/handle/10044/1/25760> (Accessed: 17/9/2023).

- [53] P. Bergveld, "ISFET, Theory and Practice," presented at the IEEE Sensor Conference, Toronto, 2003, pp. 1–26, [Online]. Available: https://www.idc-online.com/technical_references/pdfs/mechanical_engineering/ISFET-Bergveld.pdf.
- [54] A. J. Bard and L. R. Faulkner, *Electrochemical Methods: Fundamentals and Applications*, 2nd ed. New York: Wiley, 2001, 833 pp., ISBN: 978-0-471-04372-0.
- [55] A. Fog and R. P. Buck, "Electronic semiconducting oxides as pH sensors," *Sensors and Actuators*, vol. 5, no. 2, pp. 137–146, Feb. 1984, ISSN: 02506874, DOI: 10.1016/0250-6874(84)80004-9.
- [56] C. Bock and V. Birss, "Anion and water involvement in hydrous Ir oxide redox reactions in acidic solutions," *Journal of Electroanalytical Chemistry*, vol. 475, no. 1, pp. 20–27, Oct. 1999, ISSN: 15726657, DOI: 10.1016/S0022-0728(99)00330-7.
- [57] W.-D. Huang *et al.*, "A flexible pH sensor based on the iridium oxide sensing film," *Sensors and Actuators A: Physical*, vol. 169, no. 1, pp. 1–11, Sep. 2011, ISSN: 09244247, DOI: 10.1016/j.sna.2011.05.016.
- [58] G. Jerkiewicz, "Standard and Reversible Hydrogen Electrodes: Theory, Design, Operation, and Applications," *ACS Catalysis*, vol. 10, no. 15, pp. 8409–8417, Aug. 7, 2020, ISSN: 2155-5435, 2155-5435, DOI: 10.1021/acscatal.0c02046.
- [59] M. W. Shinwari *et al.*, "Microfabricated Reference Electrodes and their Biosensing Applications," *Sensors*, vol. 10, no. 3, pp. 1679–1715, Mar. 2, 2010, ISSN: 1424-8220, DOI: 10.3390/s100301679.
- [60] U. Guth *et al.*, "Solid-state reference electrodes for potentiometric sensors," *Journal of Solid State Electrochemistry*, vol. 13, no. 1, pp. 27–39, Jan. 2009, ISSN: 1432-8488, 1433-0768, DOI: 10.1007/s10008-008-0574-7.
- [61] C. Duarte-Guevara *et al.*, "On-chip metal/polypyrrole quasi-reference electrodes for robust ISFET operation," *The Analyst*, vol. 140, no. 10, pp. 3630–3641, 2015, ISSN: 0003-2654, 1364-5528, DOI: 10.1039/C5AN00085H.
- [62] ALS Japan. *Reference electrode for Aqueous solution (Ag/AgCl type) RE-1CP*, (2023), [Online]. Available: <https://www.als-japan.com/1388.html#defaultTab14> (Accessed: 18/6/2023).
- [63] K. Lemon. *What is the difference between a single junction and double junction pH electrode?*, Camlab. (June 2017), [Online]. Available: <https://camlab.info/what-is-the-difference-between-a-single-junction-and-double-junction-ph-electrode/> (Accessed: 23/8/2023).
- [64] ALS Japan. *Silver-silver chloride electrode - Technical Note*, (2023), [Online]. Available: <https://www.als-japan.com/1638.html> (Accessed: 18/6/2023).

- [65] P. Bergveld, "Development of an Ion-Sensitive Solid-State Device for Neurophysiological Measurements," *IEEE Transactions on Biomedical Engineering*, vol. BME-17, no. 1, pp. 70–71, Jan. 1970, ISSN: 0018-9294, DOI: 10.1109/TBME.1970.4502688.
- [66] J. M. Rothberg *et al.*, "An integrated semiconductor device enabling non-optical genome sequencing," *Nature*, vol. 475, no. 7356, pp. 348–352, Jul. 2011, ISSN: 0028-0836, 1476-4687, DOI: 10.1038/nature10242.
- [67] C. Toumazou *et al.*, "Simultaneous DNA amplification and detection using a pH-sensing semiconductor system," *Nature Methods*, vol. 10, no. 7, pp. 641–646, Jul. 2013, ISSN: 1548-7091, 1548-7105, DOI: 10.1038/nmeth.2520.
- [68] A. Errachid *et al.*, "FET-Based Chemical Sensor Systems Fabricated with Standard Technologies," *Electroanalysis*, vol. 16, no. 22, pp. 1843–1851, Nov. 2004, ISSN: 1040-0397, 1521-4109, DOI: 10.1002/elan.200403072.
- [69] T. Yeow *et al.*, "A very large integrated pH-ISFET sensor array chip compatible with standard CMOS processes," *Sensors and Actuators B: Chemical*, vol. 44, no. 1-3, pp. 434–440, Oct. 1997, ISSN: 09254005, DOI: 10.1016/S0925-4005(97)00207-4.
- [70] J. Bausells *et al.*, "Ion-sensitive field-effect transistors fabricated in a commercial CMOS technology," *Sensors and Actuators B: Chemical*, vol. 57, no. 1-3, pp. 56–62, Sep. 1999, ISSN: 09254005, DOI: 10.1016/S0925-4005(99)00135-5.
- [71] E. Salm *et al.*, "Electrical Detection of Nucleic Acid Amplification Using an On-Chip Quasi-Reference Electrode and a PVC REFET," *Analytical Chemistry*, vol. 86, no. 14, pp. 6968–6975, Jul. 15, 2014, ISSN: 0003-2700, DOI: 10.1021/ac500897t.
- [72] B. Veigas *et al.*, "Ion sensing (EIS) real-time quantitative monitorization of isothermal DNA amplification," *Biosensors and Bioelectronics*, vol. 52, pp. 50–55, Feb. 2014, ISSN: 09565663, DOI: 10.1016/j.bios.2013.08.029.
- [73] J. Zhang *et al.*, "Sweat Biomarker Sensor Incorporating Picowatt, Three-Dimensional Extended Metal Gate Ion Sensitive Field Effect Transistors," *ACS Sensors*, vol. 4, no. 8, pp. 2039–2047, Aug. 23, 2019, ISSN: 2379-3694, 2379-3694, DOI: 10.1021/acssensors.9b00597.
- [74] N. Moser *et al.*, "ISFETs in CMOS and Emergent Trends in Instrumentation: A Review," *IEEE Sensors Journal*, vol. 16, no. 17, pp. 6496–6514, Sep. 2016, ISSN: 1530-437X, 1558-1748, 2379-9153, DOI: 10.1109/JSEN.2016.2585920.
- [75] J.-L. Chiang *et al.*, "Study on Light and Temperature Properties of AlN pH-Ion-Sensitive Field-Effect Transistor Devices," *Japanese Journal of Applied Physics*, vol. 44, p. 4831, 7R Jul. 1, 2005, ISSN: 0021-4922, 1347-4065, DOI: 10.1143/JJAP.44.4831.

- [76] J.-L. Chiang *et al.*, “Drift and Hysteresis Effects on AlN/SiO₂ Gate pH Ion-Sensitive Field-Effect Transistor,” *Japanese Journal of Applied Physics*, vol. 42, pp. 4973–4977, Part 1, No. 8 Aug. 15, 2003, ISSN: 0021-4922, DOI: 10.1143/JJAP.42.4973.
- [77] S. Jamasb *et al.*, “A physical model for drift in pH ISFETs,” *Sensors and Actuators B: Chemical*, vol. 49, no. 1-2, pp. 146–155, Jun. 1998, ISSN: 09254005, DOI: 10.1016/S0925-4005(98)00040-9.
- [78] N. Moser *et al.*, “Mechanisms for enhancement of sensing performance in CMOS ISFET arrays using reactive ion etching,” *Sensors and Actuators B: Chemical*, vol. 292, pp. 297–307, Aug. 2019, ISSN: 09254005, DOI: 10.1016/j.snb.2019.04.031.
- [79] A. Errachid, “A simple REFET for pH detection in differential mode,” *Sensors and Actuators B: Chemical*, vol. 60, no. 1, pp. 43–48, Nov. 2, 1999, ISSN: 09254005, DOI: 10.1016/S0925-4005(99)00242-7.
- [80] N. Mokhtarifar *et al.*, “ITO/Glass as Extended-Gate of FET: A Low-Cost Method for Differential pH-Sensing in Alkaline Solutions,” *Journal of The Electrochemical Society*, vol. 166, no. 12, B896–B902, 2019, ISSN: 0013-4651, DOI: 10.1149/2.0401912jes.
- [81] J. van der spiegel *et al.*, “The extended gate chemically sensitive field effect transistor as multi-species microprobe,” *Sensors and Actuators*, vol. 4, pp. 291–298, Jan. 1983, ISSN: 02506874, DOI: 10.1016/0250-6874(83)85035-5.
- [82] S. Pullano *et al.*, “Deep Submicron EGFET Based on Transistor Association Technique for Chemical Sensing,” *Sensors*, vol. 19, no. 5, p. 1063, Mar. 2, 2019, ISSN: 1424-8220, DOI: 10.3390/s19051063.
- [83] C. H. Kao *et al.*, “Effects of Ti addition and annealing on high-k Gd₂O₃ sensing membranes on polycrystalline silicon for extended-gate field-effect transistor applications,” *Applied Surface Science*, vol. 286, pp. 328–333, Dec. 2013, ISSN: 01694332, DOI: 10.1016/j.apsusc.2013.09.080.
- [84] P. Bergveld, “Thirty years of ISFETOLOGY,” *Sensors and Actuators B: Chemical*, vol. 88, no. 1, pp. 1–20, Jan. 2003, ISSN: 09254005, DOI: 10.1016/S0925-4005(02)00301-5.
- [85] S. Pullano *et al.*, “EGFET-Based Sensors for Bioanalytical Applications: A Review,” *Sensors*, vol. 18, no. 11, p. 4042, Nov. 20, 2018, ISSN: 1424-8220, DOI: 10.3390/s18114042.
- [86] A. Hierlemann and H. Baltes, “CMOS-based chemical microsensors,” *The Analyst*, vol. 128, no. 1, pp. 15–28, Dec. 23, 2003, ISSN: 00032654, DOI: 10.1039/b208563c.
- [87] L.-L. Chi *et al.*, “Study on extended gate field effect transistor with tin oxide sensing membrane,” *Materials Chemistry and Physics*, vol. 63, no. 1, pp. 19–23, Feb. 2000, ISSN: 02540584, DOI: 10.1016/S0254-0584(99)00184-4.

- [88] N. M. Ahmed *et al.*, “Characteristics of Extended-Gate Field-Effect Transistor (EGFET) Based on Porous n-Type (111) Silicon for Use in pH Sensors,” *Journal of Electronic Materials*, vol. 46, no. 10, pp. 5804–5813, Oct. 2017, ISSN: 0361-5235, 1543-186X, DOI: 10.1007/s11664-017-5604-8.
- [89] T. Prodromakis *et al.*, “A Low-Cost Disposable Chemical Sensing Platform Based on Discrete Components,” *IEEE Electron Device Letters*, vol. 32, no. 3, pp. 417–419, Mar. 2011, ISSN: 0741-3106, 1558-0563, DOI: 10.1109/LED.2010.2099098.
- [90] S.-C. Hung *et al.*, “Investigation of extended-gate field-effect transistor pH sensors based on different-temperature-annealed bi-layer MWCNTs-In₂O₃ films,” *Nanoscale Research Letters*, vol. 9, no. 1, p. 502, Dec. 2014, ISSN: 1556-276X, DOI: 10.1186/1556-276X-9-502.
- [91] L.-T. Yin *et al.*, “Separate structure extended gate H⁺-ion sensitive field effect transistor on a glass substrate,” *Sensors and Actuators B: Chemical*, vol. 71, no. 1-2, pp. 106–111, 2000, DOI: 10.1016/S0925-4005(00)00613-4.
- [92] W.-J. Cho and C.-M. Lim, “Sensing properties of separative paper-based extended-gate ion-sensitive field-effect transistor for cost effective pH sensor applications,” *Solid-State Electronics*, vol. 140, pp. 96–99, Feb. 2018, ISSN: 00381101, DOI: 10.1016/j.sse.2017.10.025.
- [93] N. Mokhtarifar *et al.*, “Low-cost EGFET-based pH-sensor using encapsulated ITO/PET-electrodes,” in *2018 IEEE International Instrumentation and Measurement Technology Conference (I2MTC)*, Houston, TX: IEEE, May 2018, pp. 1–5, ISBN: 978-1-5386-2222-3, DOI: 10.1109/I2MTC.2018.8409571.
- [94] M. Zamora *et al.*, “Potentiometric textile-based pH sensor,” *Sensors and Actuators B: Chemical*, vol. 260, pp. 601–608, May 2018, ISSN: 09254005, DOI: 10.1016/j.snb.2018.01.002.
- [95] M. Kaisti *et al.*, “Hand-Held Transistor Based Electrical and Multiplexed Chemical Sensing System,” *ACS Sensors*, vol. 1, no. 12, pp. 1423–1431, Dec. 23, 2016, ISSN: 2379-3694, 2379-3694, DOI: 10.1021/acssensors.6b00520.
- [96] D. Moschou *et al.*, “Surface and Electrical Characterization of Ag/AgCl Pseudo-Reference Electrodes Manufactured with Commercially Available PCB Technologies,” *Sensors*, vol. 15, no. 8, pp. 18 102–18 113, Jul. 24, 2015, ISSN: 1424-8220, DOI: 10.3390/s150818102.
- [97] D. Moschou *et al.*, “All-plastic, low-power, disposable, continuous-flow PCR chip with integrated microheaters for rapid DNA amplification,” *Sensors and Actuators B: Chemical*, vol. 199, pp. 470–478, Aug. 2014, ISSN: 09254005, DOI: 10.1016/j.snb.2014.04.007.

- [98] D. Haci *et al.*, “Thermally Controlled Lab-on-PCB for Biomedical Applications,” in *2018 IEEE Biomedical Circuits and Systems Conference (BioCAS)*, Cleveland, OH: IEEE, Oct. 2018, pp. 1–4, ISBN: 978-1-5386-3603-9, DOI: 10.1109/BIOCAS.2018.8584664.
- [99] T.-H. Yang *et al.*, “Sensing Performance of EGFET pH Sensors with CuO Nanowires Fabricated on glass substrate,” *ECS Meeting Abstracts*, vol. MA2012-02, no. 35, pp. 2770–2770, Jun. 4, 2012, ISSN: 2151-2043, DOI: 10.1149/MA2012-02/35/2770.
- [100] S. Zaman *et al.*, “CuO nanoflowers as an electrochemical pH sensor and the effect of pH on the growth,” *Journal of Electroanalytical Chemistry*, vol. 662, no. 2, pp. 421–425, Nov. 2011, ISSN: 15726657, DOI: 10.1016/j.jelechem.2011.09.015.
- [101] N. C. S. Vieira *et al.*, “Indium tin oxide synthesized by a low cost route as SEG-FET pH sensor,” *Materials Research*, vol. 16, no. 5, pp. 1156–1160, Jul. 2, 2013, ISSN: 1980-5373, 1516-1439, DOI: 10.1590/S1516-14392013005000101.
- [102] I.-K. Lee *et al.*, “A Study on a Differential-Measurement Biosensor Using High Performance Extended-Gate Field-Effect-Transistors with TiO₂ Sensing Membranes,” *Sensor Letters*, vol. 12, no. 6, pp. 1003–1007, Jun. 1, 2014, ISSN: 1546-198X, DOI: 10.1166/sl.2014.3193.
- [103] T. Prodromakis *et al.*, “A novel design approach for developing chemical sensing platforms using inexpensive technologies,” in *2011 IEEE Biomedical Circuits and Systems Conference (BioCAS)*, San Diego, CA, USA: IEEE, Nov. 2011, pp. 369–372, ISBN: 978-1-4577-1470-2, DOI: 10.1109/BioCAS.2011.6107804.
- [104] T. Trantidou *et al.*, “The dual role of Parylene C in chemical sensing: Acting as an encapsulant and as a sensing membrane for pH monitoring applications,” *Sensors and Actuators B: Chemical*, vol. 186, pp. 1–8, Sep. 2013, ISSN: 09254005, DOI: 10.1016/j.snb.2013.05.077.
- [105] L. Manjakkal *et al.*, “Metal oxides based electrochemical pH sensors: Current progress and future perspectives,” *Progress in Materials Science*, vol. 109, p. 100635, Apr. 2020, ISSN: 00796425, DOI: 10.1016/j.pmatsci.2019.100635.
- [106] W. Olthuis *et al.*, “pH sensor properties of electrochemically grown iridium oxide,” *Sensors and Actuators B: Chemical*, vol. 2, no. 4, pp. 247–256, Oct. 1990, ISSN: 09254005, DOI: 10.1016/0925-4005(90)80150-X.
- [107] S. F. Cogan, “Neural Stimulation and Recording Electrodes,” *Annual Review of Biomedical Engineering*, vol. 10, no. 1, pp. 275–309, Aug. 1, 2008, ISSN: 1523-9829, 1545-4274, DOI: 10.1146/annurev.bioeng.10.061807.160518.
- [108] K. A. Yusof *et al.*, “EGFET pH Sensor Performance Dependence on Sputtered TiO₂ Sensing Membrane Deposition Temperature,” *Journal of Sensors*, vol. 2016, pp. 1–9, 2016, ISSN: 1687-725X, 1687-7268, DOI: 10.1155/2016/7594531.

- [109] Y. Xi *et al.*, “Fabrication and Characterization of Iridium Oxide pH Microelectrodes Based on Sputter Deposition Method,” *Sensors*, vol. 21, no. 15, p. 4996, Jul. 23, 2021, ISSN: 1424-8220, DOI: 10.3390/s21154996.
- [110] L. D. Burke *et al.*, “Preparation of an oxidized iridium electrode and the variation of its potential with pH,” *Journal of Electroanalytical Chemistry and Interfacial Electrochemistry*, vol. 163, no. 1-2, pp. 117–128, Mar. 1984, ISSN: 00220728, DOI: 10.1016/S0022-0728(84)80045-5.
- [111] P. Steegstra *et al.*, “Revisiting the Redox Properties of Hydrous Iridium Oxide Films in the Context of Oxygen Evolution,” *The Journal of Physical Chemistry C*, vol. 117, no. 40, pp. 20 975–20 981, Oct. 10, 2013, ISSN: 1932-7447, DOI: 10.1021/jp407030r.
- [112] A. R. Hillman *et al.*, “X-Ray spectroscopy of electrochemically deposited iridium oxide films: Detection of multiple sites through structural disorder,” *Phys. Chem. Chem. Phys.*, vol. 13, no. 12, pp. 5252–5263, 2011, ISSN: 1463-9076, DOI: 10.1039/C0CP01472A.
- [113] M. Hüppauff and B. Lengeler, “Valency and Structure of Iridium in Anodic Iridium Oxide Films,” *Journal of The Electrochemical Society*, vol. 140, no. 3, pp. 598–602, Mar. 1, 1993, ISSN: 0013-4651, 1945-7111, DOI: 10.1149/1.2056127.
- [114] L. D. Burke and D. P. Whelan, “A voltammetric investigation of the charge storage reactions of hydrous iridium oxide layers,” *Journal of Electroanalytical Chemistry and Interfacial Electrochemistry*, vol. 162, no. 1, pp. 121–141, Mar. 9, 1984, ISSN: 0022-0728, DOI: 10.1016/S0022-0728(84)80159-X.
- [115] T. Y. Kim and S. Yang, “Fabrication method and characterization of electrodeposited and heat-treated iridium oxide films for pH sensing,” *Sensors and Actuators B: Chemical*, vol. 196, pp. 31–38, Jun. 2014, ISSN: 09254005, DOI: 10.1016/j.snb.2014.02.004.
- [116] S. A. M. Marzouk, “Improved Electrodeposited Iridium Oxide pH Sensor Fabricated on Etched Titanium Substrates,” *Analytical Chemistry*, vol. 75, no. 6, pp. 1258–1266, Mar. 1, 2003, ISSN: 0003-2700, DOI: 10.1021/ac0261404.
- [117] M. Zea *et al.*, “Enhanced Performance Stability of Iridium Oxide-Based pH Sensors Fabricated on Rough Inkjet-Printed Platinum,” *ACS Applied Materials & Interfaces*, vol. 11, no. 16, pp. 15 160–15 169, Apr. 24, 2019, ISSN: 1944-8244, 1944-8252, DOI: 10.1021/acscami.9b03085.
- [118] S. A. N. Gowers *et al.*, “Development of a Minimally Invasive Microneedle-Based Sensor for Continuous Monitoring of β -Lactam Antibiotic Concentrations in Vivo,” *ACS Sensors*, vol. 4, no. 4, pp. 1072–1080, Apr. 26, 2019, ISSN: 2379-3694, 2379-3694, DOI: 10.1021/acssensors.9b00288.

- [119] H. A. Elsen *et al.*, “Effects of Electrodeposition Conditions and Protocol on the Properties of Iridium Oxide pH Sensor Electrodes,” *Journal of The Electrochemical Society*, vol. 156, no. 1, F1, 2009, ISSN: 00134651, DOI: 10.1149/1.3001924.
- [120] P. Woias *et al.*, “Modelling the short-time response of ISFET sensors,” *Sensors and Actuators B: Chemical*, vol. 24, no. 1-3, pp. 211–217, Mar. 1995, ISSN: 09254005, DOI: 10.1016/0925-4005(95)85045-7.
- [121] Y.-J. Kim *et al.*, “A Novel pH Microsensor with a Built-in Reference Electrode,” *Journal of the Korean Physical Society*, vol. 43, no. 5, p. 769, Nov. 15, 2003, DOI: 10.3938/jkps.43.769.
- [122] J. Hendrikse *et al.*, “A drift free nernstian iridium oxide pH sensor,” in *Proceedings of International Solid State Sensors and Actuators Conference (Transducers '97)*, vol. 2, Chicago, IL, USA: IEEE, 1997, pp. 1367–1370, ISBN: 978-0-7803-3829-6, DOI: 10.1109/SENSOR.1997.635491.
- [123] S. Anastasova *et al.*, “Multi-parametric rigid and flexible, low-cost, disposable sensing platforms for biomedical applications,” *Biosensors and Bioelectronics*, vol. 102, pp. 668–675, Apr. 2018, ISSN: 09565663, DOI: 10.1016/j.bios.2017.10.038.
- [124] N. Elgrishi *et al.*, “A Practical Beginner’s Guide to Cyclic Voltammetry,” *Journal of Chemical Education*, vol. 95, no. 2, pp. 197–206, Feb. 13, 2018, ISSN: 0021-9584, 1938-1328, DOI: 10.1021/acs.jchemed.7b00361.
- [125] Palmsens. *Knowledge Base - What is a Cyclic Voltammogram?*, (2023), [Online]. Available: <https://www.palmsens.com/knowledgebase-article/cyclic-voltammetry-what-is-a-cyclic-voltammogram/> (Accessed: 20/6/2023).
- [126] R. Meyer *et al.*, “Electrodeposited iridium oxide for neural stimulation and recording electrodes,” *IEEE Transactions on Neural Systems and Rehabilitation Engineering*, vol. 9, no. 1, pp. 2–11, Mar. 2001, ISSN: 1534-4320, 1558-0210, DOI: 10.1109/7333.918271.
- [127] H. Wang and L. Pilon, “Physical interpretation of cyclic voltammetry for measuring electric double layer capacitances,” *Electrochimica Acta*, vol. 64, pp. 130–139, Mar. 2012, ISSN: 00134686, DOI: 10.1016/j.electacta.2011.12.118.
- [128] K. Yamanaka, “Anodically Electrodeposited Iridium Oxide Films (AEIROF) from Alkaline Solutions for Electrochromic Display Devices,” *Japanese Journal of Applied Physics*, vol. 28, pp. 632–637, Part 1, No. 4 Apr. 20, 1989, ISSN: 0021-4922, 1347-4065, DOI: 10.1143/JJAP.28.632.
- [129] M. A. Petit and V. Plichon, “Anodic electrodeposition of iridium oxide films,” *Journal of Electroanalytical Chemistry*, vol. 444, no. 2, pp. 247–252, Mar. 1998, ISSN: 15726657, DOI: 10.1016/S0022-0728(97)00570-6.

- [130] J. E. Baur and T. W. Spaine, "Electrochemical deposition of iridium (IV) oxide from alkaline solutions of iridium(III) oxide," *Journal of Electroanalytical Chemistry*, vol. 443, no. 2, pp. 208–216, Feb. 1998, ISSN: 15726657, DOI: 10.1016/S0022-0728(97)00532-9.
- [131] P. Steegstra and E. Ahlberg, "Involvement of nanoparticles in the electrodeposition of hydrous iridium oxide films," *Electrochimica Acta*, vol. 68, pp. 206–213, Apr. 2012, ISSN: 00134686, DOI: 10.1016/j.electacta.2012.02.058.
- [132] P. Steegstra, "Hydrous iridium oxide for in situ pH sensing: Electrodeposition, properties and applications," Department of Chemistry and Molecular Biology, Faculty of Science, University of Gothenburg, Göteborg, 2013, [Online]. Available: <https://gupea.ub.gu.se/handle/2077/29100>.
- [133] H. A. Elsen, "Thermodynamic and Dynamic Investigations of Hydrated Iridium Oxide Potentiometric pH Micro-Sensors," University of California, Berkeley, 2008.
- [134] S. Kakooei *et al.*, "Electrochemical Study of Iridium Oxide Coating on Stainless Steel Substrate," *International Journal of Electrochemical Science*, vol. 8, no. 3, pp. 3290–3301, Mar. 2013, ISSN: 14523981, DOI: 10.1016/S1452-3981(23)14390-2.
- [135] I. Ges *et al.*, "Thin-film IrO pH microelectrode for microfluidic-based microsystems," *Biosensors and Bioelectronics*, vol. 21, no. 2, pp. 248–256, Aug. 15, 2005, ISSN: 09565663, DOI: 10.1016/j.bios.2004.09.021.
- [136] I. G. Casella *et al.*, "Anodic electrodeposition of iridium oxide particles on glassy carbon surfaces and their electrochemical/SEM/XPS characterization," *Journal of Electroanalytical Chemistry*, vol. 736, pp. 147–152, Jan. 2015, ISSN: 15726657, DOI: 10.1016/j.jelechem.2014.11.012.
- [137] A. Awad *et al.*, "Removal of tarnishing and roughness of copper surface by electropolishing treatment," *Applied Surface Science*, vol. 256, no. 13, pp. 4370–4375, Apr. 2010, ISSN: 01694332, DOI: 10.1016/j.apsusc.2010.02.033.
- [138] G. Yang *et al.*, "Electropolishing of surfaces: Theory and applications," *Surface Engineering*, vol. 33, no. 2, pp. 149–166, Feb. 2017, ISSN: 0267-0844, 1743-2944, DOI: 10.1080/02670844.2016.1198452.
- [139] K. Park *et al.*, "Study of Cu Electrochemical Polishing Mechanism With Observation of Water Acceptor Diffusion," *Frontiers in Chemistry*, vol. 9, p. 763 508, Oct. 21, 2021, ISSN: 2296-2646, DOI: 10.3389/fchem.2021.763508.
- [140] O. Lebedeva *et al.*, "Surface State of Sacrificial Copper Electrode by Electropolishing in Hydrophobic Ionic Liquid 1-Butyl-3-methylimidazolium bis(trifluoromethylsulfonyl)imide," *ACS Applied Materials & Interfaces*, vol. 5, no. 21, pp. 10 551–10 558, Nov. 13, 2013, ISSN: 1944-8244, 1944-8252, DOI: 10.1021/am402213r.

- [141] E. Pircher *et al.*, “Electropolishing of Copper Alloys in Phosphoric Acid Solutions with Alcohols,” Echem Kompetenzzentrum für Angewandte Electrochemie GmbH, Technical Article, May 2003, [Online]. Available: <https://www.nmfr.org/pdf/psf2003/050374.pdf> (Accessed: 22/7/2023).
- [142] O. Lebedeva *et al.*, “Advantages of Electrochemical Polishing of Metals and Alloys in Ionic Liquids,” *Metals*, vol. 11, no. 6, p. 959, Jun. 14, 2021, ISSN: 2075-4701, DOI: 10.3390/met11060959.
- [143] Karim *et al.*, “The Anodic Behaviour of Bulk Copper in Ethaline and 1-Butyl-3-Methylimidazolium Chloride,” *Applied Sciences*, vol. 9, no. 20, p. 4401, Oct. 17, 2019, ISSN: 2076-3417, DOI: 10.3390/app9204401.
- [144] G. Di Carmine *et al.*, “Deep eutectic solvents: Alternative reaction media for organic oxidation reactions,” *Reaction Chemistry & Engineering*, vol. 6, no. 4, pp. 582–598, 2021, ISSN: 2058-9883, DOI: 10.1039/D0RE00458H.
- [145] P. Moraille *et al.*, “Experimental methods in chemical engineering: Atomic force microscopy – AFM,” *The Canadian Journal of Chemical Engineering*, vol. 100, no. 10, pp. 2778–2806, Oct. 2022, ISSN: 0008-4034, 1939-019X, DOI: 10.1002/cjce.24407.
- [146] Oxford Instruments Asylum Research, *Measuring Surface Roughness with the Asylum Research Jupiter XR Atomic Force Microscope*, Mar. 24, 2020, [Online]. Available: <https://afm.oxinst.com/outreach/is-afm-the-best-tool-for-your-surface-roughness-measurements> (Accessed: 8/2/2023).
- [147] ThermoFisher Scientific, “Scanning Electron Microscopy Working Principle,” 2019, [Online]. Available: <https://assets.thermofisher.com/TFS-Assets/MSD/Reference-Materials/WP0016-scanning-electron-microscopy-working-principle.pdf> (Accessed: 21/5/2023).
- [148] ThermoFisher. *Principles of Scanning Electron Microscopy - Material Science Learning Centre*, (2021), [Online]. Available: <https://www.thermofisher.com/uk/en/home/materials-science/learning-center/applications/scanning-electron-microscope-sem-electron-column.html> (Accessed: 21/6/2023).
- [149] P. Whiteside *et al.*, “Techniques and Challenges for Characterizing Metal Thin Films with Applications in Photonics,” *Coatings*, vol. 6, no. 3, p. 35, Aug. 17, 2016, ISSN: 2079-6412, DOI: 10.3390/coatings6030035.
- [150] Ponor. *Electron–matter interaction volume and types of signal generated*, Wikipedia. (2020), [Online]. Available: https://commons.wikimedia.org/wiki/File:Electron-matter_interaction_volume_and_various_types_of_signal_generated_-_v2.svg (Accessed: 21/6/2023).

- [151] JEOL, “Scanning Electron Microscope A To Z,” Japan, Knowledge Base, 2013, [Online]. Available: https://www.jeol.com/applications/pdf/sm/sem_atoz_all.pdf (Accessed: 13/8/2023).
- [152] Oxford Instruments. *What is EDS/EDX?*, (2023), [Online]. Available: <https://nano.oxinst.com/campaigns/what-is-eds/edx> (Accessed: 21/6/2023).
- [153] R. Jenkins *et al.*, “IUPAC—nomenclature system for x-ray spectroscopy,” *X-Ray Spectrometry*, vol. 20, no. 3, pp. 149–155, Jun. 1991, ISSN: 0049-8246, 1097-4539, DOI: 10.1002/xrs.1300200308.
- [154] Wikipedia. *Siegbahn notation*, (2023), [Online]. Available: https://en.wikipedia.org/wiki/Siegbahn_notation (Accessed: 30/6/2023).
- [155] Muso. *Principle of EDS*, Wikipedia. (2007), [Online]. Available: <https://commons.wikimedia.org/wiki/File:EDX-scheme.svg> (Accessed: 21/6/2023).
- [156] J. Moulder *et al.*, *Handbook of X-ray Photoelectron Spectroscopy*. Perkin-Elmer Corporation, 1992.
- [157] ThermoFisher Scientific. *X-Ray Photoelectron Spectroscopy*, (2023), [Online]. Available: <https://www.thermofisher.com/uk/en/home/materials-science/xps-technology.html> (Accessed: 9/7/2023).
- [158] ThermoFisher Scientific, *X-Ray Photoelectron Spectroscopy*. John Wiley and Sons Inc., 2016, [Online]. Available: <https://assets.thermofisher.com/TFS-Assets/MSD/brochures/xps-wiley-booklet.pdf> (Accessed: 9/7/2023).
- [159] National Institute of Standards and Technology, *X-ray Photoelectron Spectroscopy Database XPS, Version 4.1, NIST Standard Reference Database 20*, 2000, DOI: 10.18434/T4T88K.
- [160] V. Pfeifer *et al.*, “The electronic structure of iridium and its oxides: The electronic structure of iridium and its oxides,” *Surface and Interface Analysis*, vol. 48, no. 5, pp. 261–273, May 2016, ISSN: 01422421, DOI: 10.1002/sia.5895.
- [161] S. J. Freakley *et al.*, “The X-ray photoelectron spectra of Ir, IrO₂ and IrCl₃ revisited: The X-ray photoelectron spectra of Ir, IrO₂ and IrCl₃ revisited,” *Surface and Interface Analysis*, vol. 49, no. 8, pp. 794–799, Aug. 2017, ISSN: 01422421, DOI: 10.1002/sia.6225.
- [162] C. D. Wagner *et al.*, “Empirical atomic sensitivity factors for quantitative analysis by electron spectroscopy for chemical analysis,” *Surface and Interface Analysis*, vol. 3, no. 5, pp. 211–225, Oct. 1981, ISSN: 0142-2421, 1096-9918, DOI: 10.1002/sia.740030506.
- [163] S. D. Giri and A. Sarkar, “Electrochemical Study of Bulk and Monolayer Copper in Alkaline Solution,” *Journal of The Electrochemical Society*, vol. 163, no. 3, H252–H259, 2016, ISSN: 0013-4651, 1945-7111, DOI: 10.1149/2.0071605jes.

- [164] A. Naseer and A. Y. Khan, "A study of growth and breakdown of passive film on copper surface by electrochemical impedance spectroscopy," *Turkish Journal of Chemistry*, Jan. 1, 2009, ISSN: 1303-6130, DOI: 10.3906/kim-0708-23.
- [165] A. A. Shaikh *et al.*, "Electrochemical Studies of the pH Dependence of Cu(II) Reduction in Aqueous Britton-Robinson Buffer Solution," *Int. J. Electrochem. Sci.*, vol. 6, p. 11, 2011, DOI: 10.1016/S1452-3981(23)18188-0.
- [166] J. Juodkazytė *et al.*, "Iridium Anodic Oxidation to Ir(III) and Ir(IV) Hydrrous Oxides," *Electroanalysis*, vol. 17, no. 11, pp. 947–952, Jun. 2005, ISSN: 1040-0397, 1521-4109, DOI: 10.1002/elan.200403200.
- [167] N. Otsu, "A Threshold Selection Method from Gray-Level Histograms," *IEEE Transactions on Systems, Man, and Cybernetics*, vol. 9, no. 1, pp. 62–66, Jan. 1979, ISSN: 0018-9472, 2168-2909, DOI: 10.1109/TSMC.1979.4310076.
- [168] J. Hu *et al.*, "Electrodeposition of highly ordered macroporous iridium oxide through self-assembled colloidal templates," *Journal of Materials Chemistry*, vol. 19, no. 23, p. 3855, 2009, ISSN: 0959-9428, 1364-5501, DOI: 10.1039/b900279k.
- [169] P. Steegstra and E. Ahlberg, "Influence of oxidation state on the pH dependence of hydrrous iridium oxide films," *Electrochimica Acta*, vol. 76, pp. 26–33, Aug. 2012, ISSN: 00134686, DOI: 10.1016/j.electacta.2012.04.143.
- [170] H. Kresse *et al.*, "The antibacterial drugs market," *Nature Reviews Drug Discovery*, vol. 6, no. 1, pp. 19–20, Jan. 2007, ISSN: 1474-1776, 1474-1784, DOI: 10.1038/nrd2226.
- [171] D. Moore. *Antibiotic Classification And Mechanism*, Ortho Bullets. (2023), [Online]. Available: <https://www.orthobullets.com/basic-science/9059/antibiotic-classification-and-mechanism> (Accessed: 19/7/2023).
- [172] L. M. Lima *et al.*, "B-lactam antibiotics: An overview from a medicinal chemistry perspective," *European Journal of Medicinal Chemistry*, vol. 208, p. 112829, Dec. 2020, ISSN: 02235234, DOI: 10.1016/j.ejmech.2020.112829.
- [173] B. Thakuria, "The Beta Lactam Antibiotics as an Empirical Therapy in a Developing Country: An Update on Their Current Status and Recommendations to Counter the Resistance against Them," *Journal of Clinical and Diagnostic research*, 2013, ISSN: 2249782X, DOI: 10.7860/JCDR/2013/5239.3052.
- [174] L. Fernández and R. E. W. Hancock, "Adaptive and Mutational Resistance: Role of Porins and Efflux Pumps in Drug Resistance," *Clinical Microbiology Reviews*, vol. 25, no. 4, pp. 661–681, Oct. 2012, ISSN: 0893-8512, DOI: 10.1128/CMR.00043-12.

- [175] T. P. T. Cushnie *et al.*, “Morphological and ultrastructural changes in bacterial cells as an indicator of antibacterial mechanism of action,” *Cellular and Molecular Life Sciences*, vol. 73, no. 23, pp. 4471–4492, Dec. 2016, ISSN: 1420-682X, 1420-9071, DOI: 10.1007/s00018-016-2302-2.
- [176] K. Bush, “Past and Present Perspectives on β -Lactamases,” *Antimicrobial Agents and Chemotherapy*, vol. 62, no. 10, e01076–18, Oct. 2018, ISSN: 0066-4804, 1098-6596, DOI: 10.1128/AAC.01076-18.
- [177] D. M. Livermore and D. F. J. Brown, “Detection of β -lactamase-mediated resistance,” *Journal of Antimicrobial Chemotherapy*, vol. 48, pp. 59–64, suppl_1 Jul. 1, 2001, ISSN: 1460-2091, 0305-7453, DOI: 10.1093/jac/48.suppl_1.59.
- [178] J. H. Jorgensen and M. J. Ferraro, “Antimicrobial Susceptibility Testing: A Review of General Principles and Contemporary Practices,” *Clinical Infectious Diseases*, vol. 49, no. 11, pp. 1749–1755, Dec. 2009, ISSN: 1058-4838, DOI: 10.1086/647952.
- [179] N. Woodford and A. Sundsfjord, “Molecular detection of antibiotic resistance: When and where?” *Journal of Antimicrobial Chemotherapy*, vol. 56, no. 2, pp. 259–261, Aug. 1, 2005, ISSN: 1460-2091, 0305-7453, DOI: 10.1093/jac/dki195.
- [180] G. M. Voets *et al.*, “A set of multiplex PCRs for genotypic detection of extended-spectrum β -lactamases, carbapenemases, plasmid-mediated AmpC β -lactamases and OXA β -lactamases,” *International Journal of Antimicrobial Agents*, vol. 37, no. 4, pp. 356–359, Apr. 2011, ISSN: 09248579, DOI: 10.1016/j.ijantimicag.2011.01.005.
- [181] L. Váradi *et al.*, “Methods for the detection and identification of pathogenic bacteria: Past, present, and future,” *Chemical Society Reviews*, vol. 46, no. 16, pp. 4818–4832, 2017, ISSN: 0306-0012, 1460-4744, DOI: 10.1039/C6CS00693K.
- [182] S. Khan *et al.*, “Rapid optical determination of β -lactamase and antibiotic activity,” *BMC Microbiology*, vol. 14, no. 1, p. 84, Dec. 2014, ISSN: 1471-2180, DOI: 10.1186/1471-2180-14-84.
- [183] A. Pitkälä *et al.*, “Comparison of Tests for Detection of β -Lactamase-Producing Staphylococci,” *Journal of Clinical Microbiology*, vol. 45, no. 6, pp. 2031–2033, Jun. 2007, ISSN: 0095-1137, 1098-660X, DOI: 10.1128/JCM.00621-07.
- [184] P. Nordmann *et al.*, “Rapid Detection of Extended-Spectrum- β -Lactamase-Producing Enterobacteriaceae,” *Journal of Clinical Microbiology*, vol. 50, no. 9, pp. 3016–3022, Sep. 2012, ISSN: 0095-1137, 1098-660X, DOI: 10.1128/JCM.00859-12.
- [185] S. D. Kotsakis *et al.*, “Detection of carbapenemase producing enterobacteria using an ion sensitive field effect transistor sensor,” *Scientific Reports*, vol. 11, no. 1, p. 12 061, Jun. 8, 2021, ISSN: 2045-2322, DOI: 10.1038/s41598-021-91202-6.

- [186] S. G. Waley, "The pH-dependence and group modification of β -lactamase I," *Biochemical Journal*, vol. 149, no. 3, pp. 547–551, Sep. 1, 1975, ISSN: 0264-6021, DOI: 10.1042/bj1490547.
- [187] R. Bicknell *et al.*, "The pH-dependence of class B and class C β -lactamases," *Biochemical Journal*, vol. 213, no. 1, pp. 61–66, Jul. 1, 1983, ISSN: 0264-6021, DOI: 10.1042/bj2130061.
- [188] B. R. Meyers *et al.*, "Pharmacokinetics of ampicillin-sulbactam in healthy elderly and young volunteers," *Antimicrobial Agents and Chemotherapy*, vol. 35, no. 10, pp. 2098–2101, Oct. 1991, ISSN: 0066-4804, 1098-6596, DOI: 10.1128/AAC.35.10.2098.
- [189] E. T. Urbansky and M. R. Schock, "Understanding, Deriving, and Computing Buffer Capacity," *Journal of Chemical Education*, vol. 77, no. 12, p. 1640, Dec. 2000, ISSN: 0021-9584, 1938-1328, DOI: 10.1021/ed077p1640.
- [190] M. Akova, "Sulbactam-containing β -lactamase inhibitor combinations," *Clinical Microbiology and Infection*, vol. 14, pp. 185–188, Jan. 2008, ISSN: 1198743X, DOI: 10.1111/j.1469-0691.2007.01847.x.
- [191] M. J. Zaworotko *et al.*, "Ampicillin acidity and formation constants with some metals and their thermodynamic parameters in different media. Crystal structures of two polymorphs isolated from the reaction of ampicillin with copper(II)," *Journal of Coordination Chemistry*, vol. 59, no. 1, pp. 65–84, Jan. 10, 2006, ISSN: 0095-8972, 1029-0389, DOI: 10.1080/00958970500330028.
- [192] D. A. Armbruster and T. Pry, "Limit of blank, limit of detection and limit of quantitation," *The Clinical Biochemist. Reviews*, vol. 29 Suppl 1, S49–52, Aug. 2008, ISSN: 0159-8090, pmid: 18852857, [Online]. Available: <https://www.ncbi.nlm.nih.gov/pmc/articles/PMC2556583/> (Accessed: 14/1/2023).
- [193] S. M. Mitchell *et al.*, "pH and temperature effects on the hydrolysis of three β -lactam antibiotics: Ampicillin, cefalotin and cefoxitin," *Science of The Total Environment*, vol. 466–467, pp. 547–555, Jan. 2014, ISSN: 00489697, DOI: 10.1016/j.scitotenv.2013.06.027.
- [194] W. Zhao *et al.*, "The review of Lab-on-PCB for biomedical application," *ELECTROPHORESIS*, vol. 41, no. 16-17, pp. 1433–1445, Sep. 2020, ISSN: 0173-0835, 1522-2683, DOI: 10.1002/elps.201900444.
- [195] Y. Temiz *et al.*, "Lab-on-a-chip devices: How to close and plug the lab?" *Microelectronic Engineering*, vol. 132, pp. 156–175, Jan. 2015, ISSN: 01679317, DOI: 10.1016/j.mee.2014.10.013.
- [196] Y.-J. Chang and H. You, "Progress of Microfluidics Based on Printed Circuit Board and its Applications," *Chinese Journal of Analytical Chemistry*, vol. 47, no. 7, pp. 965–975, Jul. 2019, ISSN: 18722040, DOI: 10.1016/S1872-2040(19)61169-2.

- [197] J. Li *et al.*, “USB-driven microfluidic chips on printed circuit boards,” *Lab on a Chip*, vol. 14, no. 5, p. 860, 2014, ISSN: 1473-0197, 1473-0189, DOI: 10.1039/c3lc51155c.
- [198] T. Mérian *et al.*, “Development and surface characterization of an electrowetting valve for capillary-driven microfluidics,” *Colloids and Surfaces A: Physicochemical and Engineering Aspects*, vol. 414, pp. 251–258, Nov. 2012, ISSN: 09277757, DOI: 10.1016/j.colsurfa.2012.08.020.
- [199] J. Tu *et al.*, “PDMS-based microfluidic devices using commoditized PCBs as masters with no specialized equipment required,” *RSC Advances*, vol. 7, no. 50, pp. 31 603–31 609, 2017, ISSN: 2046-2069, DOI: 10.1039/C7RA03899B.
- [200] Y. Xia and G. M. Whitesides, “Soft Lithography,” *Annual Review of Materials Science*, vol. 28, no. 1, pp. 153–184, Aug. 1998, ISSN: 0084-6600, DOI: 10.1146/annurev.matsci.28.1.153.
- [201] F. Perdignes, “Lab-on-PCB and Flow Driving: A Critical Review,” *Micromachines*, vol. 12, no. 2, p. 175, Feb. 10, 2021, ISSN: 2072-666X, DOI: 10.3390/mi12020175.
- [202] Y. Arango *et al.*, “Electrogates for stop-and-go control of liquid flow in microfluidics,” *Applied Physics Letters*, vol. 112, no. 15, p. 153 701, Apr. 9, 2018, ISSN: 0003-6951, 1077-3118, DOI: 10.1063/1.5019469.
- [203] P. G. De Gennes, “Wetting: Statics and dynamics,” *Reviews of Modern Physics*, vol. 57, no. 3, pp. 827–863, Jul. 1, 1985, ISSN: 0034-6861, DOI: 10.1103/RevModPhys.57.827.
- [204] J. Gillis. *Contact Angle - A diagram that shows the contact angle and interphase-energy between 3 phases (gas, liquid, solid)*, Wikipedia. (2006), [Online]. Available: https://commons.wikimedia.org/wiki/File:Contact_angle.svg (Accessed: 30/7/2023).
- [205] H. Moon *et al.*, “Low voltage electrowetting-on-dielectric,” *Journal of Applied Physics*, vol. 92, no. 7, pp. 4080–4087, Oct. 1, 2002, ISSN: 0021-8979, 1089-7550, DOI: 10.1063/1.1504171.
- [206] A. Gökaltun *et al.*, “Simple Surface Modification of Poly(dimethylsiloxane) via Surface Segregating Smart Polymers for Biomicrofluidics,” *Scientific Reports*, vol. 9, no. 1, p. 7377, May 14, 2019, ISSN: 2045-2322, DOI: 10.1038/s41598-019-43625-5.
- [207] J. R. Vig, “UV/ozone cleaning of surfaces,” *Journal of Vacuum Science & Technology A: Vacuum, Surfaces, and Films*, vol. 3, no. 3, pp. 1027–1034, May 1, 1985, ISSN: 0734-2101, 1520-8559, DOI: 10.1116/1.573115.
- [208] E. Spooner. *UV Ozone Cleaner - Overview*, Ossila. (2021), [Online]. Available: <https://www.ossila.com/products/uv-ozone-cleaner> (Accessed: 29/6/2023).

- [209] M. Mozetič, “Plasma-Stimulated Super-Hydrophilic Surface Finish of Polymers,” *Polymers*, vol. 12, no. 11, p. 2498, Oct. 27, 2020, ISSN: 2073-4360, DOI: 10.3390/polym12112498.
- [210] Henniker Plasma. *Plasma Technology - Surface Activation*, (2019), [Online]. Available: <https://plasmatreatment.co.uk/pt/plasma-technology-overview/plasma-surface-activation> (Accessed: 15/7/2023).
- [211] E. Spooner. *Surface Energy - Plasma Energy*, Ossila. (2021), [Online]. Available: <https://www.ossila.com/pages/a-guide-to-surface-energy> (Accessed: 30/6/2023).
- [212] W. Satoh *et al.*, “Electrowetting-based valve for the control of the capillary flow,” *Journal of Applied Physics*, vol. 103, no. 3, p. 034903, Feb. 2008, ISSN: 0021-8979, 1089-7550, DOI: 10.1063/1.2832629.
- [213] S. Mondal *et al.*, “Estimation of solid–liquid interfacial tension using curved surface of a soft solid,” *Proceedings of the National Academy of Sciences*, vol. 112, no. 41, pp. 12563–12568, Oct. 13, 2015, ISSN: 0027-8424, 1091-6490, DOI: 10.1073/pnas.1502642112.
- [214] Shijian Luo and C. Wong, “Effect of UV/ozone treatment on surface tension and adhesion in electronic packaging,” *IEEE Transactions on Components and Packaging Technologies*, vol. 24, no. 1, pp. 43–49, Mar. 2001, ISSN: 15213331, DOI: 10.1109/6144.910801.
- [215] N. Vasilakis *et al.*, “Long-lasting FR-4 surface hydrophilisation towards commercial PCB passive microfluidics,” *Applied Surface Science*, vol. 368, pp. 69–75, Apr. 2016, ISSN: 01694332, DOI: 10.1016/j.apsusc.2015.12.123.
- [216] T.-Y. Lin *et al.*, “Stability of UV/ozone-treated thermoplastics under different storage conditions for microfluidic analytical devices,” *RSC Adv.*, vol. 7, no. 59, pp. 37374–37379, 2017, ISSN: 2046-2069, DOI: 10.1039/C7RA07435B.
- [217] E. Cunaj *et al.*, “Stable hydrophilization of FR4 and polyimide-based substrates implemented in microfluidics-on-PCB,” *Surface and Coatings Technology*, vol. 334, pp. 292–299, Jan. 2018, ISSN: 02578972, DOI: 10.1016/j.surfcoat.2017.11.039.
- [218] K. J. Land *et al.*, “Low cost fabrication and assembly process for re-usable 3D polydimethylsiloxane (PDMS) microfluidic networks,” *Biomicrofluidics*, vol. 5, no. 3, Sep. 2011, ISSN: 1932-1058, DOI: 10.1063/1.3641859.
- [219] G. Comina *et al.*, “PDMS lab-on-a-chip fabrication using 3D printed templates,” *Lab Chip*, vol. 14, no. 2, pp. 424–430, 2014, ISSN: 1473-0197, 1473-0189, DOI: 10.1039/C3LC50956G.
- [220] B. Venzac *et al.*, “PDMS Curing Inhibition on 3D-Printed Molds: Why? Also, How to Avoid It?” *Analytical Chemistry*, vol. 93, no. 19, pp. 7180–7187, May 18, 2021, ISSN: 0003-2700, 1520-6882, DOI: 10.1021/acs.analchem.0c04944.

- [221] A. R. Naik *et al.*, “Electrowetting valves for sweat-based microfluidics,” *Microfluidics and Nanofluidics*, vol. 25, no. 1, p. 2, Jan. 2021, ISSN: 1613-4982, 1613-4990, DOI: 10.1007/s10404-020-02403-w.
- [222] Gwyddion. *Data Processing and Analysis - Graph Processing*, (2020), [Online]. Available: <http://gwyddion.net/documentation/user-guide-en/graph-processing.html> (Accessed: 11/5/2023).
- [223] F. He *et al.*, “A hybrid paper and microfluidic chip with electrowetting valves and colorimetric detection,” *The Analyst*, vol. 139, no. 12, p. 3002, 2014, ISSN: 0003-2654, 1364-5528, DOI: 10.1039/c3an01516e.
- [224] F. Leonardi *et al.*, “Modification of the gate electrode by self-assembled monolayers in flexible electrolyte-gated organic field effect transistors: Work function vs. capacitance effects,” *RSC Advances*, vol. 8, no. 48, pp. 27 509–27 515, 2018, ISSN: 2046-2069, DOI: 10.1039/C8RA05300F.
- [225] L. Tang and N. Y. Lee, “A facile route for irreversible bonding of plastic-PDMS hybrid microdevices at room temperature,” *Lab on a Chip*, vol. 10, no. 10, p. 1274, 2010, ISSN: 1473-0197, 1473-0189, DOI: 10.1039/b924753j.
- [226] M. Agostini *et al.*, “Polydimethylsiloxane (PDMS) irreversible bonding to untreated plastics and metals for microfluidics applications,” *APL Materials*, vol. 7, no. 8, p. 081 108, Aug. 2019, ISSN: 2166-532X, DOI: 10.1063/1.5070136.
- [227] N. R. Ali-Hasim *et al.*, “Irreversible bonding techniques for the fabrication of a leakage-free printed circuit board-based lab-on-chip in microfluidic platforms—a review,” *Measurement Science and Technology*, vol. 32, no. 5, p. 052 001, May 1, 2021, ISSN: 0957-0233, 1361-6501, DOI: 10.1088/1361-6501/abeb92.
- [228] Y. Chang and H. You, “Efficient Bond of PDMS and Printed Circuit Board with An Application on Continuous-flow Polymerase Chain Reaction,” *BioChip Journal*, vol. 14, no. 4, pp. 349–357, Dec. 2020, ISSN: 1976-0280, 2092-7843, DOI: 10.1007/s13206-020-4403-0.
- [229] H. Liu *et al.*, “Dielectric materials for electrowetting-on-dielectric actuation,” *Microsystem Technologies*, vol. 16, no. 3, pp. 449–460, Mar. 2010, ISSN: 0946-7076, 1432-1858, DOI: 10.1007/s00542-009-0933-z.
- [230] T. Patois *et al.*, “Microtribological and corrosion behaviors of 1H,1H,2H,2H-perfluorodecanethiol self-assembled films on copper surfaces,” *Surface and Coatings Technology*, vol. 205, no. 7, pp. 2511–2517, Dec. 2010, ISSN: 02578972, DOI: 10.1016/j.surfcoat.2010.09.052.
- [231] A. L. Eckermann *et al.*, “Electrochemistry of redox-active self-assembled monolayers,” *Coordination Chemistry Reviews*, vol. 254, no. 15-16, pp. 1769–1802, Aug. 2010, ISSN: 00108545, DOI: 10.1016/j.ccr.2009.12.023.

- [232] H. T. N. Le *et al.*, “Removal of Thiol-SAM on a Gold Surface for Re-Use of an Interdigitated Chain-Shaped Electrode,” *Materials*, vol. 15, no. 6, p. 2218, Mar. 17, 2022, ISSN: 1996-1944, DOI: 10.3390/ma15062218.
- [233] C. Miller *et al.*, “Adsorbed .omega.-hydroxy thiol monolayers on gold electrodes: Evidence for electron tunneling to redox species in solution,” *The Journal of Physical Chemistry*, vol. 95, no. 2, pp. 877–886, Jan. 1991, ISSN: 0022-3654, 1541-5740, DOI: 10.1021/j100155a072.
- [234] F. He and S. R. Nugen, “Automating fluid delivery in a capillary microfluidic device using low-voltage electrowetting valves,” *Microfluidics and Nanofluidics*, vol. 16, no. 5, pp. 879–886, May 2014, ISSN: 1613-4982, 1613-4990, DOI: 10.1007/s10404-013-1317-3.
- [235] M. M. Walczak *et al.*, “Reductive desorption of alkanethiolate monolayers at gold: A measure of surface coverage,” *Langmuir*, vol. 7, no. 11, pp. 2687–2693, Nov. 1991, ISSN: 0743-7463, 1520-5827, DOI: 10.1021/1a00059a048.
- [236] K. Sun *et al.*, “Electrochemical desorption of self-assembled monolayers and its applications in surface chemistry and cell biology,” *Journal of Electroanalytical Chemistry*, vol. 656, no. 1-2, pp. 223–230, Jun. 2011, ISSN: 15726657, DOI: 10.1016/j.jelechem.2010.11.008.
- [237] N. C. Ramos *et al.*, “Electrochemical Stability of Thiolate Self-Assembled Monolayers on Au, Pt, and Cu,” *ACS Applied Materials & Interfaces*, acsami.3c01224, Mar. 10, 2023, ISSN: 1944-8244, 1944-8252, DOI: 10.1021/acsami.3c01224.
- [238] S. C. Kwok *et al.*, “Chemisorption Threshold of Thiol-based Monolayer on Copper: Effect of Electric Potential and Elevated Temperature,” *Electrochimica Acta*, vol. 198, pp. 185–194, Apr. 2016, ISSN: 00134686, DOI: 10.1016/j.electacta.2016.03.068.
- [239] H. Keller *et al.*, “Surface chemistry of thiols on copper: An efficient way of producing multilayers,” *Thin Solid Films*, vol. 244, no. 1-2, pp. 799–805, May 1994, ISSN: 00406090, DOI: 10.1016/0040-6090(94)90574-6.
- [240] L. A. Pray. *Discovery of DNA Structure and Function: Watson and Crick*, Nature Education. (2008), [Online]. Available: <https://www.nature.com/scitable/topicpage/discovery-of-dna-structure-and-function-watson-397/> (Accessed: 19/6/2023).
- [241] T. Nolan *et al.*, “Quantification of mRNA using real-time RT-PCR,” *Nature Protocols*, vol. 1, no. 3, pp. 1559–1582, Aug. 2006, ISSN: 1754-2189, 1750-2799, DOI: 10.1038/nprot.2006.236.
- [242] P. Kralik and M. Ricchi, “A Basic Guide to Real Time PCR in Microbial Diagnostics: Definitions, Parameters, and Everything,” *Frontiers in Microbiology*, vol. 8, Feb. 2, 2017, ISSN: 1664-302X, DOI: 10.3389/fmicb.2017.00108.

- [243] F. Zhang *et al.*, “Portable pH-inspired electrochemical detection of DNA amplification,” *Chemical Communications*, vol. 50, no. 61, p. 8416, 2014, ISSN: 1359-7345, 1364-548X, DOI: 10.1039/c4cc03011g.
- [244] P. Gill and A. Ghaemi, “Nucleic Acid Isothermal Amplification Technologies—A Review,” *Nucleosides, Nucleotides and Nucleic Acids*, vol. 27, no. 3, pp. 224–243, Feb. 8, 2008, ISSN: 1525-7770, 1532-2335, DOI: 10.1080/15257770701845204.
- [245] T. Notomi, “Loop-mediated isothermal amplification of DNA,” *Nucleic Acids Research*, vol. 28, no. 12, 63e–63, Jun. 15, 2000, ISSN: 13624962, DOI: 10.1093/nar/28.12.e63.
- [246] N. Tomita *et al.*, “Loop-mediated isothermal amplification (LAMP) of gene sequences and simple visual detection of products,” *Nature Protocols*, vol. 3, no. 5, pp. 877–882, May 2008, ISSN: 1754-2189, 1750-2799, DOI: 10.1038/nprot.2008.57.
- [247] K. Nagamine *et al.*, “Accelerated reaction by loop-mediated isothermal amplification using loop primers,” *Molecular and Cellular Probes*, vol. 16, no. 3, pp. 223–229, Jun. 2002, ISSN: 08908508, DOI: 10.1006/mcpr.2002.0415.
- [248] M. Khan *et al.*, “Comparative Evaluation of the LAMP Assay and PCR-Based Assays for the Rapid Detection of *Alternaria solani*,” *Frontiers in Microbiology*, vol. 9, p. 2089, Sep. 3, 2018, ISSN: 1664-302X, DOI: 10.3389/fmicb.2018.02089.
- [249] G. J. Randhawa *et al.*, “Loop-Mediated Isothermal Amplification: Rapid Visual and Real-Time Methods for Detection of Genetically Modified Crops,” *Journal of Agricultural and Food Chemistry*, vol. 61, no. 47, pp. 11 338–11 346, Nov. 27, 2013, ISSN: 0021-8561, 1520-5118, DOI: 10.1021/jf4030085.
- [250] F. Wang *et al.*, “Rapid and Specific Detection of *Escherichia coli* Serogroups O26, O45, O103, O111, O121, O145, and O157 in Ground Beef, Beef Trim, and Produce by Loop-Mediated Isothermal Amplification,” *Applied and Environmental Microbiology*, vol. 78, no. 8, pp. 2727–2736, Apr. 15, 2012, ISSN: 0099-2240, 1098-5336, DOI: 10.1128/AEM.07975-11.
- [251] N. A. Tanner *et al.*, “Visual detection of isothermal nucleic acid amplification using pH-sensitive dyes,” *BioTechniques*, vol. 58, no. 2, pp. 59–68, Feb. 2015, ISSN: 0736-6205, 1940-9818, DOI: 10.2144/000114253.
- [252] M. Goto *et al.*, “Colorimetric detection of loop-mediated isothermal amplification reaction by using hydroxy naphthol blue,” *BioTechniques*, vol. 46, no. 3, pp. 167–172, Mar. 2009, ISSN: 0736-6205, 1940-9818, DOI: 10.2144/000113072.
- [253] A. T. Scott *et al.*, “Comparative Evaluation and Quantitative Analysis of Loop-Mediated Isothermal Amplification Indicators,” *Analytical Chemistry*, vol. 92, no. 19, pp. 13 343–13 353, Oct. 6, 2020, ISSN: 0003-2700, 1520-6882, DOI: 10.1021/acs.analchem.0c02666.

- [254] R. A. Jefferson *et al.*, “Beta-Glucuronidase from *Escherichia coli* as a gene-fusion marker,” *Proceedings of the National Academy of Sciences*, vol. 83, no. 22, pp. 8447–8451, Nov. 1986, ISSN: 0027-8424, 1091-6490, DOI: 10.1073/pnas.83.22.8447.
- [255] N. M. Nichols and N. A. Tanner, “Using aptamers to control enzyme activities: Hot Start Taq and beyond,” New England Biolabs (NEB), 2022, [Online]. Available: https://uk.neb.com/-/media/nebus/files/feature-articles/nebexpressions_aptamer_taq_feature_issuei_2018.pdf?rev=32fea417c85c40f791c98e0c0e18fed4&hash=C93DB1B954DBA5C3127C4417827AD155 (Accessed: 15/8/2023).
- [256] D. Zhou *et al.*, “Establishment and application of a loop-mediated isothermal amplification (LAMP) system for detection of cry1Ac transgenic sugarcane,” *Scientific Reports*, vol. 4, no. 1, p. 4912, May 9, 2014, ISSN: 2045-2322, DOI: 10.1038/srep04912.
- [257] I. Lazar. *GelAnalyzer*, GelAnalyzer. (June 2022), [Online]. Available: <http://www.gelanalyzer.com/index.html> (Accessed: 6/9/2023).
- [258] M. N. Aoki *et al.*, “Colorimetric RT-LAMP SARS-CoV-2 diagnostic sensitivity relies on color interpretation and viral load,” *Scientific Reports*, vol. 11, no. 1, p. 9026, Apr. 27, 2021, ISSN: 2045-2322, DOI: 10.1038/s41598-021-88506-y.
- [259] P. Held, “Using Phenol Red to Assess pH in Tissue Culture Media,” Agilent, Application Note, 2022, [Online]. Available: <https://www.agilent.com/cs/library/applications/phenol-red-to-assess-ph-in-tissue-culture-media-5994-3391EN-agilent.pdf> (Accessed: 15/8/2023).
- [260] B. Özay and S. E. McCalla, “A review of reaction enhancement strategies for isothermal nucleic acid amplification reactions,” *Sensors and Actuators Reports*, vol. 3, p. 100 033, Nov. 2021, ISSN: 26660539, DOI: 10.1016/j.snr.2021.100033.
- [261] New England Biolabs (NEB). *How can I reduce nonspecific or non-template amplification?*, (2023), [Online]. Available: <https://uk.neb.com/faqs/2013/10/24/how-can-i-reduce-nonspecific-or-non-template-amplification> (Accessed: 12/8/2023).
- [262] E. Prediger. *Converting from nanograms to copy number*, Integrated DNA Technologies (IDT). (2008), [Online]. Available: <https://eu.idtdna.com/pages/education/decoded/article/calculations-converting-from-nanograms-to-copy-number> (Accessed: 11/9/2022).
- [263] F. R. Blattner *et al.*, “The Complete Genome Sequence of *Escherichia coli* K-12,” *Science*, vol. 277, no. 5331, pp. 1453–1462, Sep. 5, 1997, ISSN: 0036-8075, 1095-9203, DOI: 10.1126/science.277.5331.1453.

- [264] X. Gao *et al.*, “Pullulan reduces the non-specific amplification of loop-mediated isothermal amplification (LAMP),” *Analytical and Bioanalytical Chemistry*, vol. 411, no. 6, pp. 1211–1218, Feb. 2019, ISSN: 1618-2642, 1618-2650, DOI: 10.1007/s00216-018-1552-2.
- [265] M. Jang and S. Kim, “Inhibition of Non-specific Amplification in Loop-Mediated Isothermal Amplification via Tetramethylammonium Chloride,” *BioChip Journal*, vol. 16, no. 3, pp. 326–333, Sep. 2022, ISSN: 1976-0280, 2092-7843, DOI: 10.1007/s13206-022-00070-3.
- [266] Pine Research. *Reference Electrode Storage and Master Reference Electrodes*, (Nov. 2016), [Online]. Available: <https://pineresearch.com/shop/wp-content/uploads/sites/2/2016/12/DRP10031-Reference-Electrode-Storage-and-Master-Reference-Electrodes-REV001.pdf> (Accessed: 13/8/2023).
- [267] K. Davalieva and G. D. Efremov, “Influence of salts and PCR inhibitors on the amplification capacity of three thermostable DNA polymerases,” *Macedonian Journal of Chemistry and Chemical Engineering*, vol. 29, no. 1, pp. 57–62, Feb. 2010, ISSN: 1857–5552, DOI: 10.20450/mjccce.2010.173.
- [268] C. Schrader *et al.*, “PCR inhibitors - occurrence, properties and removal,” *Journal of Applied Microbiology*, vol. 113, no. 5, pp. 1014–1026, Nov. 2012, ISSN: 13645072, DOI: 10.1111/j.1365-2672.2012.05384.x.
- [269] D. Cai *et al.*, “Capacity of rTth polymerase to detect RNA in the presence of various inhibitors,” *PLOS ONE*, vol. 13, no. 1, C. Dash, Ed., e0190041, Jan. 2, 2018, ISSN: 1932-6203, DOI: 10.1371/journal.pone.0190041.
- [270] M. Bruce *et al.*, *Analysis of the Effect of a Variety of PCR Inhibitors on the Amplification of DNA using Real Time PCR, Melt Curves and STR Analysis*, National Criminal Justice Reference Service (NCJRS), 2015, [Online]. Available: <https://www.ojp.gov/sites/g/files/xyckuh241/files/media/document/249148.pdf>.
- [271] R. Kodzius *et al.*, “Inhibitory effect of common microfluidic materials on PCR outcome,” *Sensors and Actuators B: Chemical*, vol. 161, no. 1, pp. 349–358, Jan. 2012, ISSN: 09254005, DOI: 10.1016/j.snb.2011.10.044.
- [272] A. Kuffel *et al.*, “Impact of metal ions on PCR inhibition and RT-PCR efficiency,” *International Journal of Legal Medicine*, vol. 135, no. 1, pp. 63–72, Jan. 2021, ISSN: 0937-9827, 1437-1596, DOI: 10.1007/s00414-020-02363-4.
- [273] L. I. Moreno and B. R. McCord, “Understanding metal inhibition: The effect of copper (Cu²⁺) on DNA containing samples,” *Forensic Chemistry*, vol. 4, pp. 89–95, Jun. 2017, ISSN: 24681709, DOI: 10.1016/j.forc.2017.03.005.